Université de Lille

中国科学技术大学
University of Science and Technology of China

PC2A

Science Island

AIOFM

Une thèse de doctorat présentée dans le cadre de l'accord de cotutelle entre l'Université de Lille et l'Université des Sciences et Technologies de Chine

par

ZHANG Cuihong

en vue de l'obtention du grade de docteur en

"Optique" et en "Chimie théorique, physique, analytique"

Étude expérimentale des réactions élémentaires d'importance atmosphérique: la réactivité des radicaux peroxyles

12 décembre 2023

Comité de jury

Prof. OKUMURA Mitchio *California Institute of Technology*	**Rapporteur**
Prof. KAJII Yoshizumi *Qingdao University and Kyoto University*	**Rapporteur**
Dr. SCHOEMAECKER Coralie *Université de Lille*	**Présidente de jury**
Prof. YU Yuanqin *Anhui University*	**Examinatrice**
Dr. LOISON Jean-Christophe *Université de Bordeaux*	**Examinateur**
Dr. FITTSCHEN Christa *Université de Lille*	**Directrice de thèse**
Prof. ZHANG Weijun *University of Science and Technology of China*	**Co-Directeur de thèse**
Prof. TANG Xiaofeng *University of Science and Technology of China*	**Co-Encadrant de thèse**

PhD thesis presented under the cotutelle agreement between the University of Lille and University of Science and Technology of China

by

ZHANG Cuihong

For obtaining the PhD degree in

"Optics" and "Theoretical, Physical, Analytical Chemistry"

Rate constants and product yields of atmospherically relevant reactions: case of the ethyl peroxy radical

December 12th 2023

Jury committee

Prof. OKUMURA Mitchio *California Institute of Technology*	**Reviewer**
Prof. KAJII Yoshizumi *Qingdao University and Kyoto University*	**Reviewer**
Dr. SCHOEMAECKER Coralie *University of Lille*	**President of the jury**
Prof. YU Yuanqin *Anhui University*	**Examiner**
Dr. LOISON Jean-Christophe *University of Bordeaux*	**Examiner**
Dr. FITTSCHEN Christa *University of Lille*	**Thesis director**
Dr. ZHANG Weijun *University of Science and Technology of China*	**Thesis Co-director**
Dr. TANG Xiaofeng *University of Science and Technology of China*	**Thesis Co-supervisor**

Contents

Résumé

Les radicaux peroxys sont des intermédiaires importants dans les réactions chimiques atmosphériques et jouent un rôle crucial dans les réactions en chaîne radicalaires atmosphériques. La cinétique des réactions chimiques et les informations sur les produits des radicaux sont des paramètres clés dans la simulation des modèles atmosphériques mondiaux et revêtent une grande importance pour la compréhension de questions scientifiques telles que la capacité d'oxydation atmosphérique, la pollution photochimique et la formation d'aérosols organiques secondaires. L'éthane est l'un des hydrocarbures non méthane les plus abondants dans l'atmosphère, et sa réaction d'oxydation dans l'atmosphère génère le radical peroxy éthylique $C_2H_5O_2$. Cependant, il y a des résultats de mesure incohérents dans l'étude de ses cinétiques d'auto- et de réaction croisée et encore des questions sur les cinétiques et des produits réactionnelles. Mesurer avec précision la constante de vitesse de réaction d'auto- et de réaction croisée et obtenir les informations sur le taux de ramification des produits de $C_2H_5O_2$ aidera à comprendre la chimie des radicaux peroxy $C_2H_5O_2$ dans les environnements à faible NOx et sa contribution aux OVOCs et aux sources d'aérosols organiques secondaires dans l'atmosphère.

Cette thèse utilise principalement la spectroscopie d'absorption dans le proche infrarouge et la spectrométrie de masse par photoionisation pour étudier la cinétique et les produits des réactions liées au $C_2H_5O_2$. Les spectres d'absorption des radicaux peroxys dans la région du proche infrarouge présentent des pics typiques, et l'absorption de différents radicaux peroxys peut être utilisée pour une détection sélective. Sur la base de la spectroscopie de cavité à déclin en mode continu (CRDS) à double chemin combinée à la photolyse par laser excimère, l'auto-réaction de $C_2H_5O_2$ et sa réaction croisée avec les radicaux peroxys CH_3O_2 ont été étudiées, et la constante de vitesse et le rapport de branchement ont été obtenus. De plus, les produits de la réaction d'auto- et de réaction croisée des radicaux peroxys ont été étudiés plus en détail à l'aide de la

spectrométrie de masse par photoionisation dans l'ultraviolet lointain, la spectroscopie de coïncidence photoélectron-photoion combinée à une source de lumière de rayonnement synchrotron. Les principaux contenus de cette thèse sont :

1. Mesures de la cinétique et des produits de la réaction d'auto-réaction du $C_2H_5O_2$. La photolyse au laser excimère pulsé à 351 nm d'un mélange $Cl_2/C_2H_6/O_2$ a été utilisée pour créer du $C_2H_5O_2$. Tout d'abord, la section efficace d'absorption du $C_2H_5O_2$ a été mesurée par deux méthodes pour quantifier le $C_2H_5O_2$, à savoir (1) la méthode aller-retour et (2) la méthode cinétique en mesurant la réaction de $C_2H_5O_2 + HO_2$. Les deux méthodes conduisent à la même section efficace d'absorption pour le $C_2H_5O_2$ de $\sigma = (1.0 \pm 0.2) \times 10^{-20}$ cm^2 au nombre d'onde de 7596.47 cm^{-1}. Ensuite, les cinétiques d'absorption sélectives et quantitatives de HO_2 et de $C_2H_5O_2$, mesurées simultanément, ont permis d'obtenir la constante de vitesse k et le rapport de branchement α de l'auto-réaction du $C_2H_5O_2$: $k(C_2H_5O_2 + C_2H_5O_2) = (1.0 \pm 0.2) \times 10^{-13}$ cm^3 s^{-1} et $\alpha(C_2H_5O) = 0.31 \pm 0.06$. Étant donné que des réactions secondaires telles que $C_2H_5O_2 + HO_2$ et $C_2H_5O_2 + C_2H_5O$ peuvent influencer les mesures cinétiques de l'auto-réaction du $C_2H_5O_2$, des expériences séparées ont été menées pour mesurer les constantes de vitesse de ces deux réactions : $k(C_2H_5O_2 + HO_2) = 6.2 \times 10^{-12}$ cm^3 s^{-1} et $k(C_2H_5O_2 + C_2H_5O) = 7 \times 10^{-12}$ cm^3 s^{-1}. Des constantes de vitesse et des rapports de branchement des produits ont été obtenus pour la réaction d'auto-réaction du $C_2H_5O_2$ par les mesures cinétiques, ce qui a résolu une divergence récemment apparue dans la littérature concernant la constante de vitesse et le rapport de branchement de cette réaction. À l'heure actuelle, le comité de l'IUPAC a mis à jour les valeurs recommandées, y compris la constante de vitesse et le rapport de branchement pour l'auto-réaction du $C_2H_5O_2$ et a déjà adopté les nouveaux résultats de la présente thèse.

Enfin, un réacteur d'écoulement rapide à décharge micro-onde combiné à la spectrométrie de masse par photoionisation dans l'ultraviolet lointain ainsi qu'un réacteur de photolyse laser combiné à la spectroscopie de coïncidence photoélectron-photoion avec source de lumière de rayonnement synchrotron ont également été utilisés pour étudier les produits et la cinétique de l'auto-réaction du $C_2H_5O_2$. Les résultats ont

montré que le rapport de branchement pour le produit dimère $C_2H_5OOC_2H_5$ était de (0.10 ± 0.05). Après avoir pris en compte la perte de transmission, la valeur limite supérieure de ce rapport de branchement pourrait expliquer la différence dans $\alpha(C_2H_5O)$ entre nos mesures et les mesures du produit final stable, c'est-à-dire que le rapport de branchement de $C_2H_5OOC_2H_5$ dans l'auto-réaction du $C_2H_5O_2$ peut peut-être ne pas être ignoré et sa décomposition pourrait contribuer dans les mesures du produit final stable à CH_3CHO, et donc entraîner un $\alpha(C_2H_5O)$ apparemment plus élevé.

2. Mesures de cinétique de $C_2H_5O_2$ avec CH_3O_2. Le $C_2H_5O_2$ et le CH_3O_2 ont été créés simultanément par photolyse au laser excimère à 351 nm d'un mélange $Cl_2/C_2H_6/CH_4/O_2$. L'absorption du $C_2H_5O_2$ et du CH_3O_2 a été mesurée de manière relativement sélective à 7601.66 cm^{-1} et 7488.13 cm^{-1}, et la cinétique d'apparition de HO_2 a également été mesurée. En utilisant un modèle pour ajuster les profils d'absorption-temps mesurés, la constante de vitesse et le rapport de branchement de la réaction croisée des deux radicaux ont été obtenus: $(3.8 \pm 1.0) \times 10^{-13}$ cm^3 s^{-1}, α (voie radicalaire): 0.40 ± 0.20.

Afin de minimiser l'absorption de la lumière proche infrarouge par les précurseurs méthane et éthane, ce qui entraîne une dégradation du signal, des concentrations des précurseurs suffisantes pour consommer rapidement les atomes de chlore n'ont pas pu être ajoutées dans l'expérience, ce qui entraîne à son tour une petite quantité de chlore réagissant avec RO_2 ($C_2H_5O_2$ et CH_3O_2). Par conséquent, des expériences séparées ont été menées pour étudier la cinétique des réactions $C_2H_5O_2$ + Cl et CH_3O_2 + Cl, respectivement. La photolyse laser excimère à 351 nm de $Cl/C_2H_6/O_2$ ou $Cl/CH_4/O_2$ a été utilisée pour créer du $C_2H_5O_2$ ou du CH_3O_2 individuellement. La cinétique de $C_2H_5O_2/CH_3O_2$ et de HO_2 a été mesurée, avec un modèle développé pour ajuster les résultats expérimentaux, la constante de vitesse et le rapport de branchement de $C_2H_5O_2/CH_3O_2$ avec Cl ont été obtenus. Enfin, le mécanisme RO_2 + Cl a été inclus dans le modèle utilisé pour déterminer la constante de vitesse de la réaction croisée $C_2H_5O_2$ + CH_3O_2.

3. Le CH_3CHO est produit dans l'auto-réaction du $C_2H_5O_2$ et dans la réaction

croisée du $C_2H_5O_2$ avec le CH_3O_2. La détection des produits de la réaction d'oxydation du CH_3CHO a été réalisée avec un tube à écoulement rapide couplé à une décharge micro-onde combiné à la spectroscopie de coïncidence photoélectron-photoion avec lumière de rayonnement synchrotron. La réaction de F/Cl avec le CH_3CHO donne deux radicaux isomères CH_3CO/CH_2CHO. Les spectres de photoionisation des deux radicaux isomères et des produits formés dans la réaction de F + CH_3CHO ont été déterminés. Le rapport de branchement des deux radicaux isomères dans la réaction de Cl + CH_3CHO a également été déterminé. Le processus de tautomérisation du CH_3CHO-CH_2CHOH et du CH_3COCH_3-CH_3COHCH_3 dans la réaction de F/Cl + CH_3CHO a été observé. L'oxydation du CH_3CO et du CH_2CHO génère les radicaux peroxys $CH_3C(O)O_2$ et O_2CH_2CHO. Les calculs théoriques indiquent que $CH_3C(O)O_2^+$ est instable et se dissociera pour générer CH_3CO^+ et O_2. L'un des $O_2CH_2CHO^+$ est calculé pour être stable, tandis que les autres structures ne le sont pas et se dissocieront. Les deux radicaux peroxys ainsi que leurs ions fragmentaires n'ont pas pu être détectés. Les ions d'un autre produit de la réaction d'oxydation du CH_3CO, l'α-lactone, sont instables et se dissocieront, et les énergies d'apparition des ions fragmentaires ont été mesurées.

Mots-clés: radical peroxys; cinétique des reactions; spectroscopie d'anneau à déclin; spectrométrie de masse par photoionisation dans l'ultraviolet lointain; spectroscopie de coïncidence photoélectron-photoion; lumière de rayonnement synchrotron

Abstract

Peroxy radicals are important intermediates in atmospheric chemical reactions and play an important role in atmospheric radical chain reactions. Chemical reaction kinetics and product information of radicals are key parameters in global atmospheric model simulation, and are of great significance for understanding scientific questions such as atmospheric oxidation capacity, photochemical pollution, and secondary organic aerosol formation. Ethane is one of the most abundant non-methane hydrocarbon in the atmosphere, and its oxidation reaction in the atmosphere generates the ethyl peroxy radical $C_2H_5O_2$. However, there are still problems such as insufficient information about kinetic parameters and reaction products and inconsistent measurement results in the study of its self- and cross-reaction kinetics. Accurately measuring the self- and cross reaction rate constant, and product branching ratio information of $C_2H_5O_2$ will help to understand the $C_2H_5O_2$ peroxy radical chemistry in low NOx environments and its contribution to OVOCs and secondary organic aerosol sources in the atmosphere.

This thesis mainly uses near-infrared absorption spectroscopy and photoionization mass spectrometry to study the kinetics and products of reactions related to $C_2H_5O_2$. The absorption spectra of peroxy radicals in the near-infrared region feature typical peaks, and the absorption of different peroxy radicals can be used for selective detection. Based on continuous wave dual-path cavity ringdown spectroscopy (CRDS) combined with excimer laser photolysis, the self-reaction of $C_2H_5O_2$ and its cross-reaction with CH_3O_2 peroxy radicals have been studied, and the rate constant and branching ratio have been obtained. In addition, based on vacuum ultraviolet photoionization time-of-flight mass spectrometry, photoelectron photoion coincidence spectroscopy, combined with synchrotron radiation light source, the products of peroxy radicals self- and cross-reaction were further studied. The main contents of this thesis are:

1. Kinetics and products measurements of the self-reaction of $C_2H_5O_2$. 351 nm pulsed excimer laser photolysis of $Cl_2/C_2H_6/O_2$ mixture was employed to create $C_2H_5O_2$. First, the absorption cross section of $C_2H_5O_2$ was measured by two methods to quantify $C_2H_5O_2$, namely (1) back-to-back method and (2) kinetic method by measuring the reaction of $C_2H_5O_2 + HO_2$. Both methods lead to the same absorption cross-section for

$C_2H_5O_2$ of $\sigma = (1.0 \pm 0.2) \times 10^{-20}$ cm^2 at the peak wavenumber of 7596.47 cm^{-1}.

Then, selective and quantitative absorption kinetics of HO_2 and $C_2H_5O_2$, measured at the same time, allowed obtaining the rate constant k and branching ratio α of the $C_2H_5O_2$ self-reaction: $k(C_2H_5O_2 + C_2H_5O_2) = (1.0 \pm 0.2) \times 10^{-13}$ cm^3 s^{-1} and $\alpha(C_2H_5O) = 0.31 \pm 0.06$. Considering that secondary reactions such as $C_2H_5O_2 + HO_2$ and $C_2H_5O_2 + C_2H_5O$ may influence the kinetic measurements of $C_2H_5O_2$ self-reaction, separate experiments were conducted to measure the rate constants of these two reactions: $k(C_2H_5O_2 + HO_2) = 6.2 \times 10^{-12}$ cm^3 s^{-1} and $k(C_2H_5O_2 + C_2H_5O) = 7 \times 10^{-12}$ cm^3 s^{-1}. Reliable rate constants and product branching ratios were obtained for the $C_2H_5O_2$ self-reaction by the kinetic measurements resolved a recently appeared discrepancy in literature regarding the rate constant and the branching ratio of this reaction. At present, the IUPAC committee has already updated the recommended values, including rate constant and branching ratio for $C_2H_5O_2$ self-reaction and adopted the new results from the current thesis.

Finally, a microwave discharge flow tube reactor combined with vacuum ultraviolet photoionization mass spectrometry as well as a laser photolysis reactor combined with synchrotron radiation light source photoelectron photoion coincidence spectroscopy were also employed to study the products and kinetics of the $C_2H_5O_2$ self-reaction. The results showed that the branching ratio for the dimer product $C_2H_5OOC_2H_5$ was (0.10 ± 0.05). After considering the transmission loss, the upper limit value of this branching ratio could explain the difference in $\alpha(C_2H_5O)$ between our and the stable end-product measurements, that is, the branching ratio of $C_2H_5OOC_2H_5$ in $C_2H_5O_2$ self-reaction can maybe not be ignored and its decomposition could contribute in the stable end-product measurements to CH_3CHO, and thus resulting in an apparently higher $\alpha(C_2H_5O)$.

2. Kinetics measurements of $C_2H_5O_2$ with CH_3O_2. $C_2H_5O_2$ and CH_3O_2 were created simultaneously by 351 nm excimer laser photolysis of $Cl_2/C_2H_6/CH_4/O_2$ mixture. The absorption of $C_2H_5O_2$ and CH_3O_2 were relative selectively measured at 7601.66 cm^{-1} and 7488.13 cm^{-1}, and the kinetics of appearance of HO_2 was also measured. Using a model to fit the measured absorption-time profiles, the rate constant and branching ratio of the cross reaction between the two radicals was obtained: $(3.8 \pm 1.0) \times 10^{-13}$ cm^3 s^{-1}, α (radical channel): 0.40 ± 0.20.

In order to minimize absorption of the near-infrared light by the precursors

methane and ethane, which leads to signal degradation, sufficient concentrations of the precursors were not able to be added in the experiment to quickly consume Cl-atoms, which in turn leads to a small amount of Cl reacting with RO_2 ($C_2H_5O_2$ and CH_3O_2). Therefore, separate experiments were conducted to investigate the kinetics of $C_2H_5O_2$ + Cl and CH_3O_2 + Cl reactions, respectively. 351 nm excimer laser photolysis of $Cl/C_2H_6/O_2$ or $Cl/CH_4/O_2$ were used to create $C_2H_5O_2$ or CH_3O_2 individually. The kinetics of $C_2H_5O_2/CH_3O_2$ and HO_2 were measured, with a model developed to fit the experimental results, the rate constant and branching ratio of $C_2H_5O_2/CH_3O_2$ with Cl were obtained. Finally, the RO_2 + Cl mechanism has been included in the model used for determining the rate constant of the $C_2H_5O_2$ + CH_3O_2 cross reaction.

3. CH_3CHO is produced in the self-reaction of $C_2H_5O_2$, and in the cross reaction of $C_2H_5O_2$ with CH_3O_2. Product detection of the oxidation reaction of CH_3CHO was performed with a microwave discharge flowtube reactor combined with synchrotron radiation photoelectron photoion coincidence spectroscopy. The reaction of F/Cl with CH_3CHO gives two isomer radicals CH_3CO/CH_2CHO. The photoionization spectra of the two isomer radicals and products formed in the reaction of F + CH_3CHO were determined. The branching ratio of the two isomer radicals in Cl + CH_3CHO reaction was also determined. The tautomerization process of CH_3CHO-CH_2CHOH and CH_3COCH_3-CH_3COHCH_3 in F/Cl + CH_3CHO reaction were observed.

The oxidation of CH_3CO and CH_2CHO generates the peroxy radicals $CH_3C(O)O_2$ and O_2CH_2CHO. Theoretical calculations indicate that $CH_3C(O)O_2^+$ is unstable and will dissociate to generate CH_3CO^+ and O_2. One of the $O_2CH_2CHO^+$ is calculated to be stable, while the other structures are not and will dissociate. The two peroxy radicals as well as their fragment ions were not able to be detected. The ions of another product of CH_3CO oxidation reaction, α-lactone, are unstable and will dissociate, and the appearance energies of fragment ions were measured.

Key Words: peroxy radical; reaction kinetics; cavity ring down spectroscopy; vacuum ultraviolet photoionization mass spectrometry; photoelectron photoion coincidence spectroscopy; synchrotron radiation

Chapter 1. Introduction

1.1 Atmospheric peroxy radical chemistry

Peroxy radical plays a vital role in atmospheric chemistry and have attracted extensive research on its kinetics and reaction products [1-6]. The volatile organic compounds (VOCs) emitted into the atmosphere are oxidized to form peroxy radicals RO_2. The subsequent reaction of RO_2 leads to the formation of ozone O_3 and secondary pollutants. Hydroxy radicals (OH) are one of the most important oxidants in the atmosphere, and almost all gases in the troposphere can be oxidized and removed by reaction with OH. Species directly emitted to the atmosphere are called primary pollutants and their oxidation products with OH and other oxidants (such as Cl, NO_3, et al.) are called secondary pollutants. As one of the most important oxidants in the atmosphere, OH maintains the oxidation capacity of the troposphere and plays a crucial role in the self-purification of the atmosphere. There are several sources of OH in the atmosphere, the most important being the photolysis of O_3 by UV light leading to $O(^1D)$ atoms, which in presence of water vapor are converted to OH radicals:

$$O_3 + h\nu(\lambda \leq 335nm) \rightarrow O(^1D) + O_2 \quad (1.1)$$

$$O(^1D) + H_2O \rightarrow OH + OH \quad (1.2)$$

Other OH sources include the photolysis of HONO, HCHO (the photolysis of HCHO leads to HO_2 radicals, which are subsequently converted to OH radicals by reaction with NO) and the reaction of O_3 with alkene. The major loss of OH is its reaction with NO_X, VOCs, CO and O_3 and the resulting steady-state concentration of OH radicals in the atmosphere is around 10^6 to 10^7 molecule/cm^3. The product of the reaction of OH with NO leads to HONO, which as mentioned above leads after photolysis back to OH and NO, while the reaction of OH with NO_2 is an important sink of OH radicals and produces HNO_3.

$$OH + NO \rightarrow HONO \quad (1.3)$$

$$OH + NO_2 \rightarrow HNO_3 \quad (1.4)$$

The reaction of OH with CO and O_3 is not only a sink of OH but also acts as a source of HO_2 radical, which is also reactive and is linked to OH by its reaction with NO,

$$OH + CO + O_2 \rightarrow CO_2 + HO_2 \quad (1.5)$$

$$OH + O_3 \rightarrow HO_2 + O_2 \quad (1.6)$$

The reactions of OH with hydrocarbons (RH) leads, in the presence of O_2, to the formation of peroxy radicals RO_2,

$$OH + RH \rightarrow R + H_2O \quad (1.7)$$

$$R + O_2 \rightarrow RO_2 \quad (1.8)$$

Not only OH, other radicals as Cl, NO_3 also react with hydrocarbons and lead to the formation of RO_2 radicals. These radicals are important intermediates in the radical cycles, which controls the oxidative capacity of the atmosphere and leads to the formation of secondary pollutants.

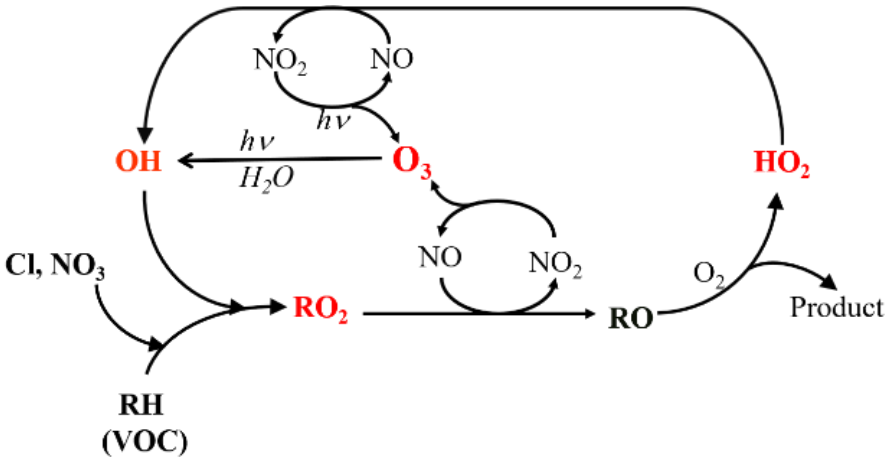

Figure 1.1 Radical reactions in polluted environments.

The subsequent reactions of RO_2 radical are controlled by the composition of the environment: as shown in Figure 1.1, in polluted conditions with high concentration of

NO_x, the sink of RO_2 is its reaction with NO, which leads to formation of alkoxy radicals, RO. With high concentration of O_2 such as present in the atmosphere, RO is oxidized to a carbonyl compound with concomitant formation of HO_2, and the reaction of HO_2 will also oxidize NO to NO_2 and thus re-generate OH radicals. The photolysis of the produced NO_2 leads to O_3, and also because of this cyclic reaction, NO is continuously transformed to NO_2 and through photolysis again to O_3.

The reaction of RO_2 with NO has two product channels, either as radical termination channel to give the stable product $RONO_2$ or the radical propagating channel to give RO and NO_2.

$$RO_2 + NO \rightarrow RONO_2 \quad (1.9.a)$$

$$RO_2 + NO \rightarrow RO + NO_2 \quad (1.9.b)$$

The reaction (1.9.a) causes RO_2 to no longer participate in the atmospheric radical cycle, thereby reducing its contribution to O_3 formation. Studying the rate constants and product branching ratios of different RO_2 with NO reactions help to understand the contribution of different RO_2 to O_3. The rate constant of RO_2 with NO and the branching ratio are temperature and pressure dependent, but small peroxy radicals such as CH_3O_2 radicals nearly exclusively react through channel (1.9.b).

$$RO_2 + NO_2 \leftrightarrow RO_2NO_2 \quad (1.10)$$

The reaction of RO_2 with NO_2 is a reversible reaction, the produced RO_2NO_2 can at room temperature and atmospheric pressure decompose back to RO_2 and NO_2, but in the cold upper troposphere, the thermal decomposition rate of RO_2NO_2 slows down and its lifetime in the atmosphere increases. RO_2NO_2 is then mainly consumed by photolysis or its reaction with OH. The typical case is the reaction of $CH_3C(O)O_2$ with NO_2, the produced $CH_3C(O)O_2NO_2$ is called PAN (peroxyacetyl nitrate). The life time of PAN in the troposphere is relative long and will decompose thermally after long distance transportation and thus react as a reservoir of NO_2, which transport NO_x away

from primary NO_x emission sources, thus influences the concentration distribution of atmospheric NO_2 and can lead to O_3 formation in remote environments.

Stratospheric O_3 is beneficial for absorbing ultraviolet (UV) radiation ($\lambda \lesssim 290$ nm), the short wavelength of UV light with high energy, which results in DNA damage, cancer and even death [7]. Thus, the existence of O_3 in the stratosphere avoids direct UV radiation from the sun on human and other lives. However, tropospheric O_3 not only acts as greenhouse gas and contributes to global warming, but also as a strong oxidant it is also bad for human health. High mixing ratio of O_3 in stratosphere leads to some continuous transport of O_3 into the troposphere, however the major tropospheric O_3 source is its production by photochemical reactions involving VOCs and NO_x. Therefore, a better understanding of RO_2 reactions can help to discover their contribution to troposphere O_3.

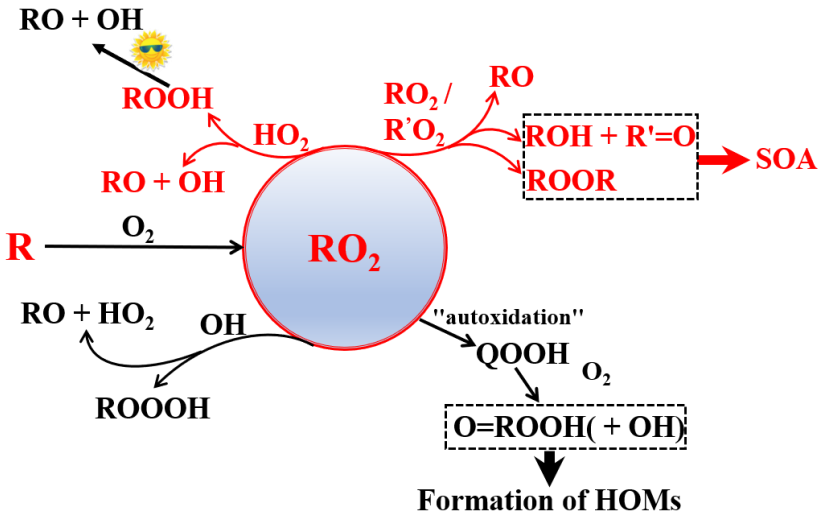

Figure 1.2 Radical reactions in clean environment with low NO_X.

In clean environments with low NO, unimolecular autoxidation reaction, the reactions with OH, HO_2, its self-reaction, and cross reaction with other peroxy radicals become more important fates for peroxy radicals.

In the autoxidation reaction, defined and summarized by Bianchi et al [8], RO_2 radicals first undergo an intramolecular hydrogen-atom shift forming a hydroperoxide

functionality and an alkyl radical, to which molecular oxygen then rapidly attaches to form a new, more oxidized peroxy radical, described as highly oxygenated organic molecules, HOMs. The produced HOMs have usually low vapor pressures, and contributes to the new particle formation (NPF) and secondary organic aerosol (SOA).

For the reaction of RO_2 with OH, the work from Fittschen's group has shown that the formerly ignored reaction of RO_2 with OH is in fact very fast and plays a role in remote environments when the concentration of NO is low [9-11]. Series investigations and theoretical calculations of this reaction for C1-C4 alkyl peroxy radicals were carried out. For the simplest alkyl peroxy radical, CH_3O_2, the reaction first forms an intermediate CH_3OOOH^* which then either stabilizes to ROOOH or decompose to product CH_3O with HO_2, or CH_3OH with O_2. The possible formation of CH_2OO with H_2O has not been confirmed.

$$CH_3O_2 + OH \rightarrow CH_2OO + H_2O \quad (1.11.a)$$

$$CH_3O_2 + OH \rightarrow CH_3OOOH^* \quad (1.11.b)$$

$$CH_3OOOH^* \rightarrow CH_3O + HO_2 \quad (1.12.a)$$

$$\rightarrow CH_3OH + O_2 \quad (1.12.b)$$

$$\rightarrow CH_3OOOH \quad (1.12.c)$$

The product yield measurements show that the major product is CH_3O with HO_2 and accounts for nearly 90%. But with increasing size of the alkane, the product yield of RO with HO_2 decrease from 90% for CH_3O_2 + OH to 15% for $C_4H_9O_2$ + OH, and the yield of ROOOH will then increase and become the major product for peroxy radicals. The rate constant for the reaction of C1 - C4 peroxy radicals with OH is about (1-1.5) $\times 10^{-10}$ cm^3 s^{-1}. Due to its importance in understanding peroxy radical chemistry in low NO_x conditions, the reaction of RO_2 with OH has been included in the atmospheric chemistry model.

Recently the work of Berndt et al [12] further studied the reaction of RO_2 with OH, RO_2 was created from several different precursors, as trimethylamine, dimethyl sulfide,

α-pinene, toluene, and 1-butene. The rate constants of these reactions were revealed and also the products of the corresponding ROOOH from individual reactions were all detected. The life time of ROOOH is estimated to be about one hour, and those ROOOH formed from highly oxidized RO_2 radical result in highly oxygenated organic molecules (HOMs) which may contribute to the formation of SOA and thus influence the radiation budget. More field measurements are needed to verify experimental results and to reveal its subsequent fate in the atmosphere.

For the reaction of RO_2 with HO_2, there are three possible channels leading to ROOH + O_2, ROH + O_3 and RO + OH + O_2,

$$RO_2 + HO_2 \rightarrow ROOH + O_2 \quad (1.13.a)$$

$$\rightarrow ROH + O_3 \quad (1.13.b)$$

$$\rightarrow RO + OH + O_2 \quad (1.13.c)$$

But for simple alkyl peroxy radicals, the product yield of channel (1.13.a) is near unity, the yield for the other channels are small and normally ignored. But there are exceptions, such as for $CH_3OCH_2O_2$ and CH_3COO_2 radicals, other channels play important roles and can't be ignored. For $CH_3OCH_2O_2$, channel (1.13.b) and (1.13.c) account for around 0.5, and for CH_3COO_2 these two product channels account for around 0.6. The reaction of RO_2 with HO_2 with relative high rate constant is the major sink of RO_2 in remote areas, its product ROOH can be removed by deposition, photolysis and by the reaction with OH.

The self-reaction of RO_2 or its cross reaction with other RO_2 have generally three product channels,

$$RO_2 + RO_2 \rightarrow RO + RO + O_2 \quad (1.14.a)$$

$$\rightarrow ROH + R_{-H} = O + O_2 \quad (1.14.b)$$

$$\rightarrow ROOR + O_2 \quad (1.14.c)$$

Only channel (1.14.a) is a radical maintaining reaction with RO radicals produced, while channel (1.14.b) and (1.14.c) lead to stable products, for simple alkyl peroxy radical, such as CH_3O_2 and $C_2H_5O_2$ the stable products are alcohols and aldehydes. Alkanes with more than two carbons have normally several isomers, the products formed for the branched alkyl peroxy radicals are different and give alcohols and ketones, such as for *i*-C_3H_7, the products of its corresponding peroxy radicals are isopropanol and acetone. The rate constant for the self-and cross reaction of simple alkyl and unsubstituted peroxy radicals is normally slower than those of more complex oxygenated radicals, for CH_3O_2, CH_3COO_2 and $CH_3OCH_2O_2$ the rate constants are 3.5×10^{-13} cm^3 s^{-1} [13], 1.3×10^{-11} cm^3 s^{-1} [14] and 2.1×10^{-11} cm^3 s^{-1} respectively [13].

In conclusion, the reactions of RO_2 in low NOx conditions will leads to organic compounds with low volatility, studies on theses reactions will help to understand the contribution of RO_2 chemistry to new particle formation and secondary organic aerosol.

1.2 Brief introduction to the kinetics study of $C_2H_5O_2$

1.2.1 Kinetics study of $C_2H_5O_2$ self-reaction

Ethane is the most abundant non-methane hydrocarbon (NMHC) in remote atmospheric environments [15]. NMHCs play an important role in tropospheric chemistry and are precursors of oxygen-containing volatile organic compounds (OVOCs) such as formaldehyde, acetaldehyde, and acetone in the atmosphere [16]. Their major sink in the atmosphere is its reaction with OH, which consume OH and effects the atmospheric oxidation capacity [15]. The main sources of ethane are the emissions from fossil fuel and biomass combustion, etc. The annual emission of ethane into the atmosphere is about 13 Tg (1 Tg=10^{12} g) [15]. The oxidation of ethane by OH in the atmosphere leads to the formation of the ethyl peroxy radical, $C_2H_5O_2$. Under low NO_x conditions the following reactions can occur for $C_2H_5O_2$:

- its self-reaction [17-27]:

$$C_2H_5O_2 + C_2H_5O_2 \rightarrow C_2H_5O + C_2H_5O + O_2 \quad (1.15.a)$$

$$C_2H_5O_2 + C_2H_5O_2 \rightarrow C_2H_5OH + CH_3CHO + O_2 \quad (1.15.b)$$

$$C_2H_5O_2 + C_2H_5O_2 \rightarrow C_2H_5OOC_2H_5 + O_2 \quad (1.15.c)$$

- its reaction with HO_2 [17, 18, 24, 28-31]:

$$C_2H_5O_2 + HO_2 \rightarrow C_2H_5OOH + O_2 \quad (1.16)$$

- its cross-reaction with other peroxy radicals, mainly CH_3O_2 [32]:

$$C_2H_5O_2 + CH_3O_2 \rightarrow C_2H_5O + CH_3O + O_2 \quad (1.17.a)$$

$$C_2H_5O_2 + CH_3O_2 \rightarrow C_2H_5OH / CH_3CHO + HCHO / CH_3OH + O_2 \quad (1.17.b)$$

$$C_2H_5O_2 + CH_3O_2 \rightarrow C_2H_5OOCH_3 + O_2 \quad (1.17.c)$$

- its reaction with OH radicals [33, 34]:

$$C_2H_5O_2 + OH \rightarrow C_2H_5O + HO_2 \quad (1.18.a)$$

$$C_2H_5O_2 + OH \rightarrow C_2H_5OOH \quad (1.18.b)$$

While the reaction of $C_2H_5O_2$ with HO_2 has only one reaction path, the self- and cross reactions with other peroxy radicals can either lead to stable products (alcohols, aldehydes and the accretion product ROOR) or maintain the radical pool by formation of RO. Due to the partial formation of RO, secondary chemistry cannot be avoided when investigating the reaction in the laboratory: the C_2H_5O product of the $C_2H_5O_2$ self-reaction leads after rapid reaction with O_2 to formation of the HO_2 radicals and carbonyl compounds $R_{-H}=O$,

$$C_2H_5O + O_2 \rightarrow CH_3CHO + HO_2 \quad (1.19)$$

whereby the HO_2 radicals will subsequently react with $C_2H_5O_2$. As the rate constant of the reaction of $C_2H_5O_2$ with HO_2 is faster than the rate constant of the $C_2H_5O_2$ self-reaction, the secondary reaction of $C_2H_5O_2$ with HO_2 has to be considered in the measurements of $C_2H_5O_2$ self-reaction, because the decay of $C_2H_5O_2$ is accelerated by HO_2. Therefore, the measured kinetics of $C_2H_5O_2$ are sometimes given as k_{obs}, with $k_{obs} = (1+\alpha)k$, where α is the branching ratio for radical channel, and k is the total rate constant of the $C_2H_5O_2$ self-reaction. Determining the rate constant of the $C_2H_5O_2$ self-reaction from observed $C_2H_5O_2$ decays depends on the branching ratio α leading to the C_2H_5O radical used in the data treatment: for a given experimental $C_2H_5O_2$ decay, the retrieved rate constant $k(C_2H_5O_2 + C_2H_5O_2)$ will decrease with increasing branching ratio. A reliable determination of the branching fraction is therefore important.

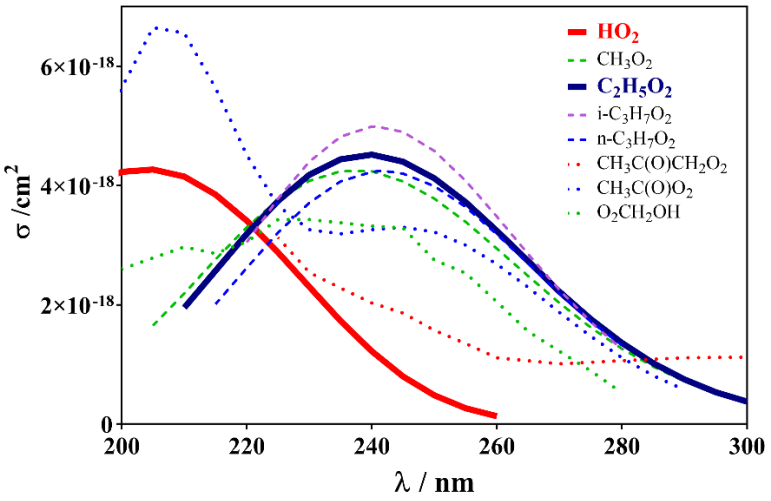

Figure 1.3 UV absorption spectra for different peroxy radicals, red and bule bold solid lines are HO_2 and $C_2H_5O_2$.

Earlier studies of peroxy chemistry have either used time resolved UV absorption spectroscopy for the determination of the overall rate constant or, for the determination of the branching ratio, end-product studies by FTIR [22, 26] or by gas chromatography [20]. Direct observations of the HO_2 yield and thus measurement of the branching ratio is not possible in UV absorption studies because the steady-state HO_2 concentration, that builds-up from the $C_2H_5O + O_2$ reaction, is rather low due to the fast consumption of HO_2 through $C_2H_5O_2$ with HO_2 reaction. A relative selectivity between $C_2H_5O_2$ and HO_2 can principally be obtained by UV absorption spectroscopy, as shown in Figure 1.3: the absorption cross section for $C_2H_5O_2$ at 250 nm is ~8 times higher than for HO_2, while at 210 nm the ratio is ~2 in favour of HO_2. "Clean" $C_2H_5O_2$ decays can be observed when studying the self-reaction of $C_2H_5O_2$, however the corresponding HO_2 profiles cannot be extracted, because even at short wavelengths the much higher $C_2H_5O_2$ concentration compared to HO_2 always makes up the major fraction of the absorption signal, and a correction of the HO_2 profile for the contribution of $C_2H_5O_2$ would induce very large error bars. Therefore, time-resolved UV absorption studies used the branching ratio, obtained from end-product studies, to extract the rate constant from the measured $C_2H_5O_2$ decays. In end-product measurements, the dimer product $C_2H_5OOC_2H_5$ was considered to be minor and normally be ignored. In the

measurements from Wallington et al. [22], the dimer product was not detected, in the measurement from Niki et al., [26] after subtracting the absorption of other products the signal at 2993 cm^{-1} was assigned to the dimer $C_2H_5OOC_2H_5$ and the upper limit of 0.06 for its branching ratio was given. The measurement of the products (CH_3CHO, C_2H_5OH and C_2H_5OOH) from $C_2H_5O_2$ self-reaction and from the cross reaction of $C_2H_5O_2$ with HO_2, branching ratios for the other two product channels in $C_2H_5O_2$ self-reaction were thus obtained.

$$\frac{C_2H_5OH}{CH_3CHO} = \frac{k_{1.15.b}}{2k_{1.15.a} + k_{1.15.b}}, \quad \frac{C_2H_5OOH}{C_2H_5OH} = \frac{2k_{1.15.a}}{k_{1.15.b}}$$

This way, UV absorption measurements came to a relatively good agreement for the absolute value of the overall rate constant and end-product studies also came to a fairly good agreement on the branching ratio. Thus, it was agreed in almost all studies that the radical channel is the major path, a branching fraction of $\alpha = 0.63$ for the C_2H_5O channel and a total rate constant of $k(C_2H_5O_2+C_2H_5O_2) = 7.6\times10^{-14}$ cm^3s^{-1} were recommended by the IUPAC committee [13].

More recently, Noell *et al*. [18] have carried out in 2010 for the first time a more selective measurement of this reaction: UV absorption was still used to monitor $C_2H_5O_2$, but HO_2 was directly measured in a selective way using wavelength modulation spectroscopy in the near IR. Interestingly, this work is in large disagreement with the earlier recommendations: while the observed $C_2H_5O_2$ decays were in agreement with the older data, a branching fraction of only $\alpha = 0.28$ was found for the radical path. This leads to an overall rate constant of $k(C_2H_5O_2+C_2H_5O_2) = 1.19\times10^{-13}$ cm^3s^{-1}, around 56% higher than the value previously recommended by IUPAC. A possible explanation given in Noell's work for this disagreement was considered due to a non-negligible yield of dimer-formation, ROOR, in the self-reaction of peroxy radicals. The decomposition of such dimer could lead through decomposition on reactor walls to formation of aldehydes and thus appear as additional radical formation when measuring stable end products.

To our knowledge, no new measurements have been carried out on the $C_2H_5O_2$ self-reaction since this interesting finding of the important disagreement between the recommended IUPAC values and the results from Noell *et al*. [18]. It seems therefore important to reinvestigate this reaction with yet another selective detection method.

1.2.2 Kinetics study of the cross reaction of $C_2H_5O_2$ with CH_3O_2

Methane is the most abundant VOC, even though the growth rate of atmospheric CH_4 seems to stabilize since a few years, the concentration currently is already around 1.9 ppm, to be compared with only 0.7 ppm in preindustrial times[35]. CH_4 sources comprise anaerobic environments such as natural wetlands and rice paddies, oxygen-poor freshwater reservoirs, digestive systems of ruminants and termites, and organic waste deposits (such as manure, sewage and landfills). CH_4 being a fossil fuel gas, it escapes also from the subsurface terrestrial, marine, glaciers into the atmosphere, as well as during the exploitation of fossil fuels and from leaks in pipelines during transportation. CH_4 is also a greenhouse gas and contributes to global warming. The most important removal mechanism of CH_4 is by chemical reaction with OH radicals, thus CH_4 reduces the oxidation capacity of the atmosphere. The produced CH_3 is immediately converted to CH_3O_2 in the atmosphere, in low NOx conditions, the major cross reaction of CH_3O_2 with other peroxy radical is its reaction with $C_2H_5O_2$.

For both $C_2H_5O_2$ and CH_3O_2 radicals, the kinetic and product distribution for the self-reaction has been studied numerous times (for CH_3O_2 [36-44] and for $C_2H_5O_2$ [17-24, 26, 45, 46]), the same is true for their reaction with HO_2 (for CH_3O_2 [28, 30, 31, 37, 41, 47-49] and for $C_2H_5O_2$ [18, 24, 28, 30, 31, 46, 50, 51]). Their reaction with OH radicals has been the subject of a few studies (for CH_3O_2 [9, 10, 52-56] and for $C_2H_5O_2$ [33, 34, 57]).

Currently, only one paper studied the kinetics of the cross reaction of $C_2H_5O_2$ with CH_3O_2, the kinetics of the total absorption at 235 nm from reactants and products was measured by UV absorption spectroscopy, and with a model to fit the total absorption,

Villenave et al [32] determined the rate constant for the cross reaction. But as the same challenge for measuring the rate constant of $C_2H_5O_2$ self-reaction, UV absorption spectroscopy was not able to separate the absorption of CH_3O_2 and $C_2H_5O_2$, and the absorption of HO_2 which is used to get the branching ratio for C_2H_5O + CH_3O channel was also difficult to obtain. Thus only the rate constant was given in their measurements. And with only the total absorption kinetics at one wavelength fitted, the obtained rate constant might have a large uncertainty.

In summary, different methods have been used in the literature to study the kinetics of $C_2H_5O_2$ self-reaction. However, the branching ratio of the self-reaction of $C_2H_5O_2$ measured with different methods is inconsistent. Only one measurement has been carried out for the cross reaction of $C_2H_5O_2$ with CH_3O_2, but the branching ratio of this reaction has not been determined.

1.2.3 Product study of the oxidation reaction of CH_3CHO

Acetaldehyde, CH_3CHO, is a key intermediate in the degradation of many VOCs in the troposphere [58]. Almost all alkanes containing more than one carbon atom (C>1, such as C_2H_6, C_3H_8, *n*-C_4H_{10}) and alkenes containing more than two carbon atoms (C>2, such as C_3H_6, 2-C_4H_8) undergo oxidation reactions to produce CH_3CHO. And in many cases, the branching ratio towards the product CH_3CHO is more than 50%. Among them, the oxidation of ethane is the most important photochemical reaction source of CH_3CHO, approximately 15-20 Tg yr^{-1} [59]. In the atmosphere, the oxidation reaction of C_2H_6 by OH generates $C_2H_5O_2$ peroxy radicals, and the self-reaction of $C_2H_5O_2$ and the cross reaction of $C_2H_5O_2$ with CH_3O_2 all give CH_3CHO. In clean atmosphere, the measurements of Singh et al. [59]. show that the concentration of acetaldehyde in the troposphere is highest at an altitude of 0-2 km above ground level, about 300 pptv, and decreases with altitude. In winter polluted environments, the concentration of CH_3CHO is about 1000 pptv [60]. The oxidation reaction of acetaldehyde in polluted environment with high NO_x generates peroxyacetyl nitrates ($CH_3C(O)O_2NO_2$, PAN). Typically, the

life time of PAN is relatively short, within a few hours, its pyrolysis regenerates NO_2. However, in the cold upper troposphere, PAN can survive for a long time and only decompose into NO_2 when transported to high temperature areas. PAN thus act as the reservoir of NO_2 transporting NO_2 from the polluted area to remote clean environments [61], therefore it influence the distribution of atmospheric NO_x. CH_3CHO is mainly removed in the atmosphere through reactions with OH, NO_3, and photolysis [2]. The reaction for $CH_3C(O)O_2$ in clean environment with low NO_x is also interesting, its reaction with HO_2 leads to the formation of low-volatility acids and peracids and therefore contributes to the nucleation and formation of aerosols[62].

Although CH_3CHO is normally attacked in the atmosphere by the OH radical,

$$OH + CH_3CHO \rightarrow CH_3CO + H_2O \qquad (1.20)$$

to study the reaction of radicals from CH_3CHO in laboratory, the reaction with Cl or F-atoms is widely used to initiate their formation. This is because it is much easier to create F and Cl instead of OH in the laboratory, and the second reason is that the reaction rate for F or Cl with hydrocarbons are faster than analogous reactions with OH [29]. Both F and Cl can give two radicals, CH_3CO and CH_2CHO, but with different fractions:

$$F / Cl + CH_3CHO \rightarrow CH_3CO + HF / HCl \qquad (1.21.a)$$

$$F / Cl + CH_3CHO \rightarrow CH_2CHO + HF / HCl \qquad (1.21.b)$$

Sehested et al. [63] obtained the branching ratios of two radicals in the F + CH_3CHO + O_2/NO reaction by measuring the products $CH_3C(O)O_2$ and NO_2 with UV-visible absorption spectroscopy: they found CH_3CO, (65 ± 9)% and CH_2CHO, (35 ± 9)% respectively. For the Cl-atom, its reaction with CH_3CHO was considered as only leading to CH_3CO and the channel to give CH_2CHO is thought to be very minor [64]. As the product CH_2CHO cannot be directly detected, Bartels et al. [64] and Niki et al. [65] measured the product CH_2ClCHO ($CH_2CHO + Cl_2 \rightarrow CH_2ClCHO+Cl$) from the secondary reaction of CH_2CHO with Cl_2 with mass spectrometry and Fourier transform

spectroscopy respectively. They obtained upper limit branching ratios of CH_2CHO in the Cl + CH_3CHO reaction of 7% and 1%, respectively.

For studying the reaction of CH_3CHO and to detect the radical using mass spectrometry, it is necessary to know the ionization energy. While there is less information about the ionization energy for both radicals, for the CH_3CO radical the available results show a little difference. Zamanpour et al. [66] measured the products in F + CH_3CHO reaction using He I photoelectron spectroscopy. Only CH_3CO was detected, the adiabatic ionization energy (AIE = (7.21 ± 0.05) eV) and vertical ionization energy (VIE = (8.39 ± 0.05) eV) of CH_3CO were obtained. However, the ionization energy of CH_3CO in the measurement from Reed et al. [67] was different from Zamanpour et al.: 8.05 ± 0.17 eV. The CH_2CHO radical was not detected and thus no ionization energy information was obtained.

In the presence of oxygen, the produced radicals oxidize to peroxy radicals, $CH_3C(O)O_2$ and O_2CH_2CHO,

$$CH_3CO + O_2 + M \rightarrow CH_3COO_2 + M \quad (1.22)$$

$$CH_2CHO + O_2 + M \rightarrow O_2CH_2CHO + M \quad (1.23)$$

The reaction of CH_3CO + O_2 is pressure dependence and there are already several studies about this reaction to get the pressure dependence of the rate constant and branching ratio. Especially in the work of Papadimitriou [68], different techniques and a wide pressure range (0.009-600 Torr) were studied. Their results show that the rate constant increases with pressure, and the yield of the peroxy radical $CH_3C(O)O_2$ also increases with pressure. Thus, in the low-pressure range there are other products formed:

$$CH_3CO + O_2 + M \rightarrow co - products + OH + M \quad (1.24)$$

Their results show that the yield of OH at atmosphere pressure is small, ~1 to 2%, but the yield increases at low pressure, for example 0.81 at 1 Torr He. Although the rate constant was well studied, and OH is detected in the literature, the co-product of the OH channel is still in controversy. Theoretical results show that the co-product should

be α-lactone ($C_2H_2O_2$) [69], but this product has not yet been detected. In the work of Butkovskaya et al [70], CH_2O was detected as the co-product and CO is also supposed to be the other co-product. In the work of Devolder et al [58], laser photolysis coupled to TDLAS were applied to monitor the two possible co-products. In this work, only CH_2O was observed and the formation rate of CH_2O was found to be much slower than the formation of OH, and compatible with the know mechanism of secondary reactions to give CH_2O in the reaction of the $CH_3C(O)O_2$ peroxy radical.

In summary, even for the initial oxidation reaction of CH_3CHO, there is still some unknown information. The ionization energy for the isomer radicals in F/Cl + CH_3CHO reaction are in little disagreement (CH_3CO) or unknown (CH_2CHO). There is also some disagreement in the branching ratio of the two radicals in the reaction Cl + CH_3CHO. The co-product of the OH channel in the oxidation reaction of CH_3CO is still unclear. Although the theoretical results suggest that it could be $C_2H_2O_2$, this product was not observed in experiments. There is also a lack of information on the ionization energies of the two peroxy radicals $CH_3C(O)O_2$ and O_2CH_2CHO.

1.3 Major content and chapter arrangement of this manuscript

This thesis aims to further investigate the kinetics and products of $C_2H_5O_2$ reactions in low NO_x conditions. The absorption spectrum of the peroxy radical in the near-infrared region has structural characteristics, but their absorption cross section in this range is relatively small. Benefiting from the development of cavity ringdown spectroscopy technology, a selective measurement of peroxy radical in the near-infrared region has been achieved. Continuous wave dual path cavity ringdown spectroscopy (CRDS) was applied in this thesis to achieve selective and quantitative absorption kinetic measurements of related radicals such as $C_2H_5O_2$, CH_3O_2 and HO_2 in the near infrared region, and the rate constants and product branching ratios of $C_2H_5O_2$ self-reaction, and the cross reaction of $C_2H_5O_2$ with CH_3O_2. In addition, synchrotron radiation photoelectron photoion coincidence spectroscopy was applied to further detect the products from the initial oxidation reaction of CH_3CHO, which is the main products formed in the self-reaction of $C_2H_5O_2$ and in the cross reaction of $C_2H_5O_2$ with CH_3O_2. Combined with synchrotron radiation light sources, isomer products were distinguished and structure information about the relevant products were obtained. The results obtained in this thesis will contribute to a better understanding of $C_2H_5O_2$ chemistry in low NO_x environments and provide reliable data for global atmospheric models. The chapters of this thesis were arranged as follows:

Chapter 1: Brief introduction to the atmospheric radical chemistry and kinetics as well as product studies of $C_2H_5O_2$.

Chapter 2: Description of the experimental instruments used in this thesis, including dual path cavity ringdown spectroscopy, photoionization mass spectrometry, and photoelectron photoion coincidence spectroscopy, about working principle, performance, alignment and calibration process.

Chapter 3: Kinetics and product measurements of $C_2H_5O_2$ self-reaction. First, the

absorption cross section of $C_2H_5O_2$ was measured by two methods. Then, with the absorption cross section of $C_2H_5O_2$ and HO_2, their concentration time profiles in the $C_2H_5O_2$ self-reaction were selectively and quantitatively measured, and with a model to fit the experimental data, the rate constant and branching ratio of $C_2H_5O_2$ self-reaction were determined. Finally, microwave discharge flowtube combined with vacuum ultraviolet photoionization mass spectrometry was used to measure the products including the dimer $C_2H_5OOC_2H_5$ and their kinetics of $C_2H_5O_2$ self-reaction, and a preliminary value for the branching ratio of the dimer was obtained.

Chapter 4: Kinetics measurements of the cross reaction of $C_2H_5O_2$ with CH_3O_2. The kinetic profiles of $C_2H_5O_2$, CH_3O_2 and HO_2 were quantitatively measured with relative selectivity, and with a model to fit the experimental results, the rate constant and branching ratio of the radical channel (C_2H_5O + CH_3O) of the $C_2H_5O_2$ + CH_3O_2 cross reaction were obtained. In addition, due to the strong absorption of methane and ethane in the near infrared region, it was not possible to add the precursors in high enough excess to convert Cl atoms fast enough to peroxy radicals, which results in participation of some Cl-atoms reacting with RO_2 radicals. Therefore, individual experiments of Cl with $C_2H_5O_2$ and CH_3O_2 were performed, the rate constants and branching ratios were obtained and the simplified mechanism of Cl + $C_2H_5O_2$/CH_3O_2 was included in the mechanism of $C_2H_5O_2$ + CH_3O_2 cross reaction.

Chapter 5: Product measurements of the oxidation reaction of CH_3CHO. Microwave discharge flowtube combined with synchrotron radiation photoelectron photoion coincidence spectroscopy was used to measure the products of the oxidation reaction of CH_3CHO. Diluted F_2 was added into the microwave discharge to produce F atom, then the products of F + CH_3CHO reaction were measured. To obtain relative high concentration of Cl, Cl was produced by F + Cl_2 reaction, then the branching ratio of the isomer radical CH_3CO and CH_2CHO in Cl + CH_3CHO reaction were measured. Finally, O_2 was added into the flowtube and the products of F + CH_3CHO + O_2 reaction were measured.

Chapter 6: Conclusion and perspective.

Chapter 2. Experimental technique

To investigate the kinetics and products properties of peroxy radical reactions, various techniques have been applied, including absorption spectroscopy and mass spectrometer [71-81] as well as theoretical calculations [82, 83]. Cavity ring down spectroscopy as a direct absorption technique owns high sensitivity and performs well especially in the measurement of gas phase species and thus peroxy radicals, by detection of the absorption spectrum and measurements of their kinetics behavior. CRDS is a sophisticated, selective and sensitive detection method for several species, but it only allows detection of a limited number of species. Photoionization mass spectrometry (PIMS) is more versatile in detection of reactive intermediates as well as stable reaction products. The combination of PIMS with synchrotron radiation makes the detection even more multi-functional, as species with the same mass (isomers) can be identified by their photoionization spectra. Furthermore, photoelectron photoion coincidence spectroscopy analyzes both the photoelectrons and photoions in coincidence and offers richer and more accurate information on the structure information of species by measuring their photoelectron spectra. However, some cations formed in the ionization process maybe not be stable and prefer to dissociate. Therefore, we can see that different techniques show advantages in specific aspects and the combination of them helps to get more information of radical chemistry.

In this thesis, CRDS was applied to obtain kinetic information of peroxy radical reactions, including rate constant and branching ratio. Isomers of radicals and product discrimination and specification were accomplished with MS, PEPICO and associated with synchrotron radiation. Since the major part of the present work was accomplished with CRDS, more details about the CRDS setup are written, while for MS only a relative brief description is given.

2.1 Cavity ringdown spectroscopy

2.1.1 The principle of absorption spectroscopy

The Lambert-Beer law is applied to quantitatively describe the relationship between the decrease of light intensity and the concentration of the absorbing species it passes through:

$$I = I_0 e^{-\alpha L}$$

I_0 is the light intensity of the incident beam, I is the light intensity of the transmitted beam, α is the absorbance and L is the length where the absorber is present. With known L, by directly measuring the transmission ratio $\frac{I}{I_0}$, the absorbance due to the absorbing species is obtained. As the absorbance α is a function of frequency, by scanning the incident beam in a wide wavelength range, the absorbances at different wavelengths is obtained. α is related to the concentration N and the absorption cross section σ of the absorber:

$$\alpha = \sigma N.$$

Therefore, when the concentration N is known, σ of the absorbing species can be obtained by measuring the absorbance. Vice versa, when σ is known, the absolute concentration N is determined.

But there are disadvantages of direct absorption measurements. As the light only passes through a limited length of the absorber, the change in light intensity is small. Therefore, the sensitivity of direct absorption is limited by the precision of absolute light intensity measurements and it becomes challenging to detect species, especially when the absorption cross section and/or the concentration of absorber are small.

Cavity ringdown spectroscopy as a cavity enhanced direct absorption spectroscopy technique makes the light reflected back and forth multiple times in the cavity and therefore extends the effective absorption length and achieves higher sensitivity and lower limits of detection.

A typical CRDS set-up includes a laser source, a cavity consisting of a pair of high reflectivity mirrors and the time-resolved detection of the light exciting this cavity. Compared to pulsed cavity ringdown spectroscopy, a threshold trigger circuit and an optical switch are needed for a continuous wave cavity ringdown spectroscopy to cut off the laser beam, and allow the laser coupled to the cavity to freely ringdown in the cavity.

Figure 2.1 Different standing waves formed in a cavity.

A system with two reflecting mirror is considered as an open cavity. The major part of the incident laser light is reflected on the outer surface of the first mirror, and only a small fraction enters into the cavity. This light is reflected between the two mirrors and carries out multiple round trips in the cavity, if the cavity length L is a multiple of the ½ wavelength of the incident light, $L = n\frac{\lambda}{2}$. The light is in resonance with the cavity and the optical cavity or resonator is formed, the light keeps oscillating inside the cavity. The standing wave with specific wavelengths represents a distribution of the light field within the cavity along the longitudinal axis, which is conventionally called a mode, or a longitudinal mode. Due to the transmission loss of light in the cavity, the light with destructive interference is consumed in the cavity, and thus only when the interference is constructive, light is allowed to pass the cavity. For a laser emitting at a specific wavelength, in order to be sure to be in resonance between cavity and laser light, it is therefore necessary to modulate the length of the cavity at least by $\lambda/2$.

Except the longitudinal mode, the light field in the plane perpendicular (i.e., transverse) to the radiation's propagation direction also represents distribution and is called transverse mode and is described as TEM_{mn}. The fundamental transverse mode TEM_{00} is a round spot, and the light intensity changes according to the law of Gaussian

function, i.e., with high energy at the axis and decrease with increasing distance to the axis. Modes, for which the light intensity distributions changes not only with the distance to the axis but also with azimuth angle, are called higher-order modes.

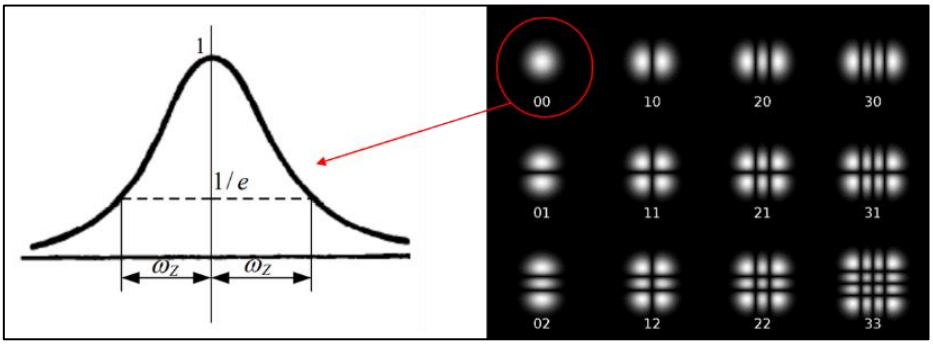

Figure 2.2 Left: light intensity distribution of fundamental transverse mode and right: different transverse modes of the cavity[84].

In order to make the light coupled efficiently into the cavity, not only its wavelength should be resonant to the cavity, but also the transverse mode along the optical axis should be stable. As TEM_{00} has high energy focused in the center, it is normally the preferred mode.

2.1.2 Principle of cavity ringdown spectroscopy

For an optical cavity, supposed that the light intensity of the incoming beam is I_0, the transmitted light after *n* round trips is *I*,

$$I = I_0 R^{2n} \exp(-\alpha 2nl)$$

α is the absorbance, *R* is the reflectivity of both mirrors, l is the absorption distance, through simple mathematical transformation,

$$I = I_0 \exp[2nln(R) - \alpha 2nl]$$

with high reflectivity mirrors, then $\ln(R) \sim R - 1$

$$I = I_0 \exp[2n(R-1) - \alpha 2nl]$$

the time used after *n* round trips is *t*,

$$t = \frac{2nL}{c}$$

L is the distance between two mirrors, then

$$I = I_0 \exp\left\{\frac{tc}{L}[(R-1) - \alpha l]\right\}$$

the time it takes for the transmitted light intensity to decrease to $\frac{1}{e}\ I$ is called life time τ,

$$\tau = \frac{L}{c}\frac{1}{(1-R) + \alpha l}$$

when there is no absorber, the time it takes for the transmitted light intensity to decrease to $\frac{1}{e}\ I$ is τ_0,

$$\tau_0 = \frac{L}{c}\frac{1}{(1-R)}$$

by measuring the life time with and without absorber, the absorbance of the medium is obtained:

$$\alpha = \frac{R_l}{c}\left(\frac{1}{\tau} - \frac{1}{\tau_0}\right)$$

with R_l is the ratio between cavity length L and the absorption path length l.

2.2 Dual path continuous wave cavity ringdown spectroscopy

2.2.1 General description

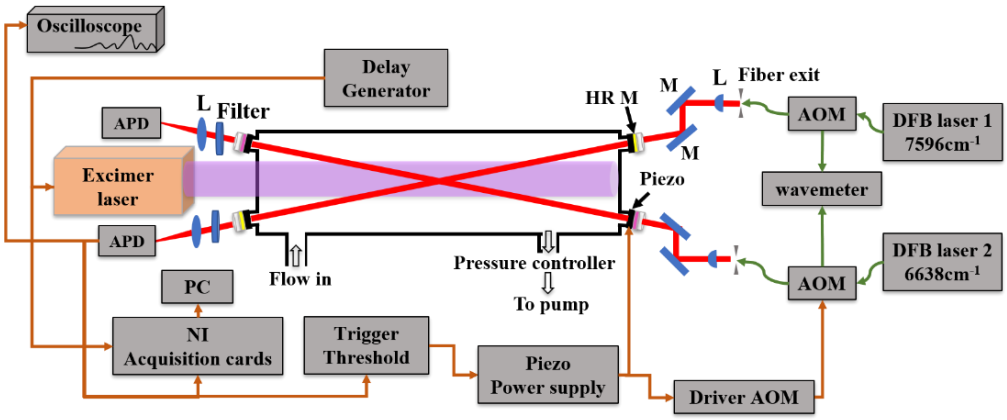

Figure 2.3 Laser photolysis coupled with dual path continuous wave cavity ringdown spectrometer.

The instrument is designed and applied to study kinetics of peroxy radical reactions in a wide pressure and temperature range. An Excimer laser is used to create radicals by photolysis of appropriate precursors. The schematic diagram of the CRDS is shown in Figure 2.3, which mainly includes detection lasers, two optical cavities, fibered acousto-optical modulator (AOM), photodiode, data acquisition system, etc. The detection lasers consist of distributed-feedback (DFB) lasers in different wavelength ranges, the light emitted from the DFB laser is initially transported by a fiber, then it passes an isolator to avoid reflected light going back into the DFB, and thereafter it passes through an AOM. The AOM generates through diffraction the 1st order of the beam, ie. the laser beam is physically divided into two parts, order 1 and order 0. Order 1 is stirred into the cavity and order 0 enters into a wavemeter to measure continuously the output wavelength. After the AOM, order 1 exits the fiber and is aligned into the center of a mode-matching lens and is finally stirred by two mirrors into the cavity. One of the mirrors is glued to a piezo transducer, used to modulate periodically the length of the cavity. Through this, the resonance between the cavity and the wavelength of the

laser light is periodically achieved and the laser beam can couple successfully to the cavity. An avalanche photodiode is aligned at the exit of the cavity to detect light transmitted from the cavity. Once resonance between cavity length and wavelength is achieved, the light intensity exiting the cavity increases and when it exceeds a preset threshold, a homemade trigger circuit will send a signal to the AOM driver to turn off the AOM and thus completely turn off the 1st order beam of the laser. Following that, no light enters the cavity anymore and the light intensity will decrease exponentially and can be measured after A/D conversion by a Labview based acquisition program. By fitting the exponential decay of light intensity with a computer program, the ring down time is thus obtained. In front of the photodiode a filter is placed allowing to remove reflected straylight from the Excimer laser, which otherwise perturbs the avalanche photodiodes.

2.2.2 Reactor specifications

The reactor is made of stainless tubes, the longest one is 0.79m (X-axis), and two short ones are both 0.27m (Y-axis and Z-axis), forming a three dimensional cross. The inner diameter of each tube is 6 cm and their inner surfaces all are coated with Teflon to reduce deterioration of the surface due to aggressive chemicals. The schematic representation of the photolysis cell and the detailed structure of the junction between CRDS mirrors and cell are shown below.

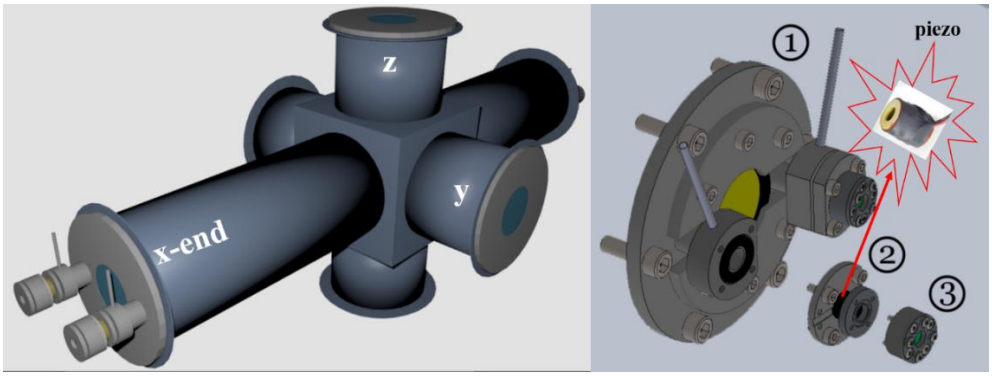

Figure 2.4 Left: structure of the cavity and right: detail structure for the connection of cavity, piezo and mirror.

The X-axis is used for the CRDS detection and the photolysis laser and the Y and Z axis are used for the LIF excitation and detection, respectively. The flanges at the end of the X-axis are sealing the cell and contain in the center quartz windows with 3 cm diameter that are transparent for UV light and allow the entrance of the photolysis beam. The junction between the CRDS mirror and the flange has an angle of 4° to maximize the overlap distance between the volume where the radicals are generated by laser photolysis and the inner-cavity CRDS laser beam. With a photolysis beam of 2 cm width, the geometrically calculated overlap distance is 30 cm. A constant flow of helium passes through an additional tube of 2 mm inner diameter soldered to the part ① to protect the mirrors from dust or corrosive gases. Two CRDS mirror holders (part ②) are fixed directly on the flange, which improves the stability of the CRDS compared to a former version, where the mirror holders were fixed on the table. The connection between parts 1 and 2 uses an O-ring to seal the cell. Four screws are pushing on the O-ring, allowing enough movement to align the CRDS mirrors. The alignment procedure of the CRDS cavity is described below. The piezo links the mirror holder (part 2) and the mirror box (part 3).

2.2.3 Gas injection system

The flows of the precursor and carrier gases were controlled by flowmeters (Bronkhorst, Tylan). and the typical total flow rate is around 700 sccm min^{-1}. The pressure of the reactor was kept constant by a pressure controller and pumped by an oil pump. Typically, experiments were carried out in 100 torr O_2, and the liner velocity of gases inside the cavity can be calculated as follows: according to Boyle's law, pressure multiplied by volume equals constant k,

$$pV = k$$

where p and V are pressure and volume of the gas. Boyle's Law states that when the temperature of a given mass of confined gas is constant, the product of its pressure and

volume is also constant. When comparing the same substance under two different sets of conditions, the law can be expressed as:

$$p_1 V_1 = p_2 V_2$$

showing that as volume increases, the pressure of a gas decreases proportionally, and vice versa. Thus, a flow of 700 cm^3 min^{-1} at atmosphere pressure and 293 K for one minute is 700 cm^3, while in 100 torr condition, the volume is

$$V_2 = \frac{760\ torr}{100\ torr} 700\ \text{cm}^3 = 5320\ \text{cm}^3$$

Thus, the flow rate is 5320 cm^3 min^{-1} at 100 torr cell pressure. The diameter of the reactor is 6 cm, thus leading to a flow velocity of the gas mixture insider the reactor of

$$f = \frac{5320\ \text{cm}^3}{\pi(\frac{6}{2})^2\ cm^2 \times 60\ s} = 3.14\ cm/s$$

Bubbler and pre-mixing in balloons are common ways of preparing VOCs sources. VOCs with low vapor pressure, ie. in liquid state at atmospheric pressure and room temperature, are mostly carried to the reactor by flowing a small flow of carrier gas through a thermostated bubbler. The flow of the gas saturated with the VOC is controlled by a flowmeter placed after passing through the bubbler. The concentration of the VOC in the gas flow is then determined by the ratio of the vapor pressure of the liquid at the temperature of the thermostated bath and the total pressure in the bubbler, supposing that the gas flow has been saturated with the vapor pressure. Balloons are also widely used for preparing mixtures of liquid VOCs, mostly for VOCs with higher vaper pressures and also for diluting gases when very low concentrations are needed. To prepare a gas mixture, the balloon is first cleaned by several cycles of pumping down to low pressures after filling with Helium. For liquid VOCs, several freeze-thaw cycles using liquid N_2 are carried out to remove dissolved air from the liquid. The VOC is then expanded into the balloon by taking care that the pressure is always well below the vapor pressure of the liquid in order to avoid condensation in the balloon.

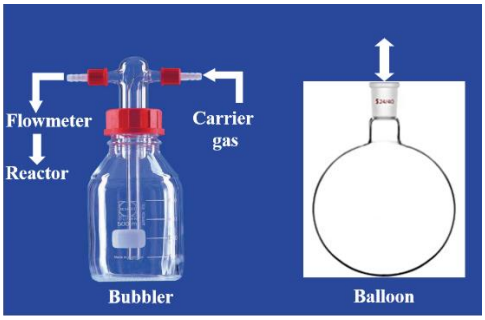

Figure 2.5 Bubbler and balloon used for gas or liquid injection.

2.2.4 Pulsed laser photolysis system

An excimer laser was used in the current thesis to photolysis the precursor Cl_2 and to produce the Cl atom as radical initiator. Excimer is the short name of excited dimer or complex of noble gas and halogen atoms. Generally, the noble gas is an inert gas (Ar, Xe or Kr) and do not react with chemical compounds, but at specific electric stimulation conditions, ground state noble gases are transferred to excited states and the excited noble elements can react with themselves or with halogen atoms to create an excimer, such as Ar_2^*, Kr_2^*, Xe_2^*, ArF, XeF, KrF. These excimers are temporarily bonded and quickly go back to ground states by spontaneous or stimulated radiation, thus generating laser light. Light at different wavelengths is generated by using different gas mixtures.

Table 2.1 Mixture of excimer gas and corresponding wavelengths.

Excimer	ArF	KrF	XeF
Wavelength	193 nm	248 nm	351 nm

For 351 nm laser, there is a strong absorption of Cl_2 and highly reactive Cl atoms are formed, Figure 2.6 shows the absorption cross section of Cl_2 in the 260 nm - 500 nm range, with the absorption cross section at 351nm being 1.82×10^{-19} cm^2.

$$Cl_2 + h\nu(\lambda \leq 495nm) \rightarrow Cl + Cl \qquad (2.1)$$

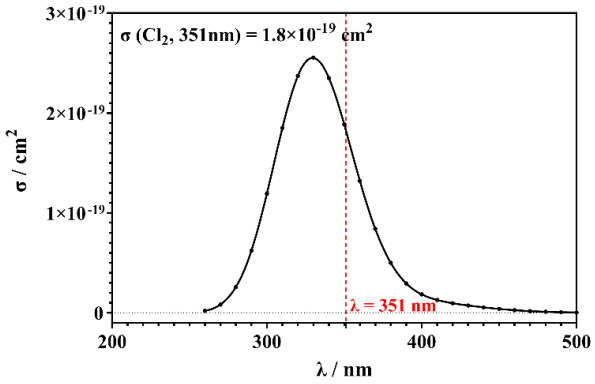

Figure 2.6 Absorption cross section of Cl_2 at 260 nm – 500 nm [85].

The produced radical concentration in a photolysis process, for example Cl is,

$$Cl = 2[Cl_2]P\,\Phi$$

where 2 represents two Cl atoms produced for each photolyzed Cl_2, $[Cl_2]$ is the concentration of Cl_2, Φ is the quantum yield of molecule for decompose to atom after absorption of a photon,

$$\Phi = \frac{molecules\ decomposed\ after\ absorbing\ photons}{moleculers\ absorbed\ photons}$$

P is the probability of absorbing photons for each Cl_2,

$$P = 1 - \exp(-N\sigma)$$

where N is the number of photons per pulse. This is related to the energy of the photolysis laser per pulse E_l and the energy of a photon E_p,

$$N = \frac{E_l}{E_p}, \qquad E_p = h\frac{c}{\lambda}$$

where h = 6.626×10^{-34} J s, c is 2.998×10^{8} m/s, so the calculated photon energy E_p is 5.66×10^{-19} J for photons at 351nm. In our experiments, the pulse energy of the excimer laser at 351nm was typically 0.1 J/cm^2, the calculated N is then 1.77×10^{17} /cm^2. With an absorption cross section of Cl_2 of 1.82×10^{-19} cm^2 at 351 nm, we calculate P = 3.16×10^{-2}. With a quantum yield of unity, and a typical concentration of $[Cl_2]$ equals to 5×10^{15} cm^{-3}, the produced Cl concentration is 3.16×10^{14} cm^{-3}. Therefore, for excimer laser at 351nm with 0.1 J energy, the produced concentration of Cl-atoms corresponds to 6.3% of the initial concentration of Cl_2. Cl atoms as a radical initiator react with

hydrocarbons, RH, through H-abstraction and lead to formation of the radical R, and in the presence of high concentration of O_2, R is converted to RO_2 immediately.

1. Alignment for excimer laser

In our laboratory, we used a Lambda Physik LPX 202i series excimer laser which emits a rectangular laser beam with dimension of 16 mm (height) × 28 mm (width). The beam exits the laser at the same heights as the center of the reaction cell, and the beam is aligned into the reactor by a dielectric mirror. It is very important (see further down) that the excimer laser propagates perfectly straight within the reactor: entering in a slight angle would introduce a systematic error on the absorption pathlength, which is only obtained by geometrical calculations. Aligning the excimer is not straightforward, as the beam is rather big and somewhat divergent. Therefore, several steps are carried out to align the beam:

(1) To align the dielectric mirror in a first step, a HeNe laser, emitting continuously a small beam of visible light with low energy, is used instead of the excimer laser. The red beam is first centered in the entrance and exit windows of the reactor, and then the dielectric mirror is adjusted so that the HeNe beam enters into the center of the excimer. Then with light-sensitive paper the position of excimer laser is checked and some fine tuning of the dielectric mirror is done.

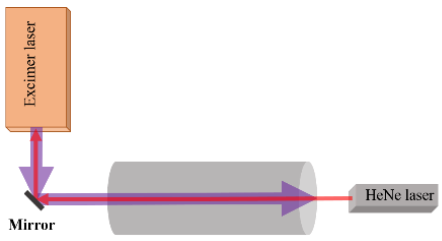

Figure 2.7 Schematic diagram for alignment of excimer laser by using HeNe laser.

(2) After step one the excimer laser enters and exits the windows roughly in the center and can thus be considered parallel to the reactor. But only step one is not enough, as the absorption pathlength is only calculated from geometrical considerations, and a

small deviation of angle of the excimer laser beam could cause a large difference in the absorption path lengths of the 2 CRDS paths. As show in the following Figure 2.8 in an exaggerated way, the absorption for path 1 is longer than path 2.

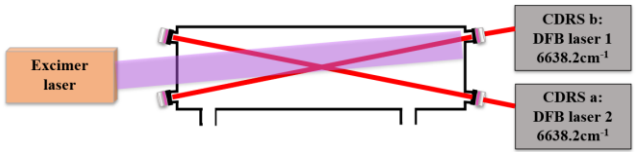

Figure 2.8 Schematic diagram for showing a non-parallel excimer laser beam.

The second step is therefore measuring the absorption of HO_2 simultaneously on both CRDS paths to check if the overlap of excimer laser and DFB laser is identical for both paths. Some minor adjustments of the Excimer laser alignment are sometimes needed until the measured absorption for both paths agree with each other.

(3) The light intensity of an Excimer beam is possibly not totally homogeneous, ie. is strongest in the center, and weaker on the sides of the rectangle. Thus step 3 is aimed to find the most homogeneous part of the photolysis beam with the highest energy.

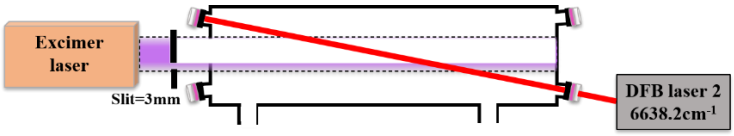

Figure 2.9 The measurements for the absorption of HO_2 in a 3 mm photolysis width.

First, a slit of 3 mm width is placed in the excimer laser beam and in front of the entrance of the reactor, one CRDS path is used to measure the absorption of HO_2 in the 3 mm photolysis width. HO_2 is produced by reaction of Cl-atoms with CH_3OH in 100 torr O_2. Then the slit is moved from the present position named as p = 0 mm step by step to p = 27 mm to cover all of the laser beam and the obtained absorption for every slit position is shown in left graph of Figure 2.10, with the y axis transformed to HO_2 concentration using the known absorption cross section. The initial concentraion of HO_2 at time 0 after the photolysis pulse is then derived by an exponential fit of the

signals. With high energy of the excimer laser, more HO_2 is formed and leads to a high intial concentration. On the right graph of the Figure, these intial concentrations are then plotted as a function of the slit position. Thus the measurement shows that the energy of the excimer laser is highest in the center and decreases at the edges.The most intense light is found between the positions p = 6 and p = 21 as shown within the blue dotted line. To get a beamwidth of 20 mm, the adjustable slit has been positioned for most experiments at the positions corresponding to the red dotted lines.

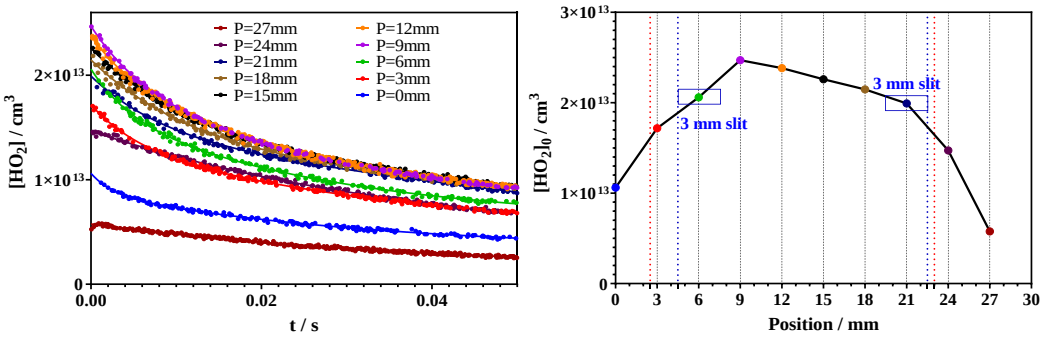

Figure 2.10 Concentration time profiles (left) and initial concentration (right) of HO_2 in different slit positions.

(4) Finally, detailed experiments were conducted to check the alignment, as shown in Figure 2.11 both CRDS were applied to measure the absorption of HO_2 at the same time and with a slit width of 20 mm. Absorption time profiles of HO_2 for both paths with different initial Cl concentrations agree with each other, the absorption at time 0 as a function of the Cl_2 flow for both paths agrees within 5%, demonstrating the good alignement of our excimer laser.

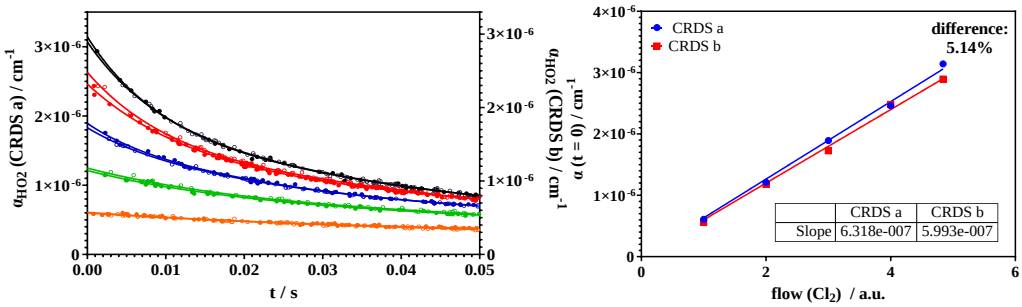

Figure 2.11 Left: absorption time profiles of HO_2 for both CRDS and right: absorption of HO_2 at time 0 for both path as a function of initial flow of Cl_2.

2.2.5 CRDS system

In this part the main contents is to describe the function of specific devices and how they are sychronized to successfully measure the time-resolved absorption of radicals, including DFB laser, piezo and AOM, and introductions to measurements of ring two time, and the absorption time kinetics of radicals, and finally the alignment procedure of CRDS.

1. DFB laser

There are five DFB lasers availble in our lab in the wavenumber range from 6479 to 7634 cm^{-1}. Each one corresponds to an absorption a of specific radical, which allow us to detect different radicals.

Table 2.2 DFB laser and corresponding wavenumber for detecting different radicals in our laboratory

DFB laser	Wavenumber/cm-1	Radical
Alcatel A1905LMI 3CN004 1 0CR	6497 ± 18	$CH_3C(O)O_2$
NELNLK1E5GAAA	6629 ± 17	HO_2
Fitel FOL15DCWB-A81-W1509	7014 ± 18	OH
NEL NLK1B5EAAA	7480 ± 20	CH_3O_2
DFB-1312-BF-20-CW-F1-H2-N127	7616 ± 18	$C_2H_5O_2$/$CH_3OCH_2O_2$

2. Piezo

As already mentioned before, to ensure that the cavity is resonant with the laser, the cavity length needs to be modulated to always have $L = n\frac{\lambda}{2}$, and for this purpose, a piezo transducer is used. Due to the converse piezoelectric effect of ceramic materials, displacement is induced when high voltage is applied to the piezo. A stacked piezo linear actuator (P-010.00H) is utilized in our experiment, and specifications are shown in table 2.3. A 0-10 V triangular wave signal from a function generator is first amplified 100 times and then acts on the piezo, with a maximum voltage the modulated displacement is 5 μm.

Table 2.3 Specifications of piezo P-010.00H.

	Displacement	Diameter OD	Diameter ID	Length	Resonant frequency	Operating voltage
	μm	mm	mm	mm	kHz	V
P-010.00H	5	10	5	7	144	0-1000

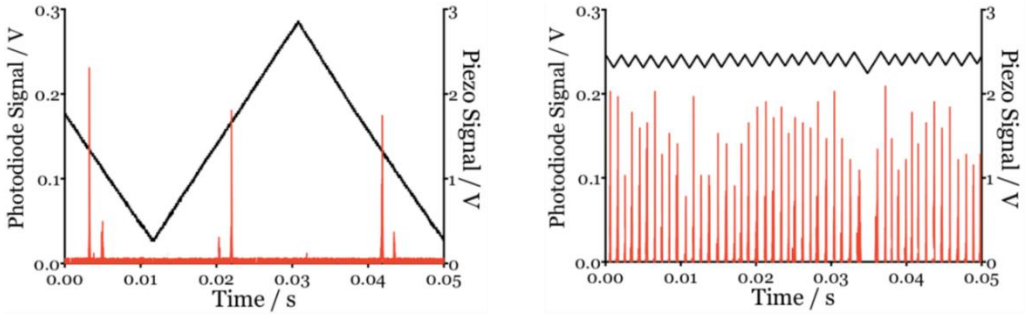

Figure 2.12 Resonant evens in full scan mode (left) and tracking mode (right) of the piezo in same time window[86].

For example, for detecting the absorption of $C_2H_5O_2$ at 1316.4 nm, the cavity length needs to be modulated by around 660 nm: this corresponds to the full scan procedure shown in the left graph of Figure 2.12. However, only three ringdown events occurred in the 0.05s time window necessary for the full scan, ie. much time is lost during the

modulation far away from resonance. Therefore, a home-made tracking module has been added, which allows modulating the cavity length in a small range around the resonant position and thus increase the probability of ring down events. As shown in right graph of Figure 2.12, around 50 events for the same time window are now obtained in tracking mode.

3. AOM

The DFB lasers are continously emitting and thus the AOM is needed to switch off the light in order to measure the ring down time of the light. The AOM is an acousto-optical modulator (AA optoelectronics MT110-IIR25-3Fio-PM0,5-J3-A), it is composed of a TeO_2 cystal and a frequency switch of 100 MHz. When a radio frequency signal (RF) is sent from the AOM driver to the AOM, its acoustic transducer transfers the RF signal to an acoustic wave, and the periodic vibration of the crystal results in a periodic change of its refractive index, which will then behave like a diffraction grating and results in 1^{st} order diffraction of light. By adjusting the incidence angle of the incident beam, or the frequency of the RF signal, the angle and intensity of diffraction light is thus varied. When there is no RF signal, diffraction stops and the 1^{st} order light completely disappear. Thus order 1 is injected into the cavity and allows to stop the propagation of the radiation within 350 ns, while the order 0 goes into a wavemeter (Burleigh WA-1100) having an accuracy of 0.01 cm^{-1}. When the modulated cavity length is resonant to the wavelength of the incident beam, light intensity received by the avalanche photodiode is enhanced up to a user-defined threshold, the trigger to the AOM is interrupted, thus completely removing the order 1 at the exit of the AOM, and the ringdown event is able to occur.

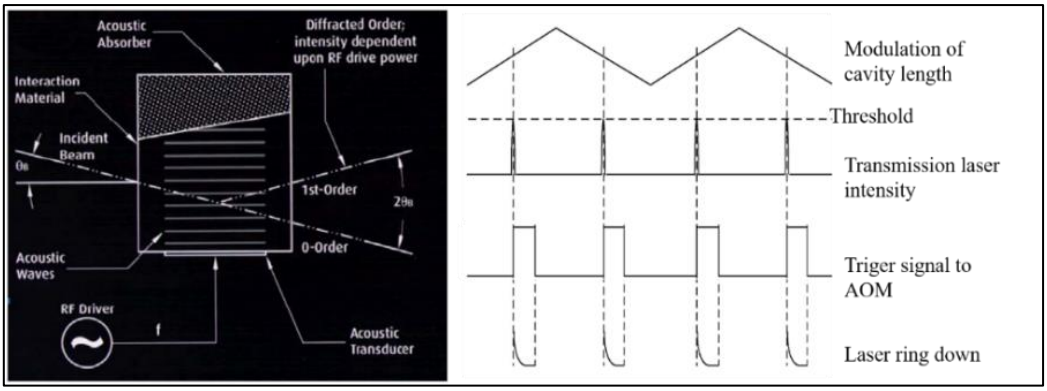

Figure 2.13 Left: schematic diagram of AOM working principle. Right: synchronization of CRDS system to have ring down events.

4. Ringdown time measurement

For an empty cavity with only noble gas and no absorber, the transmitted light decays exponentially with time t :

$$I = I_0 \exp\left(-\frac{t}{\tau_0}\right)$$

τ_0 is the ring down time,

$$\tau_0 = \frac{L}{c}\frac{1}{(1-R)}$$

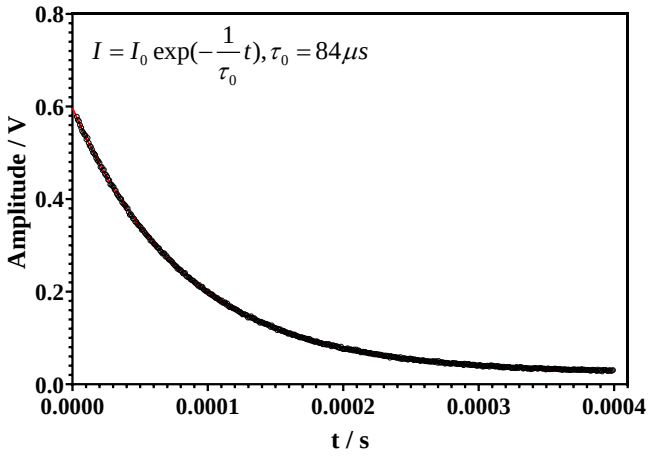

Figure 2.14 Ringdown signal for an empty cavity containing only noble gas.

Figure 2.14 shows the measured light intensity as a function of time and a Levenberg-Marquardt fit results in a ringdown time of 84 μs, with the derived ringdown

time and the known cavity length (0.79 m) and the speed of light (2.998×10^8 m/s), the calculated reflectivity of the mirrors is 99.997%. Therefore, when the cell is filled with absorber, the calculated effective optical path L_{eff} will be L_{eff} = L/(1-R) = 26.33 km, where L is the cavity length and R is the calculated reflectivity of the mirror. When the absorber is generated by the excimer laser, it is only presented in the region where the photolysis light pass through, then the calculated effective absorption path length L_{eff} will be L_{eff} = L/(1-R) = 10 km, where L now is the overlapping distance between the photolysis laser and the detection laser, which is 0.3 m.

5. Absorption-time profile measurement of radicals

When there is an absorber such as stable gas A present in the reactor, the measured ringdown time is τ, the absorbance is obtained by measuring ringdown time τ_0 and τ in absence and presence of the absorber, respectively

$$\alpha = \frac{R_l}{c}\left(\frac{1}{\tau} - \frac{1}{\tau_0}\right)$$

when the concentration of A is known, the absorption cross section is obtained. And by measuring the absorbance in a wide wavwwelength range, one can get the absorption spectrum.

Radical absorption measurements are more challenging and different from the measurement of stable molecules, because radicals are highly reactive and this leads to a short life time. Laser photolysis is used to create radicals in laboratory, but there are always chemical or physical reactions to consume radicals once they are produced, and these rection are often rapid. Thus the concentration of radicals changes with time and leads also to a change of the absorption with time. As a result, the measurement of radicals generally needs to be done in a time-resolved way, i.e. to get the absorption-time profile. The ringdown time before photolysis (ie. absence of radicals) is τ_0, and after photolysis (ie. presence of radical) is $\tau(t)$. Therefore, it is important to know at what time with respect to the photolysis pulse a ringdown event has occurred. For this purpose, a delay generator is used to synchronize the timing between the photolysis

laser and the two ringdown time measurements. When an experiment starts, the delay generator first sends a trigger signal to the acquisition card to start the data acquisition from the photodiode detector. Randomly occurring ringdown times are then obtained by fitting the individual light intensity decays. After typically 0.5 s, the delay generator will send a second trigger signal to fire the excimer laser. Entering into the acquisition program the delay between start of acquisition and delay for the Excimer laser then allows the acquisition program to assign a time-stamp to each ringdown time with respect to the Excimer pulse.

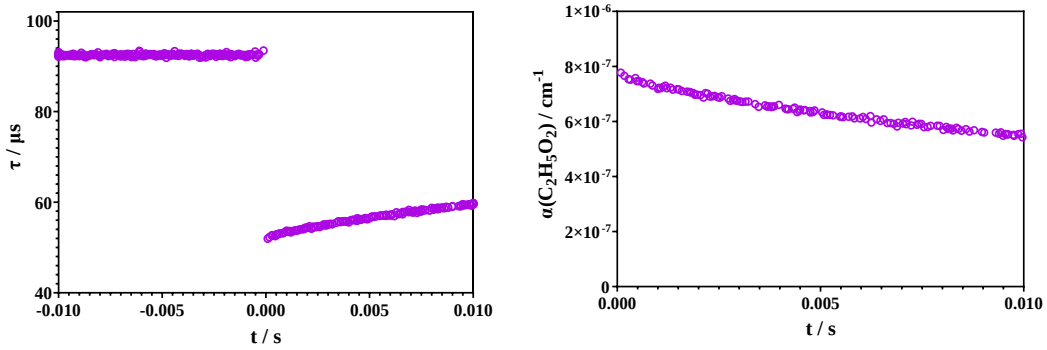

Figure 2.15 Left: typical ringdown time τ_0 and $\tau(t)$ measurements of $C_2H_5O_2$ radical, and right: absorbance time profiles of $C_2H_5O_2$ radical.

Figure 2.15 left shows the typical ringdown time τ_0 and $\tau(t)$ of $C_2H_5O_2$ radicals, at time 0 the excimer laser was fired to produce the radicals. The radicals were produced just after photolysis, which leads to strong increase in absorption and therefore a decrease in ringdown time. With reaction time increasing, the radicals are consumed and thus their concentraion decreases, and leads to longer ringdown time. Applying the above function, $\alpha(t)$ is deduced, as shown in right graph of Figure 2.15. With known absorption cross section σ_A, the concentration time profile can then be obtained.

$$\alpha_A(t) = \sigma_A \times [A]_t$$

In addition, we can see that the ring down time τ_0 is around 90 µs. This is a sign of very good and clean mirrors, but also an excellent alignment. There is a mature

procedure in our laboratory to align the cavity to get such a good perfomance and thus it is also specified.

6. Alignment of CRDS

As the DFB laser beam becomes invisible after passing through the highly reflecting mirrors, the wavelength of the HeNe laser at 632 nm shows visible light and is thus used as indicator light to aid alignment: the HeNe wavelength is partially reflected by the mirrors, but still visibly even at the exit of the cavity. Figure 2.16 shows the simplified diagram for the alignment of the CRDS, including a DFB laser, AOM, HeNe laser, mode matching lens L_1, two folding mirrors M, high reflectivity mirrors M_1 and M_2, focusing lens L_2 and photodiode APD. A coupler is used to join the HeNe laser to the DFB laser at the exit of the AOM and they enter together to the cavity. To get the mode matching of the cavity, a lens L_1 is mounted on a x-y-z stage and close to the exit of the fiber. Two folding mirrors M in between the mode matching lens and the cavity entrance mirror are used to adjust the propagation of the laser beam. The high reflectivity mirrors are wedged and are named M_1 for the right entrance side and M_2 for the left exit side. The advange of wedged mirrors, ie. the outer surface is slightly inclined, is that formation of parasite cavities between the outer surface of the mirror and for example the mode matching lense is avoided. The avalanche photodiode is also placed on a x-y-z stage after a focus lens L_2.

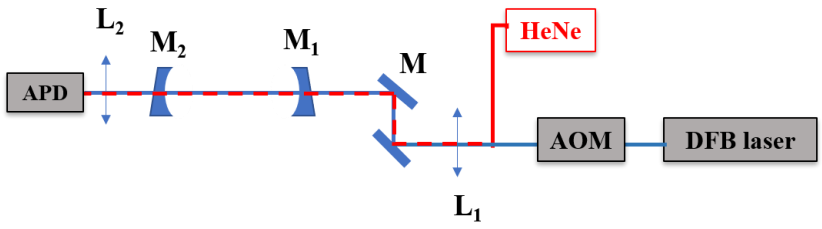

Figure 2.16 Diagram for the alignment of the cavity. (this is a simplified schematic diagram, as the deviation of the laser beam when it passes through the mirrors is not

shown.)

Due to the wedged mirrors, the alignment procedure is more complicated than with plan mirrors, because the beam is slighly deviated during the passage within the mirrors. In a first step, it must be assured, that both the HeNe laser beam and the DFB laser beam pass perfectly in the center of the mode matching lense, because otherwise HeNe and DFB beam would be differently deviated within the lense and the HeNe beam could not be used as an indicator of the position of the DFB beam. This is done by checking that the position of the DFB and HeNe laser beam are the same after passing through L_1 even after a relative long distance.

The second step is without M_1 and M_2: the HeNe laser is aligned to the center of the CRDS mirror holders, both entrance and exit, by adjusting two folding mirrors.

In step three, the exit mirror M_2 is mounted and adjusted such as to bring the reflection from the inner surface collinear with the incident beam. The reflection from the inner surface can be distinguished from the reflection of the outer surface, because it is collimated. As M_2 is connected to the cavity by an O-ring and fixed with four screws, by tighting or loosing the four screws one can change the orientation of M_2. A pinhole is placed after the exit of the mode matching lens to help to check the reflection beam and make sure it is reflected back to the center of the incident beam. This step can also be double checked with the NIR beam from the DFB laser, as only the reflection from the inner surface is with higher energy and able to be observed with an infrared sensitive card at the pinhole, while the reflection from the outer suface is too weak to be detected. At the same time the NIR laser beam transmittd through M_2 is also measured by the photodiode: by adjusting the focus distance and the position of the photodiode to get the highest light intensity for both HeNe laser and NIR laser, the position of the photodiode is also fixed at this step, taking into account the slight deviation of the beam while traveling through the rear mirror.

In step four, the entrance mirror M_1 is mounted, and the same procedure as in step three is done, ie. adjusting M_1 to get the reflection from the inner surface of M_1 to the center of the pinhole. The reflection beam from the outer surface is an unfocused spot and from the inner surface it is a defocused spot. After this procedure, the two inner surfaces of the wedged mirrors are parallel to each other and perpendicular to the incident beam. However, due to the wedged surfaces, the light transmitted through M_1 is deviated from the incident beam and thus does not hit anymore the center of M_2. To correct for this, the two folding mirrors M are ajusted in a way to bring the transmitted HeNe laser beam back to the center of M_2: this can be done visually be checking the position of the HeNe beam at the exit, but also by measuring the transmitted light intensity with photodiode, because the photodiode is aligned and the highest signal intensity is obtained when the laser beam is in the center of M_2. Finally, also M_1 needs to be slighly re-adjusted, as the angle of the incident beam has changed. The 2 final steps are repeated until the laser beam in the center of both CRDS mirrors M_1 and M_2.

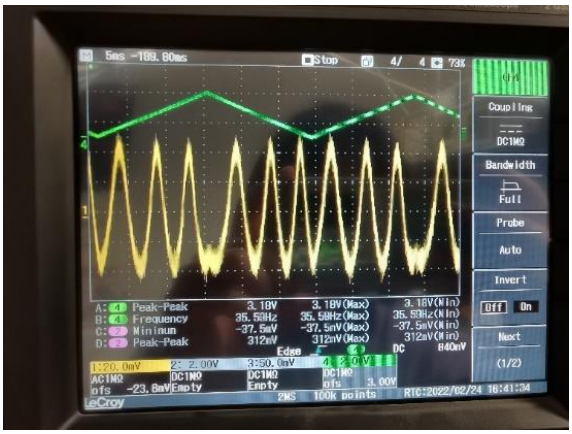

Figure 2.17 Modulated signal of piezo (green line) and constructive interference waves (yellow line) of HeNe laser.

With the piezo used to modulate the cavity length, a constructive interference can be observed from the He-Ne laser, shown in Figure 2.17. This is due to the partial reflection of the HeNe light, however the reflectivity of the mirrors in this wavelength range is poor, and therefore the finesse of the cavity is also poor. We know that only

when the cavity length is equal to an integral multiple of λ/2, the standing wave of the HeNe laser is formed and can be detected. Three resonant events are formed during the modulation and thus the cavity length is modulated around 3λ/2 = 948 nm. Because for a NIR laser at 6638.2 nm, the cavity length needs to be modulate at least by 753 nm, thus the full scan of piezo with 948 nm is enough to have resonance between the wavelenght of the NIR laser and cavity.

Once this alignement procedure has been carried out with the HeNe laser, the position of the mode matching lens is adjusted to get the best signal on the photodiode from the NIR light, and in princple there should be ringdown events visible from only the foundamental mode TEM_{00}. However, the reality is that higher modes are also always presented and thus final fine alignment of the CRDS mirrors, the photodiode and the mode matching lense is needed to have the best signal intensity and the longest ringdown time.

2.3 Photoionization mass spectrometer

2.3.1 General description

Mass spectrometry as a versatile and sensitive tool is widlely used in providing qualitative and quantitative analysis for a wide range of species in gas, liquid and solid phases. In our work, a home made VUV-lamp photoionization orthogonal acceleration reflectron time-of-flight mass spectrometer (VUVPI-TOFMS) was used for online analysis of radical reactions of atmospheric interest for obtaining preliminary information about target reactants and products. A general description about the set-up is based on the Figure 2.18.

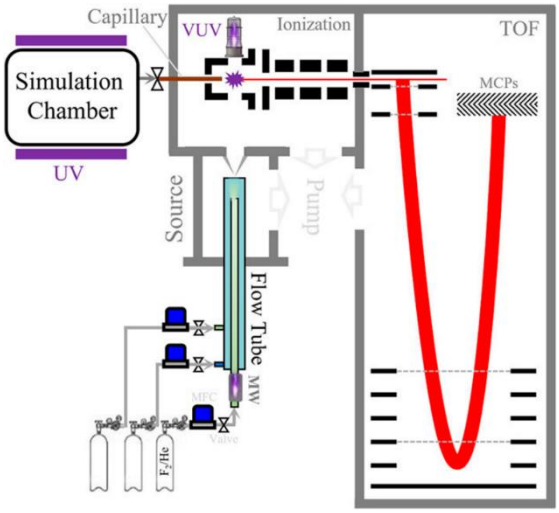

Figure 2.18 Schematic diagram of the mass spectrometer [87].

There are two reactors connected to the mass spectrometer, including a fast flow tube and an atmospheric simulation chamber. The fast flow tube is suited for reactions at low pressure (up to 10 Torr) in the milliseconds time scale, while simulation chambers are designed for atmospheric pressure reactions at long reaction times from minutes to hours. A fused silica capillary was connected to the exit of the simulation chamber to introduce gases to the ionization region. For sampling from the flow tube, a skimmer was placed to extract a moleculer beam from the gas coming out of the flow tube, while the extra gases were pumped out by a mechanical pump.

The samples from the flow tube and simulation chamber are transferred into the photoionization region, where commercial lamps were mounted to ionize neutral molecules to ions. A cage shaped electrode was developed to focuse ions and then ions were transported by einzel lens to the mass analyzer. Thus the mass spectra corresponing to the reactants and products were obtained. In the following part, detailed information about flow tube reactor, ionization region and mass analyzer are presented.

1. Fast flow tube reactor

A fast flow tube was used as reactor for studying radical reactions. It is composed of a 55 cm long pyrex main tube (30 mm-od, 26 mm-id), and a 60 cm long coaxial moveable inner tube (6 mm-od, 4 mm-id). F and Cl atom were normally used as radical

initiator due to their fast H-atom abstraction reactions with hydrocarbons RH. By passing diluted F_2/He, or Cl_2/He through a microwave discharge generator (GMS-200W, Sairem) F/Cl was created. The microwave discharge generator worked at 2.45 GHz and 100 W with a high efficiency (~90%) for production of F-atoms, ie. 90% F_2 dissociated and formed F atoms. The diluted F_2/He or Cl_2/He mixture was introduced into the inner tube, other gases were introduced into the main tube. Both tubes were coated with halocarbon wax to minimize radical wall loss.The exit of the inner tube closed with only 3 small holes used to release gases, in this case F/Cl atom are thus considered to rapidly mix with reactants. The inner tube was movable, so that the reaction time can be adjusted by changing the position of the inner tube with respect to the skimmer. All gas flows were measured by mass flow controllers (D07-7B, Sevenstar, China). The pressure of the reactor was regulated by a capacitance manometer (CDG-500, Agilent) and typically maintained at around 2 torr (~266pa). After partial or complete reaction, reactants along with products in the flow tube are sampled through the skimmer into the ionization region.

2. Ionization region

Mass spectrometry (MS) is an analytical technique that measures the mass-to-charge ratio (m/z) of ions to separate different species and present the signal intensity as a function of m/z value as mass spectrum. Therefore the ionization ability for a MS is an important step to get high detection limit and sensitivity. In our laboratory in Hefei, three different kinds of gas discharge lamps were utilized, Deuterium lamp (115-180 nm, 6.9-10.8 eV), Kr lamp (10.0/10.6 eV, 124/117 nm) and Xe lamp(8.4/9.6 eV, 147/129 nm). The three lamps could be switched freely for various species with different ionization energy to efficiently ionize gas molecules and minimize the generation of fragments. The lamps are sealed by MgF_2 windows, which have the advantage of transmitting VUV light with high efficiency. The light from the lamp directly radiates on the molecule without further focusing. In addition, the signal intensity of ions also depends on the photoionization cross section (PICS) of the

detected species: high PICS results in high signal intensity. Besides the ionization light source, the other parts in this region are the cage shaped electrode and the einzel lens (or ion guider) to both focus and transfer ions. From the simulation results by Simon software, it was shown that for an ion beam with a radius equal to 2 mm, which was considered as the dimension of a Kr lamp, it was focused to 0.2 mm at the end of the ion guider. The skimmer worked as a differential pressure element thus the pressure in the ionization region decreases to ~10^{-2} Pa. Similarly a 2 × 6 mm^2 slit in between the ionization region and the TOF chamber was used for both, ions transportation and depressurization.

3. Mass analyzer

The mass analyzer was made of a series of electrodes which were applied with different voltage and were used to control the flight trajectory and time of ions. 304 stainless steel was used as the material of the electrode plates for its resistance against corrosion and deformation. Only the first electrode is a solid plate which is supplied with a positive pulse voltage to extract ions, the others are all made of plates with the center hollowed out, metal meshes (Ni) are attached to the surface of some electrode plates which helps to shield electric fields and to avoid mutual interference of electric fields in different regions. The analyzer was mainly composed of three parts, namely the two-stage acceleration zone, free flight zone, and two-stage reflection zone from top to bottom. The acceleration and reflection zones are respectively connected on both sides of the free flight zone, as shown in Figure 2.18, those zones are seperated and marked by dashed lines. The first two dashed lines represent two acceleration zones, including a pulse extraction zone (12 mm) and a DC electric field acceleration zone (30 mm). The lengths of the free flight zone, the first and the second stage reflection zone are 320 mm, 90 mm and 48 mm. Therefore, ions reach the detector after undergoing acceleration, free flight, reflection, and another free flight. The detector is made of two micro-channel plates (MCP, 10 μm), which are displayed in a V shape as shown in Figure 2.18. The inner layer of a micro channel in MCP is made of a special material

which yields electrons after collision of ions, and because high voltage was applied on it, the produced electrons are accelerated and collide again within the micro channel and these process is repeated and thus large amounts of electrons are produced and then the signal of electrons is converted into voltage and finally amplified by a voltage amplifier and then transmitted to the data acquisition card.

2.3.2 Mass spectrometer performance

A standard gas mixture of benzene, toluene, and p-xylene was used to check the performance of the mass spectrometer, including mass resolution, sensitivity, and the limit of detection.

1. Mass resolution

Mass resolution is a parameter which is used to characterize the ability of a mass spectrometer for separating two adjacent masses, and is defined as $M/\Delta M$, where M is the mass to charge ratio and ΔM is the full width at half maximum. For a standard gas cylinder containing a mixture of 100 ppbv of BTEx (benzene, C_6H_6, m/z = 78; toluene, C_7H_8, m/z = 92; p-xylene, C_8H_{10}, m/z = 106), the measured ΔM at m/z = 78 is 0.028 and thus coorresponding to a mass resolution of around 2800.

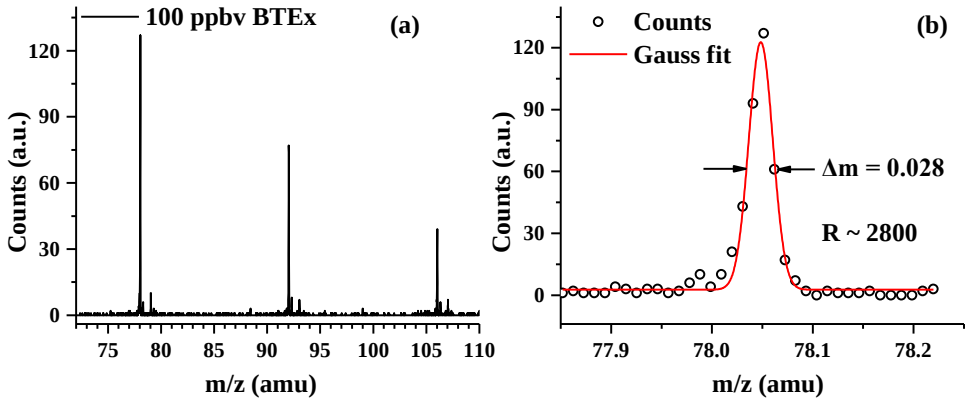

Figure 2.19 (a) Mass spectrum of BTEx and (b) fitted results of mass resolution for benzene at m/z = 78.

2. Sensitivity

To get the detection sensitivity, the standard gas mixture of BTEx of 100 ppbv is diluted by a bypass helium flow, and the concentration is varied by the flow of the two gases. As shown in Figure 2.20, with an acquistion time of 1 min, the signal intensity as a function of concentration shows good linear relationship, and the following equation is obtained from linear regression:

$$y = 4.15x + 0.2$$

A concentration of 20 ppbv corresponds to a signal intensity of 90, which leads to a sensitivity of 4 counts per ppbv.

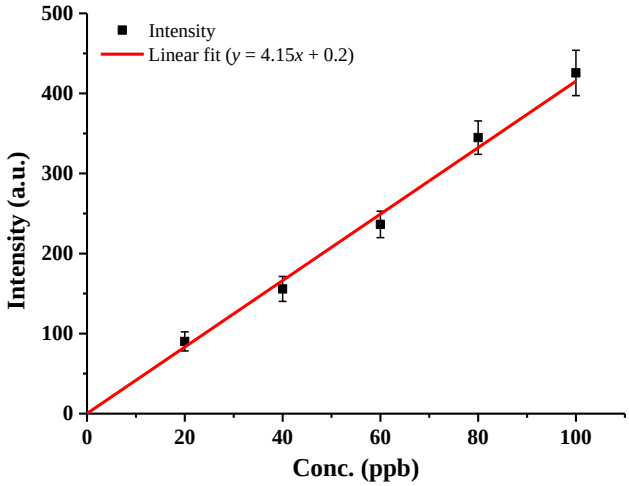

Figure 2.20 Sensitivity test for the detection of benzene

3. Limit of detection

The limit of detection(LOD) of mass spectrometer is defined and calculated according to the following equation,

$$LOD = \frac{3\sigma c}{S - B}$$

where σ is the variance of the signal amplitude between two mass peaks, c is the

concentration, S is the signal intensity of mass peaks and B is the mean value of noise. The detailed information is summrized in the paper published by our group, and only the results are given here. The LOD is measured to be 1.94×10^{7} cm^{-3} for benzene, and for methyl radicals is 8.42×10^{7} cm^{-3} [87].

2.3.3 Photoelectron photoion coincidence spectroscopy

Although gas discharge lamps already provide a big help in ionizing molecules, due to its limitation in energy, there are still products created in the flow tube which can not be ionized with the lamps. The conbination of synchrotron radiation light source with MS can provide more information about the products, based on the measured PIES the isomer products are able to be detected. In addition, to get information on the structure of products, photoelectron photoion coincidence spectroscopy (PEPICO) at French (SOLEIL) and Swiss (SLS) synchrotron radiation light sources were also applied, thus a brief introduction of PEPICO is also presented.

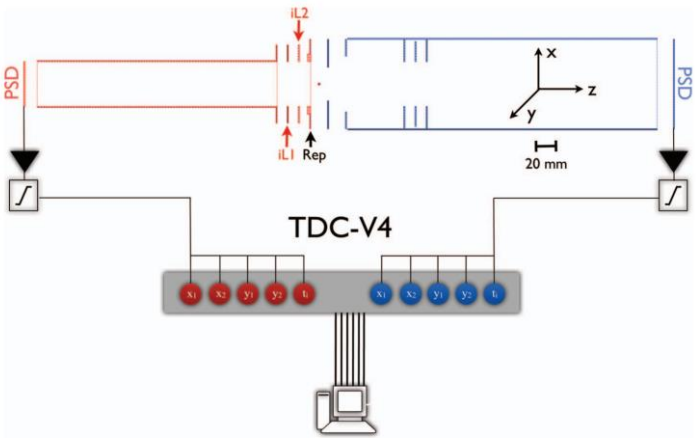

Figure 2.21 Schematic diagram of the double imaging photoelectron photoion coincidence (i^2PEPICO) spectrometer, DELICIOUS III, at SOLEIL synchrotron [88].

At the French national synchrotron radiation facility SOLEIL and on the beamline DESIRS, a double imaging photoelectron photoion coincidence (i^2PEPICO) spectrometer, named DELICIOUS III is installed. The detailed configurations of the synchrotron beamline and the spectrometer [79, 88, 89] are well explained in the

literature and only a short description is presented here. The i^2 PEPICO spectrometer is composed of a modified Wiley–McLaren ion time-of-flight (TOF) 3D-momentum imaging device (red, left side) and an electron velocity map imaging (VMI) analyzer (blue, right side), equipped with two position-sensitive detectors (PSDs) for the analysis of ions and electrons, respectively. Briefly, photons emitted from a variable polarization undulator were dispersed by a 6.65 m normal incidence monochromator equipped with a 200 L/mm grating, which was set to provide an energy resolution of ~3 meV. A gas filter located upstream of the beamline and filled with Ar gas was employed to suppress high harmonics emitted from the undulator. The multiplex coincidence scheme between the ion and electron yields mass-selected photoelectron spectra (PES) as a function of photon energy, which are then reduced to SPES. Meanwhile, the coincidence scheme can provide spectral finger prints to identify and separate isomers, and accurately measure thermochemical data such as fragment appearance energies and bond energies.

In conclusion, the technique applied in this thesis, along with the experiment carried out, as well as the corresponding chapter and published journal are the summarized and shown in Table 2.4.

Table 2.4 The summarized technique applied in this thesis, along with the experiment carried out, as well as the corresponding chapter and published journal.

Technique	Experiment	Chapter	Journal
CRDS coupled to laser photolysis (Lille)	Absorption cross section of $C_2H_5O_2$ Rate constant of $C_2H_5O_2 + HO_2$	3	*Photonics 2021, 8 (8), 296.*
	Rate constant of $C_2H_5O_2 + C_2H_5O$ Rate constant and branching ratio of $C_2H_5O_2 + C_2H_5O_2$		*ACS Earth Space Chem. 2021, 6 (1), 181.*
	Rate constant and branching ratio of $C_2H_5O_2 + CH_3O_2$	4	*PCCP. 2023, 25, 17840.*
	Rate constant and branching ratio of $C_2H_5O_2$ / $CH_3O_2 + Cl$		--

Mass spectroscopy with VUV lamp photoionization coupled to flow tube (Hefei)	Branching ratio of $C_2H_5OOC_2H_5$	3	*IJMS. 2023, 24 (4), 3731.*
Synchrotron PEPICO coupled to laser photolysis (PSI, Suisse)	Structure of $C_2H_5OOC_2H_5$		
Synchrotron PEPICO coupled to microwave discharge flow tube and heated oven (Soleil, France)	Photoionization and dissociative photoionization of CH_3CHO Products of F + CH_3CHO Branching ratio of Cl + CH_3CHO	5	--
	Photoionization and dissociative photoionization of H_2SO_4	--	*PCCP. 2022, 24 (4), 2015.*

Chapter 3. Kinetics and product measurements of the self-reaction of $C_2H_5O_2$

There are three product channels for $C_2H_5O_2$ self-reaction, leading to the radical C_2H_5O, stable products C_2H_5OH, CH_3CHO and the dimer $C_2H_5OOC_2H_5$:

$$C_2H_5O_2 + C_2H_5O_2 \rightarrow C_2H_5O + C_2H_5O + O_2 \quad (3.1.a)$$

$$C_2H_5O_2 + C_2H_5O_2 \rightarrow C_2H_5OH + CH_3CHO + O_2 \quad (3.1.b)$$

$$C_2H_5O_2 + C_2H_5O_2 \rightarrow C_2H_5OOC_2H_5 + O_2 \quad (3.1.c)$$

In the frame of this thesis, the rate constant of the overall reaction as well as the branching product between the different pathways was studied. Ethylperoxy radicals were generated by pulsed 351 nm photolysis of $C_2H_6/Cl_2/O_2$ mixtures:

$$Cl + C_2H_6 \rightarrow C_2H_5 + HCl \quad (3.2)$$

$$C_2H_5 + O_2 + M \rightarrow C_2H_5O_2 \quad (3.3)$$

100 Torr O_2 (Air Liquide, Alphagaz 2) was normally used to convert C_2H_5 rapidly to $C_2H_5O_2$ and also to react with C_2H_5O,

$$C_2H_5O + O_2 \rightarrow CH_3CHO + HO_2 \quad (3.4)$$

Reaction (3.4) results in a very low steady-state concentration of C_2H_5O, and when the oxygen concentration is high, HO_2 is almost instantaneously generated. Therefore, HO_2 can be used to characterize the branching ratio of the C_2H_5O radical channel. However, as mentioned in the introduction, HO_2 continues to react with $C_2H_5O_2$ and thus accelerates the decay of $C_2H_5O_2$. At this point, the kinetics of $C_2H_5O_2$ are determined by both the self-reaction of $C_2H_5O_2$ and the reaction between $C_2H_5O_2$ and HO_2. In the measurement of $C_2H_5O_2$ self-reaction, only when the branching ratio of the C_2H_5O channels is known, the impact of HO_2 + $C_2H_5O_2$ reaction on the total $C_2H_5O_2$ kinetics can be correctly taken into account, thereby obtaining the $C_2H_5O_2$ decay kinetics caused

by $C_2H_5O_2$ self-reaction and obtaining the self-reaction rate constant. The absorption-time profiles of $C_2H_5O_2$ and HO_2 in the near-infrared region were selectively and quantitatively measured using dual path cavity ringdown spectroscopy, the rate constant and branching ratio of the self-reaction of $C_2H_5O_2$ were determined. To quantitatively measure $C_2H_5O_2$ and HO_2, experiments to obtain the absorption cross sections of $C_2H_5O_2$ and HO_2 under the experimental conditions of 100 Torr O_2 were first performed. These were used to convert the absorption time profiles of both radicals into concentration time profiles.

As the near-IR cavity ringdown set-up is not able to measure stable products with a high enough sensitivity, vacuum ultraviolet photoionization mass spectrometry was also applied to measure the products of $C_2H_5O_2$ self-reaction.

3.1 Measurement of the $C_2H_5O_2$ absorption spectrum

To study the reactivities of $C_2H_5O_2$ radicals and thus understand its chemistry, a reliable detection of this radical is highly desirable. Previous studies of peroxy chemistry have mostly been carried out by UV absorption spectroscopy in the $\tilde{B}\leftarrow\tilde{X}$ electronic transition: this method gives a good sensitivity for peroxy radicals due to large absorption cross-sections, but the selectivity is poor because the absorption spectra are unstructured and the spectra of many different species are overlapping.

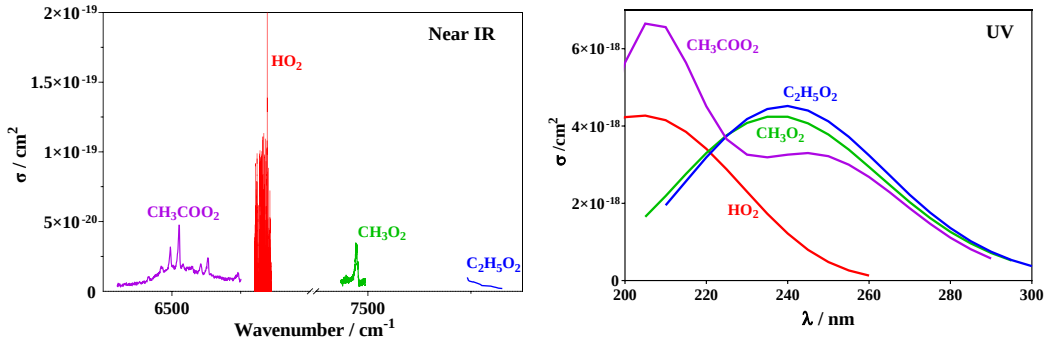

Figure 3.1 Absorption spectra for different RO_2 radicals in the near IR (left) and UV (right) region.

The $\tilde{A}\leftarrow\tilde{X}$ electronic transition of peroxy radicals is located in the near IR region. At room temperature, these transitions form rotationally unresolved envelopes with typical features about 1 cm^{-1} or more wide and allow a more selective detection of peroxy radicals, compared to UV absorption, as shown in Figure 3.1. The shape of such unresolved absorption features is typically only very little influenced by temperature or pressure, in contrast to the resolved spectra of small species like OH or HO_2: sharp lines are observed for transitions between different rotational or vibration states, where pressure is broadening the lines and temperature can change the relative populations of the different states and thus the cross-sections of the lines. However, due to small absorption cross-sections of the $\tilde{A}\leftarrow\tilde{X}$ electronic transition of peroxy radicals (~10^{-20}–10^{-21} cm^2), these transitions have not attracted much attention after they had been located for the first time by Hunziker and Wendt in 1976 [90, 91]. Interest has been revived many years later when the highly sensitive absorption technique of cavity ring down spectroscopy (CRDS) has been developed [80, 81], which can make up for the small absorption cross-sections. The first report on using this technique for the detection of peroxy radicals was in 2000 [92]: T. Miller and coworkers obtained pulsed near IR radiation by stimulated Raman shifting of the output of a pulsed dye laser in molecular hydrogen. The output of such a laser source has typical bandwidth of about 0.03 cm^{-1} and is thus much narrower than the $\tilde{A}\leftarrow\tilde{X}$ electronic transition of peroxy radicals. They measured the absorption spectra of the methyl and ethyl peroxy radicals, but determined only the absorption cross-section for the methyl peroxy radical. The peak of the $\tilde{A}\leftarrow\tilde{X}$ transition for $C_2H_5O_2$ was found around 7596 cm^{-1}.

A few years later, Atkinson and Spillman [93] measured again the spectra of both radicals, now using a continuous external cavity diode laser to perform cw-CRDS with a much narrower bandwidth (~3×10^{-5} cm^{-1}). They confirmed the overall shape of the absorption spectrum, and measured for the first time the absorption cross-section for $C_2H_5O_2$ using the kinetic method [87, 94-96]. This method can be applied, if the rate constant of a radical-radical reaction is known, because the initial concentration and thus the absorption cross-section can in principle be determined from the shape of the

kinetic decay. The self-reaction can be described as follows,

$$A + A \rightarrow B$$

$$\frac{d[A]}{dt} = -2k[A]^2 \quad \text{(E3.1)}$$

integration of Equation (3.1) leads to

$$\frac{1}{[A]} = \frac{1}{[A]_0} + 2kt \quad \text{(E3.2)}$$

plotting 1/[A] as a function of time leads to a straight line with the slope being $2k$. In the case where the rate constant is known, but not the absolute concentration of A, the absorption coefficient $\alpha = \sigma \times [A]$ can be used in Equation (3.2) instead of [A], leading to

$$\frac{1}{\alpha} = \frac{1}{\alpha_0} + \frac{2k}{\sigma}t \quad \text{(E3.3)}$$

plotting $1/\alpha$ leads to a straight line with the slope being $m = 2k/\sigma$ and the intercept $I = 1/\alpha_0$. However, different complications can arise from this method: (1) radicals can be lost through other processes too, for example through diffusion out of the photolysed volume or through unidentified secondary reactions in which case the decays are faster than expected from pure self-reaction only, and the retrieved absorption cross-section would be too small. (2) In the case of peroxy radicals, this method has another complication: as mentioned above, the self-reaction of the $C_2H_5O_2$ peroxy radical leads to C_2H_5O radicals, and the following oxidation reaction of C_2H_5O leads to the formation of HO_2 radicals. As a result, the $C_2H_5O_2$ decays are accelerated by the formation of HO_2, and therefore when using Equation (E3.3), the obtained rate constant k is the so called k_{obs} and the acceleration has to be taken into account to retrieve the "real" rate constant k from $C_2H_5O_2$ decays. Using the recommended value of k_{obs} in the kinetic method, Atkinson and Spillman [93] obtained an absorption cross-section for $C_2H_5O_2$ at 7596 cm^{-1} of $\sigma = (3.0 \pm 1.5) \times 10^{-21}$ cm^2.

Another work on the ethyl peroxy spectrum from the Miller group [97] scanned the $\tilde{A} \leftarrow \tilde{X}$ electronic transition over a large wavelength range and identified the transitions for the two different isomers. Indeed, ethyl peroxy radicals exist in an equilibrium between two stable conformers with the dihedral angles between the O-O-C and O-C-

C planes being 0° for the T (trans) and 120° for the G (gauche) conformer. The peak absorptions for both conformers were located well separated at 7362 cm^{-1} for the T- and 7592 cm^{-1} for the G-conformer. In this work, they used a different method to estimate the absorption cross-section: peroxy radicals were generated by the reaction of Cl-atoms with C_2H_6, with the Cl-atoms being generated by 193 nm photolysis of oxalylchloride, $(COCl)_2$. To obtain the concentration of $C_2H_5O_2$, they measured the photolysis laser energy with and without precursor, and calculated the Cl-atom concentration from the difference. Supposing that each Cl-atom generated one $C_2H_5O_2$ radical, they obtained $\sigma = 4.4 \times 10^{-21}$ cm^2 for $C_2H_5O_2$ at 7596 cm^{-1}.

The next work on the ethyl peroxy spectrum from the Miller group [98] used a different method to obtain the absorption cross-section: in a dual-path CRDS set-up, the concentration of HCl (generated from the reaction of Cl-atoms with C_2H_6) was measured on one path while the absorption of $C_2H_5O_2$ was measured simultaneously on the other path. Again supposing that each HCl-molecule had generated one $C_2H_5O_2$ radical, they obtained $\sigma = (5.29 \pm 0.20) \times 10^{-21}$ cm^2 for $C_2H_5O_2$ at 7596 cm^{-1}.

Table 3.1 Summary of the $C_2H_5O_2$ absorption cross-section at 7596 cm^{-1}.

$\sigma/10^{-21}$ cm^2	Method	Reference
3.0 ± 1.5	Kinetic method, no other radical losses considered	Atkinson and Spillman[93]
4.4	Depletion of photolysis energy through precursor with [Cl] = [$C_2H_5O_2$], i.e., no secondary reactions considered	Rupper et al.[97]
5.29 ± 0.20	Measurement of HCl in dual path CRDS with [Cl] = [$C_2H_5O_2$], i.e., no secondary reactions considered	Melnik et al.[98]
5.29	Kinetic method used for validation of Ref. [98]	Melnik et al.[99]
10 ± 2	Measurement of HO_2/$C_2H_5O_2$ in dual path CRDS with [Cl] = [HO_2] = [$C_2H_5O_2$]	This work
10 ± 2	Kinetic method from $C_2H_5O_2$ + HO_2	This work

In the most recent work from the Miller group [99], the above absorption cross-section was validated indirectly through the kinetic method: the $C_2H_5O_2$ absorption

profiles were converted to $C_2H_5O_2$ concentration-time profiles using the above absorption cross-section, and the rate constant k_{obs} for the self-reaction was extracted. Good agreement with other literature data was found, which was taken as an indication that the absorption cross-section is valid. A summary of previous results as well as the results obtained in this work is presented in Table 3.1.

In the frame of my thesis, I carried out a new determination of the absorption cross-section, based on two different approaches. The first one is comparable to one of the Miller methods [98] and will be called back-to-back method: in our dual-path CRDS set-up we generate Cl-atoms and transform them to HO_2 through reaction with CH_3OH, with HO_2 being quantified on one path at 6638.2 cm^{-1}.

$$Cl + CH_3OH \rightarrow CH_2OH + HCl \tag{3.4}$$

$$CH_2OH + O_2 \rightarrow HCHO + HO_2 \tag{3.5}$$

Directly after, the Cl-atoms were transformed to $C_2H_5O_2$ by adding C_2H_6 instead of CH_3OH to the reaction mixture and the $C_2H_5O_2$ absorption was measured on the second path. Supposing that the Cl concentration stays the same between both experiments and that in both cases all Cl-atoms are converted to either HO_2 (which can be quantified reliably) or to $C_2H_5O_2$, the absorption cross-section of $C_2H_5O_2$ is determined relative to the one of HO_2.

The second approach is a variation of the kinetic method such as used by Atkinson and Spillman [93] and Melnik et al. [99], but not based on the self-reaction of $C_2H_5O_2$, but on the cross reaction between HO_2 and $C_2H_5O_2$.

$$C_2H_5O_2 + HO_2 \rightarrow C_2H_5O_2H + O_2 \tag{3.6}$$

This reaction has been measured in a wide range of concentrations under either excess of HO_2 or excess of $C_2H_5O_2$. In the first case, the rate constant is retrieved by adjusting the $C_2H_5O_2$ decays with the absolute concentration of HO_2 being fixed, while in the second case the rate constant is fixed to the value determined just before, and now the best fit of the HO_2 decay is achieved by adjusting the absolute concentration of $C_2H_5O_2$, i.e., the absorption cross-section.

The Cl_2 concentration was typically around 1×10^{16} cm^{-3}, leading with a photolysis energy of 120 mJ/cm^2 to initial Cl-atom concentrations of around 1×10^{14} cm^{-3}. A small flow of pure ethane was added directly from the cylinder (Mitry-Mory, N35) to the mixture through a calibrated flow meter (Bronkhorst, Tylan). Methanol (Sigma-Aldrich) was added to the mixture by flowing a small fraction of the main flow through a bubbler containing liquid methanol, kept in ice or in a thermostated water bath. All experiments were carried out at 298 K. In the following, the two different methods applied in this work for the determination of the absorption cross-section of $C_2H_5O_2$ at its peak wavelength 7596 cm^{-1} are described.

3.1.1 Quantification of $C_2H_5O_2$ in Back-to-Back Experiments

In the first method, the absorption cross-section of $C_2H_5O_2$ is measured in a rather direct way in back-to-back experiments relative to the absorption cross-section of HO_2. Therefore, the reliability of the measurement depends on the reliability of the absorption cross-section of HO_2. The absorption spectrum and cross-sections of HO_2 in the near IR have been measured several times and pressure broadening of selected lines has also been carried out. In this work, HO_2 was quantified on two different absorption lines with the cross-section varying about a factor of 9 between both lines: for most experiments, HO_2 has been detected on the strongest line of the $2\nu_1$ band at 6638.2 cm^{-1}, but for experiments with high initial radical concentrations a small line at 6638.58 cm^{-1} has been used to avoid saturation. The absorption cross-section of the strongest line in helium ($\sigma_{50\ Torr\ he} = 2.72 \times 10^{-19}$ cm^2) [96, 100] and in synthetic air ($\sigma_{100\ Torr\ air} = 1.44 \times 10^{-19}$ cm^2) [101-103] has been measured several times, the cross-section of the small line has only been measured once in 50 and 100 Torr helium (2.8 and 2.1×10^{-20} cm^2, respectively) [102, 104], but no measurements in pure O_2 have been carried out. Therefore, we have determined both cross-sections in 100 Torr O_2 in the frame of this work, using the kinetic method.

Figure 3.2 shows a typical example: HO_2 decays have been measured for 3 different initial Cl-atom concentrations and the raw signals are presented in graph (a). The decays have then been plotted following Equation (3.3) and the result is shown in graph (b).

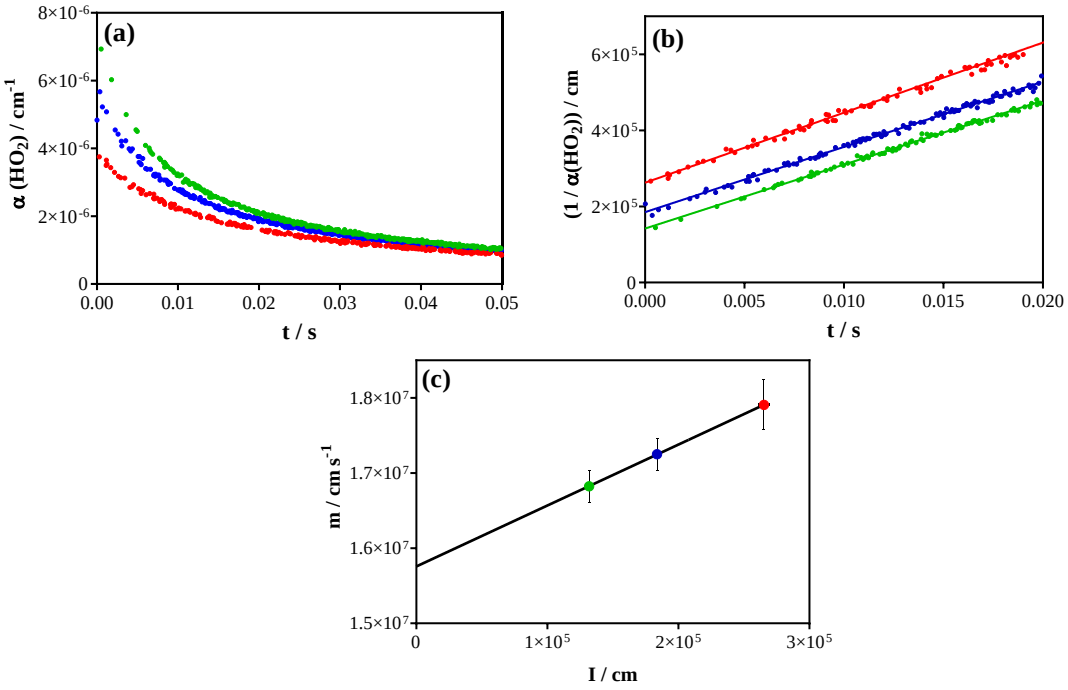

Figure 3.2 Example of measurement of HO_2 absorption cross-section using the kinetic method: graph (a) shows kinetic decays for 3 different Cl-atom concentrations, graph (b) shows the same signals plotted following Equation (3.3) with the linear regression over the first 20 ms, graph (c) shows the plot of slope *m* as a function of *I*, obtained in graph (b) for the 3 experiments.

The slope of a linear regression of this plot can in principle be converted to the absorption cross-section using the known rate constant of the HO_2 self-reaction. However, as has been mentioned above, radicals can be lost also through other processes, and in the case of laser photolysis experiments one possible loss is diffusion out of the photolysis volume. The relative impact of this loss process decreases with increasing initial HO_2 concentration and in order to correct this influence, an extrapolation to infinite $[HO_2]_0$ is used, shown in graph (c): the slope m from graph (b) is plotted as a function of the intercept I ($=1/\alpha_0$). Extrapolating the m-values to $I = 0$ therefore removes the influence of the diffusion on the slope m. In the example of Figure

3.2, using the slope *m* obtained from extrapolation instead of using the directly determined slope *m* leads to an increase in the absorption cross-section of 6% for the highest initial concentration and 13% for the lowest initial concentration. Error bars in graph (c) correspond to 95% confidence interval of the linear regression from the graph (b): the error bars on the x-values are too small to be seen within the symbols. Several such series have been measured for both absorption lines, and the following absorption cross-sections in 100 Torr O_2 have been deduced for HO_2 for the two lines:

$$6638.2\ cm^{-1}: \sigma = (2.0 \pm 0.3) \times 10^{-19}\ cm^2$$
$$6638.58\ cm^{-1}: \sigma = (2.1 \pm 0.3) \times 10^{-20}\ cm^2$$

The uncertainty on σ reflect the uncertainty of ±15% on the rate constant of the HO_2 self-reaction, such as estimated by the IUPAC committee [105].

These absorption cross-sections are now used to obtain the absorption cross-section of $C_2H_5O_2$ in back-to-back experiments. Figure 3.3 shows the principle of these measurements: Cl_2 is first photolysed in the presence of excess CH_3OH, leading to quantitative formation of HO_2 radicals: typical absorption-time profiles for 4 different Cl_2 concentrations are shown in the upper right graph (b) of Figure 3.3. In the next step, CH_3OH is removed from the gas flow, and excess C_2H_6 is added instead, all other conditions are kept constant. The corresponding $C_2H_5O_2$ absorption time profiles are shown in the upper left graph (a). It can be seen that the HO_2 profiles decay much faster than the corresponding $C_2H_5O_2$ profiles: this is in line with the rate constant of the HO_2 self-reaction being around 10 times faster than the rate constant of the $C_2H_5O_2$ self-reaction. In order to get a reliable extrapolation of $\alpha_{t=0\ ms}$, a plot of $1/\alpha = f(t)$ is generated for both species (graph (c) and (d) for $C_2H_5O_2$ and HO_2, respectively) and a linear regression allows retrieving $\alpha_{t=0\ ms}$ from the intercept. For HO_2, the $\alpha_{t=0\ ms}$ values can now be converted to absolute concentrations ($[HO_2]_{t=0\ ms}$) using the above determined absorption cross-section. Supposing that each Cl-atom is converted into either one HO_2 radical or into one $C_2H_5O_2$ radical, i.e., $[HO_2]_{t=0ms} = [C_2H_5O_2]_{t=0ms}$, a plot of $\alpha(C_2H_5O_2)_{t=0ms} = f([HO_2]_{t=0ms})$ leads to a linear relationship with the slope equal to the

absolute absorption cross-section of $C_2H_5O_2$. The lower graph (e) in Figure 3.3 summarizes the results, obtained on four different days using either the big HO_2 line at 6638.2 cm^{-1} (open circles and open diamonds) or the small line at 6635.58 cm^{-1} (all other symbols, with the colored symbols representing the results from the experiment in Figure 3.3).

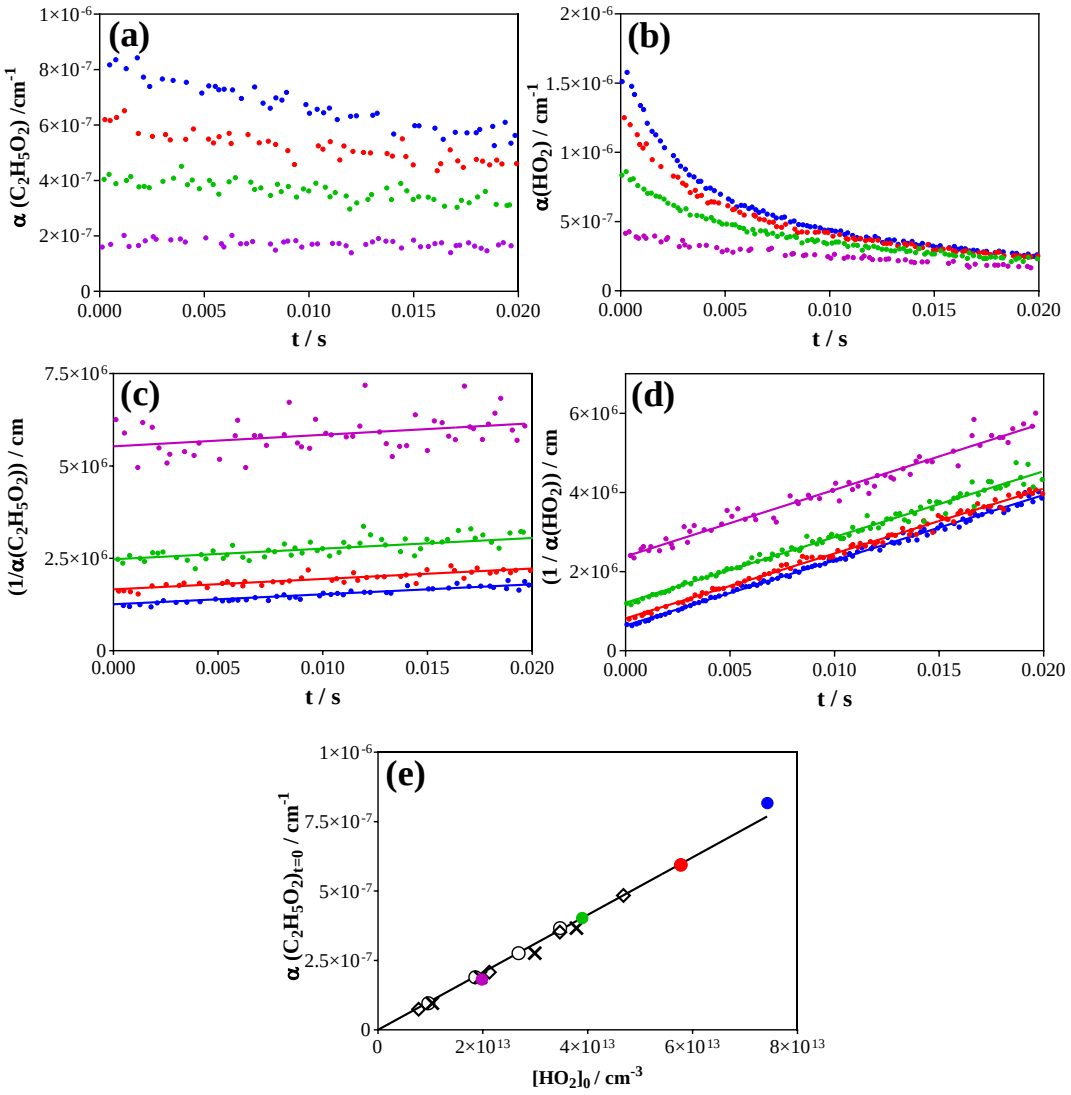

Figure 3.3 Example of measurement of the $C_2H_5O_2$ absorption cross-section relative to the HO_2 absorption cross-section. Upper graphs: $C_2H_5O_2$ (a) and HO_2 (b) absorption time profiles. Graphs (c) and (d): same profiles, converted to 1/α, and linear regression over the first 20 ms following the photolysis pulse. Lower graph (e) shows plot of $\alpha(C_2H_5O_2)_{t=0\ ms} = f([HO_2]_{t=0\ ms})$: open circles and open diamonds are obtained using HO_2 measurements at 6638.2 cm^{-1}, colored points (from above graphs) and crosses are obtained using HO_2 measurements at 6638.58 cm^{-1}. $[O_2] = 2.8 \times 10^{18}$ cm^{-3}, $[C_2H_6] =$

3.7×10^{16} cm^{-3} for all experiments.

From these experiments, an absorption cross-section for $C_2H_5O_2$ at 7596 cm^{-1} of $\sigma = (1.0 \pm 0.2) \times 10^{-20}$ cm^2 is obtained. The error bar is mostly due to the uncertainty in the rate constant of the HO_2 self-reaction, to which the absorption cross-section of $C_2H_5O_2$ is directly linked.

In imitation of the kinetic method such as used by Melnik et al.[99], the above experiments can also be used to validate the absorption cross-section obtained using the back-to-back method by determining k_{obs} and comparing it with data from the literature. Indeed, the $C_2H_5O_2$ data from Figure 3.3 (c) can be treated with the same method as shown for the HO_2 data in Figure 3.2, and the obtained intercept is then equal to $2 \times k_{obs}/\sigma$. Figure 3.4 shows this type of plot for the data from Figure 3.3 (c).

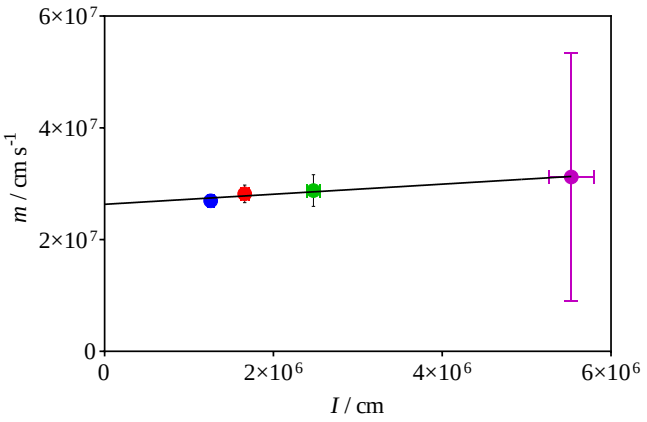

Figure 3.4 Plot of slope m as a function of I from the linear regressions obtained in Figure 3.3 (c).

Now, using the above retrieved absorption cross-section for $C_2H_5O_2$ at 7596 cm^{-1} of $\sigma = (1.0 \pm 0.2) \times 10^{-20}$ cm^2, we can obtain from the intercept of the linear regression in Figure 3.4 a value for $k_{obs} = (1.3 \pm 0.3) \times 10^{-13}$ $cm^3\,s^{-1}$, in good agreement with the currently recommended literature value (1.24×10^{-13} $cm^3\,s^{-1}$) [13].

3.1.2 Quantification of $C_2H_5O_2$ by Measuring the Rate Constant of $C_2H_5O_2 + HO_2$

Another way to determine the absorption cross-section of $C_2H_5O_2$ has been applied by determining the rate constant of the cross reaction between $C_2H_5O_2$ and HO_2. Indeed, the rate constant can be determined under different conditions: using an excess of HO_2 over $C_2H_5O_2$ leads to $C_2H_5O_2$ decays that are sensitive to the absolute concentration of HO_2, while in the reverse case the HO_2 decay will be sensitive to the absolute $C_2H_5O_2$ concentration, and thus to its absorption cross-section. Therefore, measuring simultaneously the decays of both species over a large range of concentration ratio allows determining the rate constant (from excess HO_2 experiments) and the absorption cross-section of $C_2H_5O_2$ (from excess $C_2H_5O_2$ experiments). Figure 3.5 illustrates this using two examples from Figure 3.6.

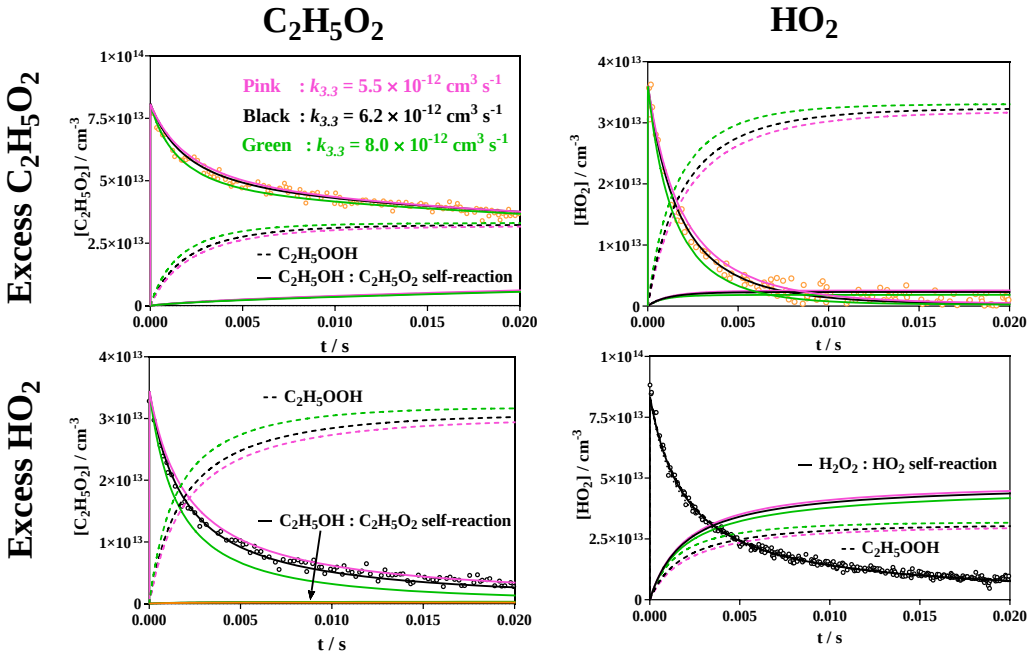

Figure 3.5 Experimental profiles taken under excess $C_2H_5O_2$ conditions (upper graphs) and under excess HO_2 conditions (lower graph). The dashed lines represent modelled profiles of C_2H_5OOH, the product from $C_2H_5O_2 + HO_2$ reaction, while the full lines represent the product of the corresponding self-reaction (C_2H_5OH for $C_2H_5O_2$ and H_2O_2 for HO_2). Different colors represent the result from a model with different $k(C_2H_5O_2 + HO_2)$.

Both species show different behavior: $C_2H_5O_2$ always decreases rapidly over the first few ms, given by the loss through $C_2H_5O_2$ + HO_2 reaction (C_2H_5OOH concentration time profile given as dashed lines). Then the decays slow down at longer reaction times, when HO_2 concentration gets low, because the self-reaction becomes the major loss process, and this reaction is slow for $C_2H_5O_2$ radicals (C_2H_5OH concentration time profile given as full lines). This behavior is especially visible when $C_2H_5O_2$ is the excess species (upper graph in Figure 3.5 and pink and orange circles in Figure 3.6: $[C_2H_5O_2] \approx 3 \times [HO_2]$). HO_2 on the other hand approaches low concentrations at longer reaction times under all conditions, even when it is the excess species (lower graph in Figure 3.5 and black circles in Figure 3.6: $[HO_2] \approx 3 \times [C_2H_5O_2]$): its self-reaction ($H_2O_2$ concentration time profile given as full lines) is much faster than the self-reaction of $C_2H_5O_2$ and is a major loss process under all conditions and all reaction times, the reaction with $C_2H_5O_2$ (dashed lines) plays a major role only under excess $C_2H_5O_2$ conditions. Under excess HO_2 concentrations, the HO_2 profile is barely influenced by $C_2H_5O_2$ + HO_2: an increased loss through an increase in k($C_2H_5O_2$ + HO_2) is counterbalanced by a decreased loss through self-reaction.

The profiles of all condition shown in Figure 3.6 have simultaneously been fitted to a simple mechanism, given in Table 3.3. The initial Cl-atom concentration was fixed to 1.2×10^{14} cm^{-3} for all experiments, obtained in initial experiments from measuring pure HO_2 decays (no C_2H_6 added). $[C_2H_6]$ has been varied between 1.9–7.5×10^{15} cm^{-3} and $[CH_3OH]$ has been varied between 2.8–5.0×10^{15} cm^{-3}. Using these conditions, the ratio of $[HO_2]/[C_2H_5O_2]$ has been varied between 0.3 (pink circles) and 2.5 (black circles).

For all graphs in Figure 3.6, the above determined absorption cross-section (σ = 1.0×10^{-20} cm^2) has been used to convert the $C_2H_5O_2$ absorption coefficients into absolute concentrations.

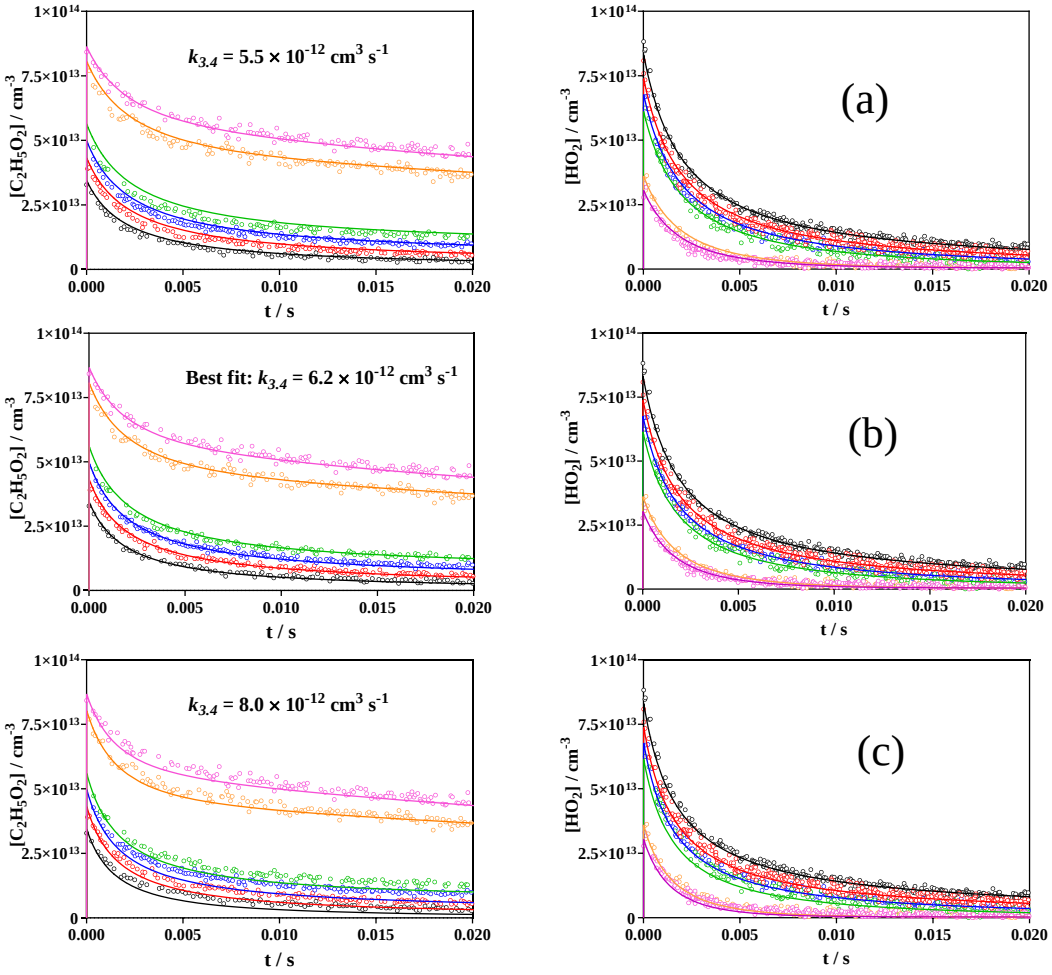

Figure 3.6 $C_2H_5O_2$ (left graphs) and HO_2 (right graphs) concentration time profiles for a total radical concentration of 1.2 × 10^{14} cm^{-3}. $C_2H_5O_2$ absorption time profiles have been converted using σ = 1.0 × 10^{-20} cm^2. The applied k($C_2H_5O_2$ + HO_2) of the model is (b): best fit with 6.2 × 10^{-12} cm^3 s^{-1}, upper graphs (a): 5.5 × 10^{-12} cm^3 s^{-1}, lower graphs (c): 8.0 × 10^{-12} cm^3 s^{-1}.

Table 3.2 Conditions for experiments shown in Figure 3.6. Initial Cl-atom concentration was for all experiments 1.2 × 10^{14} cm^{-3}, total pressure was 100 Torr O_2, T = 295 K. [$C_2H_5O_2$] and [HO_2] concentration taken from the model. Total radical concentrations are slightly below initial Cl-concentration due to Cl + $C_2H_5O_2$ reaction.

[C_2H_6]/10^{15} cm^{-3}	[CH_3OH]/10^{15} cm^{-3}	[$C_2H_5O_2$]$_{max}$/10^{13} cm^{-3}	[HO_2]$_{max}$/10^{13} cm^{-3}
1.94	5.0	3.4	8.3
2.74	5.0	4.3	7.4
3.45	5.0	5.0	6.7
4.30	5.0	5.6	6.1
5.91	2.8	8.1	3.6
7.50	2.8	8.6	3.0

The profiles for both species could be well reproduced over the entire concentration range using a rate constant of $k(C_2H_5O_2 + HO_2) = 6.2 \times 10^{-12}$ cm^3 s^{-1}, shown in the center graph (b). In a next step, different rate constants for the cross reaction have been tested: indeed, despite several measurements of this rate constant over the last decades [17, 18, 24, 28-31], there is no good agreement for this rate constant. An excellent summary on previous measurements of this rate constant can be found in Noell *et al*. [18] and will not be repeated here. The two recent determinations from Noell *et al*. [18] and Boyd *et al.* [30] are considered by the IUPAC committee as being carried out by the most reliable methods, however they vary by about a factor of 1.5 (8.14×10^{-12} cm^3 s^{-1} for Boyd *et al*. from UV absorption and 5.57×10^{-12} cm^3 s^{-1} for Noell *et al.* from UV/near IR absorption). We have tested these two limits by trying to adjust both profiles over the entire concentration range. In the upper graphs (a), the rate constant $k(C_2H_5O_2 + HO_2)$ has been set to the lower limit such as obtained by Noell *et al*. (5.5×10^{-12} cm^3 s^{-1}), leading to $C_2H_5O_2$ and (less pronounced) HO_2 decays that are too slow. Increasing the initial $C_2H_5O_2$ concentration by about 10% (corresponding to a decreased absorption cross-section for $C_2H_5O_2$: $\sigma = 0.9 \times 10^{-20}$ cm^2) can lead again to less good, but still acceptable HO_2 and $C_2H_5O_2$ decays (which would also imply a slight deviation of the overall initial radical concentration from 1.2×10^{14} cm^{-3}). In the lower graphs (c), the upper limit has been tested by setting $k(C_2H_5O_2 + HO_2) = 8 \times 10^{-12}$ cm^3 s^{-1}: decays of both species are too fast and a decrease in concentration does not lead to an acceptable adjustment of both species.

Table 3.3 Reaction mechanism used to fit all experiments in this work.

Reaction	k/cm^3 s^{-1}	Reference
$2\ C_2H_5O_2 \rightarrow 2\ C_2H_5O + O_2$	3.1×10^{-14}	This work*
$2\ C_2H_5O_2 \rightarrow C_2H_5OH + CH_3CHO + O_2$	7×10^{-14}	This work*
$C_2H_5O_2 + HO_2 \rightarrow C_2H_5OOH + O_2$	6.2×10^{-12}	This work
$C_2H_5O + O_2 \rightarrow CH_3CHO + HO_2$	8×10^{-15}	Ref [106]
$Cl + C_2H_6 \rightarrow C_2H_5 + HCl$	5.9×10^{-11}	Ref [13]
$C_2H_5 + O_2 + M \rightarrow C_2H_5O_2 + M$	4.8×10^{-12}	Ref [107]
$C_2H_5 + O_2 \rightarrow C_2H_4 + HO_2$	$3\text{-}4\times 10^{-14}$	This work **
$2\ HO_2 \rightarrow H_2O_2 + O_2$	1.7×10^{-12}	Ref [105]

$C_2H_5O_2 + Cl \rightarrow$ products	1.5×10^{-10}	Ref [29]
$C_2H_5O_2 \rightarrow$ diffusion	2 s^{-1}	This work
$HO_2 \rightarrow$ diffusion	3 s^{-1}	This work
$Cl + CH_3OH \rightarrow CH_2OH + HCl$	5.5×10^{-11}	Ref [13]
$CH_2OH + O_2 \rightarrow CH_2O + HO_2$	9.6×10^{-12}	Ref [13]

* They were first used in our published paper with the values from Noell *et al*. [18], as the preliminary results from our measurement for the $C_2H_5O_2$ self-reaction agree well with their work, and now it is modified to the values obtained in the current thesis, see below. It should be noted that the rate constant of the $C_2H_5O_2$ self-reaction is slow, the absorption cross section of $C_2H_5O_2$ depends mostly on the absolute initial concentration instead of the decay of $C_2H_5O_2$. And in the measurements with HO_2 in excess, the decay of $C_2H_5O_2$ mostly due to its cross reaction with HO_2, thus the influence of the self-reaction on the rate constant of $C_2H_5O_2 + HO_2$ was small. ** This reaction is likely due to excited C_2H_5 radicals and the branching ratio of it depends on pressure and also on the mode of generation of the C_2H_5 radicals.

In conclusion, using the absorption cross-section for $C_2H_5O_2$ obtained in back-to-back experiments leads in these kinetic experiments to the best fit for both species over the entire concentration range. However, it should of course be noted, that in the end both methods rely on the absorption cross-section of HO_2 and therefore both approaches cannot be considered as independent methods: the initial Cl-atom concentration used as input parameter in the model and being vital for retrieving the rate constant $k(C_2H_5O_2 + HO_2)$ and with this the absorption cross-section for $C_2H_5O_2$ depend entirely on the rate constant for the HO_2 self-reaction. The absorption cross-section of HO_2 varies through pressure broadening (which is taken into account), but it might also vary during the experiment through small and unnoted shifts in the wavelength of the DFB laser emission (the linewidth of the HO_2 absorption lines is on the order of 0.02 cm^{-1} FWHM at 50 Torr He). However, in our experiments the absorption cross-section of HO_2 is under most conditions constantly being "measured": a major HO_2 loss in most experiments is the self-reaction, and thus the HO_2 decays are sensitive to the absolute HO_2 concentration, i.e., to the absorption cross-section that has been used to convert the absorption time profiles to concentration time profiles. Therefore, it can be said that both methods have determined the $C_2H_5O_2$ absorption cross-section relative to the rate constant of the HO_2 self-reaction. The IUPAC committee [105] estimates the

uncertainty of this rate constant to ± 15%, which we use as a basis to estimate the uncertainty of our rate constant, with an additional 10% for uncertainties in the fitting of the rate constant: $k(C_2H_5O_2 + HO_2) = (6.2 \pm 1.5) \times 10^{-12}$ cm^3 s^{-1}.

3.1.3 Measuring the Relative Absorption Spectrum

In order to obtain the shape of the $C_2H_5O_2$ absorption spectrum, kinetic decays have been measured under identical conditions at 15 different wavelengths in the range accessible with our DFB laser (7596–7630 cm^{-1}). The relative absorption coefficients are put on an absolute scale by comparison with the absorption cross-section at 7596.47 cm^{-1}. Table 3.4 summarizes the obtained results, and Figure 3.7 compares the present data with two literature results.

The upper graph shows that our spectrum (green symbols and green axis apply) agrees well with the results of Melnik *et al*. [98] if our data are shifted by 4 cm^{-1}. Possibly, there is a mistake in the Melnik figure (T. Miller, private communication), because the peak absorption is given in the text at 7596 cm^{-1}, just as in our case, however in the figure the peak is located at 7600 cm^{-1}, indicated by a blue vertical line. In the lower graph, our data (again in green) are overlaid to the spectrum of Atkinson and Spillman [93]. A good agreement of the shape in both comparisons can be obtained, when our data are scaled on the *y*-axis, i.e., when we suppose a shift in the baseline of both literature spectra (around 23% of the peak absorption for Atkinson and Spillman and 15% for Melnik *et al*.). Melnik *et al*. discussed in their paper such baseline shift (dashed line in their figure) and attributed it to a broadband absorber, generated simultaneously during the photolysis. Indeed, they obtained their baseline by measuring ring-down events with the photolysis laser blocked. In this case, a broadband absorber generated simultaneously to the $C_2H_5O_2$ radical would induce a baseline shift. To take into account this shift (horizontal dashed line in the upper graph of Figure 3.7), they have calculated the absorption cross-section above this plateau. No explanation for a possible baseline shift in the work of Atkinson and Spillman can be given.

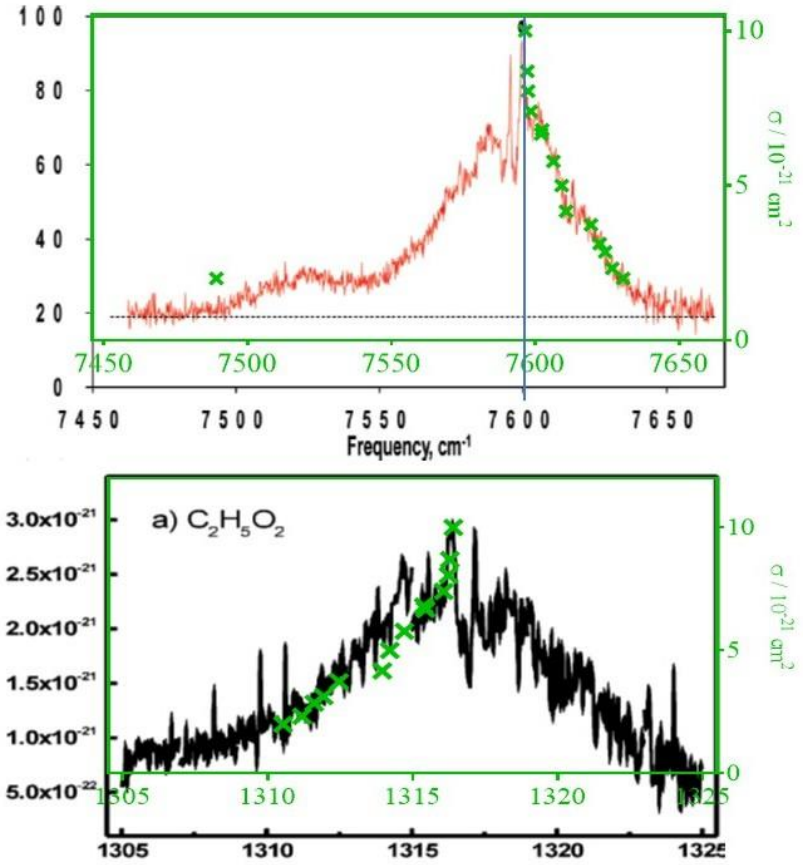

Figure 3.7 $C_2H_5O_2$ absorption coefficients at different wavelengths obtained in this work (green crosses and green axis), overlaid onto the spectrum obtained by Melnik *et al.* [98] (upper graph, Reprinted with permission from [98], Copyright 2010 American Chemical Society) and Atkinson and Spillman [93] (lower graph, Reprinted with permission from [93], Copyright 2002 American Chemical Society). In the upper graph the data have been shifted by 4 cm^{-1}, and in both graphs our data have been scaled on the *y*-axis, i.e., apparently there is a baseline shift in both comparisons.

Table 3.4 $C_2H_5O_2$ Absorption cross-sections at different wavelengths.

Wavenumber/cm^{-1}	$\sigma/10^{-20}$ cm^2
7596.47	10.0
7597.20	8.7
7597.44	8.1
7598.40	7.4
7602.02	6.7
7602.38	6.8
7606.25	5.8
7609.16	5.0
7610.66	4.2

7619.28	3.7
7622.36	3.1
7624.28	2.9
7626.72	2.3
7630.50	2.0
7489.16	2.0

3.1.4 Comparison of the Absorption Cross-section with Literature Data

The absorption cross-section of $C_2H_5O_2$ was first determined by Atkinson and Spillman [93] using 193 nm photolysis of 3-pentanone as precursor. Using the kinetic method, they determined at the peak $\sigma = (3 \pm 1.5) \times 10^{-21}$ cm^2, which is 3 times smaller than the present value. A higher absorption cross-section had also been measured previously by our group for the CH_3O_2 radical [94]. One possible reason might be that the determination from Atkinson and Spillman is based on the kinetic method using low initial radical concentrations, hence the $C_2H_5O_2$ concentration has to be measured over long reaction times in order to observe a sizeable decay, but the possible loss due to diffusion out of the photolysis volume or due to wall loss, possibly non-negligible over such long reaction times, has not been considered in the data evaluation. This can induce an overestimation of the radical concentration and therefore an underestimation of the absorption cross-section (see Figure 3.2c and Figure 3.4). Another reason might be the precursor: the reaction of $C_2H_5 + O_2$ can also lead to small amounts of HO_2, around 1% of the initial Cl-atom concentration led to formation of HO_2 in the experiments of this work. Atkinson and Spillman used 193 nm photolysis of 3-pentanone, which leaves considerably higher amounts of excess energy in the fragments than our method, based on H-atom abstraction. Therefore, the fraction of C_2H_5 radicals that react through reaction $C_2H_5 + O_2 \rightarrow C_2H_4 + HO_2$ might be considerably higher than in our case. This could induce a non-negligible initial HO_2 concentration which participates in the removal of $C_2H_5O_2$ and would thus induce a systematic error when using the kinetic

method. This is also in line with the observation of Atkinson and Spillman, that in their experiments the apparent rate constant of the $C_2H_5O_2$ self-reaction was inversely pressure dependent: the rate constant decreased with increasing pressure (D. Atkinson, private communication). An increased cooling of the hot C_2H_5 radical with increasing pressure would lead to a decreasing HO_2 concentration and thus to a slow-down of the $C_2H_5O_2$ decay.

Rupper *et al*. [97] estimated the absolute absorption cross-section to $\sigma = 4.4 \times 10^{-21}$ cm^{-2} from calculating the initial Cl-atom concentration by measuring the decrease of photolysis energy in absence and presence of the Cl-atom precursor, assuming that all generated Cl-atoms lead to formation of one $C_2H_5O_2$. In a more recent work from the same group, Melnik *et al*. [99] have determined the absorption cross-section by dual-CRDS method: on one absorption path they measured the absorption of $C_2H_5O_2$ while on the other path the concentration of HCl was quantified thanks to its known absorption cross-section. Assuming again that one $C_2H_5O_2$ has been generated for each molecule of HCl, they found an absorption cross-section of $\sigma = 5.29 \times 10^{-21}$ cm^{-2}. This is nearly 2 times lower than the value obtained in this work. Is it unlikely that the difference in the bandwidth of the excitation laser sources (0.01 cm^{-1} for Melnik and $<1 \times 10^{-4}$ cm^{-1} for this work) can explain the difference, because the absorption band is unstructured and much larger than the bandwidth of both laser sources. Also, the overall shape is, after consideration of a baseline shift, in excellent agreement between both works (see Figure 3.7).

A possible explanation might be that Melnik *et al*. and Rupper *et al*. both consider the complete conversion of Cl-atoms into $C_2H_5O_2$ radicals: a simple model is presented by Melnik *et al*. [98] showing the complete conversion of Cl-atoms into $C_2H_5O_2$. However, the very fast reactions of Cl-atoms with $C_2H_5O_2$ (1.5×10^{-10} $cm^3\,s^{-1}$) [29] and C_2H_5 (3×10^{-10} $cm^3\,s^{-1}$) [108] are omitted in this model, even though these reactions are non-negligible under their conditions of very high initial Cl-atom concentrations, well above 10^{15} cm^{-3}, combined with relatively low C_2H_6 concentrations (1×10^{16} cm^{-3}). These reactions result in a $C_2H_5O_2$ concentration that might be well below the

initial Cl-atom concentration, depending on the overall radical concentration as well as on the C_2H_6 concentration. Figure 3.8 shows a simulation using the model from Melnik *et al.*, but completed by the two fast reactions. The left graph shows the result using initial concentrations such as given by Melnik *et al.* ($[Cl]_0 = 2 \times 10^{15}$ cm^{-3} and $[C_2H_6]_0 = 1 \times 10^{16}$ cm^{-3}), the right graph shows the model result with typical conditions such as used in this work for the determination of the absorption cross-section ($[Cl]_0 = 5 \times 10^{13}$ cm^{-3}and $[C_2H_6]_0 = 3 \times 10^{16}$ cm^{-3}). Under the high Cl/low C_2H_6 conditions of Melnik *et al.*, only 63% of the Cl-atoms have been converted to $C_2H_5O_2$, while 28% of the Cl-atoms have reacted with $C_2H_5O_2$ and 8% have reacted with C_2H_5. Under the low Cl/high C_2H_6 conditions (right graph), virtually all Cl-atoms have been converted to $C_2H_5O_2$, less than 1% of the Cl-atoms have reacted with either $C_2H_5O_2$ or C_2H_5. From this model one can suspect that the absorption cross-sections of Melnik *et al.* [98] and Rupper *et al.* [97] are strongly underestimated, and a correction of the Melnik *et al.* value, based on the more complete model presented here, would lead to $\sigma = 8.8 \times 10^{-21}$ cm^{-2}, which gets into good agreement with the value found in this work.

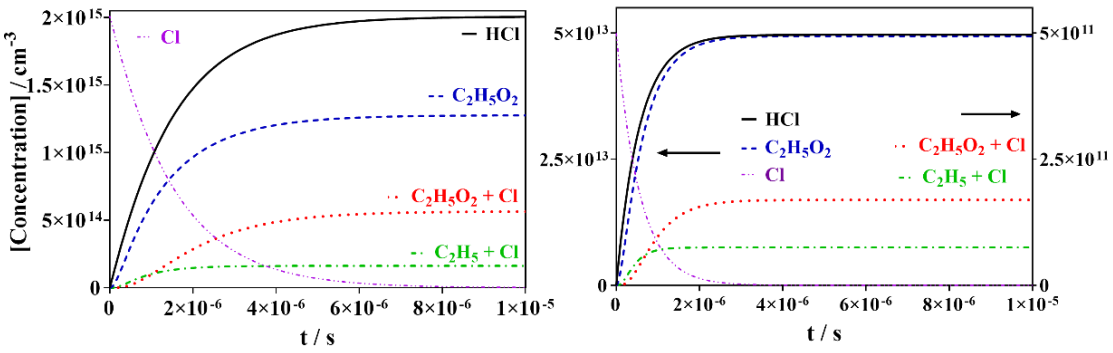

Figure 3.8 Simulation of conversion of Cl-atoms (violet dashed dot) into HCl (black) and $C_2H_5O_2$ (blue dashed): model taken from Melnik *et al.*, completed with the reactions of Cl with $C_2H_5O_2$ ($k = 1.5 \times 10^{-10}$ cm^{3}s^{-1}) [109] (red dotted) and C_2H_5 ($k = 3 \times 10^{-10}$ cm^{3}s^{-1}) [108] (green dashed dotted), left graph conditions such as used in Melnik *et al.* [98], right graph conditions such as used in this work. The products from the reaction of Cl with $C_2H_5O_2$ (red) and with C_2H_5 (green) are zoomed in the right graph by a factor of 100 (right *y*-axis applies).

3.2 Measurements of rate constant and branching ratio for $C_2H_5O_2$ self-reaction

The reliability of the measurements presented in this work depends on the selective quantification of the two radicals, HO_2 and $C_2H_5O_2$. HO_2 has been detected on the strongest line of the $2\nu_1$ band at 6638.2 cm^{-1}. Experiments were carried out in 100 Torr O_2, so the value of $\sigma_{100\ Torr\ O2} = 2.0\times10^{-19}$ cm^2 is used in this work to convert absorption-time profiles of HO_2 into concentration time profiles. The absorption spectrum of HO_2 in this wavelength range is very structured with sharp peaks, thus it is easy to verify the selectivity of the measurement towards HO_2 by taking absorption measurements on top of the line, and at a wavelength just next to it, where the HO_2 absorption is virtually zero. No absorption signal was observed off the HO_2 line in any of the current experiments, and therefore we can conclude that absorption measurements at 6638.2 cm^{-1} are highly selective for HO_2 radicals in this reaction system.

As summarised in the above part, the detection of $C_2H_5O_2$ in the near IR is less clear-cut: there was neither good agreement on the absorption cross-section [93, 97, 98] nor is the spectrum as structured as HO_2, which makes it less straightforward to verify the selectivity of the measurement. The absorption of $C_2H_5O_2$ was measured at its peak wavelength 7596.47 cm^{-1} in the $\tilde{A} \leftarrow \tilde{X}$ electronic transition and the pressure independent absorption cross-section of $\sigma = 1.0\times10^{-20}$ cm^2 is used in the current work to convert $C_2H_5O_2$ absorption time profiles into concentration time profiles.

To assure that the decays measured at the peak wavelength of $C_2H_5O_2$ are selective for this radical, it is not possible to measure, as for HO_2, decays at a wavelength where $C_2H_5O_2$ does not absorb, as the transition is too broad. Therefore, kinetic decays have been measured at several different wavelengths that are accessible with our DFB laser: in the case of an underlying absorption of another species, for example a reaction product, one can expect that the shape of the absorption spectrum for any other species would be different from the shape of the spectrum of $C_2H_5O_2$. Indeed, it has been shown

that the absorption cross-section of $C_2H_5O_2$ varies over a factor of 5 in the range between 7596 and 7630 cm^{-1} and an underlaying absorption of another species with a less or differently varying spectrum should lead to different shapes of kinetic decays at different wavelengths: the influence of the co-absorbing species on the shape of the decay should be highest at wavelengths where the $C_2H_5O_2$ absorption is lowest. In Figure 3.9 are shown examples of five decays measured at wavelengths between the peak (open orange circle) and the wavelength with the lowest $C_2H_5O_2$ cross-section (open red circle), all obtained under the same conditions following the 351 nm photolysis of Cl_2/C_2H_6 mixtures. A very high initial radical concentration has deliberately been used to force formation of high concentrations of reaction products. Even under these conditions no change in the shape of the decays can be observed for the different wavelengths, and therefore we conclude that measurements at 7596.47 cm^{-1} are selective measurements of $C_2H_5O_2$ in this reaction system.

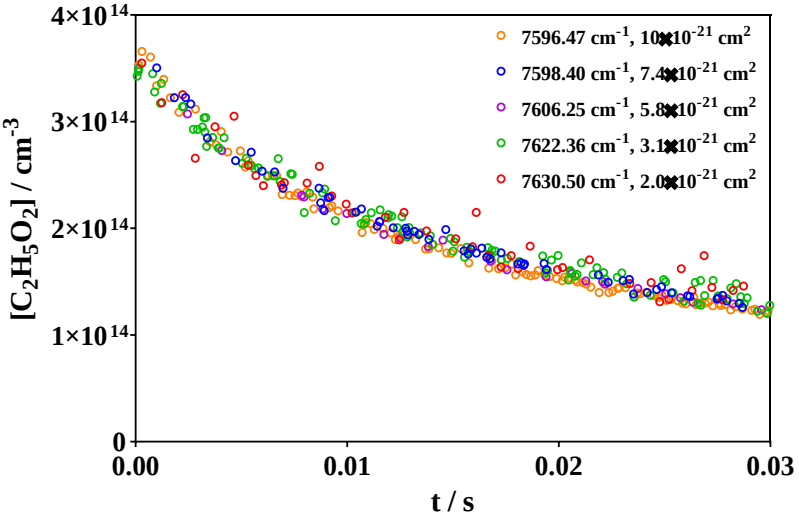

Figure 3.9 Examples of $C_2H_5O_2$ decays following the 351 nm photolysis $[Cl_2] = 3\times10^{16}$ cm^{-3} in presence of $[C_2H_6] = 2.6\times10^{16}$ cm^{-3}, obtained at 5 different wavelengths: the absorption cross-section of $C_2H_5O_2$ (given in the legend of the figure) varies over a factor of 5 for the different wavelengths.

3.2.1 Secondary reactions related to $C_2H_5O_2$ self-reaction

When studying the self-reaction of $C_2H_5O_2$, several secondary reactions can be important and will need to be taken into account: the reaction of $C_2H_5O_2$ with HO_2 and with C_2H_5O. The measurement of $C_2H_5O_2$ + HO_2 cross reaction has been explained in the last section, the measurement of $C_2H_5O_2$ + C_2H_5O will be presented in this section.

$$C_2H_5O + C_2H_5O_2 \rightarrow products \quad (3.7)$$

In the work of Noell *et al.* [18] it turned out, that the reaction of $C_2H_5O_2$ with C_2H_5O played some role under their conditions, and in experiments using different O_2 concentrations they extracted a fast rate constant of $k(C_2H_5O_2 + C_2H_5O) = 1.5\times10^{-11}$ cm^{-3} s^{-1}. Even though experiments in this work were carried out in 100 Torr O_2 (compared to 50 Torr O_2 in Noell *et al.*) making the reaction $C_2H_5O + O_2$ very rapid (≈ 24000 s^{-1}) and thus the stationary concentration of C_2H_5O very low, it turned out during data evaluation of the self-reaction experiments, that the reaction $C_2H_5O_2$ + C_2H_5O would still have a small impact on the HO_2 profiles (decreasing HO_2 with increasing initial radical concentration) when using the fast rate constant from Noell *et al*. For this reason, we have carried out some experiments with low O_2 concentration in order to re-determine $k(C_2H_5O_2 + C_2H_5O)$ under our conditions. In Figure 3.10 are shown experiments using 4 different initial Cl-concentrations: in the left graph are shown experiments carried out under low O_2 (90 Torr N_2 and 10 Torr O_2: $[O_2] \sim 3\times10^{17}$ cm^{-3}), experiments in the right graph were carried out under high O_2 (100 Torr O_2: $[O_2] \sim 3\times10^{18}$ cm^{-3}). It can be seen that the $C_2H_5O_2$ profiles (lower graphs) are very similar between the two conditions, however the HO_2 profiles (upper graphs) present strong differences:

- the HO_2 concentrations just after the photolysis pulse are higher in the case of 100 Torr O_2 compared to 90 Torr N_2/10 Torr O_2. This is in line with the hypotheses that this initial HO_2 is formed in collision between hot C_2H_5 and O_2: with increasing N_2 and decreasing O_2, collisions with N_2 will cool down excited

C_2H_5 and the reaction of C_2H_5 with O_2 to give HO_2 will get less important.

- HO_2 signals initially rise in the case of high O_2 while they decay from the beginning in the case of low O_2. At high O_2, HO_2 formation from the reaction sequence ($C_2H_5O_2$ + $C_2H_5O_2$ and C_2H_5O + O_2), is initially faster (due to the fast conversion of C_2H_5O (24000 s^{-1})) than its consumption through the reaction $C_2H_5O_2$ + HO_2, until after 2-3 ms steady-state is reached and HO_2 decays at the same pace as $C_2H_5O_2$. Under low O_2, conversion of C_2H_5O into HO_2 is 10 times slower and the reaction with $C_2H_5O_2$ becomes competitive for C_2H_5O, the formation of HO_2 through the reaction sequence ($C_2H_5O_2$ + $C_2H_5O_2$ and C_2H_5O + O_2) is slower than the reaction $C_2H_5O_2$ + HO_2.

An initial model using the rate constant for $C_2H_5O_2$ + C_2H_5O such as recommended by Noell *et al*. (1.5×10^{-11} $cm^{-3}s^{-1}$) did not allow to reproduce the HO_2 profiles under low O_2 condition: using this rate constant, the modelled HO_2 profiles decreased much faster than the experimental profiles (dashed lines in the upper graph of Figure 3.10). The HO_2 profiles were best reproduced when using a rate constant of k($C_2H_5O_2$ + C_2H_5O) = 7×10^{-12} $cm^{-3}s^{-1}$, nearly 2 times slower (full lines in the upper graphs of Figure 3.10). The rising profiles in the upper graphs of Figure 3.10 show the product of the reaction of $C_2H_5O_2$ + C_2H_5O: the right y-axis applies, and it should be noted that the axis ends at 3×10^{13} cm^{-3}, to be compared with the left scale for the HO_2 profile which ends at 2×10^{12} cm^{-3}. It can be seen that even with the lower rate constant, this reaction plays some role, especially under low O_2 conditions. Ignoring this reaction does not allow reproducing our HO_2 profiles under low O_2 neither: the modelled profile without reaction $C_2H_5O_2$ + C_2H_5O is shown as the dashed-dotted line, only for the highest radical concentration.

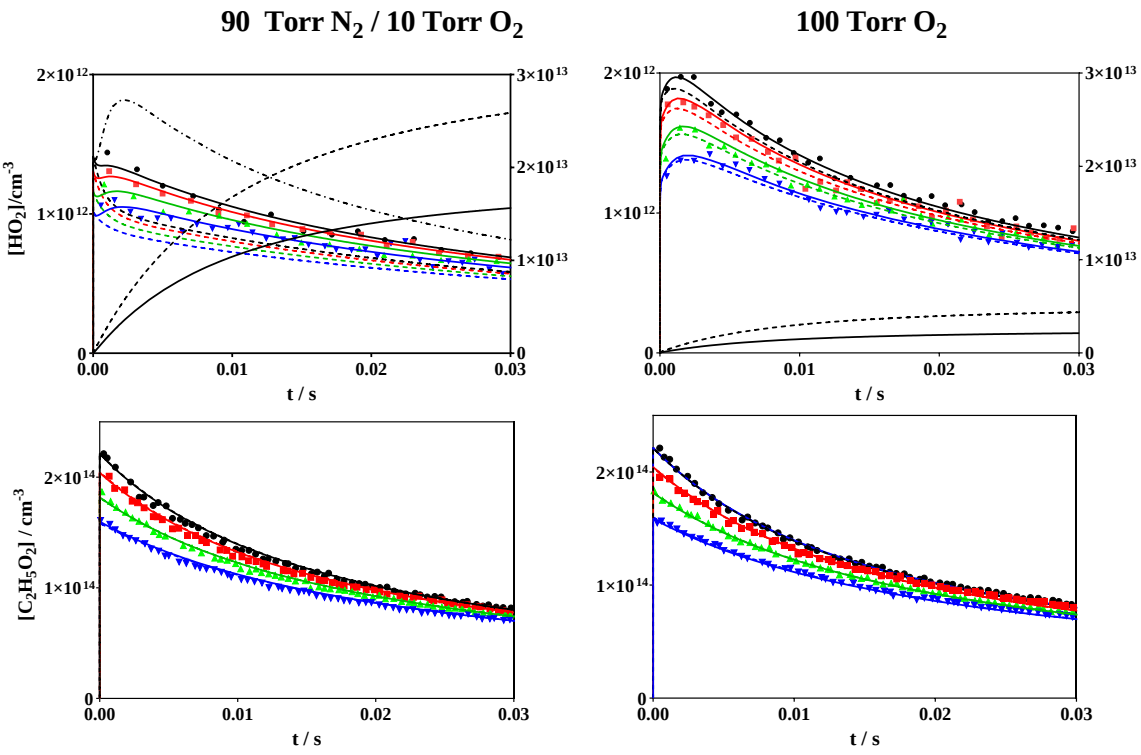

Figure 3.10 Experiments for determination of the rate constant between $C_2H_5O_2$ and C_2H_5O: upper graphs show HO_2 profiles, lower graphs show simultaneously measured $C_2H_5O_2$ profiles. Left graphs: 90 Torr N_2/10 Torr O_2, right graphs: 100 Torr O_2. Initial Cl-concentration was 2.26, 2.08, 1.85 and 1.6×10^{14} cm^{-3} for the experiments marked with black, red, green and blue dots, respectively. Full lines, dotted coloured lines and dashed-dotted black line represent model with $k(C_2H_5O_2 + C_2H_5O) = 7\times10^{-12}$ cm^3s^{-1}, 1.5×10^{-11} cm^3s^{-1}, 0 (for highest radical concentration only). Rising profiles in the upper graph show the product of the reaction $C_2H_5O_2 + C_2H_5O$ and with right y-axis applies.

Not many details are given in the earlier work of Noell *et al*. on how the rate constant was determined, therefore it is difficult to understand the differences and no good explanation can be given for the disagreement of our results with the result from Noell *et al*.. From these experiments we have chosen to use $k(C_2H_5O_2 + C_2H_5O) = 7\times10^{-12}$ cm^{-3} s^{-1} for the evaluation of the $C_2H_5O_2$ self-reaction experiments. It should however be noted that this reaction has a smaller impact on the retrieved rate constant and branching ratio of the self-reaction experiments due to the 2 times higher O_2 concentration used in our experiments, compared to Noell *et al*..

3.2.2 Rate constant and branching ratio of the self-reaction of $C_2H_5O_2$

The rate constant of the self-reaction of $C_2H_5O_2$ has been measured in this work by following simultaneously $C_2H_5O_2$ and HO_2. Figure 3.11 shows an example of profiles obtained from the photolysis of varying concentrations of Cl_2 in presence of $[C_2H_6]$ = 2×10^{16} cm^{-3} and $[O_2]$ = 3×10^{18} cm^{-3}. High C_2H_6 concentrations (2 - 3×10^{16} cm^{-3}) have always been used in order to minimize the impact of the fast reaction of Cl-atoms with $C_2H_5O_2$. A fast reaction of Cl atoms with $C_2H_5O_2$ has been included in the model with 1.5×10^{-10} cm^3 s^{-1} [29] but was always negligible: even at the highest radical concentration, only around 0.3% of the initial Cl atoms reacted with $C_2H_5O_2$. Also, most experiments have been carried out at 100 Torr O_2 in order to make reaction C_2H_5O + O_2 as fast as possible and minimize the impact of $C_2H_5O_2$ + C_2H_5O.

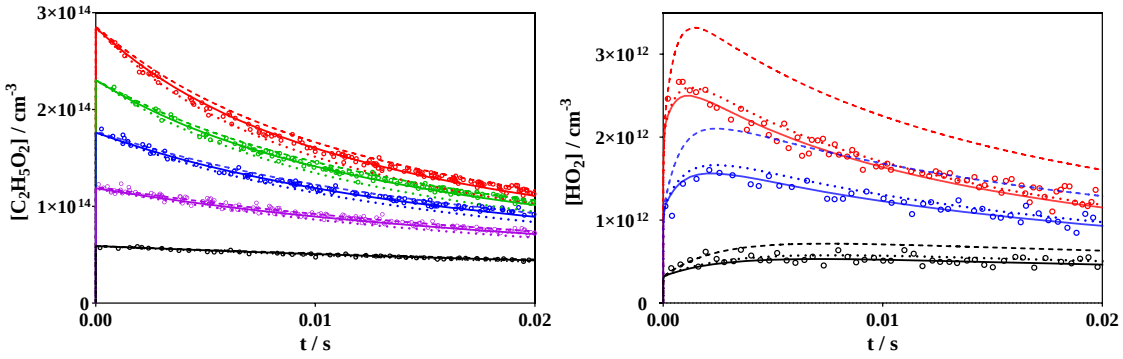

Figure 3.11 $C_2H_5O_2$ (left graph) and HO_2 (right graph) profiles obtained from the 351 nm photolysis of $[Cl_2]$ = 0.6, 1.3, 1.9, 2.5, and 3 $\times10^{16}$ cm^{-3}, from bottom to top (for clarity, green and purple HO_2 data are not shown). Full lines model from Table 3.5, dotted lines model using values from Noell *et al.*, dashed lines model with IUPAC previously recommended values (see Table 3.6).

The rate constant for $C_2H_5O_2$ self-reaction and the branching fraction α of the radical channel have then been extracted by fitting both HO_2 and $C_2H_5O_2$ profiles simultaneously for an entire series of experiments with varying Cl-concentrations. In the example in Figure 3.11, the initial radical concentration has been changed by around a factor of 6, making the reactivity of $C_2H_5O_2$ varying on our typical time scale of 20 ms from near stable for the lowest concentration (black symbols) to a loss of more than

50% of $C_2H_5O_2$ for the highest concentration (red symbols). The loss due to diffusion is nearly negligible in this time window as can be seen from the black line. The fraction of C_2H_5 radicals that leads in the reaction with O_2 to direct formation of HO_2 radicals, has been adjusted such as to best reproduce the non-zero HO_2 concentration immediately after the photolysis pulse. This fraction was always around 1%, in good agreement with earlier findings. The full lines in Figure 3.11 show the result of the model such as given in Table 3.5. Both radical profiles are very well reproduced over the full range of initial radical concentrations. Figure 3.11 also includes the results of two other models with the rate constants of ($C_2H_5O_2$ + $C_2H_5O_2$) and ($C_2H_5O_2$ + C_2H_5O) varied to match either the results from Noell *et al.*, (dotted lines) or the previous IUPAC recommendations (dashed lines): the rate constants used for these models are summarized in Table 3.6.

Table 3.5 Reaction mechanism used to fit all experiments in this work.

Reaction	k/cm^3 s^{-1}	References
2 $C_2H_5O_2$ → 2 C_2H_5O + O_2	3.1×10^{-14}	This work
2 $C_2H_5O_2$ → CH_3CHO + C_2H_5OH + O_2	7×10^{-14}	This work
$C_2H_5O_2$ + HO_2 → C_2H_5OOH + O_2	6.2×10^{-12}	[110]
C_2H_5O + O_2 → CH_3CHO + HO_2	8×10^{-15}	[111]
Cl + C_2H_6 → C_2H_5 + HCl	5.9×10^{-11}	[13]
C_2H_5O + $C_2H_5O_2$ → product	7×10^{-11}	This work
C_2H_5 + O_2 + M → $C_2H_5O_2$ + M	4.8×10^{-12}	[112]
C_2H_5 + O_2 → C_2H_4 + HO_2	3-4 $\times 10^{-14}$	This work
2 HO_2 → H_2O_2 + O_2	1.7×10^{-12}	[113]
$C_2H_5O_2$ + Cl → products	1.5×10^{-10}	[29]
$C_2H_5O_2$ → diffusion	2 s^{-1}	This work
HO_2 → diffusion	3 s^{-1}	This work

Table 3.6 Values used for models in Figure 3.11, all rate constants are in units $cm^3\ s^{-1}$.

Reaction	This work	Noell *et al.*	IUPAC**
$k(2C_2H_5O_2 \rightarrow 2C_2H_5O+O_2)/10^{-14}\ cm^3\ s^{-1}$	3.2	3.33	4.79
$k(2C_2H_5O_2 \rightarrow CH_3CHO+C_2H_5OH+O_2/10^{-14}\ cm^3\ s^{-1}$	7.0	8.57	2.81
$k(C_2H_5O_2+C_2H_5O_2)/10^{-13}\ cm^3\ s^{-1}$	1.0±0.2*	1.19±0.04	0.76±0.4
$k_{obs}/10^{-13}\ cm^3\ s^{-1}$	1.34	1.52	1.24
$\alpha(C_2H_5O)$	0.31±0.06*	0.28±0.06	0.63
$k(C_2H_5O_2+HO_2 \rightarrow C_2H_5OOH)/10^{-12}\ cm^3\ s^{-1}$	6.2±1.5	5.6±0.4	6.9
$k(C_2H_5O_2+C_2H_5O \rightarrow products)/10^{-12}\ cm^3\ s^{-1}$	7±1.5*	15±7	-

*Error bars of 20% are estimated, mostly due to uncertainties in the absolute absorption cross-sections of HO_2 and $C_2H_5O_2$. ** Values obtained from previous IUPAC recommendations, and the latest IUPAC recommendations have been updated with the results of this experiment.

Using the previous IUPAC recommended values, the deviation of the model from our $C_2H_5O_2$ measurements is very minor (the model decays too slowly), however the disagreement of the model with our HO_2 profiles is huge: the model predicts too much HO_2, far beyond any experimental uncertainty. This is due to the much higher radical yield of $C_2H_5O_2$ self-reaction, which is not counterbalanced by the overall slower rate constant of $C_2H_5O_2$ self-reaction or the faster rate constant of $C_2H_5O_2$ + HO_2. The agreement with the model using the rate constants from Noell *et al*. is very good for the HO_2 profiles (the model slightly overpredicts the HO_2 concentration by around 10%, within the experimental uncertainty), but for $C_2H_5O_2$ the model predicts too fast decays, especially at longer reaction times. This slight disagreement is due to a combination of different rate constants used in both models for the three major radical-radical reactions: the higher rate constant of reaction $C_2H_5O_2$ + C_2H_5O, a lower rate constant of $C_2H_5O_2$ + HO_2 and a slightly faster $C_2H_5O_2$ + $C_2H_5O_2$ and with a lower radical yield from the work of Noell *et al*. Again, this slight disagreement is within the experimental uncertainty, especially given that several radical-radical reactions are involved, and therefore, even though the agreement of our measurements with the data from Noell *et al*. is not perfect, it confirms their finding of an overall faster rate constant for $C_2H_5O_2$ + $C_2H_5O_2$ together with a lower branching ratio for the radical channel, compared to

previous recommendations. It should be noted that, as shown in Table 3.6, the observed second order rate coefficient k_{obs} of $C_2H_5O_2$ obtained in all experiments are in reasonable agreement. Based on the equation of $k_{obs} = (1 + \alpha)k$, with a higher branching ratio of radical channel, the same k_{obs} leads to a slower rate constant for $k(C_2H_5O_2 + C_2H_5O_2)$.

3.2.3 Dimer products measurements of the $C_2H_5O_2$ self-reaction

As explained by Noell *et al*. [18], the reason for the disagreement between their measurements with literature studies (and which could be also the reason why we are inconsistent with the literature) could be the secondary chemistry that occurred in the end product studies. The photolysis or heterogeneous decomposition of the dimer $C_2H_5OOC_2H_5$, which is always considered to be minor and only Niki et al. [26] saw some evidence for its formation, could lead to C_2H_5O radicals and thus an apparently higher radical yield: the measured CH_3CHO used to get the branching ratio of the C_2H_5O channel, would in fact be the sum of the direct $C_2H_5O_2$ self-reaction and the production from the photolysis of $C_2H_5OOC_2H_5$.

If the above hypothesis is true, it could also explain why in the end product measurements the dimer product was not detected or with a low branching ratio at the most, that is, its photolysis or heterogeneous decomposition resulted in a low concentration. However, in the CRDS experiment, it is not possible to distinguish between the two stable product channels $CH_3CHO + C_2H_5OH$ and $C_2H_5OOC_2H_5$. It should be noted that the branching ratio of the $CH_3CHO + C_2H_5OH$ channel given in the above model is due to ignoring the contribution of dimers. Thus, the rate constant of $k(C_2H_5O_2 + C_2H_5O_2 \rightarrow \text{stable products}) = 7\times10^{-14}$ cm^3 s^{-1} is actually the sum to all stable products formed in $C_2H_5O_2$ self-reaction.

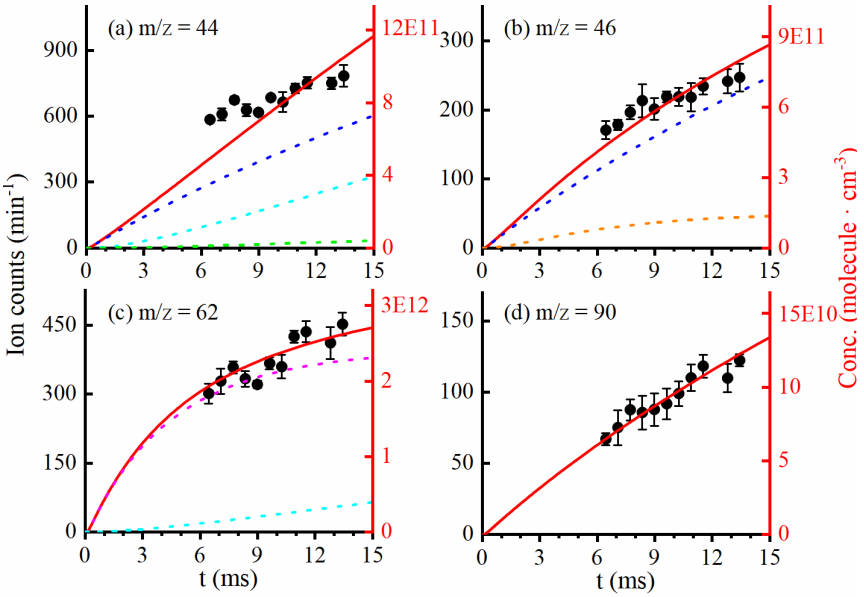

Figure 3.12 Time-evolutions of products in the self-reaction of $C_2H_5O_2$ and its cross-reaction with HO_2. (a) CH_3CHO, m/z = 44, (b) C_2H_5OH, m/z = 46, (c) C_2H_5OOH, m/z = 62, (d) $C_2H_5OOC_2H_5$, m/z = 90. Black dots are experimental data and red curves are calculated from a theoretical model. Blue line: from $C_2H_5O_2$ self-reaction contribution; cyan line: from C_2H_5O + $C_2H_5O_2$ contribution; pink line: from $C_2H_5O_2$ + HO_2 contribution; green line: from C_2H_5O + O_2 contribution; orange line: from C_2H_5O + HO_2 contribution.

To further analyze the channel branching ratio of the dimer product, the self-reaction of $C_2H_5O_2$ was reinvestigated by using a vacuum ultraviolet (VUV) lamp-based photoionization mass spectrometer in Hefei [87, 114] and a photoelectron photoion coincidence spectroscopy (PEPICO) at the Swiss Light Source [115, 116]. A microwave discharge flow tube and a laser photolysis flow tube were employed in Hefei and at the SLS, respectively, to generate radicals. Both the major products CH_3CHO, C_2H_5O, C_2H_5OH and the dimeric product $C_2H_5OOC_2H_5$ formed from the self-reaction were observed. Kinetic experiments by changing the reaction time were performed, as shown in Figure 3.12 , and through fitting the measured kinetics of the products from $C_2H_5O_2$ self-reaction (CH_3CHO, C_2H_5OH, $C_2H_5OOC_2H_5$) and secondary reactions (C_2H_5OH), a branching ratio of 0.1 ± 0.05 for the dimeric product $C_2H_5OOC_2H_5$ is suggested. In addition, the detection of the dimer with PEPICO at the Swiss light source revealed the structure of it and determined its adiabatic ionization energy, 8.75 ± 0.05

eV by measuring the photoionization spectrum and with the aid of the Franck-Condon calculations.

However, the branching ratio of the C_2H_5O channel obtained in the end product measurement is 0.63, which is around 2 times higher than the result obtained by Noell *et al*. [18] or in the current experiment using CRDS to directly measure HO_2. The upper limit branching ratio of $C_2H_5OOC_2H_5$ found in this work is 0.15, suppose that the produced $C_2H_5OOC_2H_5$ in the end product measurements all undergoes photolysis and two C_2H_5O radicals were produced in each photolysis. With considering the measured maximum branching ratio of $C_2H_5OOC_2H_5$ (0.15) in the current work, the modified branching ratio for the radical channel in the end product measurement should be $\alpha(C_2H_5O) = 0.48$, which is still clearly higher than the results of our experiment. Only when the branching ratio of the dimer is 0.3 can the difference between the two measurements be compensated for.

In a recent measurement of the self-reaction of the $HOC_2H_4O_2$ peroxy radical, which is formed in the OH + C_2H_4 + O_2 reaction, by Murphy *et al* [117], the accretion product is the dihydroxy diethyl peroxide ($HOC_2H_4OOC_2H_4OH$ = ROOR) and was detected with a branching fraction up to 23 ± 5%. They observed a loss of more than 50% of the ROOR after replacing a part of the Teflon sampling line with approximately 60 cm of quartz or metal tube. This may explain the low $C_2H_5OOC_2H_5$ measured in this work. After considering 50% transmission loss, the modified upper limit of the branching ratio of $C_2H_5OOC_2H_5$ should be 0.3, which can well explain the difference between the two measurements. But this is still to be considered as preliminary result, further experiments are needed to quantify the measured stable products and to evaluate the transmission loss of the dimer product in our experimental set-up. The preliminary results of the branching ratio of $C_2H_5OOC_2H_5$ indicate that even for the small peroxy radicals, the branching ratio of the dimer product can possibly not be ignored. The vapor pressure of dimer products is low, making them important precursors for secondary organic aerosols. Accurately measuring their channel branching ratio may help to reveal the missing SOA sources.

3.3 Conclusion

The rate constant and branching ratio of the self-reaction of $C_2H_5O_2$ radicals has been measured using a selective cw-CRDS detection of HO_2 in the overtone transition and $C_2H_5O_2$ in the Ã-$\tilde{X}$ electronic transition located in the near-IR region. To study the self-reaction of $C_2H_5O_2$, a reliable detection of this radical is highly desirable. The absorption cross-section at the peak wavelength 7596.4 cm^{-1} of the Ã←$\tilde{X}$ electronic transition of the $C_2H_5O_2$ radical was first measured with two methods. In the first approach, it was determined by direct comparison with the well-known HO_2 absorption cross-section in back-to-back experiments to be $(1.0 \pm 0.2) \times 10^{-20}$ cm^2. In further experiments, the absorption cross-section was validated by measuring the rate constant of $C_2H_5O_2$ with HO_2 in a wide range of concentration: the ratio of $[HO_2]/[C_2H_5O_2]$ has been varied between 0.3 and 2.5 and the concentration time profiles could be reproduced very well using the same absorption cross-section for $C_2H_5O_2$, which returned a rate constant for the cross reaction of 6.2×10^{-12} $cm^3 molecule^{-1} s^{-1}$. Sensitivity analysis in the upper and lower range of previous literature values did not allow for good re-production of the concentration-time profiles for both species over the entire concentration range and confirm the reliability of our results. Smaller absorption cross-sections such as obtained in previous works can convincingly be explained by unaccounted secondary reactions, which had not been taken into account in the data evaluations.

Large discrepancy existed for the rate constant and branching ratio of this reaction: a high C_2H_5O radical yield was generally admitted, based on stable end product measurements of experiments carried out in the 1990's, while a more recent work using selective detection of HO_2 radicals found the radical channel to be the minor one. In this chapter, we have also directly measured the radical yield and confirmed that it should take a low value ($\alpha = 0.31 \pm 0.06$), together with a faster overall rate constant of $(1.0 \pm 0.2) \times 10^{-13}$ $cm^3 s^{-1}$. This is therefore the second work of a low radical yield, based on direct measurement of radicals rather than end-products. Currently, the

IUPAC committee has updated the recommended values for $C_2H_5O_2$ self-reaction and has adopted the results from our measurements. Because the reaction of $C_2H_5O_2$ with the alkoxy radical C_2H_5O plays some role under our experimental conditions, presently its rate constant has also been measured and found to be $(7 \pm 1.5) \times 10^{-12}$ cm^3 s^{-1}.

To further understand the inconsistency in the branching ratio between our/Noell *et al*.'s measurements and the end product measurement, ie. the non-negligible yield of $C_2H_5OOC_2H_5$ and its following photolysis or heterogeneous decomposition which may lead to extra formation of C_2H_5O radical, microwave discharge flowtube combined with vacuum ultraviolet photoionization mass spectrometry, and laser photolysis flowtube combined with Swiss light source photoelectron photoion coincidence spectroscopy were applied to measure the products in $C_2H_5O_2$ self-reaction. The preliminary experimental results showed that the branching ratio of the dimer $C_2H_5OOC_2H_5$ was (0.10 ± 0.05), and after considering 50% transmission loss, the upper limit of the branching ratio can well explain the difference in C_2H_5O branching ratio between our and the end product measurements, ie. the contribution of $C_2H_5OOC_2H_5$ to C_2H_5O in end product measurement may not be ignored.

Chapter 4. Kinetics measurement of the cross reaction of $C_2H_5O_2$ with CH_3O_2

There are three product channels for the cross reaction of $C_2H_5O_2$ with CH_3O_2:

$$C_2H_5O_2 + CH_3O_2 \rightarrow C_2H_5O + CH_3O + O_2 \quad (4.1.a)$$

$$C_2H_5O_2 + CH_3O_2 \rightarrow C_2H_5OH / CH_3CHO + HCHO / CH_3OH + O_2 \quad (4.1.b)$$

$$C_2H_5O_2 + CH_3O_2 \rightarrow C_2H_5OOCH_3 + O_2 \quad (4.1.c)$$

The investigation of this reaction is not straightforward, because the self-reaction of the two radicals will also generate products similar to the cross reaction, such as products C_2H_5O and CH_3O, which both react with O_2 to generate HO_2:

$$C_2H_5O + O_2 \rightarrow CH_3CHO + HO_2 \quad (4.2)$$

$$CH_3O + O_2 \rightarrow HCHO + HO_2 \quad (4.3)$$

with the HO_2 radicals reacting subsequently with both peroxy radicals:

$$HO_2 + C_2H_5O_2 \rightarrow C_2H_5OOH + O_2 \quad (4.4)$$

$$HO_2 + CH_3O_2 \rightarrow CH_3OOH + O_2 \quad (4.5)$$

Similar as the measurements of the $C_2H_5O_2$ self-reaction, the rate constants for the reactions of $C_2H_5O_2$ and CH_3O_2 with HO_2 are faster than the rate constants of the cross reaction of $C_2H_5O_2$ with CH_3O_2, and thus the $C_2H_5O_2$ and CH_3O_2 decays are accelerated. Therefore, determining the rate constant of $C_2H_5O_2$ with CH_3O_2 from observed $C_2H_5O_2$ and CH_3O_2 decays depends also on the branching ratio of $C_2H_5O_2$ + CH_3O_2 as well as the branching ratios for the two self-reactions used in the data treatment: for a given experimental $C_2H_5O_2$ or CH_3O_2 decay the retrieved rate constant will decrease with increasing branching ratio of the radical channel.

In this chapter, a more direct measurement of the rate constant of the cross reaction of $C_2H_5O_2$ with CH_3O_2 is presented. Measurements have been carried out under an excess of $C_2H_5O_2$ radicals over CH_3O_2, and both radicals have been followed in a reasonably selective manner in their $\tilde{A}$-$\tilde{X}$ electronic transition using two different wavelengths. HO_2 concentration time profiles have been measured simultaneously in a highly selective way in the $2\nu_1$ vibrational overtone at 6638.21 cm^{-1}.

Due to the relatively slow rate constants for peroxy radical self- and cross-reactions, in the measurements of such kind of reactions, relatively high peroxy radical concentrations are needed to obtain a sizeable decay of the peroxy radical concentration in the experimental measurement time of a few 10 ms. Even though the oxidation reaction of VOCs in the atmosphere is mostly driven by OH radicals, Cl instead of OH is normally used in laboratory studies due to several reasons, as the H-abstraction rate constant for Cl with VOCs is normally faster than OH, and Cl is easier prepared compare to OH in the laboratory. Cl is also used in this work as radical initiator in the measurement of the cross reaction of $C_2H_5O_2$ with CH_3O_2. Cl reacts with C_2H_6 and CH_4 to produce both $C_2H_5O_2$ and CH_3O_2 in the presence of O_2. In general, it is supposed that Cl is completely consumed by VOCs, and the concentration of peroxy radicals generated is equal to the initial Cl concentration. However, the rate constants for the reaction of Cl-atoms with peroxy radicals are thought to be fast (in the range of 1-2 $\times 10^{-10}$ cm^3s^{-1}) [29, 118, 119], the reaction of Cl with peroxy radicals could also contribute to the consumption of peroxy radicals. In a recent work of Onel et al. [44], the obtained rate constant for the CH_3O_2 self-reaction is nearly two times slower compared to the recommended value from IUPAC. As Cl was used in the earlier works to generate peroxy radicals, the origin of the disagreement is believed to be the fast reaction of Cl with CH_3O_2: this reaction has been underestimated or not considered at all in older measurements and thus results in an apparently faster rate constant for the self-reaction of CH_3O_2.

In the cross reaction of $C_2H_5O_2$ with CH_3O_2, the reaction of Cl-atoms with the precursor CH_4 is much slower (1×10^{-13} cm^3s^{-1}) [120] than the reaction of Cl with C_2H_6 (5.8×10^{-11} cm^3s^{-1}) [120]. Therefore, to even obtain identical CH_3O_2 and $C_2H_5O_2$ concentrations, 580 times more CH_4 than C_2H_6 is needed. However, due to the absorption of CH_4 in the near IR region the amount of CH_4 that can be added in our experiments is limited to a few 10^{17} cm^{-3}, which may result in Cl reacting partially with peroxy radicals under our conditions.

The reaction of Cl with CH_3O_2 has been studied experimentally [29, 121, 122] and theoretically [123], Drougas and Kosmas [123] have identified three reaction pathways for the reaction of CH_3O_2 with Cl,

$$CH_3O_2 + Cl \rightarrow CH_3O + ClO \quad (4.6.a)$$

$$CH_3O_2 + Cl \rightarrow CH_2OO + HCl \quad (4.6.b)$$

$$CH_3O_2 + Cl \rightarrow CH_2O + HOCl \quad (4.6.c)$$

Currently only the first two pathways have been detected experimentally, no indication for path (4.6.c) has been found so far. Moreover, the branching ratio between both pathways are not well-known: in the case of CH_3O_2 the branching fraction for the Criegee path varies from 0.5 [29, 121] to 0.9 [122], and the rate constant varied from 1.15×10^{-10} cm^3 s^{-1} to 2.2×10^{-10} cm^3 s^{-1}.

Table 4.1 Literature results about Cl + CH_3O_2 reaction.

$k(CH_3O_2 + Cl)/10^{-10}$ cm^3 s^{-1})	$\alpha(CH_2OO)$	Technique [a]	Reference
2.0 ± 0.5	0.7	FP-UV	Bridier [124]
1.5 ± 0.2	0.49	FP-UV/IR	Maricq [29]
1.15 ± 0.5	0.48	DF-MS	Jungkamp [121]
2.2 ± 0.5	0.9	DF-LIF/MS	Daele [119]

[a] FP: flash photolysis; DF: discharge flow; UV: ultra violet; IR: infrared; MS: mass spectrometry; LIF: laser induced fluorescence.

While for $C_2H_5O_2$ [29] only one study has been published to our knowledge, based on the reaction pathways for Cl + CH_3O_2 reaction, the corresponding reactions for $C_2H_5O_2$ leading to

$$C_2H_5O_2 + Cl \rightarrow C_2H_5O + ClO \quad (4.7.a)$$

$$C_2H_5O_2 + Cl \rightarrow CH_3CHOO + HCl \quad (4.7.b)$$

$$C_2H_5O_2 + Cl \rightarrow CH_3CHO + HOCl \quad (4.7.c)$$

Radical-radical reactions are very complex and complicated to measure, especially reactions with very fast rate constants which will lead to short lifetimes for the related species. This becomes even more difficult when the reaction products are also reactive radicals which lead to secondary reactions and thus complicate the measurements even more. Taking the Cl + CH_3O_2 reaction as an example, the subsequent reactions of the products CH_3O, ClO, and CH_2OO are as follows:

1. Channel CH_3O + ClO: the produced CH_3O continues to reacts with O_2 and generate HO_2, ($CH_3O + O_2 \rightarrow HO_2 + CH_2O$), then HO_2 can also react with CH_3O_2 and accelerates the decay of CH_3O_2. The reaction of the co-product ClO with HO_2 leads to the stable products HOCl and O_2, while its reaction with CH_3O_2 gives both radical (CH_3O and ClOO) and stable product:

$$ClO + CH_3O_2 \rightarrow ClOO + CH_3O \quad (4.8.a)$$

$$ClO + CH_3O_2 \rightarrow CH_3OCl + O_2 \quad (4.8.b)$$

2. CH_2OO + HCl channel: In recent years, there were many studies related to Criegee [125]. In the reaction of alkenes with ozone, a primary ozonide is first formed and then decomposes rapidly into Criegee and carbonyl compounds. The excess energy in primary ozonides can also transfer to the product and lead to the formation of vibrationally excited Criegee, CI*, which then undergoes unimolecular decomposition or undergoes collision stabilization to form stable Criegee intermediates (CIs), which then further react with other stable substances or radicals.

The unimolecular reaction of Criegee generates OH radicals and this is an important source of night-time OH. The reaction of Criegee with stable products is mainly reaction with H_2O, especially with water dimer, with a rate constant of 6.4×10^{-12} cm^3 s^{-1}. The reaction between Criegee and SO_2 leads to the formation of SO_3, with a rate constant of $\sim 10^{-11}$ cm^3 s^{-1}, the further reaction of SO_3 leads to H_2SO_4. The self-reaction of CH_2OO generates CH_2O (7.4×10^{-11} cm^3 s^{-1}), and its reaction with peroxy radicals CH_3O_2 and $CH_3C(O)O_2$ was also reported with a rate constant of 2.4×10^{-11} cm^3 s^{-1} [126],

$$CH_2OO + CH_3O_2 / CH_3C(O)O_2 \rightarrow products \quad (4.9)$$

Therefore, the reaction of Cl-atoms with peroxy radicals might influence the data evaluation of the HO_2, CH_3O_2 and $C_2H_5O_2$ profiles in the measurements of the cross reaction of $C_2H_5O_2$ with CH_3O_2 and should be included in the reaction mechanism. However, given the difference or limited measurement in the results of $C_2H_5O_2$/CH_3O_2 with Cl, and in the measurement of the rate constant of CH_3O_2 + Cl reaction, the following reactions of CH_2OO as its self-reaction and its reaction with peroxy radicals were not considered in literature. Also, due to limitations in techniques, the Criegee products in Cl + RO_2 reaction has currently not been detected, thereby increasing the uncertainty of experimental results. Therefore, it seems necessary to evaluate these reactions again. We have carried out experiments of CH_3O_2 + Cl and $C_2H_5O_2$ + Cl individually to get the rate constant and branching ratio. The obtained results were added in the mechanism for the data evaluation of the cross reaction of $C_2H_5O_2$ with CH_3O_2.

4.1 Kinetics measurements of the reactions of CH_3O_2 and $C_2H_5O_2$ with Cl-Atoms

4.1.1 Kinetics measurement of the reaction of CH_3O_2 with Cl

Photolysis of Cl_2 in the presence of CH_4 and O_2 gives the CH_3O_2 radical:

$$Cl_2 + h\nu_{351nm} \rightarrow 2Cl \tag{4.10}$$

$$Cl + CH_4 + O_2 \rightarrow CH_3O_2 \tag{4.11}$$

To study the reaction of Cl with CH_3O_2, a high concentration of Cl-atoms together with a low concentration of CH_4 is needed to avoid rapid transformation of Cl to CH_3O_2. Different ratios of Cl_2 and CH_4 were used in the experiments, and the initial concentration of Cl-atoms is obtained before each experiment by converting them to HO_2 in the presence of excess methanol and oxygen. The pressure in the cell was maintained at 50 torr for all experiments. Table 4.2 summarizes the different initial Cl and CH_4 concentrations for all experiments, and the calculated ratios of CH_4/Cl varies in a large range from 452 to 69.

Table 4.2 Experimental conditions with different initial concentrations of the reactants.

Exp.	[Cl] /10^{13}cm^{-3}	[CH_4] /10^{15}cm^{-3}	[O_2] /10^{17}cm^{-3}	[Cl_2] /10^{15}cm^{-3}	$\frac{[CH_4]}{[Cl]}$	Symbol
1	16	25	6.0	10	156	red dot
2	11.5	30	4.8	8.3	261	teal dot
3	11.5	52	4.8	8.3	452	purple dot
4	7.9	6	5.3	4.7	76	blue circle
5	7.2	5	5.5	3.6	69	green circle
6	5.7	5	5.5	2.5	88	orange circle
7	2.3	5.5	6.0	1	239	black circle

Table 4.3 The wavelength and absorption cross-section for several measured species.

Species	Wavelength/cm^{-1}	Absorption cross-section/cm^2	Technique
CH_3O_2	7489.16	2.4×10^{-20}	CRDS
HO_2	6638.20	2.72×10^{-19}	
	6638.50	3.4×10^{-20}	
OH	7028.83(online)/7028.88(offline)	1.54×10^{-19} (online)	
X (CH_3OCl?)	7029.84	1×10^{-20} (estimated)	
CH_3O	292.602 nm		LIF

Absorption time profiles in the near IR region were measured for the following radicals: CH_3O_2 at 7489.16 cm^{-1}, HO_2 at 6638.20 cm^{-1} and 6638.58 cm^{-1} and OH at 7028.83 cm^{-1}. During the measurement of online and offline signals for the OH radical, a strong offline-absorption was noticed and therefore, the profiles of a currently unidentified product (see below) were also measured at 7029.85 cm^{-1}. Besides, laser induce fluorescence was applied to measure the CH_3O radical.

In order to possibly identify the absorbing species X and to choose the most appropriate wavelength to follow this species, the absorption spectrum was measured in the range of 7027-7030 cm^{-1}: Figure 4.1 (b) shows 2 profiles near the OH absorption line: it can be clearly seen that the species is formed during the reaction.

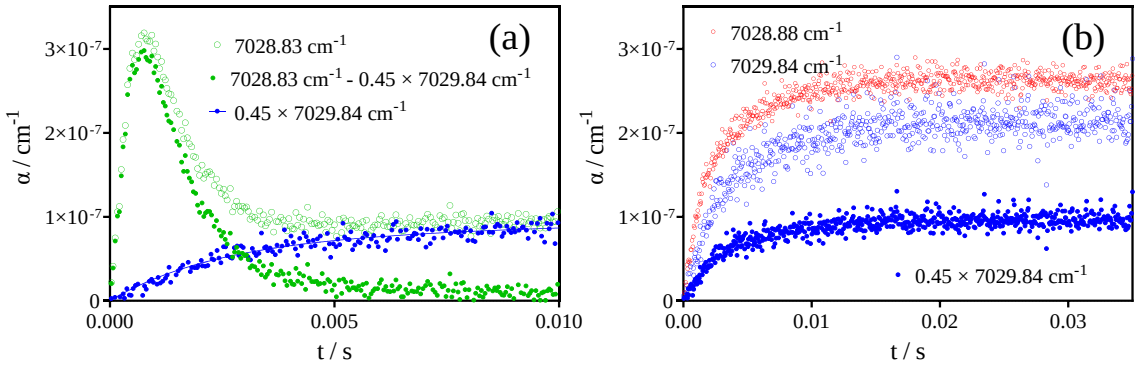

Figure 4.1 (a): Absorption time profiles of online OH (green circles), 0.45 × 7029.84 cm^{-1} (blue) and the difference (green dots). Graph b shows 2 different offline wavelengths: 7028.88cm^{-1} (red circles) and (7029.84 cm^{-1}) blue circles, all obtained in Exp.4. Note the different x-axis scales.

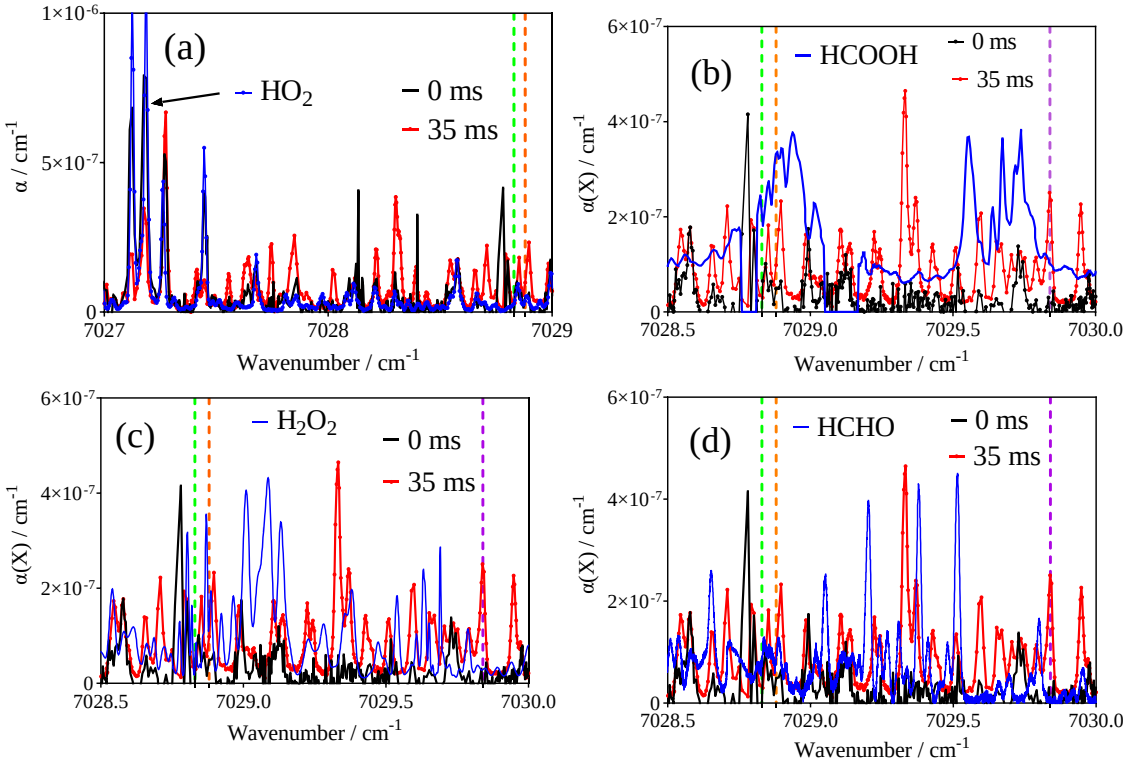

Figure 4.2 Absorption spectrum of products at t = 0 s (black line) and t = 35 ms (red line) in the photolysis of $Cl_2/CH_4/O_2$ mixtures ($Cl_2 = 8.35\times10^{15}$ cm^{-3}, $CH_4 = 5.25\times10^{15}$ cm^{-3}, $O_2 = 4.87\times10^{17}$ cm^{-3}) in the range 7027-7030 cm^{-1} and its comparison (blue lines) with the spectrum of (a) HO_2, (b) HCOOH, (c) H_2O_2, (d) HCHO. Dashed lines represent the absorption wavenumber of OH online at 7028.83 cm^{-1} (green), offline at 7028.88 cm^{-1} (orange) and the wavelength used for absorption time profiles of the unknown species X at 7029.84 cm^{-1} (purple).

From such kinetic traces, 2 spectra were extracted and are shown in Figure 4.2: the black line has been obtained by extrapolating the kinetic trace to t = 0 s, the red line corresponds to the absorbance at t = 35 ms after photolysis. The rapid formation of HO_2 radicals is seen in graph (a) by the good agreement of the t = 0 s spectrum with the HO_2 spectrum from the literature. The comparison with other possible products did not give any result: HCOOH as a possible secondary product from Criegee reactions (graph (b)), H_2O_2 (graph (c)) or CH_2O (graph (d)) didn't show any match between the spectra. Finally, the wavelength 7029.84 cm^{-1} has been chosen to follow the unidentified species, because the more intense peak at 7029.33 cm^{-1} overlaps with a strong CH_4 absorption. The shapes of the offline OH signal (7028.88 cm^{-1}) and the signal used for X are much

identical (see Figure 4.1(b)) and therefore the OH online signals have been corrected for offline absorption by subtracting the profile of X multiplied by a factor such that the OH-absorbance became 0 at longer reaction times (see Figure 4.1 (a)).

At t = 0 s, the absorbance is mostly near zero, ie. the absorbing species is well formed as a reaction product in the reaction between Cl + CH_4. Through modeling, we finally attributed the absorption in this range to CH_3OCl which is formed in the reaction of Cl_2 with CH_3O: the modelled profiles agreed well with the traces of X. More detailed information is given in the following contents.

4.1.2 Rate constant and branching ratio of the reaction of CH_3O_2 with Cl

A model as listed in Table 4.6 is developed to well reproduce the measured kinetics of the species in Table 4.2, the experimental profiles of CH_3O_2 and HO_2 together with their simulated profiles are shown in Figure 4.3, different colors represent different experimental conditions. The kinetics of CH_3O_2 and HO_2 with high Cl are different from those with low Cl. High Cl concentrations lead to high reactivity of Cl + CH_3O_2 reaction and result in fast decrease of CH_3O_2 at the very beginning. The decay of CH_3O_2 consists of two parts, a fast decay within 5 ms, which is mostly due to the reaction of Cl + CH_3O_2 and also CH_3O_2 + OH (the rate constant is also fast); and a slow decay caused mainly by CH_3O_2 self-reaction, the cross reaction of CH_3O_2 with HO_2 and other radicals. We can see that the profiles of CH_3O_2 and HO_2 with the CH_4/Cl ratio varied in a large range were fitted well with the presented model. A rate constant of 1.8×10^{-10} cm^3 s^{-1} and a branching ratio of 0.5 for each channel of Cl + CH_3O_2 reaction are obtained.

The initial concentration of CH_3O_2 is mainly determined by the Cl + CH_4 reaction that generates CH_3O_2 and the Cl + CH_3O_2 reaction that consumes CH_3O_2. Given the reaction rate constant of Cl + CH_4, the rate constant for Cl + CH_3O_2 reaction can be determined by fitting the initial concentration of CH_3O_2. The concentration of Cl in Exp.1 ([Cl] = 1.6×10^{14} cm^{-3}) is higher than Exp.2 ([Cl] = 1.15×10^{14} cm^{-3}), but [CH_4]

in both experiments is similar, $[CH_4] = (2.5 – 3) \times 10^{16}$ cm^{-3}. Even though higher CH_3O_2 would be expected for Exp 1, it can be seen that almost identical CH_3O_2 is produced in Exp.1 and Exp.2 (red and blue-green dots in Figure 4.3 (a)). This can be explained by an increased consumption of CH_3O_2 by Cl in Exp.1. It can also be seen that a higher concentration of HO_2 is formed in Exp.1 compared to Exp. 2 (red dots in Figure 4.3 (b)).

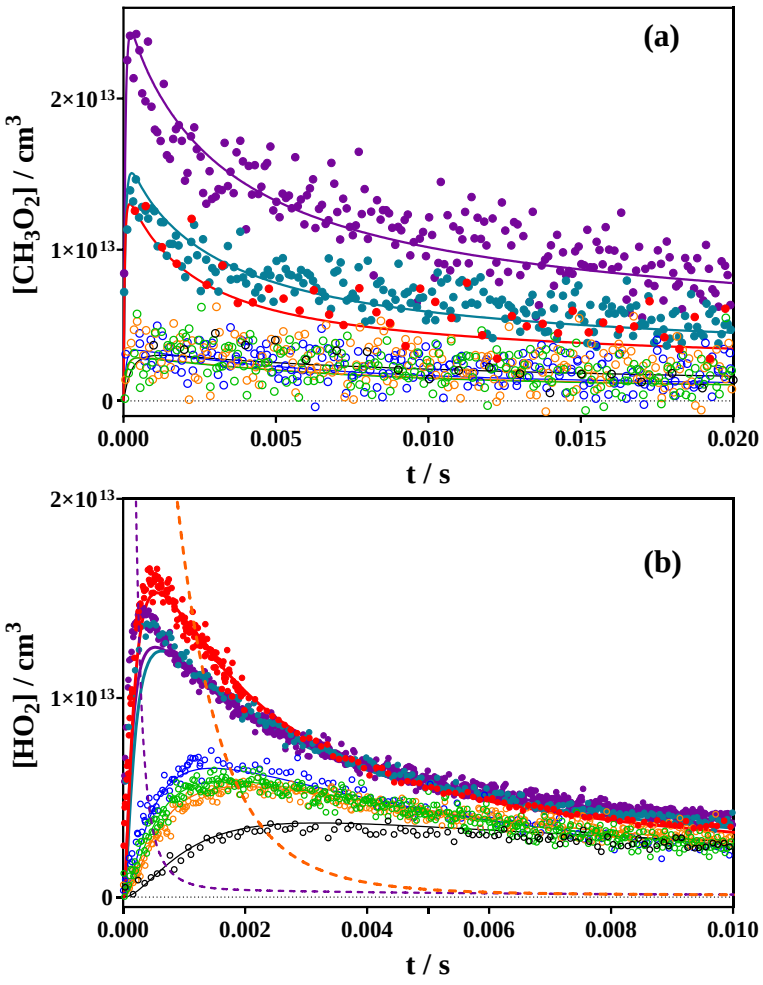

Figure 4.3 Absorption time profiles for (a) CH_3O_2 and (b) HO_2 in all conditions and the corresponding colors and symbols for different experimental conditions are summarized in Table 4.2, solid lines are simulated profiles of CH_3O_2 and HO_2 obtained with the mechanism in Table 4.6. Dashed lines are the simulated Cl profiles in Exp.3 (purple dashed line) and Exp.6 (orange dashed line).

The reaction of Cl with CH_3O_2 can lead to CH_3O + ClO and CH_2OO + HCl, and subsequent reactions of CH_3O and CH_2OO can produce HO_2. The unimolecular reaction of CH_2OO does not directly generate HO_2, but rather generates CO_2 and 2 H atoms, which react with O_2 to generate HO_2 [29]. Under the high O_2 concentration in our experiments, we simplify the mechanism and let two HO_2 directly be generated with a rate constant of 1.3×10^5 s^{-1},

$$CH_2OO \rightarrow HO_2 + HO_2 \tag{4.12}$$

The reaction (4.12) will rapidly produce high concentrations of HO_2. The reaction of OH radicals, generated by the decomposition of CH_2OO, with CH_3O_2 also produces HO_2. Except for unimolecular reactions, the collision of CH_2OO will give stable Criegee (sCH_2OO). The reaction of sCH_2OO with CH_3O_2 and HO_2 consumes CH_3O_2 and HO_2,

$$CH_2OO \rightarrow sCH_2OO \tag{4.13}$$

$$sCH_2OO + HO_2 / CH_3O_2 \rightarrow product \tag{4.14}$$

The HO_2 in Exp.1 is well fitted by the model, but there are clear disagreements of the simulation and experimental profiles of HO_2 before 1 ms in Exp.2 and Exp.3, the experimental data shows unexpected fast formation rates and even faster than the data in Exp.1. As mentioned above, the subsequent reactions of the products CH_3O and CH_2OO from Cl + CH_3O_2 reaction rapidly generate HO_2, thus the Cl + CH_3O_2 reaction is the rate limiting step and determines the concentration of HO_2. When the concentration of CH_3O_2 is the same, the higher the concentration of Cl, the faster is the formation rate of HO_2. Thus, the formation rate of HO_2 in Exp.1 should be the fastest compared to Exp.2. Therefore, we believe that other factors lead to the rapid generation of HO_2 in Exp.2. In experiments Exp.2 and 3, the repetition frequency of the photolysis laser was 0.5 Hz, while in other experiments it was 0.2 Hz. The rapid repetition rate may result in a second photolysis event before the gas in the observation volume is replaced, causing the products generated in the first photolysis event (such as CH_2O formed in the CH_3O + O_2 reaction and other secondary reactions) to react with Cl

generated in the second photolysis, thereby introducing additional HO_2. The reaction of Cl with CH_2O generates HCO and HCl, the following reaction of HCO with O_2 gives HO_2. With high concentration of O_2, the mechanism is simplified as follows:

$$Cl + CH_2O \rightarrow HO_2 + HCl \tag{4.15}$$

Only with an extra CH_2O added in the model with an initial concentration of 8×10^{12} cm^{-3}, the fast formation rate of the time traces of HO_2 for both Exp.2 and 3 can be reproduced, as shown in Figure 4.4. Another point to notice is that the HO_2 formation is very fast and on the time scale of the time resolution of our experimental technique: ring-down times are typically between 50 and 100 μs and the ring-down times are obtained by a single exponential fit under the approximation that the concentration of the absorbing species is constant during ring-down. As can be seen in the below figures, the rise of HO_2 in these experiments takes place in a few 100μs, so this approximation might not be valid anymore for the sharp HO_2 rise.

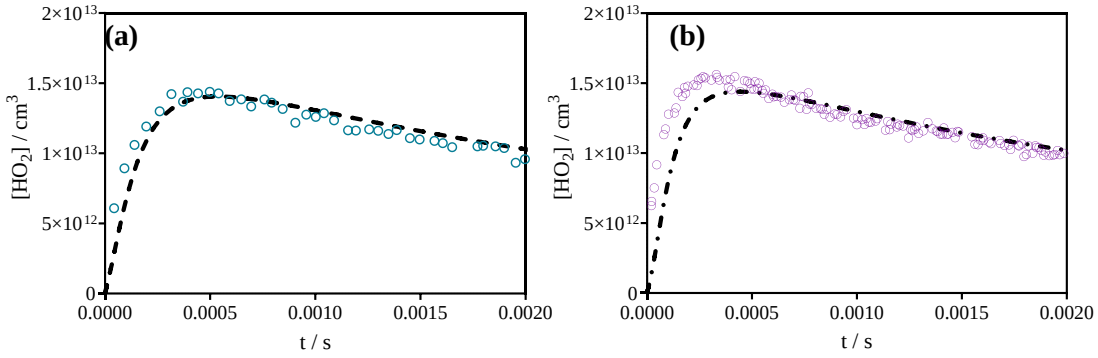

Figure 4.4 Zoomed HO_2 profiles over the first 2 ms for Exp.2 (a) and Exp.3 (b), the black dashed line (a) and dash-dotted line (b) are the simulation profiles with additional HO_2 formed by Cl + CH_2O reaction, the added concentration of CH_2O is 8×10^{12} cm^{-3}.

Exp.6 contains on half the concentration of Cl compared with Exp.3, however the steady-state concentration of CH_3O_2 is 10 times lower for Exp.6 (2.6×10^{12} cm^{-3}, orange circle) compared to Exp.3 (2.4×10^{13} cm^{-3}, purple dot). This is due to around 10 times lower concentration of CH_4 in Exp.6, thus a large fraction of CH_3O_2 is consumed by its reaction with Cl. Both Cl and CH_4 are relatively low in Exp.6, the reaction rate of Cl

with CH_3O_2 is slow and leads to a slow formation rate of HO_2, as shown by the orange circles in the right graph of Figure 4.3. The simulated Cl of Exp.3 and 6 shows that it takes around 3 ms (purple dashed line) and 5 ms (orange dashed line) for the Cl atoms to decrease to zero. The ratio of CH_4/Cl varies in a large range, 452 for Exp.3 and 88 for Exp.6, and in both cases the reaction of Cl with CH_3O_2 is important. With the low CH_4/Cl ratio in Exp.6, the longer life time of Cl leads to its reaction with CH_3O_2. While in Exp.3 with highest CH_4/Cl ratio among all the experiments, the reaction of Cl with CH_3O_2 is still unavoidable, this can be seen from the initial concentration of CH_3O_2: without reaction of Cl + CH_3O_2, the produced CH_3O_2 should be equal to the initial concentration of Cl (1.15×10^{14} cm^{-3}), however only 2.44×10^{13} cm^{-3} CH_3O_2 are formed.

Table 4.4 A simple mechanism used to evaluate the fraction of Cl involved in the reaction of Cl + CH_3O_2.

Reaction	k / cm^3 s^{-1}
$CH_3O_2 + Cl \rightarrow CH_2OO + HCl$	$9 \times 10^{-11}/0$
$CH_3O_2 + Cl \rightarrow CH_3O + ClO$	$9 \times 10^{-11}/0$
$CH_3O_2 + CH_3 \rightarrow CH_3O + CH_3O$	9×10^{-11}
$Cl + CH_4 \rightarrow CH_3 + HCl$	1.1×10^{-13}
$CH_3 + O_2 \rightarrow CH_3O_2$	2×10^{-13}
$CH_3 + Cl_2 \rightarrow Cl + CH_3Cl$	1.6×10^{-12}

A simple calculation is applied to better understand the competition between Cl + CH_3O_2 and Cl + CH_4 reactions. The reaction between one Cl and one CH_3O_2 will result in the loss of two potential CH_3O_2, the first due to the consumption of an already formed CH_3O_2 by Cl, and second because a Cl-atom being consumed by CH_3O_2 will not react anymore with CH_4 to generate CH_3O_2. At time zero with $[Cl]_0 = 1.15\times10^{14}$ cm^{-3}, $[CH_3O_2]_0 = 0$ cm^{-3}, to reach a steady state concentration of CH_3O_2 of only 2.44×10^{13} cm^{-3} means that $[Cl] = 4.53\times10^{13}$ cm^{-3} have reacted with CH_3O_2, thus 61% of Cl is primarily converted to CH_3O_2 and 39% of Cl is consumed by the reaction with CH_3O_2. But it should be noted that the derived value overestimates the consumption of CH_3O_2 by Cl + CH_3O_2 reaction, because other secondary reactions such as CH_3 + CH_3O_2 could

also result in a decrease of CH_3O_2. The calculation above shows only a rough evaluation of the competition between Cl + CH_4 and Cl + CH_3O_2.

In addition, as shown in Table 4.4, a similar analysis could also be achieved with a simple mechanism, which includes the secondary reactions related to CH_3. Figure 4.5 compares the impact of the reaction Cl + CH_3O_2 on the CH_3O_2 concentration: the left graph shows a model with the rate constant of Cl + CH_3O_2 equals to the value in Table 4.6 while the right graph ignores the consumption of CH_3O_2 caused by the CH_3O_2 + Cl reaction. Because only the initial concentration of CH_3O_2 is needed to evaluate the competitive reaction between CH_4 + Cl and CH_3O_2 + Cl and thus to obtain the overall rate constant of the reaction CH_3O_2 + Cl, the mechanism does not involve other consumption pathways of CH_3O_2 and hence the concentration of CH_3O_2 remains constant at longer reaction times.

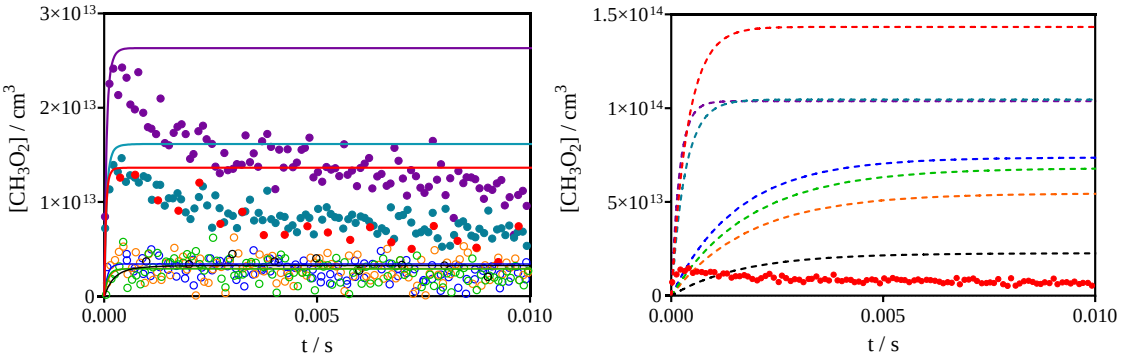

Figure 4.5 Experimental data of CH_3O_2 for all conditions as summarized in Table 4.2 (colored dots) and simulation results with the mechanism in Table 4.4, solid lines in left graph with k(Cl + CH_3O_2) = 1.8×10^{-10} cm^3 s^{-1}, dashed lines in right graph with k(Cl + CH_3O_2) = 0. Notice the difference in the y-axis scale of both graphs.

The solid lines in Figure 4.5 (left) with k (CH_3O_2 + Cl) = 1.8×10^{-10} cm^3 s^{-1} fits well the initial concentration of CH_3O_2. The dashed line in Figure 4.5 (right) shows the simulation result with k (CH_3O_2 + Cl) = 0, where almost all Cl is converted into CH_3O_2. But we can see that even without Cl + CH_3O_2 reaction, the concentration of the produced CH_3O_2 is still lower than the initial concentration of Cl, listed in Table 4.5. This is because the reaction of CH_3 with CH_3O_2 also leads to the consumption of some

CH_3O_2. Table 4.5 also summarizes the percentage of Cl which is involved in Cl + CH_3O_2 reaction for all experimental conditions and it ranges from 34% to 45%. The minimum value corresponds to the highest $[CH_4]_0/[Cl]_0$ ratio, and the maximum value corresponds to the lowest $[CH_4]_0/[Cl]_0$ ratio. We can see that, when the concentration of Cl is around 10^{14} cm^{-3}, although CH_4 is already 400 times higher than Cl, there is still 30% of Cl consumed by Cl + CH_3O_2 reaction. And even with a low initial concentration of Cl around 10^{13} cm^{-3}, ~200 times more CH_4 compared to Cl is still far from being enough to transform all Cl to CH_3O_2, and nearly half of Cl will participate in the Cl + CH_3O_2 reaction.

Table 4.5 Experimental conditions and the formed concentration of CH_3O_2 with the mechanism in Table 4.4 and the percentage of Cl involved in Cl + CH_3O_2 reaction.

Exp.	[Cl] /10^{13} cm^{-3}	$\frac{[CH_4]}{[Cl]}$	$[CH_3O_2]$_Sim[a]. /10^{13} cm^{-3}	CH_3O_2_Sim[b]. /10^{13} cm^{-3}	% Cl[c]
1	16	156	14.3	1.36	41%
2	11.5	261	10.5	1.62	38%
3	11.5	452	10.4	2.63	34%
4	7.9	76	7.37	0.34	45%
5	7.2	69	6.81	0.29	45%
6	5.7	88	5.46	0.29	45%
7	2.3	239	2.26	0.33	42%

[a]: k (Cl + CH_3O_2) = 0, [b]: k (Cl + CH_3O_2) = 1.8×10^{-10} cm^3 s^{-1}, [c]: Percentage of Cl involved in Cl + CH_3O_2 reaction.

The sensitivity of the rate constant and branching ratio of Cl + CH_3O_2 is also evaluated as shown in Figure 4.6. While the CH_3O_2 profiles are mostly sensitive to the total rate constant, the HO_2 profiles are sensitive to the branching ratio, the sensitivity of rate constant is only evaluated on CH_3O_2 and the sensitivity of the branching ratio on HO_2. To clearly show the results, only three typical conditions (the data chosen for CH_3O_2 and HO_2 are different) are presented. Solid lines represent the simulations obtained with the mechanism in Table 4.6. Figure 4.6 (a) shows the results fitted with the same branching ratio but different total rate constants for Cl + CH_3O_2: 2.2×10^{-10}

$cm^3\ s^{-1}$ (dashed line), $1.4\times10^{-10}\ cm^3\ s^{-1}$ (dashed-dotted line). Figure (b) shows the results fitted with same total rate constant ($1.8\times10^{-10}\ cm^3\ s^{-1}$) but different branching ratios: $\alpha(CH_2OO) = 0.3$ (dashed line) and 0.7 (dash dotted line). But we can see that teal ($[CH_4] = 3\times10^{16}\ cm^{-3}$, $[Cl] = 1.15\times10^{14}\ cm^{-3}$, $[CH_4]_0/[Cl]_0 = 261$) and purple data ($[CH_4] = 5.2\times10^{16}\ cm^{-3}$, $[Cl] = 1.15\times10^{14}\ cm^{-3}$, $[CH_4]_0/[Cl]_0 = 452$) are sensitive to the rate constant, and the red data ($[CH_4]=2.5\times10^{16}\ cm^{-3}$, $[Cl]=1.6\times10^{14}\ cm^{-3}$, $[CH_4]_0/[Cl]_0 = 156$) are sensitive to the branching ratio. However, the blue data ($[CH_4] = 6\times10^{15}\ cm^{-3}$, $[Cl] = 7.9\times10^{13}\ cm^{-3}$, $[CH_4]_0/[Cl]_0 = 76$) apparently are not sensitive to neither rate constant nor branching ratio. This is because when high concentration of Cl and CH_4 were applied, such as the teal and purple data, high concentration of CH_3O_2 was produced, thus the reactions of Cl with CH_3O_2 and CH_4 lead to the fast consumption of Cl, therefore the major reaction of Cl is with CH_3O_2 and CH_4. However, for the blue data, the initial concentration of Cl and CH_4 were low, and with the consumption of CH_3O_2 by Cl + CH_3O_2, the steady-state concentration of CH_3O_2 is only $\sim3\times10^{12}\ cm^{-3}$. When the rate constant of Cl + CH_3O_2 changes from $2.2\times10^{-10}\ cm^3\ s^{-1}$ to $1.4\times10^{-10}\ cm^3\ s^{-1}$, the simulated concentration of CH_3O_2 varies only by around $2\times10^{12}\ cm^{-3}$, which is within the signal noise. Due to the slow decay of Cl, the secondary reaction of Cl with other species instead of CH_3O_2 also contribute to HO_2, and which makes the profile of HO_2 seems like not sensitive to the branching ratio of Cl + CH_3O_2 reaction. The dotted lines in Figure 4.6 (a) and (b) are simulation results with the Cl + CH_3O_2 reaction not included for the blue data. It can be seen that the produced CH_3O_2 is highly overestimated and HO_2 is highly underestimated, which indicates the importance of Cl + CH_3O_2 under the current experimental conditions.

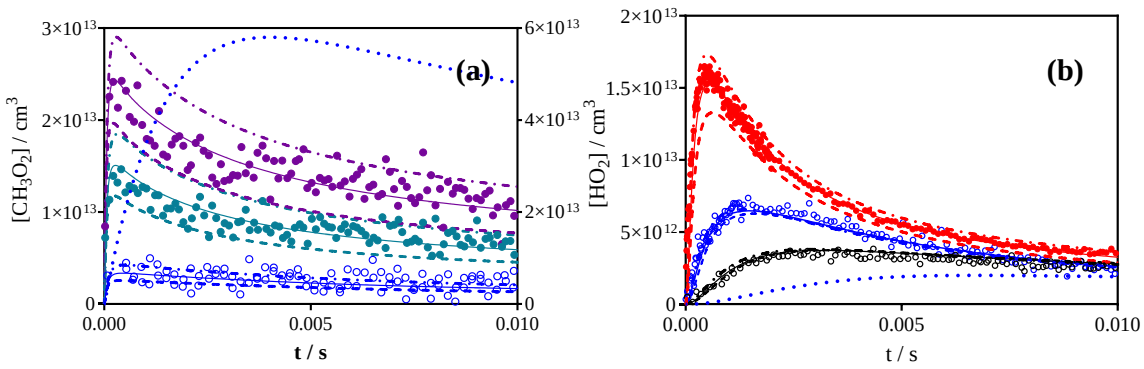

Figure 4.6 Absorption time profiles of CH_3O_2 and HO_2 in three conditions and simulation results with different rate constant and branching ratio. Different colors represent different experimental conditions as specified in Table 4.2. Solid lines represent the simulation results with mechanism shown in Table 4.6. (a) is for CH_3O_2, where dashed lines (2.2×10^{-10} cm^3 s^{-1}) and dash dotted lines (1.4×10^{-10} cm^3 s^{-1}) are simulation results with same branching ratio ($\alpha = 0.5$ for CH_2OO channel) but different rate constant for $Cl + CH_3O_2$. (b) is for HO_2, where dashed lines ($\alpha = 0.3$ for CH_2OO channel) and dash dotted lines ($\alpha = 0.7$ for CH_2OO channel) are simulation results with same rate constant (1.8×10^{-10} cm^3 s^{-1}) but different branching ratio for $Cl + CH_3O_2$. Dotted blue lines are the simulation profiles of CH_3O_2 (right y axis) and HO_2 with mechanism in Table 4.6 but $Cl + CH_3O_2$ reaction is excluded.

The products of the $Cl + CH_3O_2$ reaction are $CH_2OO + HCl$ and CH_3O+ClO. However, in the literature, only the product ClO was measured, Criegee from the other channel has never been detected. This is also the case in our measurements, the obtained rate constant and branching ratio are based only on the measurements of the reactant CH_3O_2 and the secondary products HO_2 formed in the subsequent reactions of CH_2OO and CH_3O. Therefore, further efforts were applied to evaluate the product channels. Figure 4.7 shows again the absorption time profiles for two measurements with the highest CH_3O_2 and HO_2. The dashed lines are results from simulations with the mechanism in Table 4.6, but with the reaction $Cl + CH_3O_2$ producing only CH_2OO + HCl (9×10^{-11} cm^3 s^{-1}) and the other channel leading to stable products (9×10^{-11} cm^3 s^{-1}). The dash-dotted lines are results with $Cl + CH_3O_2$ giving in one channel stable products (9×10^{-11} cm^3 s^{-1}) and in the other channel $CH_3O + ClO$ (9×10^{-11} cm^3 s^{-1}). Since stable products do not generate HO_2, these simulations can show the contribution of the

products CH_3O and CH_2OO to HO_2. We can see that with only one radical channel, the concentration of HO_2 is underestimated and this low concentration of HO_2 also leads to a slightly slower decay of CH_3O_2. In Figure 4.7 (b) is also shown the simulation result with Cl + CH_3O_2 only giving CH_2OO + HCl (1.8×10^{-10} cm^3 s^{-1}) as blue dotted line, and the blue dash dotted-dotted line with Cl + CH_3O_2 only giving CH_3O + ClO (1.8×10^{-10} cm^3 s^{-1}). The decomposition rate of CH_2OO to give HO_2 is 1.5×10^5 s^{-1}, which is higher than the pseudo first order rate constant of CH_3O with O_2, which is around 1×10^3 s^{-1} in the current conditions. Thus, with the mechanism with only CH_2OO formed, a higher concentration of HO_2 with faster formation rate is obtained while for only CH_3O channel, HO_2 is underestimated and forms with a slower rate. So, if the CH_3O channel is set with a rate constant of 9×10^{-11} cm^3 s^{-1} and the other channel giving only stable products with the same rate constant, a strong disagreement between the simulation and experimental data is seen in red dashed-dotted line. These simulations evaluate the sensitivity of the experimental data to the rate constant and branching ratio of the CH_3O_2 + Cl reaction obtained in this work, as well as the importance of the two product channels for the kinetics of HO_2.

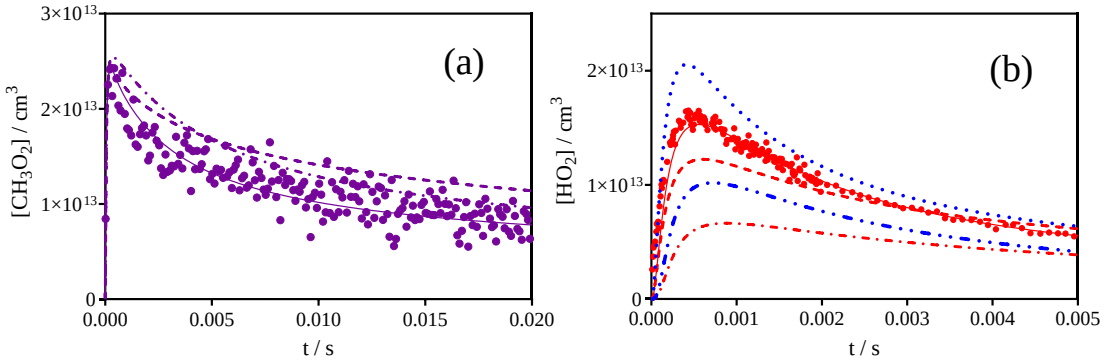

Figure 4.7 Absorption time profiles for two measurements with highest CH_3O_2 and HO_2, solid lines are simulation results with mechanism in Table 4.6, dashed lines are fitted with same mechanism, but Cl + CH_3O_2 produces CH_2OO + HCl (9×10^{-11} cm^3 s^{-1}) and stable products (9×10^{-11} cm^3 s^{-1}), and dash-dotted lines are results with Cl + CH_3O_2 gives stable products (9×10^{-11} cm^3 s^{-1}) and CH_3O + ClO (9×10^{-11} cm^3 s^{-1}). In graph (b), the blue dotted line is a simulation with Cl + CH_3O_2 leading only to CH_2OO + HCl (1.8×10^{-10} cm^3 s^{-1}), and blue dash dotted-dotted line leading only to CH_3O + ClO (1.8×10^{-10} cm^3 s^{-1}).

Maricq et al. [29] did not consider the self-reaction of the Criegee intermediate and its reaction with RO_2 radicals in their mechanism. Figure 4.8 evaluates the importance of these two reactions by fitting the kinetics of CH_3O_2 and HO_2. The solid lines show the model results with the mechanism in Table 4.6, the dashed lines show the same model but without CH_2OO self-reaction ($CH_2OO + CH_2OO$) and its reaction with HO_2 and RO_2 (sCH_2OO+HO_2/RO_2). Without these reactions, the obtained profiles of HO_2 are overestimated and the decays are too slow at longer reaction times. The applied rate constant of sCH_2OO with HO_2 is $2\times10^{-11}cm^3\ s^{-1}$, which contributes significantly to the consumption of HO_2, therefore the results omitting this reaction are in strong disagreement between the experimental measurements and model results. Further tests were carried out, but we were not able to find a mechanism that fits all HO_2 profiles without involving the reaction of sCH_2OO with HO_2. There may be other solutions by adding extra reactions to produce less HO_2 and consume more, but the current model already provides a good try to well reproduce the experimental HO_2 data. Even though the profiles of CH_3O_2 are well fitted without $CH_3O_2 + sCH_2OO$ reaction, but in fact the slower decay of CH_3O_2 caused by the absence of $CH_3O_2 + sCH_2OO$ reaction is compensated by the faster reaction of CH_3O_2 with HO_2, which is overestimated due to the higher HO_2 concentration and causes more consumption of CH_3O_2 and results in CH_3O_2 appearing unaffected.

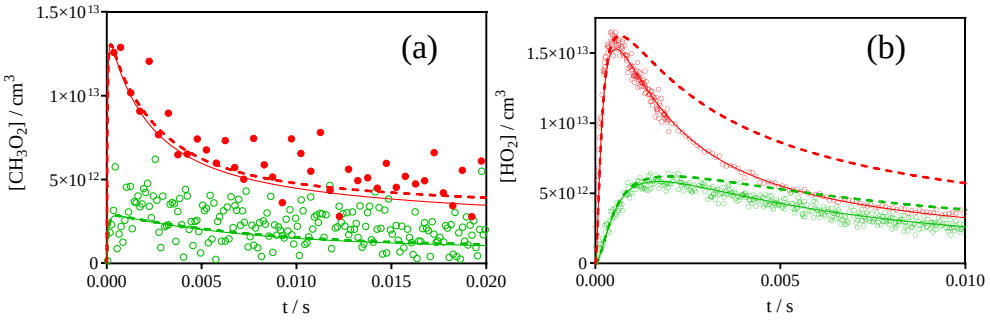

Figure 4.8 Experimental results of CH_3O_2 and HO_2 for Exp.1 and 5 and simulation results with model in Table 4.6 (solid line) and model from Table 4.6 but without the self-reaction of CH_2OO and the reaction of the stabilized Criegee sCH_2OO with HO_2 and CH_3O_2 (dashed line).

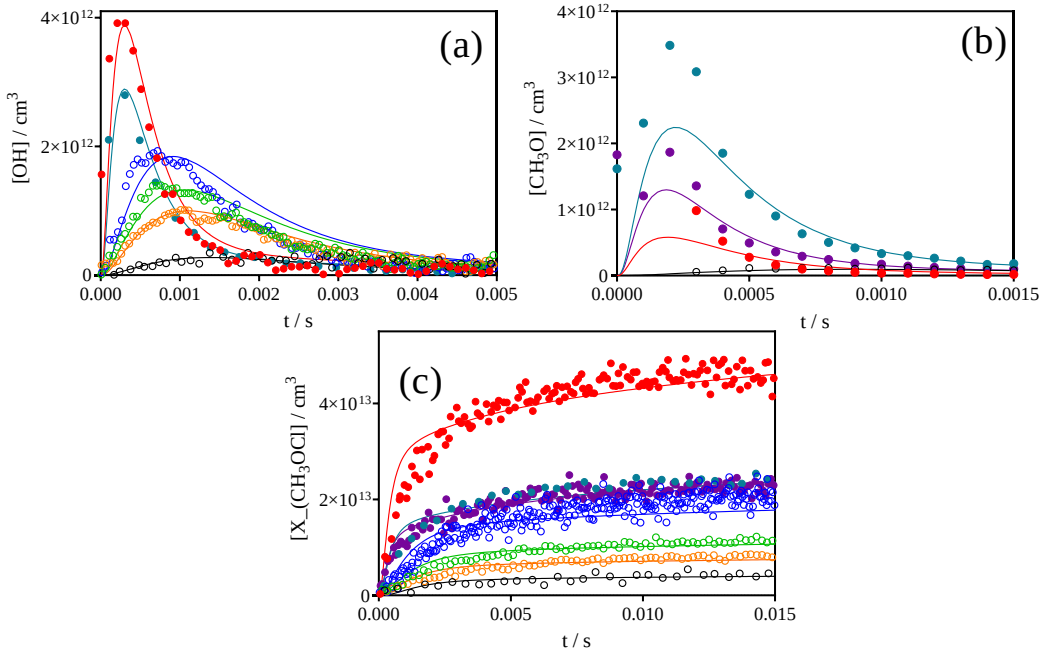

Figure 4.9 Absorption time profiles of OH, CH_3O and X(CH_3OCl), the experimental conditions and its corresponding represented symbols are summarized in Table 4.2, and solid lines are simulation results with the mechanism in Table 4.6.

Beyond HO_2 and CH_3O_2, the absorption time profiles of OH, of a stable product named X and the LIF signal of CH_3O are also fitted with the mechanism in Table 4.6, and the result is shown in Figure 4.9. It can be seen that not all profiles are well fitted due to their short lifetimes of both OH (<5 ms) and CH_3O (<2 ms) radical and the uncertain composition of the species X. The formation of OH is determined by the reaction related to Criegee, and its consumption is mostly controlled by the reaction with CH_4 and CH_3O_2. The reaction of CH_3O is also too complicated to fit as there are 11 reactions in the mechanism and the life time is shorter than 2 ms. The absorption of X at 7029.85 cm^{-1} was assigned to CH_3OCl, which is produced in the reaction CH_3O_2 + ClO with a rate constant equal to $6\times10^{-13}cm^3s^{-1}$, and the reaction of CH_3O + Cl_2 with a rate constant of $5\times10^{-13}cm^3s^{-1}$. The reaction of CH_3O_2 with ClO does not produce much CH_3OCl, but as high concentrations of Cl_2 were used, the reaction of CH_3O with Cl_2 is a major contributor to formation of CH_3OCl with a relatively fast formation rate and considerable high concentration. It cannot be excluded that the profile of X

represents the sum of two species, for example CH_3OOH could also absorb in this wavelength range, but its spectrum is not known. Therefore, all solid lines show the fitted results of X as CH_3OCl. We can see that the model is also not able to well fit them for all conditions with the current model, but no more efforts will be given because of its complicated reaction mechanism and short life time.

Table 4.6 Mechanism used to fit the reaction of Cl with CH_3O_2.

Reaction	k/ cm^3 s^{-1}	Reference
$CH_3O_2 + Cl \rightarrow CH_2OO + HCl$	9×10^{-11}	This work
$CH_3O_2 + Cl \rightarrow CH_3O + ClO$	9×10^{-11}	This work
$CH_3O_2 + CH_3O_2 \rightarrow CH_3O + CH_3O$	1.3×10^{-13}	[13]
$CH_3O_2 + CH_3O_2 \rightarrow CH_2O + CH_3OH$	2.2×10^{-13}	[13]
$CH_3O_2 + HO_2 \rightarrow CH_3OOH + O_2$	3.37×10^{-12}	[13]
$CH_3O_2 + OH \rightarrow HO_2 + CH_3O$	1×10^{-10}	[55]
$CH_3O_2 + CH_3 \rightarrow CH_3O + CH_3O$	9×10^{-11}	[127]
$CH_3O_2 + CH_3O \rightarrow$ products	2.6×10^{-12}	[29]
$CH_3O_2 + ClO \rightarrow Cl + CH_3O$	1.62×10^{-12}	[13]
$CH_3O_2 + ClO \rightarrow CH_3OCl + O_2$	6×10^{-13}	[13]
$HO_2 + HO_2 \rightarrow H_2O_2 + O_2$	1.7×10^{-12}	[113]
$HO_2 + Cl \rightarrow OH + ClO$	9.3×10^{-12}	[128]
$HO_2 + Cl \rightarrow HCl + O_2$	3.4×10^{-11}	[128]
$HO_2 + OH \rightarrow H_2O + O_2$	1.0×10^{-10}	[113]
$HO_2 + CH_3O \rightarrow$products	1.1×10^{-10}	[129]
$HO_2 + ClO \rightarrow OHCl + O_2$	5×10^{-12}	[130]
$CH_3O + O_2 \rightarrow HO_2$	1.9×10^{-15}	[13]
$CH_3O + Cl \rightarrow CH_2O + HCl$	7×10^{-11}	[29]
$CH_3O + Cl_2 \rightarrow CH_3OCl + Cl$	5×10^{-13}	This work
$Cl + CH_4 \rightarrow CH_3 + HCl$	1.1×10^{-13}	[13]
$Cl + CH_2O \rightarrow HO_2 + HCl$	7.3×10^{-11}	[131]
$CH_3 + O_2 \rightarrow CH_3O_2$	2×10^{-13}	[130]
$CH_3 + Cl_2 \rightarrow Cl + CH_3Cl$	1.6×10^{-12}	[29]
$OH + CH_4 \rightarrow CH_3 + H2O$	7×10^{-15}	[132]
$OH + ClO \rightarrow HO_2 + Cl$	1.9×10^{-11}	[128]

$OH + Cl_2 \rightarrow OHCl + Cl$	6.42×10^{-14}	[128]
$CH_2OO \rightarrow OH$	100000 s^{-1}	This work
$CH_2OO \rightarrow sCH_2OO$	170000 s^{-1}	This work
$CH_2OO + Cl_2 \rightarrow OH$	1×10^{-14}	This work
$CH_2OO \rightarrow HO_2 + HO_2$	130000 s^{-1}	This work
$CH_2OO + CH_2OO \rightarrow CH_2O + CH_2O + O_2$	7.4×10^{-11}	[133]
$sCH_2OO + HO_2 \rightarrow$products	2×10^{-11}	[126]
$sCH_2OO + CH_3O_2 \rightarrow$products	5×10^{-12}	[126]
$CH_3O_2 \rightarrow$ diffusion	1 s^{-1}	This work
$OH \rightarrow$ diffusion	5 s^{-1}	This work
$HO_2 \rightarrow$ diffusion	3 s^{-1}	This work

4.1.3 Rate constant and branching ratio of the reaction of $C_2H_5O_2$ with Cl

$C_2H_5O_2$ was generated by pulsed 351 nm photolysis of C_2H_6/Cl_2/100 torr O_2 mixtures. To promote the reaction of Cl with $C_2H_5O_2$, a high Cl concentration together with a low C_2H_6 concentration has been used in these experiments. Three series of experiments have been carried out with either keeping C_2H_6 constant and varying the Cl_2 concentration or vice versa. Overall, the ratio of $[C_2H_6]_0/[Cl]_0$ has been varied between 4.4 to 176. $C_2H_5O_2$ radicals have been detected at 7596.47 cm^{-1} and absorption time profiles have been converted to concentration time profiles with an absorption cross-section of $\sigma_{C2H5O2,\ 7596.47\ cm\text{-}1} = 1.0\times10^{-20}$ cm^2, HO_2 profiles have been measured at 6638.21 cm^{-1}, and have been converted to concentration time profiles using an absorption cross-section of $\sigma_{HO2,\ 6638.21\ cm\text{-}1} = 2.0\times10^{-19}$ cm^2. In Figure 4.10 are shown the $C_2H_5O_2$ (left graph) and the HO_2 (right graph) concentration-time profiles of a series of experiments, where C_2H_6 has been varied to obtain $[C_2H_6]_0/[Cl]_0$ ratios in a range between 4.6 and 93.

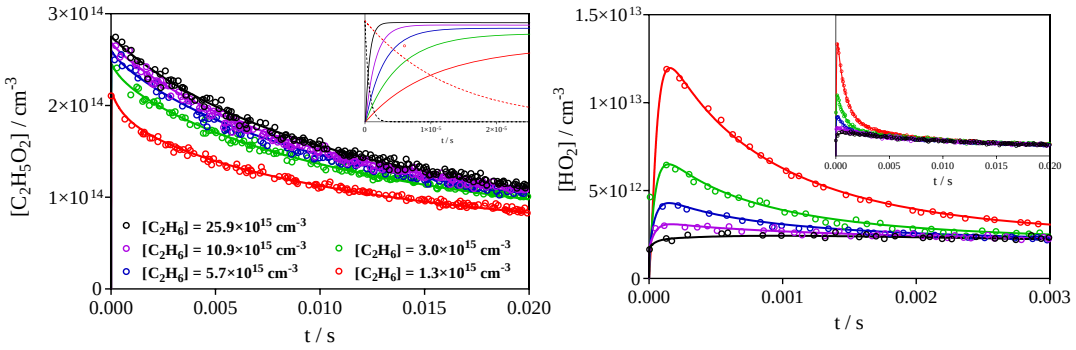

Figure 4.10 Left graph $C_2H_5O_2$ (insert shows zoom over first 25 µs, Cl profiles are shown as dashed lines only for highest and lowest $[C_2H_6]_0$), right graph HO_2 (insert shows the same signals, but on the same time scale as left graph) concentration-time profiles. To promote the reaction of Cl-atoms with $C_2H_5O_2$, a high initial Cl-concentration (2.8×10^{14} cm^{-3}) was used for all experiments, $[C_2H_6]_0$ was varied from 1.3×10^{15} cm^{-3} (red) to 25.9×10^{15} cm^{-3} (black), resulting in a ratio $[C_2H_6]_0/[Cl]_0$ between 4.6 (red) and 93 (black). Full lines represent model in Table 4.7.

It can be seen that with decreasing $[C_2H_6]_0$ (from black to red in Figure 4.10) the $C_2H_5O_2$ concentration decreases and the HO_2 concentration increases. The decrease of $C_2H_5O_2$ with decreasing $[C_2H_6]_0$ is due to an increased competition of Cl with C_2H_6 or with $C_2H_5O_2$. The insert in the left graph of Figure 4.10 shows the modeled $C_2H_5O_2$ for all concentrations and the Cl-profiles (dashed lines) only for the highest and lowest $[C_2H_6]_0$ on a 25 µs-zoom. It can be seen that at the highest $[C_2H_6]_0$, the Cl-concentration has decreased to near 0 within a few µs and near 100% of Cl-atoms are converted into $C_2H_5O_2$, while at the lowest $[C_2H_6]_0$ the decay lasts up to 50 µs and only around 70% of the Cl-atoms are converted to $C_2H_5O_2$.

While the overall shape of the $C_2H_5O_2$ is hardly influenced by the different $[C_2H_6]_0$, this is not true anymore for HO_2 profiles: for the black symbols (which represent $[C_2H_6]_0$ typically employed for the cross-reaction experiments, see below), one sees a rapid formation of some HO_2, corresponding to roughly 1% of the initial Cl-atom concentration being due to the reaction of $C_2H_5 + O_2$. For the lowest $[C_2H_6]_0$ however, the HO_2 concentration is rapidly increased by a factor of 4 compared to the highest $[C_2H_6]_0$.

A model has been developed that allows fitting simultaneously the HO_2 and $C_2H_5O_2$ profiles for all experiments. Different reactions have been integrated into the mechanism having very different impacts on the profiles such as decreasing the initial $C_2H_5O_2$ and increasing HO_2:

(i) the decrease of the initial $C_2H_5O_2$ concentration with decreasing C_2H_6 is very sensitive to the ratio of the rate constants Cl with $C_2H_5O_2$ and Cl with C_2H_6, and allows obtaining the overall rate constant Cl with $C_2H_5O_2$. The decrease of $C_2H_5O_2$ with decreasing C_2H_6 could be very well reproduced for all $[C_2H_6]_0/[Cl]_0$ ratios with an overall rate constant of $k = (7.5\pm1.0) \times 10^{-11}$ cm^3 s^{-1}.

(ii) the fast rise of the HO_2 profiles is very sensitive to the branching ratio between (4.7.a) and (4.7.b) because only the product C_2H_5O from channel (4.7.a) leads under our conditions (the pseudo first order rate constant of C_2H_5O with O_2 is 2.4×10^5 s^{-1}) to a near instantaneous formation of HO_2, while the Criegee intermediate formed in (4.7.b) influences the HO_2 profiles only on a longer time scale. The effect of the branching ratio on the profiles is shown in Figure 4.11 of the red, green and black experiment from Figure 4.10: the full line show again the model from Table 4.7, while the dotted line shows the model with $k_{(4.7.b)}= 0$, i.e. exclusive formation of ClO and alkoxy radicals with the total rate constant being $k = 7.5\times10^{-11}$ cm^3s^{-1}. The decrease of $C_2H_5O_2$ with decreasing C_2H_6 is still very well reproduced, but the modeled HO_2 profiles for the green and red experiments rise well above the measured concentration. A yield of $\alpha = 0.53 \pm 0.05$ for the formation of the Criegee intermediate allowed to reproduce the HO_2 profiles for all $[C_2H_6]_0/[Cl]_0$ ratios.

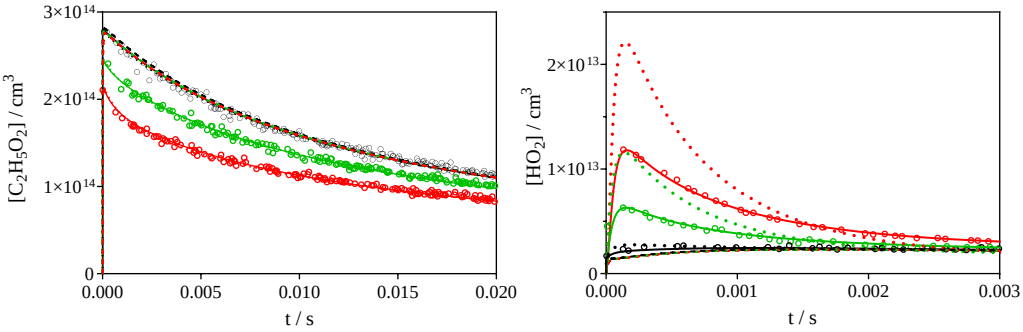

Figure 4.11 Data from Figure 4.10 (for better visibility, blue and magenta data have been omitted) with different models, showing the impact of adding the reaction between Cl and $C_2H_5O_2$ to the model: full lines as in Figure 4.10 with best model, dotted lines with the same model, but now considering the formation of ClO + C_2H_5O as the only path with k=7.5×10^{-11} cm^3 s^{-1}, dashed lines: model from Table 4.7 without Cl + $C_2H_5O_2$.

(iii) The reaction of Cl with $C_2H_5O_2$ was thought to give ClO with CH_3O and Criegee with HCl, thus the first try was carried out to fit the decay of the HO_2 profiles with Criegee intermediate formed which then leads in secondary reactions to some HO_2 formation. It is known from C_2H_4 ozonolysis experiments that the stabilized Criegee intermediate can undergo 1,4-H-atom migration, leading to the formation of vinylhydroperoxide, which subsequently decomposes to vinoxy radical and OH. The OH radicals will then react either with C_2H_6 forming C_2H_5 followed by the oxidation reaction, or with $C_2H_5O_2$, both paths leading partially to the formation of HO_2. The overall rate of the unimolecular Criegee decay has been obtained from structure activity relationships to 136 s^{-1}, and this value has tentatively been used to reproduce the HO_2 profiles. Criegee intermediates will also react with RO_2 in our mixture, the rate constant has been measured for the smallest Criegee to be 1.0×10^{-11} cm^{3}s^{-1}. It is proposed that this reaction leads initially to an adduct, which could generate HO_2 radicals in subsequent reactions: a rate constant of 150 s^{-1} was added to the mechanism to reproduce the HO_2 profiles on a longer time scale.

All profiles could be very well reproduced by the mechanism and rate constants given in Table 4.7: $k(Cl + C_2H_5O_2) = (7.5 \pm 1.0) \times 10^{-11}$ cm^3 s^{-1}, which is two times slower than the value obtained by Maricq *et al*. ($1.5 \pm 0.2 \times 10^{-10}$ cm^3 s^{-1}) [29] with the branching ratio for the formation of the C_2H_5O channel of $\alpha = 0.47 \pm 0.05$, in excellent agreement with Maricq *et al*. ($\alpha = 0.49 \pm 0.05$). Even though the mechanism developed through these experiments nicely reproduces our observed radical profiles in the wide range of $C_2H_5O_2$/Cl ratio, it is not meant to describe in detail the chemistry of Cl-atoms with $C_2H_5O_2$, or the subsequent chemistry of the Criegee intermediate. We must admit that indeed our observations are not a proof for the formation of the Criegee intermediate. While our experiments seem to show unequivocally that the reaction between $Cl + C_2H_5O_2$ leads with a yield of around 0.5 to formation of $ClO + C_2H_5O$, we can indeed not deduce anything solid about the other 50%. The formation of HO_2 on the long timescale, which was attributed to the subsequent chemistry of the Criegee intermediate, could also be modelled by a reaction of $ClO + C_2H_5O_2$ which might lead to the formation of $Cl + C_2H_5O + O_2$ and then contributes to the formation of HO_2. On the other hand, it is known that the reaction of $Cl + C_2H_5OH$ is very fast and leads to abstraction of the secondary H-atom. The equivalent reaction of $Cl + C_2H_5O_2$ would lead to formation of Criegee. However, the rate constant obtained in our laboratory for $Cl + C_2H_5O_2$ was slower than the one recommended for $Cl + C_2H_5OH$ (and in disagreement by a factor of 2 with the rate constant obtained by Maricq *et al*). The mechanism of $Cl + C_2H_5O_2$ was not presented in the paper of Maricq *et al*. Currently we are not able to explain the difference between the two measurements, and theoretical calculations or experiments with the detection and quantification of other species such as ClO, OH, C_2H_5O, CH_2CHO or Criegee to this system would be needed to better understand this reaction. Therefore, the rate constants from both the current measurements and Maricq *et al* have been tested to evaluate the influence of reaction of $Cl + C_2H_5O_2$ in the measurements of the cross reaction of $C_2H_5O_2$ with CH_3O_2.

Table 4.7 Mechanism used to fit the reaction of Cl with $C_2H_5O_2$.

Reaction	k/cm^3 s^{-1}	Reference
$Cl + C_2H_6 \rightarrow C_2H_5 + HCl$	5.9×10^{-11}	[13]
$C_2H_5 + O_2 + M \rightarrow C_2H_5O_2 + M$	4.8×10^{-12}	[112]
$C_2H_5 + O_2 \rightarrow C_2H_4 + HO_2$	3.5×10^{-14}	This work
$C_2H_5O + O_2 \rightarrow CH_3CHO + HO_2$	8×10^{-15}	[111]
$C_2H_5O_2 + HO_2 \rightarrow C_2H_5OOH + O_2$	6.2×10^{-12}	[110]
$2\ C_2H_5O_2 \rightarrow 2\ C_2H_5O + O_2$	3.2×10^{-14}	[134]
$2\ C_2H_5O_2 \rightarrow$ stable products	7.0×10^{-14}	[134]
$2\ HO_2 \rightarrow H_2O_2 + O_2$	1.7×10^{-12}	[113]
$C_2H_5O_2 + Cl \rightarrow ClO + C_2H_5O$	3.5×10^{-11}	This work
$C_2H_5O_2 + Cl \rightarrow HCl + CH_3CHO_2$ (Criegee)	4.0×10^{-11}	This work
$C_2H_5O_2 + ClO \rightarrow$ products	1.6×10^{-12}	[13]
$HO_2 + ClO \rightarrow O_2 + HOCl$	6.9×10^{-12}	[128]
$C_2H_5O + C_2H_5O_2 \rightarrow$ products	7×10^{-12}	This work
$C_2H_5O + HO_2 \rightarrow$ products	1×10^{-10}	[34]
$C_2H_5O_2 \rightarrow$ diffusion	2 s^{-1}	This work
$HO_2 \rightarrow$ diffusion	3 s^{-1}	This work
Criegee + $C_2H_5O_2/CH_3O_2 \rightarrow$ adduct	1×10^{-11}	[126]
$2\ CH_2O_2 \rightarrow 2\ CH_2O + O_2$	7.4×10^{-11}	[133]
$CH_2O_2 + CH_3CHO \rightarrow$ products	1.48×10^{-12}	[135]
Adduct $\rightarrow HO_2$ + product	150 s^{-1}	This work
$CH_3CHO_2 \rightarrow CH_2CHO_2H$ (VHP)	135 s^{-1}	[136]
VHP $\rightarrow$ OH + CH_2CHO	3000 s^{-1}	This work
$CH_2CHO + O_2 \rightarrow O_2CH_2CHO$	9.5×10^{-13}	[137]
$OH + C_2H_6 \rightarrow H_2O + C_2H_5$	2.4×10^{-13}	[13]
$OH + C_2H_5O_2 \rightarrow HO_2 + C_2H_5O$	9.75×10^{-11}	[34, 138]
$OH + C_2H_5O_2 \rightarrow C_2H_5OOOH$	3.25×10^{-11}	[34, 138]

4.2 Rate constant and branching ratio of the reaction of $C_2H_5O_2$ with CH_3O_2

Detecting peroxy radicals in the $\tilde{A}$-$\tilde{X}$ electronic transition in the near IR region has the potential of a more selective detection for peroxy radicals compared to UV absorption spectroscopy. In order to demonstrate this, we have carried out measurements for the determination of the rate constant of the cross reaction between CH_3O_2 and $C_2H_5O_2$ radicals. The rate constant of this reaction was measured only once using UV absorption spectroscopy [32] whereby the experimental details given in that paper were sparse. It is not clear how the rate constant was extracted from the absorption time profiles measured only at one wavelength where the cross sections of both radicals are very similar. To check for the mutual selectivity of the detection for both radicals, the absorption cross-sections for both radicals have been measured at three different wavelengths: at one "peak" of the $\tilde{A}$-$\tilde{X}$ transitions of the CH_3O_2 radical at 7488.14 cm^{-1} (named in the following M1, green symbols in Figure 4.12), at the maximum of the transition of $C_2H_5O_2$ at 7596.47 cm^{-1} (named E1, red symbols in Figure 4.12) and at a "plateau" at 7601.66 cm^{-1} (named E2, blue symbols in Figure 4.12).

Ethyl- and methyl peroxy radicals were generated by pulsed 351 nm photolysis of $C_2H_6/CH_4/Cl_2$/100 torr O_2 mixtures. All experiments were carried out at 298 K. Three different DFB lasers are used for the detection of the three species: HO_2: NEL NLK1E5GAAA, 6629 ± 17 cm^{-1}, on CRDS path 1, CH_3O_2: NEL NLK1B5EAAA, 7480 ± 20 cm^{-1} on CRDS path 2, $C_2H_5O_2$: AOI-1312-BF-20-CW-F1-H2-N127, 7622 ± 15 cm^{-1} on CRDS path 2.

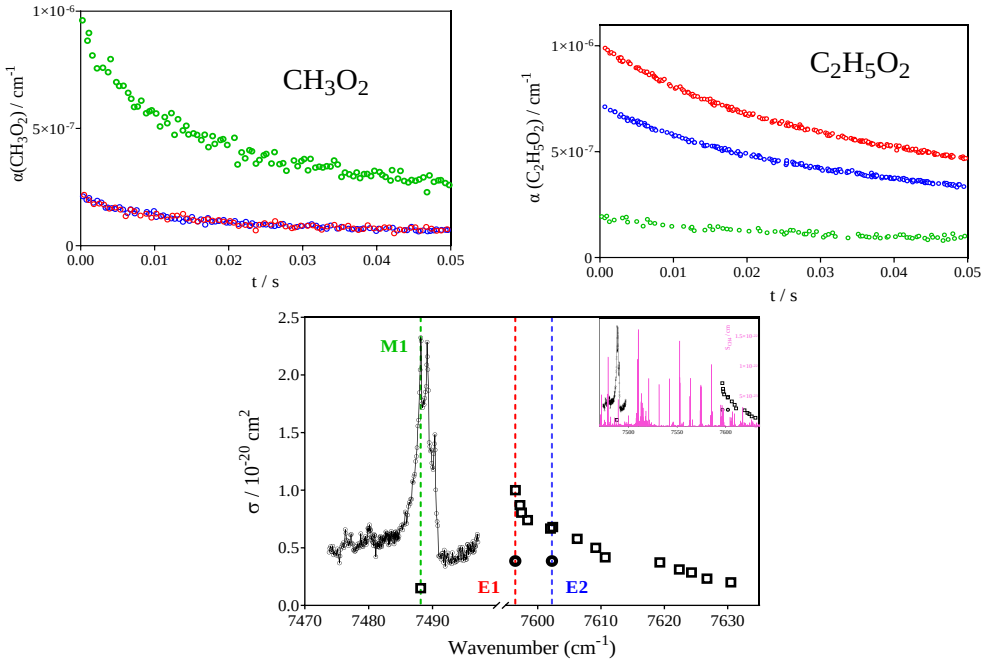

Figure 4.12 CH_3O_2 (upper left graph, $[Cl]_0 = 4.2\times10^{13}$ cm^{-3}, $[CH_4] = 1.9\times10^{17}$ cm^{-3}) and $C_2H_5O_2$ (upper right graph: $[Cl]_0 = 1.0\times10^{14}$ cm^{-3}, $[C_2H_6] = 4.4\times10^{16}$ cm^{-3}) profiles obtained at the three different wavelengths represented by colored vertical lines in the lower graph. Lower graph shows spectrum for both species (CH_3O_2 as circles, adapted from Farago *et al* [94]. and $C_2H_5O_2$ as square adapted from chapter three, main graph shows zoom on both sections with x-axis interrupted, insert shows continuous wavelength scale. Magenta lines in insert represent CH_4 spectrum from HITRAN database.

The upper graphs of Figure 4.12 show for one Cl-concentration the absorption time profiles for both radicals (left: CH_3O_2, right: $C_2H_5O_2$) at all three wavelengths. It can be seen that both radicals still absorb at the wavelength corresponding to the transition of the counterpart radical: for both radicals the absorption at its peak is around 4 times larger than at the peak of the counterpart radical (second column Table 4.8). The absorption cross-sections at the peak wavelengths are known from earlier works [9, 94] as well as in our measurements, as shown in the chapter three, and have been used here to obtain the absorption cross-sections at the peak wavelength of the counterpart radical from the relative intensities in Figure 4.12 type experiments (experiments using 3 different Cl-atom concentrations have been carried out). The results are summarized in Table 4.8 and illustrated in the lower graph of Figure 4.12.

Table 4.8 Ratio and absorption cross-sections for CH_3O_2, $C_2H_5O_2$ and CH_4 at three wavelengths.

	Ratio ($\sigma_{peak}/\sigma_{off}$)	σ (M1) / cm^2 7488.13 cm^{-1}	σ (E1) / cm^2 7596.47 cm^{-1}	σ (E2) / cm^2 7601.66 cm^{-1}
CH_3O_2	4.0	2.2×10^{-20}	*5.5×10^{-21}*	*5.5×10^{-21}*
$C_2H_5O_2$	6.6/5.0	*1.5×10^{-21}*	1.0×10^{-20}	7.6×10^{-21}
CH_4 [139]		1.2×10^{-24}	1.1×10^{-23}	5.0×10^{-25}
Ratio $\frac{\sigma(CH_3O_2)}{\sigma(C_2H_5O_2)}$		14.6	0.55 (= 1/1.81)	0.72 (= 1/1.38)

It can be seen that the absorption cross-sections for both radicals at the "counterpart wavelengths" (in *italic* in Table 4.8) are small (1.5 and 5.5×10^{-21} cm^{-1}), but not zero, and thus complete selectivity cannot be obtained. Even though the absorption-cross section for $C_2H_5O_2$ is higher on (E1) compared to (E2), all experiments have been carried out at (M1) and (E2) due to the much lower CH_4 absorption cross-sections at (E2) compared to (E1): even though $C_2H_5O_2$ is used in excess, high CH_4 concentrations (up to 3×10^{17} cm^{-3}) were still added and absorbed too much light at (E1). The absorption at 7488.14 cm^{-1} is the sum of CH_3O_2 and $C_2H_5O_2$, and also at 7601.66 cm^{-1}. So, the absorption at both wavelengths can be described as:

$$\alpha_{M1} = \sigma_{CH_3O_2,M1} \times [CH_3O_2] + \sigma_{C_2H_5O_2,M1} \times [C_2H_5O_2] \qquad \text{(Eq. 4.1)}$$

$$\alpha_{E2} = \sigma_{CH_3O_2,E2} \times [CH_3O_2] + \sigma_{C_2H_5O_2,E2} \times [C_2H_5O_2] \qquad \text{(Eq. 4.2)}$$

the corresponding absorption cross-sections are given in Table 4.8. To get best selectivity for investigating the cross reaction between both radicals, $C_2H_5O_2$ was used for all experiments in excess over CH_3O_2 for different reasons:

- To limit the reaction of Cl-atoms with peroxy radicals: the reaction of Cl-atoms with CH_4 is much slower than the reaction of Cl-atoms with C_2H_6 (0.01 and 5.9×10^{-11} cm^3 s^{-1} for CH_4 and C_2H_6, respectively) [120]. Therefore, to even obtain identical CH_3O_2 and $C_2H_5O_2$ concentrations, already 580 times more CH_4 than C_2H_6 is needed. And because CH_4 is absorbing in the near IR region (the absorption cross-sections for CH_4 at the three wavelengths are given in Table

4.8 and is shown as magenta stick spectrum [139] in Figure 4.12), the amount of CH_4 that can be added in our experiments is limited to a few 10^{17} cm^{-3}. If an excess of CH_3O_2, would have been chosen, only a few 10^{13} cm^{-3} C_2H_6 would need to be added to obtain comparable $C_2H_5O_2$ concentrations. Such low concentrations of both precursors would lead to Cl-atom decays too slow to avoid major complications due to the reaction of Cl-atoms with CH_3O_2 or $C_2H_5O_2$.

- To limit absorption of the "counterpart" radical and thus increase selectivity: the ratio of the absorption cross-sections between both radicals at a given wavelength (last row of Table 4.8) is higher at the methyl peroxy transition: $\sigma(CH_3O_2)$ is 14.6 times higher compared to $\sigma(C_2H_5O_2)$ at (M1), while the inverse ratio is only 1.81 and 1.38 at (E1) and (E2), respectively. Therefore, in the example of a 10-fold (5-fold) excess of CH_3O_2 over $C_2H_5O_2$, such as $[C_2H_5O_2] = 1\times10^{13}$ cm^{-3}, and $[CH_3O_2] = 1\times10^{14}$ cm^{-3}. The absorption for CH_3O_2 at its wavelength M1 is $\alpha(CH_3O_2@M1) = 1\times10^{14}\times2.2\times10^{-20}$ $cm^{-1}= 2.2\times10^{-6}$ cm^{-1}, at wavelength E2 is $\alpha(CH_3O_2@E2) = 1\times10^{14}\times5.5\times10^{-21}$ $cm^{-1}= 5.5\times10^{-7}$ cm^{-1}. With the same way of calculation, thus the absorption for $C_2H_5O_2$ at its wavelength E2 is $\alpha(C_2H_5O_2@E2) = 1\times10^{13}\times7.6\times10^{-21}$ cm^{-1} $= 7.6\times10^{-8}$ cm^{-1}, at wavelength M1 is $\alpha(C_2H_5O_2@M1) = 1\times10^{13}\times1.5\times10^{-21}$ $cm^{-1}= 1.5\times10^{-8}$ cm^{-1}. Thus, the absorbance at (E2) only 12% (22%) of the absorbance would be due to $C_2H_5O_2$. In the example of a 10-fold (5-fold) excess of $C_2H_5O_2$ over CH_3O_2, the absorbance at (E1) would be around 95% (90%) and at (E2) 93% (87%) due to $C_2H_5O_2$ (*i.e.* still good selectivity), but now at (M1) around 59% (75%) of the signal is due to CH_3O_2 absorption.

- To maximize the importance of the cross-reaction: the self-reaction of $C_2H_5O_2$ is 3.5 times slower than that of CH_3O_2 (or 2 times, taking the very recent determination of the CH_3O_2 self-reaction rate constant by Onel et. al. [44]), making the loss through self-reaction less important in a reaction system with excess $C_2H_5O_2$ compared to excess CH_3O_2.

Therefore, experiments with a 5- to 10-fold excess of $C_2H_5O_2$ over CH_3O_2 should lead to a good sensitivity towards the rate constant of the cross-reaction: decays at (E2) represent nearly pure $C_2H_5O_2$ decays mostly governed by the self-reaction, the correction of these profiles due to CH_3O_2 absorption is very minor. Simultaneously measured profiles obtained at (M1) can now be corrected for $C_2H_5O_2$ absorption, and the remaining CH_3O_2 decay is mostly due to the cross reaction with $C_2H_5O_2$: the rate constant of the cross reaction can be extracted with good sensitivity.

Table 4.9 Experimental conditions used for measuring the rate constant of the cross reaction between CH_3O_2 and $C_2H_5O_2$.

$[Cl]_0$/ $10^{13}cm^{-3}$	$[C_2H_6]_0$/ $10^{15}cm^{-3}$	$[CH_4]_0$/ $10^{17}cm^{-3}$	$[C_2H_5O_2]_0$ /10^{13} cm^{-3}	$[CH_3O_2]_0$/ 10^{13} cm^{-3}	$[C_2H_5O_2]_0$/ $[CH_3O_2]_0$	α_{C2H5O2} at E2	α_{CH3O2} at M1
8.1			7.25	0.85			
11.0	2.90	2.00	9.85	1.15	8.56	92.2 %	63.2 %
13.8			12.4	1.44			
7.4			5.95	1.45			
10.4	2.08	2.98	8.37	2.03	4.12	85.1 %	78.1 %
12.5			10.1	2.44			
7.1			5.05	2.05			
9.2	1.25	2.98	6.54	2.66	2.46	77.3 %	85.6 %
11.8			8.39	3.41			

Three series of experiments have been carried out, and the experimental conditions are summarized in Table 4.9. The initial Cl-atom concentrations (column 1) have been measured before each experiment through measuring and fitting HO_2 decays from the reaction of Cl-atoms with excess CH_3OH. C_2H_6 and CH_4 concentrations (column 2 and 3) have been obtained from flow and pressure measurements, and the initial peroxy radical concentrations (column 4 and 5) and their ratio (column 6) have then been

calculated using the literature values of the rate constants for Cl + CH_4 and Cl + CH_3O_2, as given in Table 4.10. To demonstrate the relatively good selectivity towards both radicals, the percentage of the absorbances at M1 and E2, that are due to the searched after radical, have then been calculated using the radical concentrations and the absorption cross-sections from Table 4.8 (column 7 and 8).

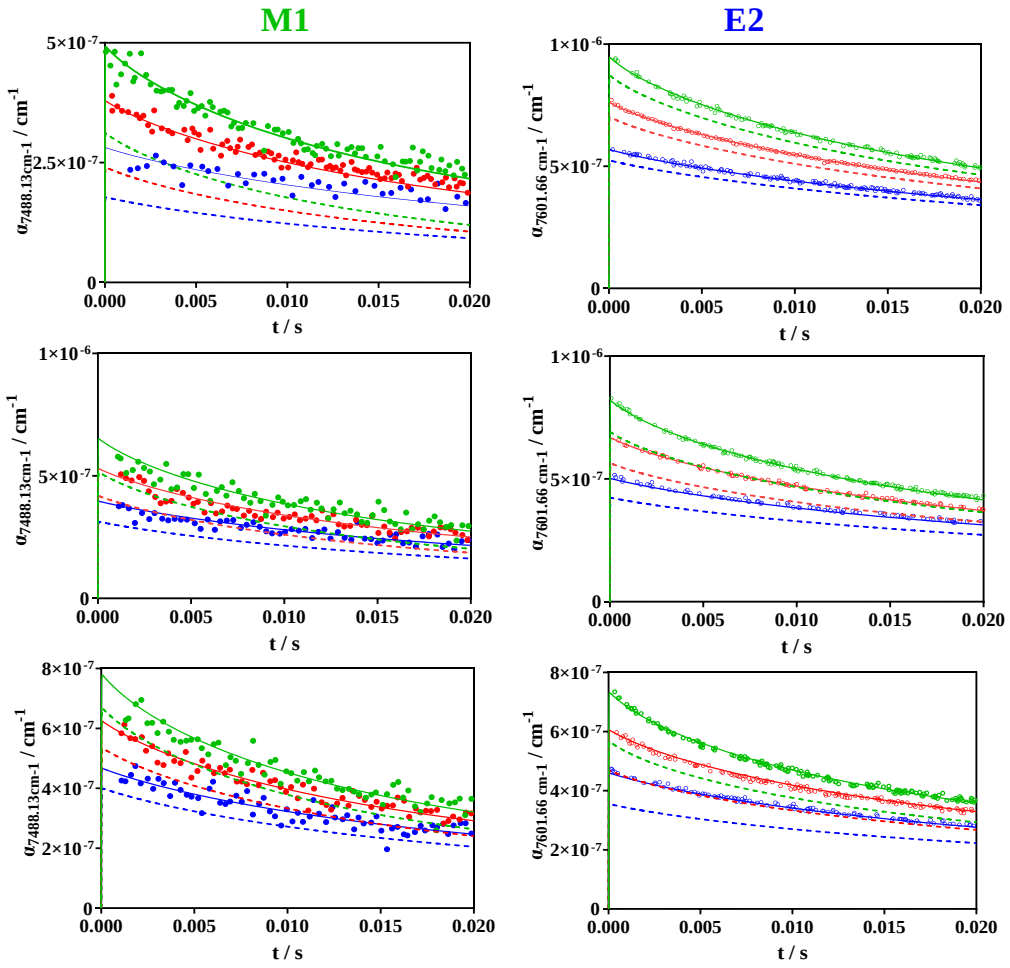

Figure 4.13 Absorption-time profiles at M1 (left graphs) and E2 (right graphs) for all three series with conditions such as given in Table 4.9. Full lines present the simulated absorption-time profiles presented as sum of absorbance due to CH_3O_2 and $C_2H_5O_2$, dotted lines represent the part of the absorbance due to one radical: CH_3O_2 in the left column, $C_2H_5O_2$ in the right column.

Figure 4.13 shows the experimental absorption time-profiles obtained at M1 and E2 for the 3 series (highest $C_2H_5O_2$ excess upper graph, note the different y-axis, and lowest $C_2H_5O_2$ excess bottom graphs) as colored dots: the absorption time-profiles obtained at M1, the wavelength mostly selective to CH_3O_2, are shown in the left column, the profiles obtained at E2, mostly selective to $C_2H_5O_2$, are shown in the right column. The profiles at both wavelengths have been simulated simultaneously using the model from Table 4.10, by best reproducing the signals at M1 and E2 with Eq. 4.1 and Eq. 4.2 using the corresponding absorption cross-sections such as given in Table 4.8. These simulations are shown as full lines. The dotted lines in each graph represent the part of the absorption that is due to the "major" radical, i.e. CH_3O_2 in the left column and $C_2H_5O_2$ in the right column.

Table 4.10 Reaction mechanism used to fit all experiments of $CH_3O_2 + C_2H_5O_2$ reaction.

Reaction	k / $cm^3 s^{-1}$	Reference
Initiation reactions		
$Cl + CH_4 \rightarrow CH_3 + HCl$	1.0×10^{-13}	Ref [120]
$Cl + C_2H_6 \rightarrow C_2H_5 + HCl$	5.9×10^{-11}	Ref [120]
$CH_3 + O_2 + M \rightarrow CH_3O_2 + M$	1.4×10^{-13}	Ref [140]
$C_2H_5 + O_2 + M \rightarrow C_2H_5O_2 + M$	4.8×10^{-12}	Ref [141]
$C_2H_5 + O_2 \rightarrow C_2H_4 + HO_2$	9×10^{-14}	This work
Peroxy radical self- and cross-reactions		
$C_2H_5O_2 + CH_3O_2 \rightarrow C_2H_5O + CH_3O + O_2$	1.5×10^{-13}	This work
$C_2H_5O_2 + CH_3O_2 \rightarrow$ stable products	2.3×10^{-13}	This work
$CH_3O + O_2 \rightarrow CH_2O + HO_2$	1.92×10^{-15}	Ref [120]
$C_2H_5O + O_2 \rightarrow CH_3CHO + HO_2$	8×10^{-15}	Ref [142]
$CH_3O_2 + HO_2 \rightarrow CH_3OOH + O_2$	5.2×10^{-12}	Ref [110]
$C_2H_5O_2 + HO_2 \rightarrow C_2H_5OOH + O_2$	6.2×10^{-12}	Ref [110]
$2\ C_2H_5O_2 \rightarrow 2\ C_2H_5O + O_2$	3.2×10^{-14}	Ref [134]
$2\ C_2H_5O_2 \rightarrow$ stable products	7.0×10^{-14}	Ref [134]
$2\ CH_3O_2 \rightarrow 2\ CH_3O + O_2$	1.3×10^{-13}	Ref [120]
$2\ CH_3O_2 \rightarrow$ stable products	2.2×10^{-13}	Ref [120]

$CH_3O + HO_2 \rightarrow$ products	1.1×10^{-10}	Ref [143]
$2\ HO_2 \rightarrow H_2O_2 + O_2$	1.7×10^{-12}	Ref [144]
Secondary Cl-atom reactions		
$Cl + C_2H_5O_2 \rightarrow ClO + C_2H_5O$	$5\text{-}8 \times 10^{-11}$	see text
$Cl + C_2H_5O_2 \rightarrow$ Products	$5\text{-}8 \times 10^{-11}$	see text
$Cl + CH_3O_2 \rightarrow ClO + CH_3O$	9×10^{-11}	This work
$Cl + CH_3O_2 \rightarrow$ Products	9×10^{-11}	This work
$Cl + CH_2O + O_2 \rightarrow HCl + HO_2 + CO$	7.32×10^{-11}	Ref [131]
$C_2H_5O_2 / CH_3O_2 + ClO \rightarrow C_2H_5O / CH_3O + ClOO$	1.6×10^{-12}	Ref [120]
$HO_2 + ClO \rightarrow O_2 + HOCl$	6.9×10^{-12}	Ref [145]
$ClOO\ (+M) \rightarrow Cl + O_2\ (+M)$	6.2×10^{-13}	Ref [145]
$Cl + O_2\ (+M) \rightarrow ClO_2\ (+M)$	1.6×10^{-33}	Ref [145]
Other secondary chemistry		
$C_2H_5O + C_2H_5O_2 \rightarrow$ products	7×10^{-12}	This work
$C_2H_5O + HO_2 \rightarrow$ products	1×10^{-10}	Ref [137]
$C_2H_5O_2 / CH_3O_2 \rightarrow$ diffusion	$2\ s^{-1}$	This work
$HO_2 \rightarrow$ diffusion	$3\ s^{-1}$	This work

The model contains, next to peroxy self-and cross reactions, also some secondary chemistry of Cl-atoms: these reactions could not completely be avoided, even though their impact is minor. As explained in the above chapter, preliminary results in our laboratory indicate that the reaction of Cl-atoms with $C_2H_5O_2$ leads with a rate constant of around 1×10^{-10} $cm^3\ s^{-1}$ and a yield of 50% to formation of C_2H_5O and ClO, while no clear statement can currently be made for the fate of the other 50%. The rate constant of this reaction has been determined by Maricq et al.[29] to be 1.6×10^{-10} $cm^3\ s^{-1}$, and therefore this reaction has been included into the mechanism (see Table 4.10) and tests have been run with the rate constant being varied between $1.0 – 1.6\times10^{-10}$ $cm^3\ s^{-1}$, but the impact on simulated profiles and thus the sought-after rate constant was within the noise of the experimental profiles. Figure 4.14 shows for the example of the highest $C_2H_5O_2$ excess (upper graphs of Figure 4.13), the breakdown of the fate of the 2 peroxy radicals into the different possible reaction paths: the left graphs represent CH_3O_2, the

right graphs $C_2H_5O_2$. The red symbols represent the fraction of the peroxy radical, which has reacted in the cross reaction of $C_2H_5O_2$ + CH_3O_2: it can be seen that for CH_3O_2, this reaction is the major fate for all initial radical concentrations (upper graph represent blue symbols from Figure 4.13, lower graph represent green symbols from Figure 4.13), while for $C_2H_5O_2$ this reaction is a minor loss. The major reaction path for $C_2H_5O_2$ is self-reaction (black symbols), with the cross reaction with HO_2 being the secondary contributor (blue symbols). These two pathways are very minor for CH_3O_2. For both radicals, the fraction having reacted with Cl-atoms (green symbols), is small, up to 5% for CH_3O_2 in the case of high initial radical concentration.

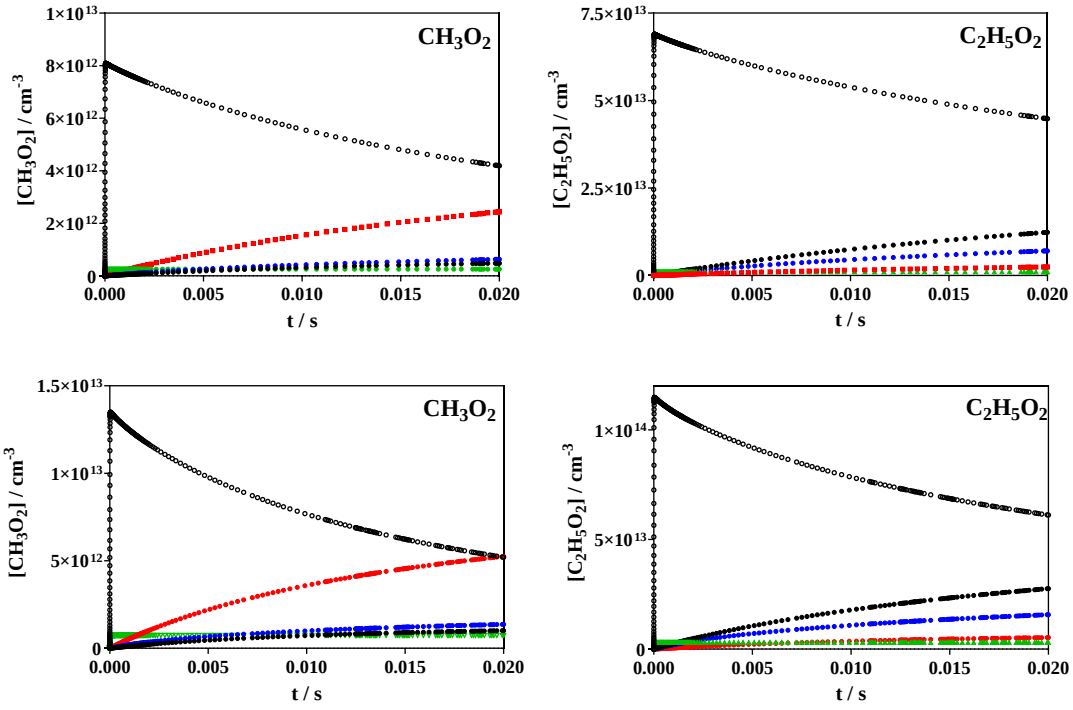

Figure 4.14 Modeling results for conditions from first raw of Figure 4.13 (highest excess of $C_2H_5O_2$). Left graph CH_3O_2, right graph $C_2H_5O_2$. Upper graphs are results for lowest Cl-concentration (blue symbols in Figure 4.13), lower graph are results for highest Cl-concentration (green symbols in Figure 4.13). Open black circles are CH_3O_2 /$C_2H_5O_2$ concentration, blue symbols represent CH_3O_2/$C_2H_5O_2$ concentration having reacted through cross reaction with **HO_2**, black symbol represent CH_3O_2/$C_2H_5O_2$ concentration having reacted through **self-reaction**, green symbols represent CH_3O_2/ $C_2H_5O_2$ concentration having reacted with **Cl-atoms**, red symbols represent CH_3O_2/ $C_2H_5O_2$ concentration having reacted through cross reaction with **$C_2H_5O_2$/ CH_3O_2**.

Simultaneously measured HO_2 profiles allow in principle the estimation of the branching ratio for radical and molecular path of the cross reaction. Figure 4.15 shows the HO_2 profiles obtained for the series with highest $C_2H_5O_2/CH_3O_2$ ratio. The initial fast rise of HO_2 has two origins: it is partially due to the reaction of Cl-atoms with the peroxy radicals and partially due to the small fraction of C_2H_5-radicals that form HO_2 in reaction with O_2 rather than the $C_2H_5O_2$ radical. The first process is taken into account in the chemical model by adding a simplified reaction schema (see Table 4.10), the second process has been implemented to best represent the initial HO_2 concentration and represents less than 1% of the initial C_2H_5 concentration. This observation is in excellent agreement with our works [110, 134] and earlier works [117, 146]. These two processes are finished within a few hundred µs, and the branching ratio of the cross reaction then influences the HO_2 concentration at longer reaction time. This is conceivable, because the HO_2 concentration at longer reaction times represents the steady-state concentration between production from peroxy self- and cross reactions and the consumption through cross reaction of HO_2 with the peroxy radicals. Best results are obtained with a branching ratio towards the radical channel of 0.40, ie. very similar to the branching fraction of the two self-reactions, 0.32 and 0.37 for $C_2H_5O_2$ and CH_3O_2, respectively. To demonstrate the influence of the cross reaction on the HO_2 profiles, the full black lines in the right graph represent for the highest radical concentration the simulation with the best rate constant and a branching ratio varied by ± 0.2. It can be seen that such variation of the branching ratio makes the model clearly deviating from the experimental results and therefore we estimate the uncertainty of the branching fraction from the comparison between model and experiment to be better than ± 0.2.

However, a major problem for estimating the branching ratio in these experiments is, that even for the self-reactions of the simplest peroxy radicals CH_3O_2 and $C_2H_5O_2$ there are still large uncertainty in rate constant and branching ratio. For CH_3O_2 the IUPAC recommendation since many years was 3.5×10^{-14} $cm^3 s^{-1}$ with a branching ratio

of 37% for the radical channel. In a very recent work, Onel *et al.* have re-determined the rate constant and found only $(2.0 \pm 0.9)\times10^{-14}$ $cm^3\ s^{-1}$, nearly 2 times smaller, but they confirmed the radical yield as recommended by IUPAC. They convincingly argue that earlier experiments suffered from interferences of the fast reaction of Cl-atoms with CH_3O_2 and this would have increased the apparent rate constant. The rate constant for the self-reaction of $C_2H_5O_2$ radicals was also recommended by IUPAC for many years at 7.6×10^{-14} cm^3s^{-1} with a radical yield of 63%, based on the measurement of stable end products. While, Noell *et al*. [18] and our measurements [134] obtained through direct radical measurements a much lower yield for the radical path and a subsequently higher rate constant (32% radical yield leading to a rate constant of $(1.0 \pm 0.2)\times10^{-13}$ cm^3s^{-1}). But even though the cross reaction of $C_2H_5O_2$ + CH_3O_2 is the major HO_2-production path in the current experiments and the two self-reactions are only minor contributors, the above-described uncertainties increase of course directly the uncertainty of the deduced yield in this work. Also, the HO_2 signal quality is poor in these experiments due to the absorption of high CH_4 and C_2H_6 concentrations, therefore we estimate a final uncertainty of the radical yield 0.40 ± 0.20. It should be noted that the uncertainty in the branching ratio has no influence on the estimation of the rate constant: a change in radical yield from 0.4 to 0.6 is not visible in the modelled absorption-time profiles at both wavelengths.

To demonstrate the sensitivity of the observed absorption-time profiles to the rate constant of the cross reaction, the left graph of Figure 4.15 shows the CH_3O_2 profiles of the same experiments, ie. high excess of $C_2H_5O_2$. The full lines show again the model from Table 4.10, while the dashed lines represent a variation of $k(C_2H_5O_2 + CH_3O_2)$ = $(3.8 \pm 1.5)\times10^{-13}$ $cm^3\ s^{-1}$. Such variation brings the simulated profiles outside the experimental profiles. In these simulations, the branching ratio of the radical channel has been adapted to best reproduce the HO_2 profiles (dashed coloured lines on the right graph): 0.31 and 0.54 for the upper (4.8×10^{-13} $cm^3\ s^{-1}$) and lower (2.8×10^{-13} $cm^3\ s^{-1}$) limit of $k(C_2H_5O_2 + CH_3O_2)$, respectively, but this variation has no influence on the

CH_3O_2 profiles: as can be seen in Figure 4.14 , the cross reaction with HO_2 is only a minor path for CH_3O_2 and therefore a change in the branching ratio has a negligible effect on the CH_3O_2 profile. From these simulations we estimate the uncertainty of the rate constant of the cross reaction to be $(3.8 \pm 1.0)\times10^{-13}$ $cm^3\,s^{-1}$.

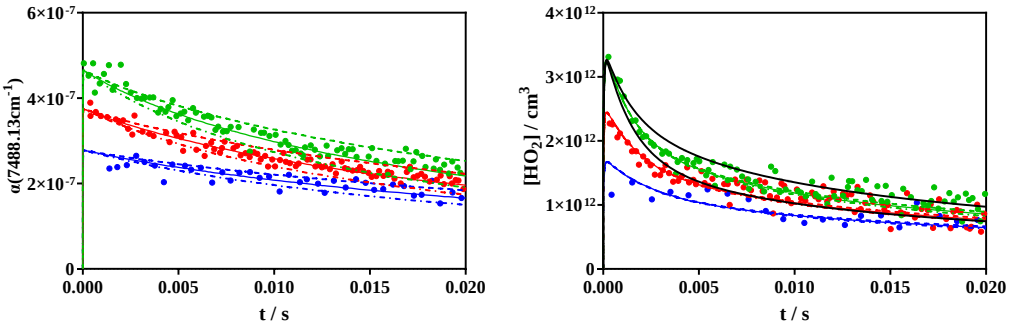

Figure 4.15 Left graph: CH_3O_2 profiles for highest $C_2H_5O_2$ excess: full lines represent best simulation with rate constants from Table 4.10 ($k(CH_3O_2 + C_2H_5O_2)$ = $(3.8 \pm 1.5)\times10^{-13}$ $cm^3\,s^{-1}$), dashed lines represent a variation of $k(CH_3O_2 + C_2H_5O_2)$ of ± 1.5 $\times10^{-13}$ $cm^3\,s^{-1}$. Right graph: HO_2 profiles for the same experiment. Full colored line represents best model with a radical yield of 0.4, dashed lines in the right graph show the model with $k(CH_3O_2 + C_2H_5O_2)$ varied as shown in left graph, but the branching ratio varied to best reproduce experiment (see text). The black lines show a variation of ±0.2 for the branching ratio for the highest radical concentration.

The simulation corresponding to the lower limit of the rate constant (upper curves in Figure 4.15) is close to the only published value for the cross reaction rate constant (2.0×10^{-13} $cm^3\,s^{-1}$) [32], and the observed absorption time profiles were poorly reproduced by such a model. In the work of Villenave *et al*. [32] no details are given on how the rate constant was obtained by solely measuring UV absorption profiles, and therefore no speculation about possible reasons for the disagreement can be proposed.

The geometric mean value rule is an empirical approach that allows for the estimation of cross-reaction rate coefficients from the self-recombination rate constants of the reacting partners [147]

$$k_{A+B} = 2 \times \sqrt{k_{A+A} \times k_{B+B}}$$

It has shown to work to better than 20% in the prediction of radical-radical rate coefficients for a series of hydrocarbon radicals [148] and has proven to be valid also for the cross reaction of HO_2 and DO_2 radicals [104]. When applying this rule to the cross reaction of CH_3O_2 and $C_2H_5O_2$ and using the values for the self-reactions from Table 4.10**,** one obtains 3.74×10^{-13} cm^3 s^{-1}, which is an excellent agreement with the rate constant obtained in this work. However, when using the value for the CH_3O_2 self-reaction recently obtained by Onel et al., [44] the geometric mean rule predicts a rate constant for the cross reaction of $C_2H_5O_2$ + CH_3O_2 at only 2.9×10^{-13} $cm^{-3}s^{-1}$. In Figure 4.16 are shown the results for both wavelength for the experiments with the lowest $C_2H_5O_2$ excess, using this rate constant for the cross reaction.

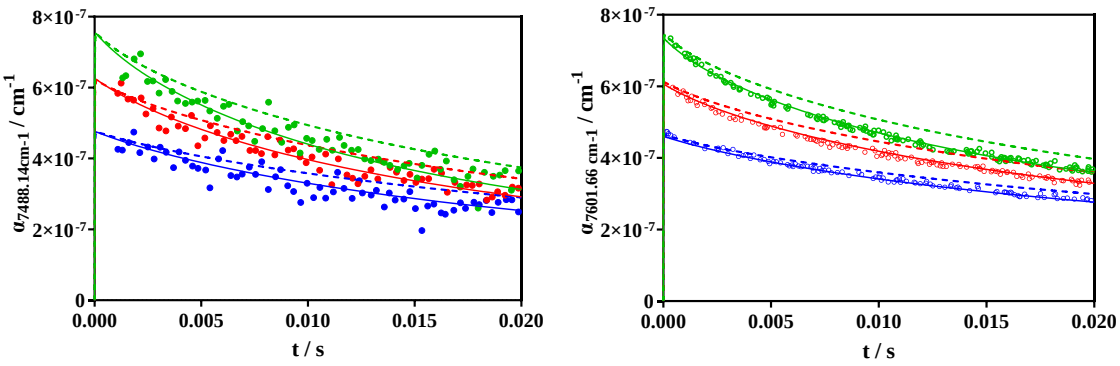

Figure 4.16 Series of lowest $C_2H_5O_2/CH_3O_2$ ratio with simulations using a rate constant for the cross reaction such as predicted by the geometric mean rule, if using data from Table 4.10 (full lines) and when using the recently determined rate constant for the CH_3O_2 self-reaction (dashed lines)

It can be seen that this rate constant does not allow to reproduce the observed absorption-time profiles, as the decays at both wavelengths are clearly too slow. However, it has not been demonstrated that in the case of cross-reactions of peroxy radicals the geometric mean rule is a good approximation, in particular because there are no reliable determinations of the rate constants for self- and cross-reactions of peroxy radicals to validate the approach. Therefore, from the current experiments one cannot infer about the rate constant of the CH_3O_2 self-reaction. But it is clear that recent

research using more selective detection methods for peroxy radicals, compared to UV absorption, have challenged long-standing results on even the simplest peroxy radicals, and more research is necessary to better understand their reactivity under low NO_x conditions.

4.3 Conclusion

Only one literature has reported on the rate constant measurement of the cross reaction of $C_2H_5O_2$ and CH_3O_2, where UV absorption spectroscopy was employed to measure the total absorption kinetics of reactants and products at 235 nm a fit of these data was used to obtain the rate constant of the cross reaction of $C_2H_5O_2$ with CH_3O_2. However, the UV absorption spectra of $C_2H_5O_2$ and CH_3O_2 are overlapping and their absorption cross sections are close to each other and thus UV absorption spectroscopy cannot distinguish between the two peroxy radicals and cannot selectively detect the product HO_2. Therefore, fitting the only total absorption kinetics of the reactant and product may introduce significant errors and does not allow obtaining the branching ratio.

In this chapter, the rate constant for the cross reaction of the two most simple and abundant peroxy radicals, CH_3O_2 and $C_2H_5O_2$, has been determined by following their concentration-time profiles in their respective $\tilde{A}$-$\tilde{X}$ electronic transition. A good selectivity has been obtained by working under excess of $C_2H_5O_2$ and by monitoring CH_3O_2 radicals at 7488.13 cm^{-1} and $C_2H_5O_2$ radicals at 7601.66 cm^{-1}. A rate constant for the cross reaction of (3.8±1.0) $\times 10^{-13}$ cm^3s^{-1} has been obtained, and with the detection of HO_2, a yield for the radical channel of 0.40 ± 0.20 has also been obtained. The present rate constant is nearly two times faster than the only earlier value, but in excellent agreement with an estimation based on the mean geometric rule.

Due to the slow rate constant of the cross reaction of peroxy radicals, high concentration of Cl was needed in the experiment to have obvious kinetic decays of related peroxy radicals. Due to the absorption of CH_4 and C_2H_6 in the near-infrared

region, we were not able to add CH_4 and C_2H_6 be in enough excess, which made participation of the reactions between $C_2H_5O_2$/CH_3O_2 and Cl unavoidable. Therefore, separate experiments were conducted to get the rate constant and branching ratio of the reaction of Cl with $C_2H_5O_2$/CH_3O_2. The obtained mechanism of Cl + $C_2H_5O_2$/CH_3O_2 has been included in the reaction model of $C_2H_5O_2$ + CH_3O_2 reaction.

This work shows again, that the chemistry of peroxy radicals under low NO conditions is still not well understood and more work is needed to improve the knowledge.

Chapter 5. Product measurement of the oxidation reaction of CH_3CHO

Acetaldehyde is one of the stable products of the self-reaction of $C_2H_5O_2$, and it is also the key intermediate in the atmospheric degradations of many VOCs in the troposphere [58]. In clean atmosphere with low NOx, the oxidation reaction of ethane C_2H_6 is the most important photochemical source for CH_3CHO. The oxidation reaction of C_2H_6 in the atmosphere by OH generates the $C_2H_5O_2$ peroxy radical, and the self-reaction of $C_2H_5O_2$ and its cross reaction with CH_3O_2 all generate CH_3CHO. In this chapter, a flowtube reactor combined with synchrotron radiation photoelectron photoion coincidence spectroscopy was applied to study the products of the oxidation reaction of CH_3CHO.

The reaction of F/Cl with CH_3CHO gives two isomer radicals CH_3CO/CH_2CHO. In the F + CH_3CHO reaction, the branching ratio of the two radicals is close, while the branching ratio for the CH_2CHO radical in the reaction Cl + CH_3CHO is thought to be negligible, confirmed by two indirect measurements of the branching ratio for CH_2CHO in Cl + CH_3CHO reaction of 7% [64] and 1% [65]. Therefore, comparing the measurements of both radicals for both, F + CH_3CHO and Cl + CH_3CHO, should allow to get information about the branching ratio of CH_3CO/CH_2CHO in the Cl + CH_3CHO reaction relative to F + CH_3CHO. In the product measurements of the F + CH_3CHO reaction with synchrotron radiation photoelectron photoion coincidence spectroscopy, high signal-to-noise ratios of the two isomer radicals can be obtained simultaneously and theoretical calculations can be used to determine the ionization energies of both radicals. After this, oxygen was added in the flowtube to further study the products of the oxidation reaction of CH_3CO/CH_2CHO.

As the dissociative photoionization of CH_3CHO was thought to give CH_3CO^+, to characterize the influence of the possible fragmentation following ionization of the

precursor to the signal at m/z = 43 during the detection of CH_3CO and CH_2CHO radical, initial experiments were carried out to measure the photoionization and dissociative photoionization of CH_3CHO. To do so, only CH_3CHO was added into the injector of the reactor and the spectrum was measured without discharge.

5.1 Photoionization and dissociative photoionization of CH_3CHO

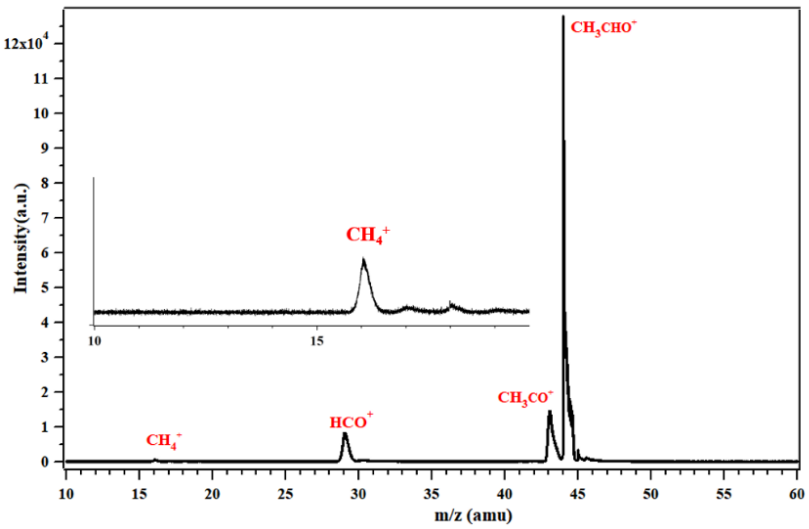

Figure 5.1 Synchrotron photoionization mass spectrum in 10.0-13.8eV energy range.

The synchrotron radiation photoionization TOF mass spectrum of CH_3CHO has been recorded in the 10.0-13.8eV photon energy range and is presented in Figure 5.1. Several mass peaks can be observed and have been assigned within a mass range of m/z=10 - 60. The most intense signal at m/z=44 is assigned to CH_3CHO, the signal at m/z=43 is CH_3CO^+, m/z=29 is assigned to HCO^+, and m/z=16 is CH_4^+. Besides this, the small signal at m/z=45 is the isotopic $^{13}CH_3CHO$, the relative signal intensity corresponding to its natural abundance. Except the signal at 44 and 45, all other peaks are attributed to fragments of CH_3CHO: as the width of TOF peaks is proportional to the square root of the ion translational energy along the detection axis, narrow peaks correspond to parent ions formed by direct ionization of the neutral molecular beam,

while broad peaks originate from fragment ions formed by dissociative ionization. It clearly shows in the integrated mass spectra of Figure 5.1, that m/z=44 and 45 are narrow, while the other peaks are broad.

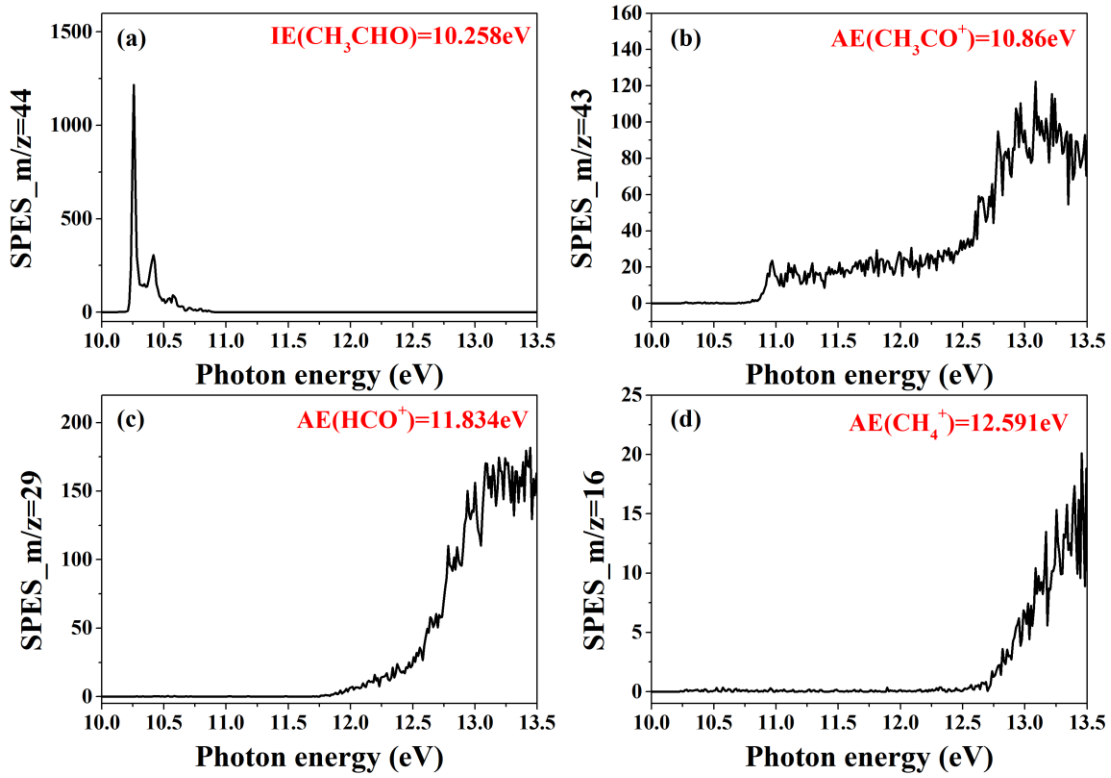

Figure 5.2 Mass selected slow photoelectron spectra (SPES) corresponding to (a) CH_3CHO^+ parent ion and fragments (b) CH_3CO^+, (c) HCO^+, (d) CH_4^+ in experiments with only CH_3CHO.

The SPES of CH_3CHO shown in Figure 5.2 (a) is structured and two obvious peaks were observed at hν =10.258eV and 10.415eV. 10.258 eV corresponds to the vertical ionization energy (VIE) and agrees well with the literature (10.24 eV [149]). The peak at 10.415 eV possibly corresponds to the vibration of CH_3CHO^+. The SPES of the other signals are rather unstructured and only the onsets of ionization are obtained. We can see that the appearance energies (AE) of the fragments are AE (HCO^+) = 11.834eV (literature value: 11.79eV), AE (CH_3CO^+) = 10.86eV (literature value: 10.82eV), AE (CH_4^+) = 12.591Ev (literature value: 12.61eV), all measurements agree well with literature results [150].

5.2 Products measurements of the oxidation reaction of F + CH_3CHO

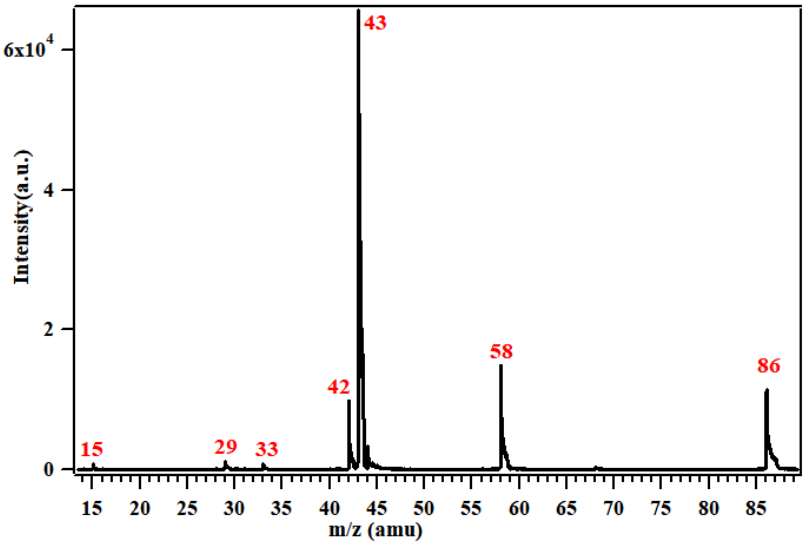

Figure 5.3 Synchrotron photoionization mass spectrum summed over 7.1-10.1eV energy range in F + CH_3CHO reaction.

Figure 5.3 shows the integrated mass spectrum obtained in F + CH_3CHO reaction and that has been recorded in the 7.1-10.1eV energy range. In this range CH_3CHO is not ionized and thus the signals obtained are only the products of F + CH_3CHO reaction and the secondary products. All peaks are located in the range of m/z = 14 – 90. The most intense peak at m/z = 43 corresponds to C_2H_3O, then the second group of peaks with similar intensity are m/z = 42, which is assigned to C_2H_2O, m/z = 58 assigned to C_3H_6O, and m/z = 86 assigned to $(C_2H_3O)_2$. Two other relatively weak signals at m/z = 15 and at m/z = 29 are assigned to CH_3 and HCO, respectively. Finally, the peak at m/z = 33 is attributed to CH_2F. With only the MS of the products measured, one can only get information on the molecular formula and can't distinguish isomers, therefore mass selected slow photoelectron spectra (SPES) were measured to get the structure information of the products.

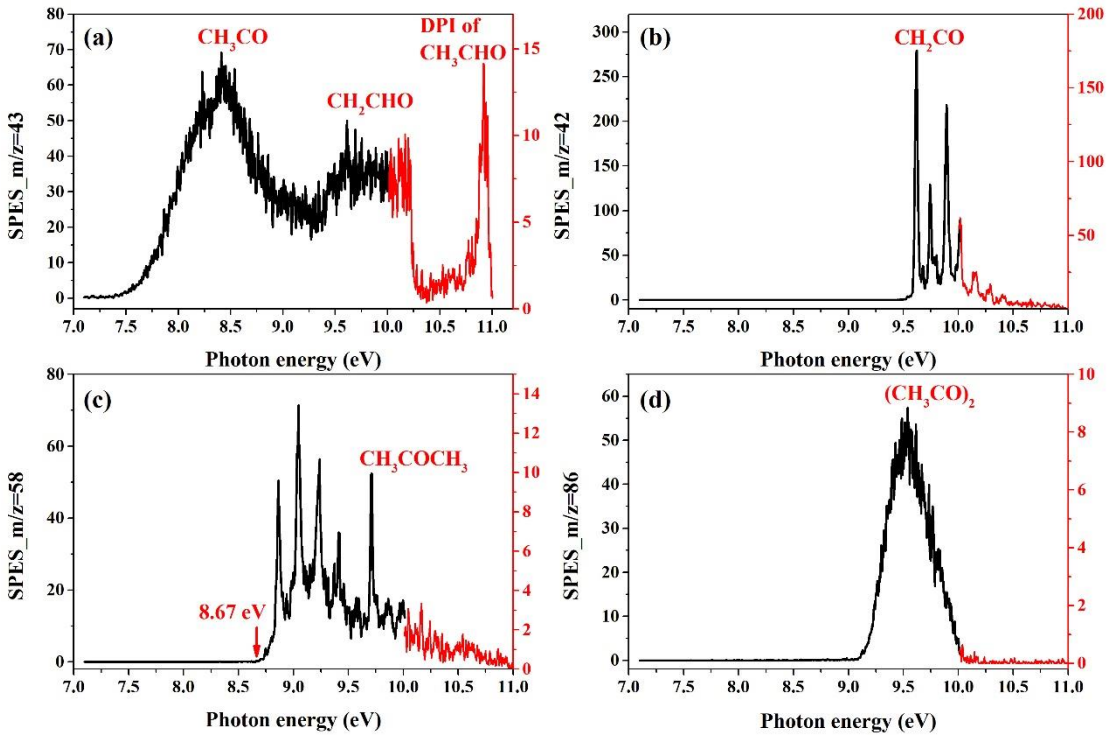

Figure 5.4 Mass selected slow photoelectron spectra (SPES) corresponding to (a) m/z = 43 (b) m/z = 42 (c) m/z = 58 (d) m/z = 86 in F + CH_3CHO reaction.

The measured mass selected SPES corresponding to the signals shown in Figure 5.3 are shown in Figure 5.4 for the four peaks at (a) m/z = 43, C_2H_3O, (b) m/z = 42, C_2H_2O, (c) m/z = 58, C_3H_6O and (d) m/z = 86, $(C_2H_3O)_2$. Only the SPES of CH_2CO and C_3H_6O are structured, C_2H_3O and $(C_2H_3O)_2$ are both broad and unstructured. There are three bulges in the spectrum of m/z = 43, the first one is assigned to the CH_3CO radical while the second one should be the CH_2CHO radical. The peak at the highest energy is the fragment of CH_3CHO. The calculation result shows that the geometry of the neutral CH_3CO is bent while the CH_3CO^+ is liner which induces a bad Franck Condon (FC) factor and a very broad photoelectron spectrum as observed in Figure 5.4 (a). Table 5.1 shows the computed first adiabatic ionization energies and vertical ionization energies (VIEs) as well as experimental values found in the literature [66] and the measured values in the current work. However, we can see that the calculated AIEs of CH_3CO with different levels of theory varied in a wide range from 6.52-7.14 eV, and the only experimental value is at 7.21±0.05 eV. The onset of the first bulges

observed in Figure 5.4 (a) is roughly at 7.3 eV, which is a little bit higher than the calculated and measured values found in literature [66]. The maximum signal at 8.4 eV corresponds to the VIE of CH_3CO, which agrees well with both calculated (G1/G2) and measured values in literature [66]. However, as shown in Figure 5.4 (a), even though CH_2CHO is observed, it is overlapping with CH_3CO and thus it is difficult to get its AIE value, and as there is no structure of its SPES, it is also difficult to get the VIE value with only experimental results. In addition, the calculated AIEs and VIEs in literature varied in a large range, therefore, high level theoretical calculations are needed to simulate the measured SPES of CH_3CO and CH_2CHO to further determine scanty information.

Table 5.1 Computed first adiabatic ionization energies (AIEs) of CH_3CO and CH_2CHO at different levels of the theory using a 6-311++G** basis set from literature [66] and measured values in literature and this measurement.

levels of the theory	CH_3CO		CH_2CHO	
（6-311++G** basis set）	AIE	VIE	AIE	VIE
ΔSCF /eV	6.52	8.23	9.77	10.06
ΔMP2 (full) /eV	6.60	8.00	9.79	9.92
ΔB3LYP /eV	7.14	8.66	9.35	10.52
ΔB3PW91 /eV	7.09	8.62	9.25	10.59
G1/G2 eV	6.89/6.66	8.38/8.39	8.98/8.97	10.23
Exp./eV	7.21 ± 0.05	8.39 ± 0.05	--	--
Exp./eV (this work)	7.37 ± 0.005	8.4 ± 0.005	--	--

Besides the radicals CH_3CO and CH_2CHO, as mentioned above, there are also other products observed. Without oxygen, the main reactions of the radical CH_3CO and CH_2CHO are their self-reactions,

$$R + R \rightarrow CH_2CO + CH_3CHO \quad (5.1.a)$$

$$R + R \rightarrow (CH_3CO)_2 / (CH_2CHO)_2 / (CH_3COCH_2CHO) \quad (5.1.b)$$

CH_3CO can also react with CH_3CHO to give CH_3COCH_3 and HCO radical,

$$CH_3CO + CH_3CHO \rightarrow CH_3COCH_3 + HCO \quad (5.2)$$

The products of its self-reaction are CH_2CO at m/z = 42, CH_3CHO at m/z = 44 and the dimer product of the two radicals at m/z = 86. Figure 5.4 (b) shows the SPES of m/z = 42, the first peak at 9.622 eV corresponding to the AIE value of the $\tilde{X}1^2B_2$ ionic state of CH_2CO^+, the other peaks are the vibrational frequencies of CH_2CHO^+, which agrees well with literature results [151]. The dimer products $(CH_3CO)_2$/$(CH_2CHO)_2$ are formed in the self-reaction of CH_3CO and CH_2CHO radicals, and another one is CH_3COCH_2CHO formed in the cross reaction between the two radicals. The SPES of m/z = 86 is shown in Figure 5.4 (d). The only known information for a molecule of m/z = 86 is $CH_3COCOCH_3$, 2,3-butanedione, with an AIE of 9.23 ± 0.03 eV [150]. This is 0.1 eV above the value measured as the first onset of m/z = 86 located at hν = 9.1 eV. The literature value for the VIE of 2,3-butanedione is 9.57 ± 0.05 eV [150], in good agreement with the energy with maximum intensity in our experiments at 9.57 eV. Therefore, the signal at m/z = 86 is assigned to 2,3-butanedione, as there are currently no information for the ionization energy for other products, it is not possible to determine their contribution to the TPES of m/z = 86.

The reaction between CH_3CO and CH_3CHO gives CH_3COCH_3 (acetone, m/z = 58) and HCO (formyl radical, m/z = 29) and the reaction between CH_3 and CH_3CO also gives CH_3COCH_3. The dissociative photoionization of CH_3COCH_3 also gives $C_2H_3O^+$ at m/z = 43, and the appearance energy for the fragment is at 10.42 eV [150] as shown in Figure 5.4 (a), its signal starts at 10.42 eV in between the second and third bulges. The SPES of m/z=58 shows in Figure 5.4 (c), the well know ionization energy of acetone is at 9.7 eV, corresponding to the last intense peak. A possible explanation for other peaks will be described in the next section.

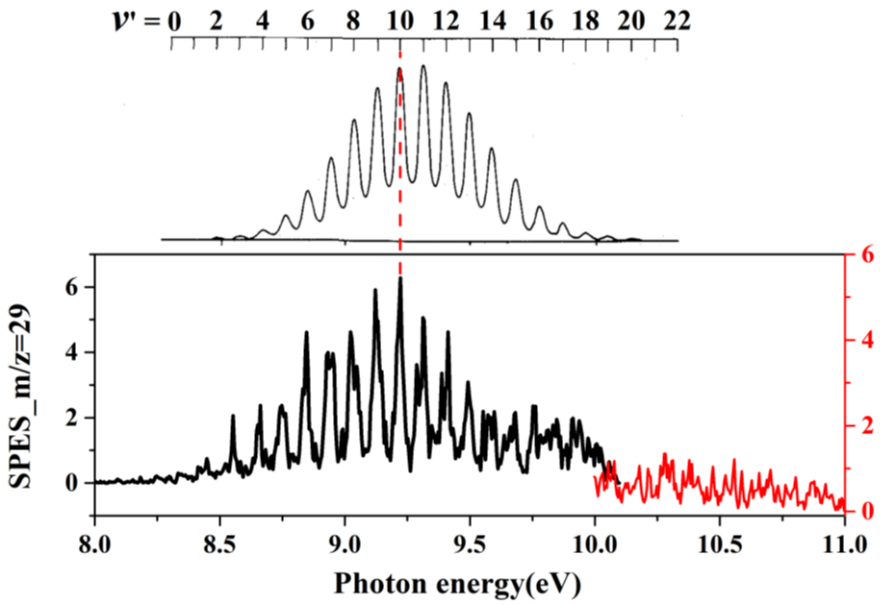

Figure 5.5 (upper graph) The computed vibrational envelope of the first band of HCO [152]. Mass selected slow photoelectron spectra of HCO obtained in F + CH_3CHO reaction

Figure 5.5 shows the measured SPES of the HCO radical in the F + CH_3CHO reaction and the calculated vibrational envelope of HCO^+ obtained from literature [152]. We can see that the spectrum obtained in our measurement agrees well with the computed vibrational envelope. The peaks distributed between 8.5 and 10.0 eV correspond to the ionization energies of the neutral radicals HCO in the X^2A' state ($v'' = 0$) state to different vibrational excited ion states $HCO^+X^1A'(v' = 3-18)$, respectively.

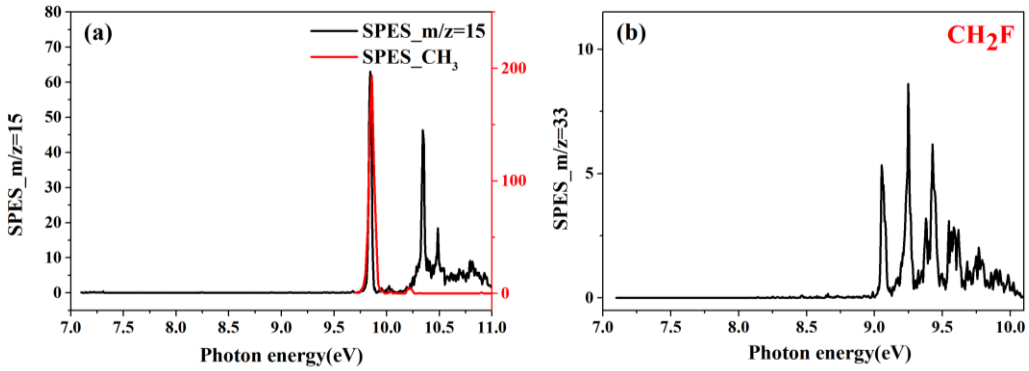

Figure 5.6 Mass selected slow photoelectron spectra obtained in F + CH_3CHO reaction: (a) CH_3, (b) CH_2F.

Figure 5.6 shows the SPES of the secondary products in F + CH_3CHO reaction: (a) CH_3 and (b) CH_2F. The first peak at m/z = 15 agree well with the TPES of CH_3 in literature [153] and is attributed to the radical CH_3 even if the reaction path for leading to this radical is not clear. The second peak at 10.34 eV may originate from the dissociative photoionization of CH_3CO, because the dissociative photoionization of stable species present in the reaction system (CH_3CHO, acetone or 2,3-butanedione) do not lead to a CH_3 fragment at such low photon energies, as direct measurement have shown: the AE of CH_3^+ from acetone is at 15.61 eV, and from 2,3-butanedione is at 14.0 eV. Theory calculations are needed to further clarify the origin of this peak.

CH_2F, fluoromethyl radical, is formed in the reaction of F + CH_2CHO

$$F + CH_2CHO \rightarrow CH_2F + HCO \tag{5.3}$$

According to literature results, the first and second peaks of the SPES of CH_2F corresponds to its AIE and VIE at 9.04 and 9.22 eV [150]. And the reaction of F with CH_2CHO also gives HCO radical.

5.3 Measurement of branching ratio of the isomer radical in Cl + CH_3CHO reaction

The concentration of Cl-atoms following discharge of Cl_2 is rather low due inefficient discharge of Cl_2, but also due to the recombination of the produced Cl atoms on the reactor walls. Therefore, it is difficult to get radical concentrations high enough for a good signal/noise ratio. A more efficient way to produce Cl-atoms is by discharging F_2 to first give F atoms and then add Cl_2 for F-atoms reacting with Cl_2 to produce Cl and ClF.

$$F + Cl_2 \rightarrow Cl + ClF \tag{5.4}$$

Although this reaction is very fast with a rate constant of 1.6×10^{-10} cm^3 s^{-1} [150], high concentrations of Cl_2 need to be added to avoid that any F-atoms are left when the hydrocarbon is added. Otherwise, a mixture of Cl and F atoms is present and is would be impossible to get the branching ratio of the two radicals for Cl + CH_3CHO reaction. With this idea, a first experiment was performed and the result is shown in Figure 5.7 (a). Surprisingly, the result is not as we expected, because the signal intensity for CH_2CHO is higher than CH_3CO which is the opposite compared to literature, which always expects that CH_3CO should be the major channel. And even if the Cl_2 is not enough and some F-atoms are still present, it is not expected that CH_2CHO in so much in excess. A simple calculation is applied to estimate the branching ratio of CH_2CHO in Figure 5.7 (a), for F + CH_3CHO shown in Figure 5.4 (a), the known branching ratio is:

$$B(CH_3CO / CH_2CHO) = 65 / 35 = 1.86$$

and the measured signal intensity ratio for the maximum value of two bulges is:

$$S(CH_3CO / CH_2CHO) = 65 / 50 = 1.3$$

For Cl + CH_3CHO in Figure 5.7 (a),

$$S'(CH_3CO/CH_2CHO) = 10/55 = 0.182$$

thus the calculated ratio for channel CH_3CO and CH_2CHO in Cl + CH_3CHO reaction is:

$$B'(CH_3CO/CH_2CHO) = 0.26$$

the branching ratio of CH_2CHO in Figure 5.7 is up to 79.4%.

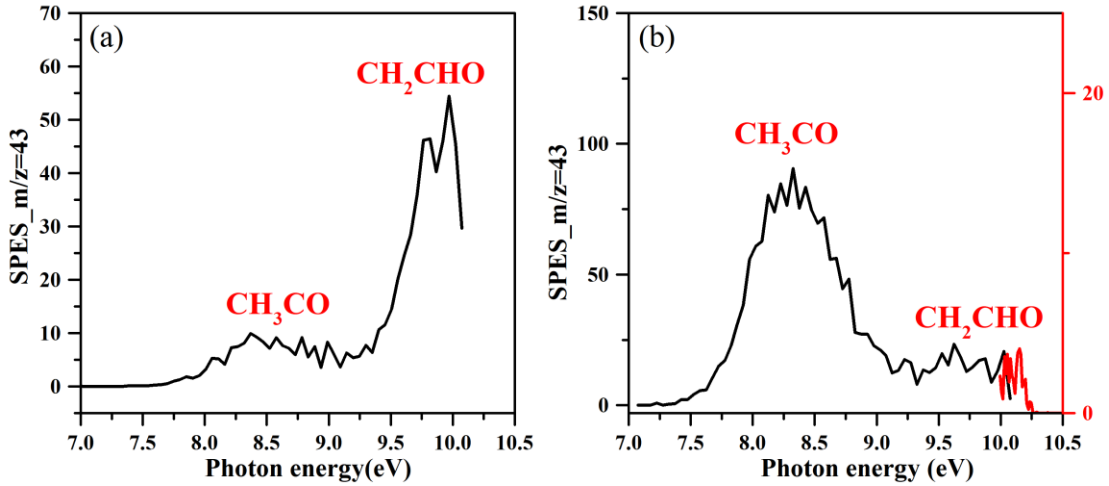

Figure 5.7 Mass selected slow photoelectron corresponds to m/z = 43 in Cl + CH_3CHO reaction (a) first measurements, (b) second measurement.

The possible reasons that lead to Figure 5.7 (a) may be: (1) experimental error. For example, the change of the power of the microwave discharger leads to the change of the concentration of Cl, and the Cl concentration is low in 7.5-9 eV. (2) the expected branching ratio of CH_2CHO in Cl + CH_3CHO reaction is wrong, CH_2CHO should be the major product. (3) unknown reaction. To further confirm our results, another experiment under the same condition was carried out, and the results are shown in Figure 5.7 (b), which is at this time very different from Figure 5.7 (a). Apparently, in this experiment we obtained the expected result, i.e., CH_3CO is in excess and CH_2CHO is the minor radical. Doing the same calculation as above with the measured signal intensity ratio is:

$$S''(CH_3CO/CH_2CHO) = 85/20 = 4.25$$

and then:

$$B"(CH_3CO / CH_2CHO) = 6.08$$

the branching ratio for the CH_2CHO channel in Figure 5.7 (b) is 14%. This branching ratio needs to be taken as the upper limit, because it cannot be fully excluded that some F-atoms were still present and lead to the formation of CH_2CHO. Due to the contradictory of the two experimental results, more experiments will be needed to further confirm the branching ratio.

5.3.1 Products measurement of Cl + CH_3CHO + O_2 reaction with CRDS

To get more information about the produced radical in the reaction of Cl + CH_3CHO, experiments were carried out with the CRDS technique in Lille. Indeed, the radical obtained from the reaction of Cl + CH_3CHO + O_2 has a spectrum in the near infrared range spreading over more than 1000 cm^{-1}. It is known that the strong absorption around 6500 cm^{-1} is due to the $CH_3C(O)O_2$ radical [83], but the weak absorption observed around 7000 – 7500 cm^{-1} [14] has not yet been assigned and might as well originate from the O_2CH_2CHO radical, in the same range of A-X transition of other alkylperoxy radicals such as CH_3O_2 [83, 94]. Therefore, the idea was to produce the $CH_3C(O)O_2$ radical from different precursors and measure its absorption spectrum over a large wavelength range to verify if the relative absorption in the different wavelength ranges depends on the precursor. Spectra have been measured following the reaction Cl + CH_3CHO + O_2 (red line in Figure 5.8) and have been compared with the spectrum obtained following the 351 nm photolysis of biacetyl $(CH_3CO)_2$ in the presence of O_2. The photolysis of $(CH_3CO)_2$ can only give the CH_3CO radical thus only $CH_3C(O)O_2$ is obtained. If Cl + CH_3CHO is also mainly producing the CH_3CO radical, then the measured spectra from both precursors should be same. However, if CH_2CHO is a major product from the reaction Cl + CH_3CHO, then the relative intensity in different wavelength ranges of the spectrum should show differences, as the absorption

of O_2CH_2CHO radical could be expected between 7000 – 7500 cm^{-1}.

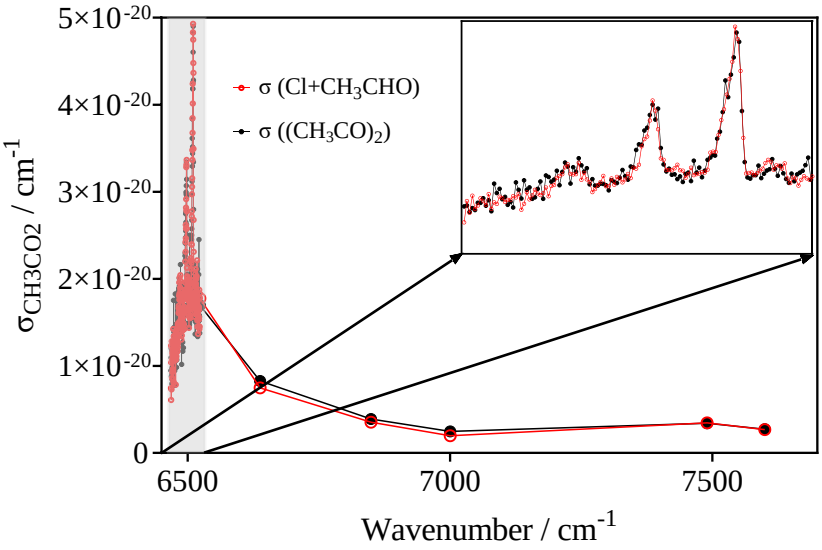

Figure 5.8 Absorption spectrum of RO_2 radicals obtained in the experiments of Cl + CH_3CHO (red) and following the photolysis of biacetyl at 351 nm (black), both experiments carried out in 100 Torr O_2.

As shown in Figure 5.8 the measured spectra in both experiments are the same over the full wavelength range. Therefore, we conclude that the major radical in the Cl + CH_3CHO reaction is CH_3CO, and formation of CH_2CHO is a minor path at the most. The CRDS measurements agree well with the results in Figure 5.7 (b), the CH_2CHO is a very minor product and the upper limit will be around 14%. Why there was a different result for our first measurements of Cl + CH_3CHO with CH_2CHO in excess is not clear and might be due to changing discharge efficiency over time. Although this experiment proves that the main product of the Cl + CH_3CHO reaction is CH_3CO, it is still uncertain whether the reason for the results in Figure 5.7 (a) is due to experimental errors or unknown reaction. Therefore, the first experimental results were not directly deleted, but retained, hoping to have the opportunity to conduct further research in the future.

5.3.2 Enol products measurements of F/Cl + CH_3CHO reaction

Since literature [154] reported the observation of the product enol during combustion, enol chemistry has attracted increasing attention from researchers. Among them, the product vinyl alcohol (CH_2CHOH, vinyl alcohol, VA) observed during thermal decomposition [155, 156] and photochemistry [157] process were believed to originate from the keto-enol tautomerization of acetaldehyde. Investigating the source of CH_2CHOH observed in the combustion can help to reveal the mechanism of hydrocarbon oxidation [154]. In addition, the oxidation of CH_2CHOH with OH in the atmosphere could leads to the formation of atmospheric organic acid [157, 158]. All the observed tautomerization processes of CH_3CHO to CH_2CHOH are under conditions of external energy input, like combustion, thermal decomposition and photochemistry, this is because the barrier between CH_3CHO and CH_2CHOH transition is high, as shown in Figure 5.9: CH_3CHO is more stable than CH_2CHOH, therefore only when CH_3CHO is formed with excess energy, tautomerization to CH_2CHOH can take place. VA can exist in two forms, syn and anti, whereby the syn rotamer has lower energy than the anti-rotamer. Their adiabatic ionization energies are IE = 9.17 eV(syn), and 9.3eV(anti) [159].

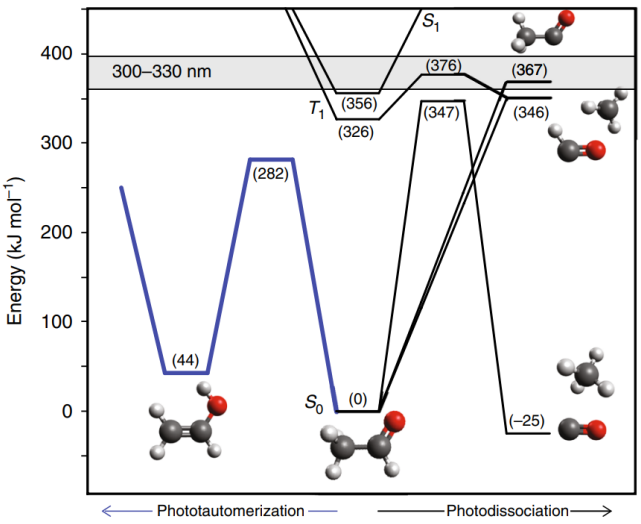

Figure 5.9 Calculated process of phototautomerization of CH_3CHO to CH_2CHOH [157].

Besides the importance of CH_2CHOH in combustion systems and photochemistry, it is also important in interstellar medium as an transient chemical intermediates [160, 161]. It was even observed in interstellar medium, the mechanism which leads to the formation of CH_2CHOH is still not clear, and researchers are still looking for revealing its mechanism [160-163].

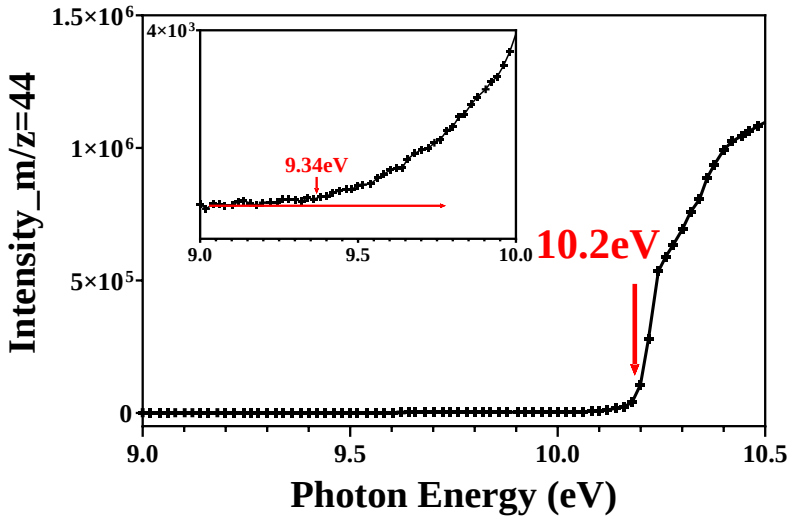

Figure 5.10 Photoionization efficiency spectra for C_2H_4O (m/z=44).

In our Cl + CH_3CHO measurements, the tautomerization process of CH_3CHO was observed, as shown in Figure 5.10. The well-known ionization energies for CH_3CHO at m/z = 44 is at 10.2 eV, while in our measured PIE curves, the signal starts at 9.34 eV and this is assigned as vinyl alcohol, CH_2CHOH.

In addition to the tautomerism of CH_3CHO-CH_2CHOH, there are also ketone-enol tautomerism, such as acetone CH_3COCH_3-propenol CH_2COHCH_3 tautomerization [155]. As shown in Figure 5.4 (c), except for the ionization energy of acetone at 9.71 eV, the signal of m/z = 58 starts at 8.67 eV and corresponds to propene-2-ol, CH_2COHCH_3, and the other peaks between 9.0 and 9.5 eV may be the vibrational structure of the $CH_2COHCH_3^+$, but further theoretical calculations are still needed to verify its structural information. The calculated potential barrier for CH_3COCH_3-CH_2COHCH_3 tautomerization in the literature is 288.28 kJ/mol [164]. Therefore, both CH_3CHO-CH_2CHOH and CH_3COCH_3-CH_2COHCH_3 tautomerization processes

require external energy for crossing the reaction barrier. However, in our measurements, there were no such sources as heat, combustion, or light radiation, so there may be other reasons leading to the tautomerism of CH_3CHO and CH_3COCH_3, but currently it is not known.

5.3.3 Products measurements of F + CH_3CHO + O_2 reaction.

After the addition of O_2, CH_3CO and CH_2CHO generated by F + CH_3CHO undergo oxidation reaction. The oxidation reaction of CH_3CO has three product channels: $CH_3C(O)O_2$ (m/z = 75), $C_2H_2O_2$ (α- Lactone, m/z = 58) + OH, CH_2CO (m/z = 42) + HO_2. The calculated potential energy surface [69] shows that the transition state of forming the products CH_2CO + HO_2 is higher than others and is considered to be a minor path. $C_2H_2O_2$ is a three-membered ring structure and is the energy favoured channel, its co-product is the OH radical, which has been detected [69, 165-167]. Calculations show that almost 60% of the formed $C_2H_2O_2$ contains excess energy above the dissociation barrier and undergoes ring opening giving the products HCHO and CO [168].

In addition, there are also secondary reactions, such as the self- and cross-reaction of the peroxy radical. The self-reaction of $CH_3C(O)O_2$ gives $CH_3C(O)O$, which is unstable and rapidly decomposes into CH_3 and CO_2,

$$CH_3COO_2 + CH_3COO_2 \rightarrow CH_3COO + CH_3COO + O_2 \quad (5.5)$$

$$CH_3COO \rightarrow CH_3 + COO \quad (5.6)$$

The oxidation of CH_3 gives CH_3O_2,

$$CH_3 + O_2 \rightarrow CH_3O_2 \quad (5.7)$$

CH_3O_2 can also react with $CH_3C(O)O_2$,

$$CH_3O_2 + CH_3COO_2 \rightarrow CH_3O + CH_3COO + O_2 \quad (5.8.a)$$

$$CH_3O_2 + CH_3COO_2 \rightarrow CH_3COOH + HCHO + O_2 \quad (5.8.b)$$

and gives the radical products CH_3O and $CH_3C(O)O$ and stable products $CH_3C(O)OH$ and HCHO. CH_3O further oxidized to HCHO and HO_2, HO_2 continue to react with CH_3O_2 and $CH_3C(O)O_2$ to give CH_3OOH and $CH_3C(O)OOH$.

The other radical produced in F + CH_3CHO reaction is CH_2CHO, its oxidation gives O_2CH_2CHO and HCHO + OH + CO (the preferred channel according to theoretical calculation [169]).

As there is no information about the ionization energy of the peroxy radicals, theoretical calculations were carried out to get the information, as shown in Figure 5.11 and Figure 5.12. For $CH_3C(O)O_2$, both anti-and syn-structure, there are singlet and triplet states of the corresponding ion $CH_3C(O)O_2^+$, but all structures of the ions are not stable and will decompose to CH_3CO^+ and molecular O_2.

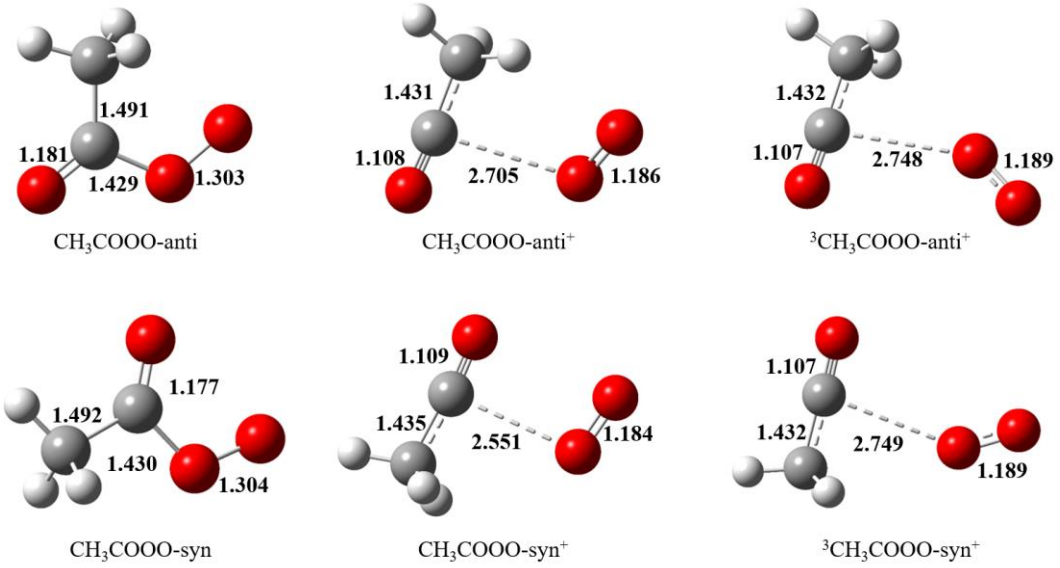

Figure 5.11 Optimized structures of CH_3COO_2 peroxy radical (M06-2x/aug-cc-pvtz) and the calculated AIE values (CCSD(t)-F12A/aug-cc-pvtz and M06-2x/aug-cc-pvtz).

For the O_2CH_2CHO radical, there are also two structures, the singlet state of syn-O_2CH_2CHO ion is stable while the other three ions are not stable and will decompose to CH_2CHO^+ ions and molecular O_2, while the singlet anti-$O_2CH_2CHO^+$ will decompose to HCO^+ and CH_2O_2 (Criegee) or $CH_2O_2^+$ with HCO radical, but the two methods applied give two values with big difference of 0.25 eV, the uncertainty in

computed results will make the assignment of these species difficult. For the only stable ion its ionization energy is calculated to be 9.94 eV and 10.15 eV. The calculated ionization energies for $CH_3C(O)O_2$ and O_2CH_2CHO are shown in Table 5.2.

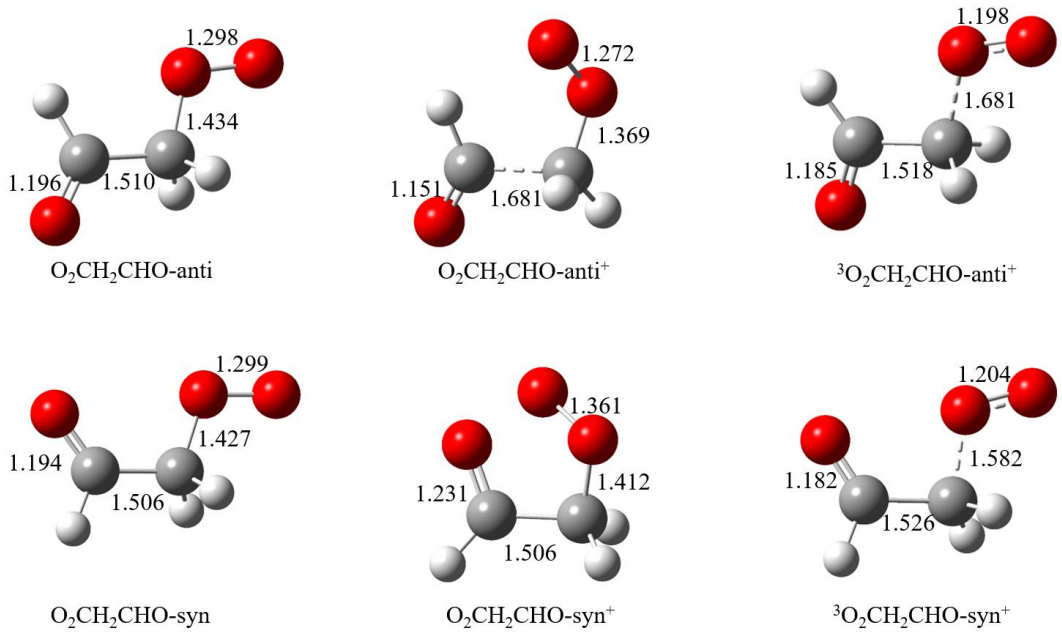

Figure 5.12 Optimized structures of O_2CH_2CHO peroxy radical (M06-2x/aug-cc-pvtz) and the calculated AIE values (CCSD(t)-F12A/aug-cc-pvtz and M06-2x/aug-cc-pvtz).

Table 5.2 The calculated ionization energies for CH_3COO_2 and O_2CH_2CHO.

	IE (eV)	
	CCSD(t)-F12A/aug-cc-pvtz	M06-2x/aug-cc-pvtz
$CH_3C(O)O_2$-anti$^+$	9.60	9.94
$^3CH_3C(O)O_2$-anti$^+$	8.38	8.41
$CH_3C(O)O_2$-syn$^+$	9.57	9.89
$^3CH_3C(O)O2$-syn+	8.35	8.38
O_2CH_2CHO-anti$^+$	10.05	10.30
$^3O_2CH_2CHO$-anti$^+$	10.42	10.42
O_2CH_2CHO-syn$^+$	9.94	10.15
$^3O_2CH_2CHO$-syn+	10.34	10.30

Although Cl with CH_3CHO is much better for studying the products of CH_3CO with O_2 to get the information of $C_2H_2O_2$, the results are not shown as the measured results for Cl + CH_3CHO + O_2 were of poor quality. The measured mass spectrum for F + CH_3CHO + O_2 is presented in Figure 5.13 with both primary and secondary products. But as expected, no signal at m/z = 75 corresponding to the two RO_2 radicals is observed, even though one of the ion structures is calculated to be stable. The signals are assigned as follows: m/z=15 (CH_3), m/z=29 (HCO), m/z=30 (HCHO), m/z=42 (CH_2CO), m/z=43 (CH_3CO^+), m/z=58 (c-CH_2OCO or other product). HCHO at m/z=30 is formed directly in the reaction of CH_2CHO + O_2 and also as secondary products in the subsequent reactions of the peroxy radicals. CH_2CO is formed in the reaction of CH_3CO with O_2.

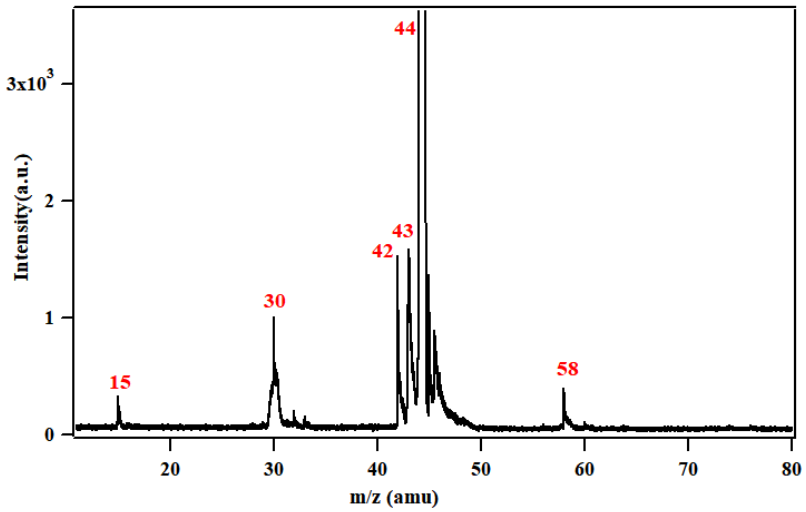

Figure 5.13 Synchrotron photoionization mass spectrum in 10.0-12 eV energy range in F + CH_3CHO + O_2 reaction.

The SPES spectra for specific products are shown in Figure 5.14, however no signal at m/z=58 was observed, and the calculated results show that the formed ion CH_2OCO^+ is prompt to dissociate to H_2CO^+ + CO above 10.4 eV and to HCO^+ + HCO above 10.85eV.

$$CH_2OCO^+ \rightarrow CH_2O^+ + CO \qquad (5.1)$$

$$CH_2OCO^+ \rightarrow HCO^+ + HCO \quad (5.2)$$

The broad spectrum of CH_2O includes two parts with the first peak corresponds to HCHO and the second one above 11.1 eV is the fragment CH_2O^+ which is formed may be by the dissociative photoionization of CH_2OCO. For the HCO^+ the signal starts at 10.85 eV, probably also from CH_2OCO. For m/z=43 corresponding to CH_3CO^+, it can be the signature of the peroxy radicals (there is no signal below 10.7 eV showing full consummation of CH_3CO/CH_2CHO by O_2). The theoretical calculation results show that the appearance energy of CH_3CO^+ of $CH_3C(O)O_2^+$ is less than 10.5 eV, but as shown in Figure 5.14, there is no signal when the energy is below 10.5 eV, while the signal at 10.85 eV is the fragment of CH_3CHO^+. Therefore, the results of this experiment were very unexpected, as our group has conducted similar experiments on various alkyl peroxy radicals. Although the ions of peroxy radicals are normally unstable and cannot be detected, their fragments have been successfully detected and their appearance energies are obtained. While the current experiment applied the same experimental methods and techniques, but neither peroxy radicals nor fragments were observed. Currently, the reason for this result cannot be given, possibly due to the poor SPES spectrum of the product.

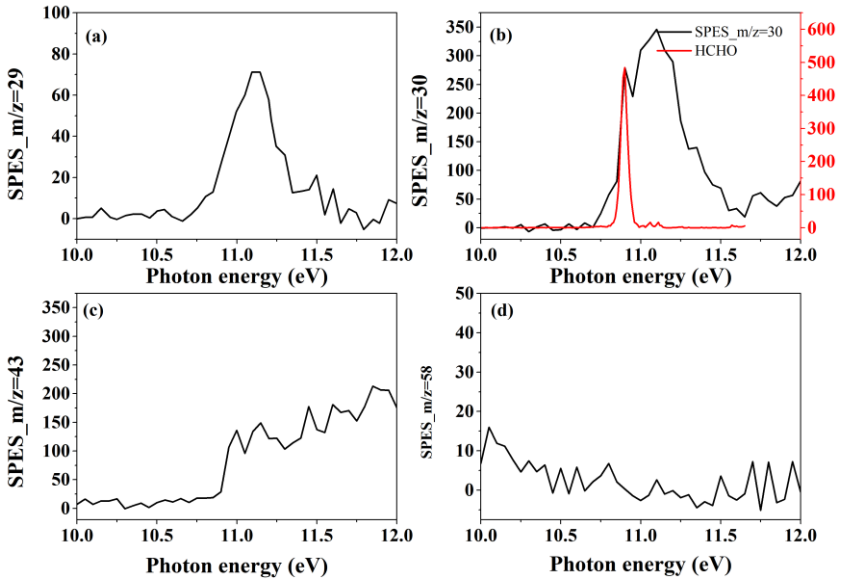

Figure 5.14 Mass selected slow photoelectron spectra corresponding to m/z = (a) 29, (b) 30, (c) 43, (d) 58 in F + CH_3CHO + O_2 reaction

5.4 Conclusion

Microwave discharge flowtube combined with synchrotron radiation photoelectron photoion coincidence spectroscopy were used to measure the products from the oxidation reaction of CH_3CHO. The reaction of F/Cl with CH_3CHO produces two isomer radicals, CH_3CO and CH_2CHO. Two radicals were detected in the F/Cl + CH_3CHO experiment, and the adiabatic ionization energy and the vertical ionization energy of CH_3CO were obtained. However, the SPES of CH_2CHO and CH_3CO are partially overlapping together, thus can't get the AIE value of CH_2CHO only from the experimental spectrum, and as there is no structure of its SPES, it is also impossible to directly get its VIE value. Therefore, further theoretical calculations are needed to separate the two radicals and then to get more information. In addition, products (CH_2CO, $(CH_3CO)_2$) from the self-reaction of the CH_3CO radical and products ($CH_3C(O)CH_3$, HCO, CH_3, CH_2F) from the secondary reactions in F + CH_3CHO reaction were determined. The upper limit (14%) of the branching ratio of CH_2CHO radicals in the reaction of Cl with CH_3CHO was determined. And the tautomerization processes of CH_3CHO-CH_2CHOH and $CH_3C(O)CH_3$-$CH_3C(OH)CH_3$ were observed in F/Cl + CH_3CHO reaction. However, currently the reason why the tautomerization processes occurred in these experiments is not known.

The oxidation reaction of CH_3CO and CH_2CHO gives peroxy radicals, $CH_3C(O)O_2$ and O_2CH_2CHO. Theoretical calculation was first applied to get the ionization energies of two peroxy radicals and the appearance energy of its fragment ions, and the results shows that $CH_3C(O)O_2^+$ is not stable and dissociates into CH_3CO^+ and O_2. The singlet state of syn-O_2CH_2CHO ion is stable and the others all dissociate into $HCO^+ + CH_2O_2$ (Criegee) or HCO radical + $CH_2O_2^+$. However, the peroxy radical and their fragments were not detected. The experimental results indicate that the α-lactone formed in the oxidation reaction of CH_3CO, its ions are unstable and dissociate to form $CH_2O^+ + CO$ and $HCO^+ + CO$, the appearance energies of the fragments were preliminary determined.

Chapter 6. Conclusion and perspective

Ethane is one of the most abundant non-methane hydrocarbons in the atmosphere, and its oxidation reaction in the atmosphere leads to the formation of the ethyl peroxy radical, $C_2H_5O_2$. The main goal of this thesis was to investigate the reaction of $C_2H_5O_2$ in low NOx environments, including its self-reaction and its cross reaction with HO_2 and CH_3O_2. The absorption time profiles of the relevant radicals have been measured using near-infrared dual path cavity ringdown spectroscopy, and the rate constants and branching ratios of $C_2H_5O_2$ self-reaction and the cross reaction of $C_2H_5O_2$ with CH_3O_2 have been determined. In addition, vacuum ultraviolet photoionization mass spectrometry and photoelectron photoion coincidence spectroscopy were applied to measure the products of radical reactions, including the detection of the dimer product formed in $C_2H_5O_2$ self-reaction and the further oxidation reaction of CH_3CHO, which is the co-product of the self-reaction of $C_2H_5O_2$ and the cross reaction of $C_2H_5O_2$ with CH_3O_2. Basic scientific research on the rate constant of peroxy radical reaction and the branching ratio of the products are important data sources for subsequent model simulations. The reliable experimental results obtained in the current thesis will further improve the accuracy of the model and achieve a better understanding of $C_2H_5O_2$ peroxy radical chemistry in low NOx environments.

The main contents of this thesis are summarized as follows:

1. Kinetic and product measurements of the self-reaction of $C_2H_5O_2$. 351 nm pulsed laser photolysis of $Cl_2/C_2H_6/O_2$ mixture to produce $C_2H_5O_2$. First, two methods were used to measure the absorption cross section of $C_2H_5O_2$ at the peak wavelength 7596.47 cm^{-1}. The obtained absorption cross section by the two methods are consistent with each other: $\sigma(C_2H_5O_2, 7596.4\ cm^{-1}) = (1.0 \pm 0.2) \times 10^{-20}\ cm^2$.

Based on the measured absorption cross-section, CRDS was used to selectively and quantitatively measure the concentration time profiles of $C_2H_5O_2$ and HO_2, and by fitting the experimental results with a simple model, the rate constant and branching

ratio of the radical channel for the self-reaction of $C_2H_5O_2$ has been determined: $k(C_2H_5O_2 + C_2H_5O_2) = (1.0 \pm 0.2) \times 10^{-13}$ cm^3 s^{-1}, $\alpha(C_2H_5O) = 0.31 \pm 0.06$. It was found that secondary reactions such as $C_2H_5O_2 + HO_2$ and $C_2H_5O_2 + C_2H_5O$ can influence the measurement of the $C_2H_5O_2$ self-reaction kinetics, and therefore separate experiments were conducted to measure the rate constants of these two reactions: $k(C_2H_5O_2 + HO_2) = 6.2 \times 10^{-12}$ cm^3 s^{-1} and $k(C_2H_5O_2 + C_2H_5O) = 7 \times 10^{-12}$ cm^3 s^{-1}. $\alpha(C_2H_5O)$ obtained in this experiment is consistent with the recent results by Noell *et al.,* based on a similar method, ie., $\alpha(C_2H_5O)$ was obtained by directly measuring HO_2, but is different from the older, IUPAC recommended values based on end product measurement using Fourier transform infrared spectroscopy ($\alpha(C_2H_5O) = 0.63$). This difference is believed to be due to the neglect of the contribution of the dimer product $C_2H_5OOC_2H_5$, which could be photolyzed or heterogeneously decompose to C_2H_5O in stable end product measurement, and resulting in an apparently higher branching ratio of C_2H_5O.

Microwave discharge flowtube combined with vacuum ultraviolet photoionization mass spectrometry and synchrotron radiation photoelectron photoion coincidence spectroscopy was used to measure the products of the self-reaction of $C_2H_5O_2$. The branching ratio of the dimer product $C_2H_5OOC_2H_5$ was obtained by measuring the kinetics of the products: (0.10 ± 0.05). After estimating a 50% transmission loss, the upper limit of $\alpha(C_2H_5OOC_2H_5)$ was 0.3. This value indicates that the dimer products can maybe not be ignored and it may help to explain the difference in $\alpha(C_2H_5O)$ between our/Noell *et al*.'s and the earlier end product measurement.

2. Kinetics and products measurements of the cross reaction of $C_2H_5O_2$ with CH_3O_2. 351 nm excimer laser photolysis of $Cl_2/C_2H_6/CH_4/O_2$ mixture to simultaneously produce $C_2H_5O_2$ and CH_3O_2. The absorption time profiles of $C_2H_5O_2$ and CH_3O_2 at 7601.66 cm^{-1} and 7488.13 cm^{-1}, as well as the concentration time profiles of their product HO_2 were relative selectively measured. With a model to fit the measured kinetics of CH_3O_2, $C_2H_5O_2$ and HO_2, the rate constant and branching ratio for the radical channel have been obtained: $k(C_2H_5O_2 + CH_3O_2) = (3.8 \pm 1.0) \times 10^{-13}$ cm^3 s^{-1}, $\alpha(C_2H_5O + CH_3O) = 0.4 \pm 0.2$

To avoid the precursors methane and ethane absorbing too much near-infrared light, the concentration of the added precursors were not high enough, which led to a small fraction of Cl reacting with RO_2 ($C_2H_5O_2$ and CH_3O_2), and thus influencing the profiles of $C_2H_5O_2$, CH_3O_2 and HO_2 during the measurement of the cross reaction of $C_2H_5O_2$ with CH_3O_2. Therefore, separate experiments were conducted to measure the rate constant and branching ratio of the reactions of Cl with $C_2H_5O_2$ and CH_3O_2, respectively. The mixture of $Cl_2/C_2H_6/O_2$ and $Cl_2/CH_4/O_2$ was photolysis by 351 nm excimer laser to produce $C_2H_5O_2$ and CH_3O_2, respectively. Then the obtained mechanism for Cl with $C_2H_5O_2$ and CH_3O_2 has been simplified and added in the model of the cross reaction of $C_2H_5O_2$ with CH_3O_2.

3. CH_3CHO is the co-product of the self-reaction of $C_2H_5O_2$ and the cross reaction of $C_2H_5O_2$ with CH_3O_2. Microwave discharge flowtube combined with synchrotron radiation photoelectron photoion coincidence spectroscopy was used to measure the products formed in the oxidation reaction of CH_3CHO. The reaction between F/Cl and CH_3CHO produces two isomer radicals, CH_3CO and CH_2CHO, whose SPESs were obtained, and the adiabatic and vertical ionization energies of CH_3CHO were determined. The branching ratio of CH_2CHO in the Cl + CH_3CHO reaction relative to its branching ratio in the F + CH_3CHO reaction were determined. The tautomerization processes of CH_3CHO-CH_2CHOH and CH_3COCH_3-CH_3COHCH_3 were observed in F/Cl + CH_3CHO reaction.

The oxidation reaction of CH_3CO and CH_2CHO gives peroxy radicals $CH_3C(O)O_2$ and O_2CH_2CHO. Theoretical calculations indicate that $CH_3C(O)O_2^+$ is unstable and will dissociate to generate CH_3CO^+ and O_2. One of the structures of $O_2CH_2CHO^+$ is stable, while the other structures are also unstable and will dissociate. However, neither the peroxy radicals nor their fragments were observed. The other product of the oxidation reaction of CH_3CO is α-lactone, its ion is unstable, the appearance energies of its fragments were investigated.

The highlights of this thesis are:

1. Dual path cavity ringdown absorption spectroscopy was used to selectively and quantitatively measure the absorption of $C_2H_5O_2$ and HO_2, *(Absolute absorption cross-section of the* $\widetilde{\boldsymbol{A}} \leftarrow \widetilde{\boldsymbol{X}}$ *electronic transition of the ethyl peroxy radical and rate constant of its cross reaction with* HO_2*. Photonics 2021, 8 (8), 296.),* the rate constant and branching ratio of the self-reaction $C_2H_5O_2$ were determined *(Rate constant and branching ratio for the reactions of the ethyl peroxy radical with itself and with the ethoxy radical. ACS Earth and Space Chemistry 2021, 6 (1), 181-188.)*. This measurement has solved the discrepancy between literature results. At present, the IUPAC website has adopted our/Noell et al.'s results and updated the recommended rate constant and branching ratio for $C_2H_5O_2$ self-reaction *(https://iupac-aeris.ipsl.fr/datasheets/pdf/ROO_26.pdf)*.

2. The relatively selective measurement of the absorption of $C_2H_5O_2$ and CH_3O_2 in the near-infrared region have been carried out to get the rate constant of the cross reaction of $C_2H_5O_2$ with CH_3O_2, and the detection of the produced HO_2 allows to get the branching ratio of the cross reaction for the first time. This work has been selected by the editors as a 2023 HOT PCCP article. *(Rate constant and branching ratio of the reaction of ethyl peroxy radicals with methyl peroxy radicals. Physical Chemistry Chemical Physics 2023, 25, 17840-17849).*

3. Vacuum ultraviolet photoionization mass spectrometry and photoelectron photoion coincidence spectroscopy combined with advanced synchrotron radiation light sources have been applied to investigate the oxidation reaction of CH_3CHO. The photoelectron spectra of the isomer radicals CH_3CO and CH_2CHO in the F + CH_3CHO reaction have been simultaneously measured for the first time. The branching ratio of the CH_2CHO in the Cl + CH_3CHO reaction was directly obtained.

But there are still some interesting studies that can be performed in the future:

1. Product detection of Cl + RO_2 ($C_2H_5O_2$/CH_3O_2) reaction. Although it is believed that the reaction of Cl with RO_2 leads to the formation of the Criegee intermediate, it has not yet been detected. Therefore, investigation of the products of these reactions

would help to improve the mechanism.

2. Further investigation of the tautomerizations of CH_3CHO-CH_2CHOH, and CH_3COCH_3-CH_2COHCH_3. The tautomerizations has been observed in F/Cl + CH_3CHO reaction, while further theoretical calculations are still be needed to well explain these processes.

3. Further analysis of the product formed in F + CH_3CHO reaction to get more information about their sources and structures. Although photoelectron spectra of the products were obtained, due to their overlapping or unknown theoretical information, further investigations are still needed to characterize and obtain their ionization energies and structure information.

Reference

[1] Atkinson R., *Atmospheric chemistry of VOCs and NOx.* Atmospheric Environment, 2000. **34**(12): p. 2063-2101.

[2] Atkinson R. and J. Arey, *Atmospheric degradation of volatile organic compounds.* Chemical Reviews, 2003. **103**(12): p. 4605-4638.

[3] Lu K., et al., *Exploring atmospheric free-radical chemistry in China: the self-cleansing capacity and the formation of secondary air pollution.* National Science Review, 2018. **6**(3): p. 579-594.

[4] Monks P.S., *Gas-phase radical chemistry in the troposphere.* Chemical Society Reviews, 2005. **34**(5): p. 376-395.

[5] Orlando J.J. and G.S. Tyndall, *Laboratory studies of organic peroxy radical chemistry: an overview with emphasis on recent issues of atmospheric significance.* Chemical Society Reviews, 2012. **41**(19): p. 6294-6317.

[6] Tyndall G.S., et al., *Atmospheric chemistry of small organic peroxy radicals.* Journal of Geophysical Research-Atmospheres, 2001. **106**(D11): p. 12157-12182.

[7] Kampa M. and E. Castanas, *Human health effects of air pollution.* Environmental Pollution, 2008. **151**(2): p. 362-367.

[8] Bianchi F., et al., *Highly oxygenated organic molecules (HOM) from gas-phase autoxidation involving peroxy radicals: a key contributor to atmospheric aerosol.* Chemical Reviews, 2019. **119**(6): p. 3472-3509.

[9] Fittschen C., *The reaction of peroxy radicals with OH radicals.* Chemical Physics Letters, 2019. **725**: p. 102-108.

[10] Fittschen C., et al., *ROOOH: a missing piece of the puzzle for OH measurements in low-NO environments?* Atmos. Chem. Phys., 2019. **19**(1): p. 349-362.

[11] Assaf E., et al., *The reaction between CH_3O_2 and OH radicals: product yields and atmospheric implications.* Environmental Science & Technology, 2017. **51**(4): p. 2170-2177.

[12] Berndt T., et al., *Hydrotrioxide (ROOOH) formation in the atmosphere.* Science, 2022. **376**(6596): p. 979-982.

[13] Atkinson R., et al., *Evaluated kinetic and photochemical data for atmospheric chemistry: Volume II - gas phase reactions of organic species.* Atmospheric Chemistry and Physics, 2006. **6**: p. 3625-4055.

[14] Assali M. and C. Fittschen, *Rate constants and branching ratios for the self-reaction of acetyl peroxy ($CH_3C(O)O_2$) and Its Reaction with CH_3O_2.* Atmosphere, 2022. **13**(2): p. 186.

[15] Simpson I.J., et al., *Long-term decline of global atmospheric ethane concentrations and implications for methane.* Nature, 2012. **488**(7412): p. 490-494.

[16] Pozzer A., et al., *Observed and simulated global distribution and budget of atmospheric C2-C5 alkanes.* Atmospheric Chemistry and Physics, 2010. **10**(9): p. 4403-4422.

[17] Cattell F.C.R., et al., *A kinetics study of reactions of HO_2 and $C_2H_5O_2$ using diode laser absorption spectroscopy.* Journal of the Chemical Society, Faraday Transactions, 1986. **82**(11): p. 1999-2018.

[18] Noell A.C., et al., *Near-infrared kinetic spectroscopy of the HO_2 and $C_2H_5O_2$ self-reactions and*

cross reactions. Journal of Physical Chemistry A, 2010. **114**(26): p. 6983-6995.

[19] Adachi H., N. Basco and D.G.L. James, *The ethylperoxy radical spectrum and rate constant for mutual interaction measured by flash photolysis and kinetic spectroscopy.* International Journal of Chemical Kinetics, 1979. **11**(11): p. 1211-1229.

[20] Anastasi C., D.J. Waddington and A. Woolley, *Reactions of oxygenated radicals in the gas phase. Part 10.—Self-reactions of ethylperoxy radicals.* Journal of the Chemical Society, Faraday Transactions 1: Physical Chemistry in Condensed Phases, 1983. **79**(2): p. 505-516.

[21] Munk J., et al., *Spectrokinetic studies of ethyl and ethylperoxy radicals.* The Journal of Physical Chemistry, 1986. **90**(12): p. 2752-2757.

[22] Wallington T.J., et al., *Fourier transform infrared study of the self reaction of $C_2H_5O_2$ radicals in air at 295 K.* International Journal of Chemical Kinetics, 1989. **21**(11): p. 1077-1089.

[23] Bauer D., J.N. Crowley and G.K. Moortgat, *The UV absorption spectrum of the ethylperoxy radical and its self-reaction kinetics between 218 and 333 K.* Journal of Photochemistry and Photobiology A-chemistry, 1992. **65**(3): p. 329-344.

[24] Fenter F.F., et al., *The ethylperoxy radical: its ultraviolet spectrum, self-reaction, and reaction with hydroperoxy, each studied as a function of temperature.* Journal of Physical Chemistry, 1993. **97**(14): p. 3530-3538.

[25] Atkinson D.B. and J.W. Hudgens, *Chemical kinetic studies using ultraviolet cavity ring-down spectroscopic detection: self-reaction of ethyl and ethylperoxy radicals and the reaction, $O_2 + C_2H_5 \rightarrow C_2H_5O_2$.* Journal of Physical Chemistry A, 1997. **101**(21): p. 3901-3909.

[26] Niki H., et al., *Fourier transform infrared studies of the self-reaction of $C_2H_5O_2$ radicals.* Journal of Physical Chemistry, 1982. **86**(19): p. 3825-3829.

[27] Wallington T.J., P. Dagaut and M.J. Kurylo, *Measurements of the gas phase UV absorption spectrum of $C_2H_5O_2$ radicals and of the temperature dependence of the rate constant for their self-reaction.* Journal of Photochemistry and Photobiology A-chemistry, 1988. **42**(2-3): p. 173-185.

[28] Dagaut P., T.J. Wallington and M.J. Kurylo, *FLASH-PHOTOLYSIS KINETIC ABSORPTION-SPECTROSCOPY STUDY OF THE GAS-PHASE REACTION HO2 + C2H5O2 OVER THE TEMPERATURE-RANGE 228-380-K.* Journal of Physical Chemistry, 1988. **92**(13): p. 3836-3839.

[29] Maricq M.M., et al., *Reaction of chlorine atoms with methylperoxy and ethylperoxy radicals.* Journal of Physical Chemistry, 1994. **98**(8): p. 2083-2089.

[30] Boyd A.A., et al., *Rate constants for $RO_2 + HO_2$ reactions measured under a large excess of HO_2.* Journal of Physical Chemistry A, 2003. **107**(6): p. 818-821.

[31] Raventos-Duran M.T., et al., *Kinetics and branching ratio studies of the reaction of C2H5O2+HO2 using chemical ionisation mass spectrometry.* Physical Chemistry Chemical Physics, 2007. **9**(31): p. 4338-4348.

[32] Villenave E. and R. Lesclaux, *Kinetics of the cross reactions of CH_3O_2 and $C_2H_5O_2$ radicals with selected peroxy radicals.* Journal of Physical Chemistry, 1996. **100**(34): p. 14372-14382.

[33] Farago E.P., et al., *Experimental determination of the rate constant of the reaction between $C_2H_5O_2$ and OH radicals.* Chemical Physics Letters, 2015. **619**: p. 196-200.

[34] Assaf E., et al., *Experimental and theoretical investigation of the reaction of RO_2 radicals with OH radicals: Dependence of the HO_2 yield on the size of the alkyl group.* International Journal

of Chemical Kinetics, 2018. **50**(9): p. 670-680.

[35] Kirschke S., et al., *Three decades of global methane sources and sinks.* Nature Geoscience, 2013. **6**(10): p. 813-823.

[36] Veyret B., J.C. Rayez and R. Lesclaux, *Mechanism of the photo-oxidation of formaldehyde studied by flash-photolysis of CH_2O-O_2-NO mixtures.* Journal of Physical Chemistry, 1982. **86**(17): p. 3424-3430.

[37] Cox R.A. and G.S. Tyndall, *Rate constants for the reactions of CH_3O_2 with HO_2, NO and NO_2 using molecular modulation spectrometry.* Journal of the Chemical Society, Faraday Transactions, 1980. **76**(0): p. 153-163.

[38] Sander S.P. and R.T. Watson, *Temperature dependence of the self-reactoin of CH_3O_2 radicals.* Journal of Physical Chemistry, 1981. **85**(20): p. 2960-2964.

[39] McAdam K., B. Veyret and R. Lesclaux, *UV absorption-spectra of HO_2 and CH_3O_2 radicals and the kinetics of their mutual reactions at 298 K.* Chemical Physics Letters, 1987. **133**(1): p. 39-44.

[40] Kurylo M.J. and T.J. Wallington, *The temperature-dependence of the rate-constant for the gas-phase disproportionation reaction of CH_3O_2 radicals.* Chemical Physics Letters, 1987. **138**(6): p. 543-547.

[41] Jenkin M.E., et al., *Kinetic study of the reactions CH_3O_2 + CH_3O_2 and CH_3O_2 + HO_2 using molecular modulation spectroscopy.* Journal of the Chemical Society, Faraday Transactions, 1988. **84**(7): p. 913-930.

[42] Simon F.G., W. Schneider and G.K. Moortgat, *UV-absorption spectrum of the methylperoxy radical and the kinetics of its disporportionation reaction at 300 K.* International Journal of Chemical Kinetics, 1990. **22**(8): p. 791-812.

[43] Lightfoot P.D., R. Lesclaux and B. Veyret, *Flash photolysis study of the methylperoxy + methylperoxy reaction: rate constants and branching ratios from 248 to 573 K.* Journal of Physical Chemistry, 1990. **94**(2): p. 700-707.

[44] Onel L., et al., *Kinetics and product branching ratio study of the CH_3O_2 self-reaction in the highly instrumented reactor for atmospheric chemistry.* Journal of Physical Chemistry A, 2022. **126**(42): p. 7639-7649.

[45] Atkinson D.B. and J.W. Hudgens, *Chemical kinetic studies using ultraviolet cavity ring-down spectroscopic detection: Self-reaction of ethyl and ethylperoxy radicals and the reaction O_2 + $C_2H_5 \rightarrow C_2H_5O_2$.* Journal of Physical Chemistry A, 1997. **101**(21): p. 3901-3909.

[46] Wen Z., et al., *Self-reaction of $C_2H_5O_2$ and its cross-reaction with HO_2 studied with vacuum ultraviolet photoionization mass spectrometry.* Chemical Physics Letters, 2022. **806**: p. 140034.

[47] Moortgat G.K., et al., *Peroxy radical reactions in the photo-oxidation of CH_3CHO.* Journal of the Chemical Society, Faraday Transactions, 1989. **85**(7): p. 809 - 829.

[48] Lightfoot P.D., B. Veyret and R. Lesclaux, *Flash photolysis study of the methylperoxy + hydroperoxy reaction between 248 and 573 K.* Journal of Physical Chemistry, 1990. **94**(2): p. 708-714.

[49] Lightfoot P.D., et al., *Flash photolysis study of the CH_3O_2 + CH_3O_2 and CH_3O_2 + HO_2 reactions between 60 K and 719 K- Unimolecular decomposition of methylhydroperoxide.* Journal of the Chemical Society-Faraday Transactions, 1991. **87**(19): p. 3213-3220.

[50] Cattell F.C., et al., *A KINETICS STUDY OF REACTIONS OF HO2 AND C2H5O2 USING*

DIODE-LASER ABSORPTION-SPECTROSCOPY. Journal of the Chemical Society-Faraday Transactions Ii, 1986. **82**: p. 1999-2018.

[51] Maricq M.M. and J.J. Szente, *A kinetic-study of the reaction between ethylperoxy radicals and HO_2.* Journal of Physical Chemistry, 1994. **98**(8): p. 2078-2082.

[52] Bossolasco A., et al., *Rate constant of the reaction between CH_3O_2 and OH radicals.* Chemical Physics Letters, 2014. **593**(11): p. 7-13.

[53] Fittschen C., L.K. Whalley and D.E. Heard, *The reaction of CH_3O_2 radicals with OH Radicals: A neglected sink for CH_3O_2 in the remote atmosphere.* Environmental Science and Technology, 2014. **118**(4): p. 7700–7701.

[54] Yan C., S. Kocevska and L.N. Krasnoperov, *Kinetics of the reaction of CH_3O_2 radicals with OH studied over the 292 – 526 K temperature range.* Journal of Physical Chemistry A, 2016. **120**(31): p. 6111–6121.

[55] Assaf E., et al., *Rate constant of the reaction between CH_3O_2 radicals and OH radicals revisited.* Journal of Physical Chemistry A, 2016. **120**(45): p. 8923-8932.

[56] Caravan R.L., et al., *The reaction of OH with CH_3O_2 is not a major source of atmospheric methanol.* Nature Communications, 2018. **9**: p. 4343.

[57] Assaf E., et al., *Rate constants of the reaction of C_2–C_4 peroxy radicals with OH radicals.* Chemical Physics Letters, 2017. **684**(16): p. 245-249.

[58] Devolder P., et al., *About the co-product of the OH radical in the reaction of acetyl with O_2 below atmospheric pressure.* Chemical Physics Letters, 2006. **417**(1): p. 154-158.

[59] Singh H.B., et al., *Analysis of the atmospheric distribution, sources, and sinks of oxygenated volatile organic chemicals based on measurements over the Pacific during TRACE-P.* Journal of Geophysical Research-Atmospheres, 2004. **109**(D15S07).

[60] Wang J., et al., *Observationally constrained modeling of peroxy radical during an ozone episode in the pearl river delta region, China.* Journal of Geophysical Research-Atmospheres, 2023. **128**(12).

[61] Tereszchuk K.A., et al., *Observations of peroxyacetyl nitrate (PAN) in the upper troposphere by the Atmospheric Chemistry Experiment-Fourier Transform Spectrometer (ACE-FTS).* Atmospheric Chemistry and Physics, 2013. **13**(11): p. 5601-5613.

[62] Seakins P.W., *Photophysical oxidation of atmospheric carbonyls.* Nature Chemistry, 2023. **15**(10): p. 1321-1323.

[63] Sehested J., et al., *Absolute rate constants for F + CH_3CHO and CH_3CO + O_2, relative rate study of CH_3CO + NO, and the product distribution of the F + CH_3CHO reaction.* International Journal of Chemical Kinetics, 1998. **30**(12): p. 913-921.

[64] Bartels M., K. Hoyermann and U. Lange, *AN EXPERIMENTAL-STUDY OF THE REACTIONS CH_3CHO+Cl, C_2H_4O+Cl, AND C_2H_4O+F IN THE GAS-PHASE.* Berichte Der Bunsen-Gesellschaft-Physical Chemistry Chemical Physics, 1989. **93**(4): p. 423-427.

[65] Niki H., et al., *FTIR study of the kinetics and mechanism for chlorine-atom-initiated reactions of acetaldehyde.* Journal of Physical Chemistry, 1985. **89**(4): p. 588-591.

[66] Zamanpour M.H.N., et al., *Observation and assignment of the first photoelectron band of the CH_3CO (X^2A) radical.* Journal of Electron Spectroscopy and Related Phenomena, 2008. **162**(3): p. 122-126.

[67] Reed R.I. and J.C.D. Brand, *Electron impact studies .4. glyoxal, methylglyoxal, and diacetyl.*

Transactions of the Faraday Society, 1958. **54**(4): p. 478-482.

[68] Papadimitriou V.C., et al., *$CH_3CO + O_2 + M$ (M = He, N_2) reaction rate coefficient measurements and implications for the OH radical product yield.* Journal of Physical Chemistry A, 2015. **119**(28): p. 7481-7497.

[69] Carr S.A., et al., *Experimental and modeling studies of the pressure and temperature dependences of the kinetics and the OH Yields in the acetyl + O_2 Reaction.* Journal of Physical Chemistry A, 2011. **115**(6): p. 1069-1085.

[70] Butkovskaya N.I., A. Kukui and G. Le Bras, *Branching fractions for H_2O forming channels of the reaction of OH radicals with acetaldehyde.* Journal of Physical Chemistry A, 2004. **108**(7): p. 1160-1168.

[71] Gao Y., K. Lu and Y. Zhang, *Review of technologies and their applications for the speciated detection of RO_2 radicals.* Journal of Environmental Sciences, 2023. **123**: p. 487-499.

[72] Mazurenka M., et al., *4 Cavity ring-down and cavity enhanced spectroscopy using diode lasers.* Annual Reports Section "C" (Physical Chemistry), 2005. **101**(0): p. 100-142.

[73] Reiner T., M. Hanke and F. Arnold, *Atmospheric peroxy radical measurements by ion molecule reaction-mass spectrometry: A novel analytical method using amplifying chemical conversion to sulfuric acid.* Journal of Geophysical Research: Atmospheres, 1997. **102**(D1): p. 1311-1326.

[74] Hanke M., et al., *Atmospheric peroxy radicals: ROXMAS, a new mass-spectrometric methodology for speciated measurements of HO_2 and $\sum RO_2$ and first results.* International Journal of Mass Spectrometry, 2002. **213**(2): p. 91-99.

[75] Edwards G.D., et al., *Chemical ionization mass spectrometer instrument for the measurement of tropospheric HO_2 and RO_2.* Analytical Chemistry, 2003. **75**(20): p. 5317-5327.

[76] Berden G., R. Peeters and G. Meijer, *Cavity ring-down spectroscopy: Experimental schemes and applications.* International reviews in physical chemistry, 2000. **19**(4): p. 565-607.

[77] Osborn D.L., et al., *The multiplexed chemical kinetic photoionization mass spectrometer: A new approach to isomer-resolved chemical kinetics.* Review of Scientific Instruments, 2008. **79**(10): p. 104103.

[78] Garcia G.A., et al., *Synchrotron-based double imaging photoelectron/photoion coincidence spectroscopy of radicals produced in a flow tube: OH and OD.* The Journal of Chemical Physics, 2015. **142**(16): p. 164201.

[79] Tang X.F., et al., *Vacuum upgrade and enhanced performances of the double imaging electron/ion coincidence end-station at the vacuum ultraviolet beamline DESIRS.* Review of Scientific Instruments, 2015. **86**(12): p. 123108.

[80] Okeefe A. and D.A.G. Deacon, *Cavity ring-down optical spectrometer for absorption-measurements using pulsed laser sources.* Review of Scientific Instruments, 1988. **59**(12): p. 2544-2551.

[81] Romanini D., et al., *CW cavity ring down spectroscopy.* Chemical Physics Letters, 1997. **264**(3-4): p. 316-322.

[82] Sharp E.N., P. Rupper and T.A. Miller, *The structure and spectra of organic peroxy radicals.* Physical Chemistry Chemical Physics, 2008. **10**(27): p. 3955-3981.

[83] Jones I.W., et al., *Calculated and empirical values of vibronic transition dipole moments of reactive chemical intermediates for determination of concentrations.* Journal of Physical Chemistry A, 2023. **127**(21): p. 4670-4681.

[84] *Wikipedia*. Available from: https://en.wikipedia.org/wiki/Main_Page.

[85] *UV/VIS Specttral*. Available from: http://satellite.mpic.de/spectral_atlas.

[86] Assaf E., *Kinetic study of reactions with interest to atmospheric chemistry by simultaneous detection of OH and RO_2 radicals coupled to laser photolysis*. 2017, University of Lille.

[87] Wen Z., et al., *Online analysis of gas-phase radical reactions using vacuum ultraviolet lamp photoionization and time-of-flight mass spectrometry.* Review of Scientific Instruments, 2020. **91**(4): p. 043201.

[88] Garcia G.A., et al., *DELICIOUS III: A multipurpose double imaging particle coincidence spectrometer for gas phase vacuum ultraviolet photodynamics studies.* Review of Scientific Instruments, 2013. **84**(5): p. 053112.

[89] Nahon L., et al., *DESIRS: a state-of-the-art VUV beamline featuring high resolution and variable polarization for spectroscopy and dichroism at SOLEIL.* Journal of Synchrotron Radiation, 2012. **19**: p. 508-520.

[90] Hunziker H.E. and H.R. Wendt, *Near-infrared absorption-spectrum of HO_2.* The Journal of Chemical Physics, 1974. **60**(11): p. 4622-4623.

[91] Hunziker H.E. and H.R. Wendt, *Electronic absorption-spectra of organic peroxyl radicals in near-infrared.* The Journal of Chemical Physics, 1976. **64**(8): p. 3488-3490.

[92] Pushkarsky M.B., S.J. Zalyubovsky and T.A. Miller, *Detection and characterization of alkyl peroxy radicals using cavity ringdown spectroscopy.* The Journal of Chemical Physics, 2000. **112**(24): p. 10695-10698.

[93] Atkinson D.B. and J.L. Spillman, *Alkyl peroxy radical kinetics measured using near-infrared CW-cavity ring-down spectroscopy.* Journal of Physical Chemistry A, 2002. **106**(38): p. 8891-8902.

[94] Farago E.P., et al., *Absorption spectrum and absolute absorption cross sections of CH_3O_2 radicals and CH_3I molecules in the wavelength range 7473-7497 cm^{-1}.* Journal of Physical Chemistry A, 2013. **117**(48): p. 12802-12811.

[95] Wen Z.Y., et al., *A vacuum ultraviolet photoionization time-of-flight mass spectrometer with high sensitivity for study of gas-phase radical reaction in a flow tube.* International Journal of Chemical Kinetics, 2019. **51**(3): p. 178-188.

[96] Thiebaud J., S. Crunaire and C. Fittschen, *Measurements of line strengths in the 2 nu(1) band of the HO2 radical using laser photolysis/continuous wave cavity ring-down spectroscopy (cw-CRDS).* Journal of Physical Chemistry A, 2007. **111**(30): p. 6959-6966.

[97] Rupper P., et al., *Investigation of ethyl peroxy radical conformers via cavity ringdown spectroscopy of the (similar to)over-barA-(similar to)over-barX electronic transition.* Journal of Physical Chemistry A, 2007. **111**(5): p. 832-840.

[98] Melnik D., R. Chhantyal-Pun and T.A. Miller, *Measurements of the Absolute Absorption Cross Sections of the (A)over-tilde <-(X)over-tilde Transition in Organic Peroxy Radicals by Dual-Wavelength Cavity Ring-Down Spectroscopy.* Journal of Physical Chemistry A, 2010. **114**(43): p. 11583-11594.

[99] Melnik D. and T.A. Miller, *Kinetic measurements of the $C_2H_5O_2$ radical using time-resolved cavity ring-down spectroscopy with a continuous source.* The Journal of Chemical Physics, 2013. **139**(9): p. 094201.

[100] Tang Y.X., G.S. Tyndall and J.J. Orlando, *Spectroscopic and Kinetic Properties of HO2 Radicals*

and the Enhancement of the HO2 Self Reaction by CH3OH and H2O. Journal of Physical Chemistry A, 2010. **114**(1): p. 369-378.

[101] Ibrahim N., et al., *Air-broadening coefficients of the HO2 radical in the 2v(1) band measured using cw-CRDS.* Journal of Molecular Spectroscopy, 2007. **242**(1): p. 64-69.

[102] Onel L., et al., *An intercomparison of HO_2 measurements by fluorescence assay by gas expansion and cavity ring-down spectroscopy within HIRAC (Highly Instrumented Reactor for Atmospheric Chemistry).* Atmospheric Measurement Techniques, 2017. **10**(12): p. 4877-4894.

[103] Assaf E., et al., *Absorption spectrum and absorption cross sections of the 2 nu(1) band of HO2 between 20 and 760 Torr air in the range 6636 and 6639 cm(-1).* Journal of Quantitative Spectroscopy & Radiative Transfer, 2018. **211**: p. 107-114.

[104] Assali M., et al., *Experimental determination of the rate constants of the reactions of HO_2 + DO_2 and DO_2 + DO_2.* International Journal of Chemical Kinetics, 2020. **52**(3): p. 197-206.

[105] Atkinson R., et al., *Evaluated kinetic and photochemical data for atmospheric chemistry: Volume I - gas phase reactions of O-x, HOx, NOx and SOx species.* Atmospheric Chemistry and Physics, 2004. **4**: p. 1461-1738.

[106] Fittschen C., et al., *Rate constants for the reactions of C2H5O, i-C3H7O, and n-C3H7O with NO and O-2 as a function of temperature.* International Journal of Chemical Kinetics, 1999. **31**(12): p. 860-866.

[107] Fernandes R.X., et al., *Experimental and Modeling Study of the Temperature and Pressure Dependence of the Reaction C2H5 + O-2 (+ M) -> C2H5O2 (+ M).* Journal of Physical Chemistry A, 2015. **119**(28): p. 7263-7269.

[108] Seakins P.W., E.L. Woodbridge and S.R. Leone, *A laser flash-photolysis, time-resolved fourier-transform infrared-emission study of the reaction Cl + C_2H_5 → HCl(v) + C_2H_4.* Journal of Physical Chemistry, 1993. **97**(21): p. 5633-5642.

[109] Maricq M.M., et al., *REACTION OF CHLORINE ATOMS WITH METHYLPEROXY AND ETHYLPEROXY RADICALS.* Journal of Physical Chemistry, 1994. **98**(8): p. 2083-2089.

[110] Zhang C., et al., *Absolute absorption cross-section of the A←X electronic transition of the ethyl peroxy radical and rate constant of its cross reaction with HO_2.* Photonics, 2021. **8**(8): p. 296.

[111] Fittschen C., et al., *Rate constants for the reactions of C_2H_5O, i-C_3H_7O, and n-C_3H_7O with NO and O_2 as a function of temperature.* International Journal of Chemical Kinetics, 1999. **31**(12): p. 860-866.

[112] Fernandes R.X., et al., *Experimental and modeling study of the temperature and pressure dependence of the reaction C_2H_5 + O_2 (+ M) → $C_2H_5O_2$ (+ M).* Journal of Physical Chemistry A, 2015. **119**(28): p. 7263-7269.

[113] Atkinson R., et al., *Evaluated kinetic and photochemical data for atmospheric chemistry: Volume 1 – gas phase reactions of O_x, HO_x, NO_x, and SO_x, species.* Atmosperic Chemistry and Physics, 2004. **4**: p. 1461-1738.

[114] Wen Z., et al., *A vacuum ultraviolet photoionization time-of-flight mass spectrometer with high sensitivity for study of gas-phase radical reaction in a flow tube.* International Journal of Chemical Kinetics, 2019. **51**(3): p. 178-188.

[115] Bodi A., et al., *A new double imaging velocity focusing coincidence experiment: i^2PEPICO.* Review of Scientific Instruments, 2012. **83**(8): p. 083105.

[116] Sztaray B., et al., *CRF-PEPICO: Double velocity map imaging photoelectron photoion*

coincidence spectroscopy for reaction kinetics studies. Journal of Chemical Physics, 2017. **147**(1): p. 013944.

[117] Murphy S.E., et al., *Accretion product formation in the self-reaction of ethene-derived hydroxy peroxy radicals.* Environmental Science: Atmospheres, 2023. **3**(5): p. 882-893.

[118] Assali M. and C. Fittschen, *Self-reaction of acetonyl peroxy radicals and their reaction with Cl Atoms.* Journal of Physical Chemistry A, 2022. **126**(28): p. 4585-4597.

[119] Daele V. and G. Poulet, *Kinetics and products of the reactions of CH_3O_2 with Cl and ClO.* Journal de Chimie Physique, 1996. **93**(6): p. 1081-1099.

[120] Atkinson R., et al., *Evaluated kinetic and photochemical data for atmospheric chemistry: volume II - gas phase reactions of organic species.* Atmosperic Chemistry and Physics, 2006. **6**(11): p. 3625-4055.

[121] Jungkamp T.P.W., A. Kukui and R.N. Schindler, *Determination of rate constants and product branching ratios for the reactions of CH_3O_2 and CH_3O with Cl atoms at room-temperature.* Berichte der Bunsen-Gesellschaft fuer Physikalische Chemie, 1995. **99**(8): p. 1057-1066.

[122] Daële V., G. Laverdet and G. Poulet, *Kinetics of the reactions of CH_3O with Cl and ClO.* International Journal of Chemical Kinetics, 1996. **28**(8): p. 589-598.

[123] Drougas E. and A.M. Kosmas, *Quantum mechanical studies on the potential energy surface of the reactions CH_3 + OClO, CH_3O + ClO and CH_3O_2 + Cl.* Chemical Physics Letters, 2003. **369**(3): p. 269-274.

[124] I. Bridier, *These de Doctorat*. 1991: Bordeaux.

[125] Cox R.A., et al., *Evaluated kinetic and photochemical data for atmospheric chemistry: Volume VII – Criegee intermediates.* Atmos. Chem. Phys., 2020. **20**(21): p. 13497-13519.

[126] Chhantyal-Pun R., et al., *Impact of criegee intermediate reactions with peroxy radicals on tropospheric organic aerosol.* ACS Earth and Space Chemistry, 2020. **4**(10): p. 1743-1755.

[127] Keiffer M., A.J. Miscampbell and M.J. Pilling, *A global technique for analyzing multiple decay curves - application to the CH_3 + O_2 system.* Journal of the Chemical Society-Faraday Transactions Ii, 1988. **84**(5): p. 505-514.

[128] Atkinson R., et al., *Evaluated kinetic and photochemical data for atmospheric chemistry: Volume III - gas phase reactions of inorganic halogens.* Atmospheric Chemistry and Physics, 2007. **7**(4): p. 981-1191.

[129] Assaf E., et al., *The reaction of fluorine atoms with methanol: yield of CH_3O/CH_2OH and rate constant of the reactions CH_3O + CH_3O and CH_3O + HO_2.* Physical Chemistry Chemical Physics, 2018. **20**(16): p. 10660-10670.

[130] Demore W.B., et al., *Tables of rate constants extracted from chemical-kinetics and photochemical data for use in stratospheric modeling evaluation number-7.* International Journal of Chemical Kinetics, 1985. **17**(10): p. 1135-1151.

[131] Atkinson R., et al., *Evaluated kinetic and photochemical data for atmospheric chemistry: Volume IV - gas phase reactions of organic halogen species.* Atmospheric Chemistry and Physics, 2008. **8**(15): p. 4141-4496.

[132] Srinivasan N.K., et al., *Reflected shock tube studies of high-temperature rate constants for OH + CH_4 → CH_3 + H_2O and CH_3 + NO_2 → CH_3O + NO.* Journal of Physical Chemistry A, 2005. **109**(9): p. 1857-1863.

[133] Chhantyal-Pun R., et al., *A kinetic study of the CH_2OO Criegee intermediate self-reaction,*

reaction with SO_2 and unimolecular reaction using cavity ring-down spectroscopy. Physical Chemistry Chemical Physics, 2015. **17**(5): p. 3617-3626.

[134] Shamas M., et al., *Rate constant and branching ratio for the reactions of the ethyl peroxy radical with itself and with the ethoxy radical.* ACS Earth and Space Chemistry, 2022. **6**(1): p. 181-188.

[135] Stone D., et al., *Kinetics of CH_2OO reactions with SO_2, NO_2, NO, H_2O and CH_3CHO as a function of pressure.* Physical Chemistry Chemical Physics, 2014. **16**(3): p. 1139-1149.

[136] Vereecken L., A. Novelli and D. Taraborrelli, *Unimolecular decay strongly limits the atmospheric impact of Criegee intermediates.* Physical Chemistry Chemical Physics, 2017. **19**(47): p. 31599-31612.

[137] Delbos E., et al., *Rate coefficients and equilibrium constant for the $CH_2CHO + O_2$ reaction system.* Journal of Physical Chemistry A, 2006. **110**(9): p. 3238-3245.

[138] Assaf E., et al., *Rate constants of the reaction of C_2-C_4 peroxy radicals with OH radicals.* Chemical Physics Letters, 2017. **684**(16): p. 245-249.

[139] Rothman L.S., et al., *The HITRAN2012 molecular spectroscopic database.* Journal of Quantitative Spectroscopy and Radiative Transfer, 2013. **130**(SI): p. 4-50.

[140] Fernandes R.X., K. Luther and J. Troe, *Falloff curves for the reaction $CH_3 + O_2 (+ M) \rightarrow CH_3O_2 (+ M)$ in the pressure range 2 - 1000 bar and the temperature range 300 - 700 K.* Journal of Physical Chemistry A, 2006. **110**(13): p. 4442-4449.

[141] Fernandes R.X., et al., *Experimental and Modeling Study of the Temperature and Pressure Dependence of the Reaction $C_2H_5 + O_2 (+ M) \rightarrow C_2H_5O_2 (+ M)$.* The Journal of Physical Chemistry A, 2015. **119**(28): p. 7263-7269.

[142] Fittschen C., et al., *Rate Constants for the Reactions of C_2H_5O, i-C_3H_7O, and n-C_3H_7O with NO and O_2 as a Function of Temperature.* Int. J. Chem. Kinet., 1999. **31**(12): p. 860-866.

[143] Assaf E., et al., *The reaction of fluorine atoms with methanol: yield of CH_3O/CH_2OH and rate constant of the reactions $CH_3O + CH_3O$ and $CH_3O + HO_2$.* Physical Chemistry Chemical Physics, 2018. **20**: p. 8707.

[144] Atkinson R., et al., *Evaluated Kinetic and Photochemical Data for Atmospheric Chemistry: Volume 1 – Gas Phase Reactions of O_x, HO_x, NO_x, and SO_x, Species, IUPAC Task Group on Atmospheric Chemical Kinetic Data Evaluation, http://iupac.pole-ether.fr." Vol 2.* Atmosperic Chemistry and Physics, 2004. **4**: p. 1461-1738.

[145] Atkinson R., et al., *Evaluated kinetic and photochemical data for atmospheric chemistry: Volume III – reactions of inorganic halogens.* Atmos. Chem. Phys. Discuss., 2007. **7**: p. 981-1191.

[146] Clifford E.P., et al., *Infrared frequency-modulation probing of product formation in alkyl plus O-2 reactions: I. The reaction of C2H5 with O-2 between 295 and 698 K.* Journal of Physical Chemistry A, 2000. **104**(49): p. 11549-11560.

[147] Jasper A.W., S.J. Klippenstein and L.B. Harding, *Secondary kinetics of methanol decomposition: Theoretical rate coefficients for $^3CH_2 + OH$, $^3CH_2 + {}^3CH_2$, and $^3CH_2 + CH_3$.* Journal of Physical Chemistry A, 2007. **111**(35): p. 8699-8707.

[148] Klippenstein S.J., Y. Georgievskii and L.B. Harding, *Predictive theory for the combination kinetics of two alkyl radicals.* Physical Chemistry Chemical Physics, 2006. **8**(10): p. 1133-1147.

[149] Johnson K., I. Powis and C.J. Danby, *A photoelectron photoion coincidence study of acetaldehyde and ethylene-oxide molecular-ions.* Chemical Physics, 1982. **70**(3): p. 329-343.

[150] *NIST*. Available from: https://webbook.nist.gov/chemistry/.

[151] Niu B., Y. Bai and D.A. Shirley, *High resolution photoelectron spectroscopy and femtosecond intramolecular dynamics of H_2CCO^+ and D_2CCO^+.* The Journal of Chemical Physics, 1993. **99**(4): p. 2520-2532.

[152] Dyke J.M., et al., *1st ionization-potential of the formyl radical, HCO(X^2A'), studied using photoelectron-spectroscopy.* Molecular Physics, 1980. **39**(3): p. 629-636.

[153] Houle F.A. and J.L. Beauchamp, *Photoelectron-spectroscopy of methyl, ethyl, isopropyl, and tert-butyl radicals - implications for the thermochemistry and structures of the radicals and their corresponding carbonium-ions.* Journal of the American Chemical Society, 1979. **101**(15): p. 4067-4074.

[154] Taatjes C.A., et al., *Enols are common intermediates in hydrocarbon oxidation.* Science, 2005. **308**(5730): p. 1887-1889.

[155] Couch D.E., et al., *Detection of the keto-enol tautomerization in acetaldehyde, acetone, cyclohexanone, and methyl vinyl ketone with a novel VUV light source.* Proceedings of the Combustion Institute, 2020. **38**(1): p. 1737-1744.

[156] Vasiliou A., et al., *The products of the thermal decomposition of CH_3CHO.* The Journal of Chemical Physics, 2011. **135**(1): p. 014306.

[157] Shaw M.F., et al., *Photo-tautomerization of acetaldehyde as a photochemical source of formic acid in the troposphere.* Nature Communications, 2018. **9**: p. 2584.

[158] Andrews D.U., et al., *Photo-tautomerization of acetaldehyde to vinyl alcohol: a potential route to tropospheric acids.* Science, 2012. **337**(6099): p. 1203-1206.

[159] Matti G.Y., et al., *Photoelectron spectroscopic detection of vinyl alcohol, CH_2CHOH: evidence for the syn and anti rotamers.* Electron Spectroscopy and Related Phenomena, 1989. **49**(2): p. 195-201.

[160] Wang J., et al., *Interstellar enols are formed in plasma discharges of alcohols.* Astrophysical Journal, 2008. **676**(1): p. 416-419.

[161] Agundez M., et al., *O-bearing complex organic molecules at the cyanopolyyne peak of TMC-1: Detection of C2H3CHO, C2H3OH, HCOOCH3, and CH3OCH3.* ASTRONOMY & ASTROPHYSICS, 2021. **649**.

[162] Bennett C.J., et al., *Laboratory studies on the formation of three C_2H_4O isomers—acetaldehyde (CH_3CHO), ethylene oxide (c-C_2H_4O), and vinyl alcohol (CH_2CHOH)—in interstellar and cometary ices.* Astrophysical Journal, 2005. **634**(1): p. 698-711.

[163] Melosso M., et al., *Astronomical search of vinyl alcohol assisted by submillimeter spectroscopy.* ACS Earth and Space Chemistry, 2019. **3**(7): p. 1189-1195.

[164] Elango M., et al., *Quantum chemistry of C_3H_6O molecules: structure and stability, isomerization pathways, and chirality changing mechanisms.* Journal of Physical Chemistry A, 2010. **114**(36): p. 9864-9874.

[165] Blitz M.A., D.E. Heard and M.J. Pilling, *OH formation from $CH_3CO + O_2$: a convenient experimental marker for the acetyl radical.* Chemical Physics Letters, 2002. **365**(5-6): p. 374-379.

[166] Carr S.A., et al., *OH yields from the $CH_3CO + O_2$ reaction using an internal standard.* Chemical Physics Letters, 2007. **445**(4-6): p. 108-112.

[167] Gross C.B.M., T.J. Dillon and J.N. Crowley, *Pressure dependent OH yields in the reactions of*

CH_3CO and $HOCH_2CO$ with O_2. Physical Chemistry Chemical Physics, 2014. **16**(22): p. 10990-10998.

[168] Hou H., et al., *Mechanistic and kinetic study of the $CH_3CO + O_2$ reaction.* The Journal of Chemical Physics, 2005. **122**(22): p. 224304.

[169] Weidman J.D., et al., *High-level theoretical characterization of the vinoxy radical ($\bullet CH_2CHO$) + O_2 reaction.* The Journal of Chemical Physics, 2018. **148**(18): p. 184308.

Acknowledgement

As a co-tutelle PhD student, it is my fortunate to have been able to study and work at both University of Science and Technology of China in Hefei, China and University of Lille in Lille, France. During my time in Hefei, I am grateful to my supervisor, researcher ZHANG Weijun, and TANG Xiaofeng, for providing me with guidance and assistance in my research work. Thank you to associate researcher LIN Xiaoxiao and professor LONG Bo for their kind help in theoretical calculations.

Thank you to my friends WEN Zuoying, WANG Chengcheng, WANG Tao, LIU Pengcheng, MA Ziji, YUE Hao, HU Rongrong, LIU Lingyu, MA Lan, XIA Yu, YANG Nana, ZHOU Jiacheng and WANG Chunhui for their help. Thank you to the other researchers for their assistance, thank you to GU Xuejun, ZHAO Weixiong, GAI Yanbo, HU Changjin, WEI Nana, WANG Shuo and ZHANG Yang. In addition, during the experiment at the National Synchrotron Radiation Laboratory in Hefei, I would like to express my gratitude to engineer YANG Jiuzhong, PhD student LI Yanbo, ZHU Long for their enthusiastic help.

During my time at Lille, I would like to express my gratitude to Dr. PILLIER Laure and SCHOEMAECKER Coralie for their kind help in the experiment. Thank you to engineers BATUT Sebastien, DEMAUX Pascal and LAHCCEN Amaury for their kind help in maintaining experimental instruments. Thank you to Gosselin Sylvie for the security guidance. Thank you to Dr. LI Chuanliang and PhD students SHAMAS Mirna, SHAMAS Nesrine and ASSALI Mohamed for their help in experiments and life. In addition, I participated in projects in SOLEIL and Swiss light source. Thank you to staff Dr. NAHON Laurent, GARCIA Gustavo A., LOISON Jean Christophe and Dr. HARTWEG Sebastian for their guidance and assistance in the experiment. Thank you to Dr. HEMBERGER Patrick, ZHANG Zihao, WU Xiangkun and LUO Peiling for their kind help in the experiment and data processing.

Finally, I sincerely thank my supervisor, FITTSCHEN Christa, your

encouragement, support, and guidance in my work will benefit me for my whole life. I will keep your guidance in mind and pass on this love to others. For my life in Lille, you have brought me endless warm and love, thank you and Didier for making me feel at home.